Optimization of Mechanical and Electrical Properties in Age-Hardened Aluminum Alloy through HPTE Processing

TECHNISCHE
UNIVERSITÄT
DARMSTADT

Dissertation approved by the department of

Materials and Earth Sciences

in fulfillment of the requirements for the degree of

Doctor of Engineering

(Dr. Ing.)

by

Vahid Tavakkolisaiej

Referee: Prof. Dr. Christian Kübel

Co-referee: Prof. Dr. Karsten Durst

Date of Oral exam: 28.04.2025

Darmstadt 2025

Vahid Tavakkolisaiej: Optimization of Mechanical and Electrical Properties in Age-Hardened Aluminum Alloy through HPTE Processing

Darmstadt, Technische Universität Darmstadt

Year thesis published in TUprints 2025

Date of the viva voce 28.04.2025

Erklärung zur Dissertation

Hiermit versichere ich, dass ich meine Dissertation selbständig und nur mit den angegebenen Quellen und Hilfsmitteln angefertigt habe. Die Arbeit wurde bisher keiner anderen Prüfungsbehörde vorgelegt und noch nicht veröffentlicht.

Karlsruhe, 10.01.2025

Vahid Tavakkolisaiej

Acknowledgement

I am deeply grateful to my mentor, Professor Christian Kübel, for inspiring me to explore complex ideas and question conventional wisdom. His mentorship not only guided me through the theoretical aspects of my research but also helped me hone my analytical and critical thinking skills. I am equally thankful to my thesis group leaders, Dr. Julia Ivanisenko, Dr. Andrey Mazilkin, and Dr. Torsten Scherer, for their constructive feedback and invaluable suggestions, which significantly improved the quality of my work.

I would also like to express my profound gratitude to my colleagues and co-workers at the Institute of Nanotechnology (INT). Their unwavering support and inspiration have been crucial to my professional development. The collaborative efforts, coupled with the friendship and intellectual discourse with my peers have made this journey both enriching and enjoyable. I would particularly like to thank Dr. Di Wang and Dr. Sabine Schlabach for their generous support, comprehensive technical training, and insightful guidance. Additionally, I am deeply thankful to the Karlsruhe Nano Micro Facility (KNMFi) for providing access to cutting-edge FIB and TEM facilities, which were instrumental in the success of my research.

Furthermore, I would like to express my deepest appreciation to the German Academic Exchange Service (DAAD) for their financial support. Their funding made it possible for me to pursue my doctoral studies at the Karlsruhe Institute of Technology (KIT) and Technische Universität Darmstadt (TUDa), enabling me to focus entirely on my research and academic development.

Additionally, I would like to extend my gratitude to ChatGPT and other AI-based language tools for their assistance in refining the grammar and enhancing the clarity of this acknowledgment.

Last but not least, I am profoundly thankful to my family and friends for their unconditional love, patience, and unwavering belief in me. My parents, whose unceasing sacrifices and resolute faith have been the cornerstone of my success, have provided me with the strength and motivation to pursue my dreams. My siblings, with their constant encouragement and shared moments of joy and support, have made even the most challenging times manageable.

Vahid Tavakkoli

Karlsruhe, 2025

Abstract

Aluminum alloys are commonly used due to their versatility and tunability of properties through addition of solutes and heat treatments. This study focuses on age-hardenable Al-Mg-Si alloys, which are lightweight and extensively used in the electrical industry. Precipitate hardening is the way to improve strength in this alloy system, where the size of precipitates depends on temperature and aging time. However, the presence of solute atoms is problematic as it degrades electrical conductivity (EC) by reducing the mean free path of conducting electrons. This inherent trade-off between strength and electrical conductivity presents significant challenges for industrial applications, where both properties are crucial for optimal overall performance.

This bottleneck serves as the primary motivation for this study, focusing on simultaneous improvement of strength and EC. In this study, we introduce an approach that combines severe plastic deformation with subsequent heat treatment to optimize both strength and conductivity. Despite the proven efficacy of severe plastic deformation in strengthening materials, previous studies in this direction have predominantly operated in a limited scope of laboratory scale. Our research aims to bridge this gap by exploring the application of high-pressure torsion extrusion (HPTE) as a viable method for implementing these techniques at a larger scale. Mechanical properties were evaluated by microhardness and tensile testing. The results showed a remarkable improvement in strength while EC remained unchanged. Furthermore, modeling of strength and EC, based on microstructural characterization, revealed good agreement with experimental values.

The second objective is to conduct an atomic-level investigation of the precipitates formed under conditions of extreme deformation and subsequent annealing. Advanced microscopy and EDX microanalysis demonstrated that the material processing led to the development of various hardening phases with distinct morphologies and compositions. The high density of defects induced by HPTE deformation resulted in a predominantly disordered structure for most particles. The particles exhibit a set of orientation relations with the Al matrix, which differ from those established for the studied alloy. Furthermore, a considerable number of nanometer-sized precipitates exhibit a core-shell structure or evidence of simultaneous co-precipitation of several secondary phase particles. These observations lead to the conclusion that nucleation and growth of hardening precipitates occur in non-equilibrium conditions.

Zusammenfassung

Aluminiumlegierungen werden aufgrund ihrer Vielseitigkeit und der Einstellbarkeit ihrer Eigenschaften durch Zugabe von Legierungselementen und Wärmebehandlungen häufig eingesetzt. Diese Studie konzentriert sich auf aushärtbare Al-Mg-Si-Legierungen, die leicht sind und in der Elektroindustrie weit verbreitet verwendet werden. Die Festigkeitssteigerung in diesem Legierungssystem erfolgt durch Ausscheidungshärtung, wobei die Größe der Ausscheidungen von der Temperatur und der Alterungszeit abhängt.

Allerdings ist die Anwesenheit von gelösten Atomen problematisch, da sie die elektrische Leitfähigkeit (EC) verschlechtert, indem sie die mittlere freie Weglänge der Leitungselektronen verringert. Dieser grundlegende Zielkonflikt zwischen Festigkeit und Leitfähigkeit stellt eine erhebliche Herausforderung für industrielle Anwendungen dar, bei denen beide Eigenschaften für eine optimale Gesamtleistung entscheidend sind.

Dieser Zielkonflikt stellt die zentrale Motivation dieser Arbeit dar, die sich auf die gleichzeitige Verbesserung von Festigkeit und Leitfähigkeit konzentriert. In dieser Studie stellen wir einen Ansatz vor, der schwere plastische Verformung mit anschließender Wärmebehandlung kombiniert, um beide Eigenschaften zu optimieren. Trotz der nachgewiesenen Wirksamkeit schwerer plastischer Verformung zur Festigkeitssteigerung beschränkten sich frühere Studien meist auf den Labormaßstab. Unser Ziel ist es, diese Lücke zu schließen, indem wir den Einsatz der Hochdruck-Torsionsextrusion (HPTE) als praktikable Methode zur Umsetzung dieser Techniken im größeren Maßstab untersuchen.

Die mechanischen Eigenschaften wurden durch Mikrohärte- und Zugversuche bewertet. Die Ergebnisse zeigten eine deutliche Festigkeitssteigerung bei gleichbleibender elektrischer Leitfähigkeit. Darüber hinaus zeigte die Modellierung von Festigkeit und Leitfähigkeit auf Grundlage mikrostruktureller Charakterisierung eine gute Übereinstimmung mit den experimentellen Werten.

Das zweite Ziel der Arbeit ist die Untersuchung der Ausscheidungen auf atomarer Ebene, die unter Bedingungen extremer Verformung und anschließender Glühbehandlung entstanden sind. Hochauflösende Mikroskopie und EDX-Analysen zeigten, dass die Materialverarbeitung zur Bildung verschiedener Härtungsphasen mit unterschiedlichen Morphologien und Zusammensetzungen führte. Die durch die HPTE-Verformung induzierte hohe Defektdichte resultierte in einer überwiegend ungeordneten Struktur der meisten Partikel. Die Partikel zeigen eine Reihe von

Orientierungsbeziehungen zur Al-Matrix, die sich von denen in der Literatur beschriebenen unterscheiden.

Darüber hinaus weisen zahlreiche Ausscheidungen im Nanometerbereich eine Kern-Schale-Struktur oder Hinweise auf eine gleichzeitige Ko-Ausscheidung mehrerer sekundärer Phasen auf. Diese Beobachtungen führen zu dem Schluss, dass die Keimbildung und das Wachstum der Härtungsausscheidungen unter Nicht-Gleichgewichtsbedingungen erfolgen.

Contents

List of figures

List of tables

List of abbreviations

ADF	Annular dark field
APT	Atom probe tomography
ARB	Accumulative role bonding
BF	Bright field
BSE	Backscatter electrons
BF-TEM	Bright field TEM
CWMP	Convolutional multiple whole profile
CBED	Convergent beam electron diffraction
CCD	Charged coupled device
CMOS	Complementary metal-oxide-semiconductor
DF-TEM	Dark field TEM
DSC	Differential scanning calorimetry
ECAP	Equal channel angular pressing
EDX	Energy-dispersive X-ray spectroscopy
EELS	Electron energy-loss spectroscopy
FEG	Field emission gun
FEM	Finite element method
FFT	Fast Fourier transform
FIB	Focus ion beam
FWHM	Full width of half maximum
GIF	Gatan image filter
HAADF	High-angle annular dark-field
HPT	High pressure torsion
HPTE	High pressure torsion extrusion
SAED	Selected area electron diffraction
SEM	Scanning electron microscopy
SFE	Stacking fault energy
SPD	Severe plastic deformation

SDD	Silicon drift detector
STEM	Scanning transmission electron microscopy
TEM	Transmission electron microscopy
UFG	Ultrafine-grain
UTS	Ultimate tensile test
XRD	X-ray diffraction
4D	Four-dimensional

Chapter 1

1. Motivation and structure of dissertation

Global industry demand for light metals is steadily increasing, driven by an urgent need to reduce costs and enhance performance in various sectors. This surge in demand is particularly fueled by the ongoing push for energy efficiency, environmental sustainability, and technology advancements. Aluminum has been a game-changer in many industries such as transportation, packaging, construction, electronic, aerospace and medical device due to its unique properties, e.g., high conductivity, resistance to corrosion and fatigue, and high strength/weight ratio. [1]–[5] Another unique property of aluminum is that it is easy to recycle: approximately 75 % of all aluminum ever produced is still in use and the energy needed to recycle aluminum is only about 5 % of the energy to produce it from ore. [6]

Initially, the use of aluminum was limited by its relatively low strength. [7] This was until the revolutionary discovery of the German scientist Alfred Wilm, who observed an unprecedented increase in strength of Al-Cu alloys at room temperature. This marked a pivotal point in the understanding of the properties and applications of aluminum alloys. [8] Subsequent studies showed that this improvement in strength was due to the formation of fine particles as a result of natural aging processes. [9]–[11] The hardening can be accelerated by aging at elevated temperatures, called artificial aging (AA). [12]–[14] However, it is important to note that this "aging" heat treatment is limited in its applicability and is primarily suitable for specific series of aluminum alloys, such as 2XXX, 6XXX, 7XXX. For effective precipitation hardening treatment, the precipitate particles must exhibit coherence and coplanarity with the matrix, [15]–[17] Which induce a strain field due to the lattice mismatch with the surrounding matrix.

The process of precipitation hardening involves complex precipitation sequences, encompassing various metastable phases. Furthermore, it involves a dynamic interaction among nucleation, growth, coarsening, and dissolution phenomena within the microstructure of the alloy, which adds a layer of complexity in processing and tuning the alloy properties. [18]–[20] The hardening mechanism can be either shear or Orowan mechanism, depending on the nature of the precipitate, such as size, shape, chemical composition, and coherence, all of which undergo significant changes over aging time. [21][22] This discovery marked a tremendous development in materials science, prompting extensive research in this field. For aluminum age hardened alloys, a sequence of precipitates which appear with increasing treatment duration was discovered and their crystal structure established. [23]–[26] Currently, there is a range of age hardened aluminum alloys doped with various elements such as Mg and Si (Al 6XXX), Cu (Al 2XXX), or Zn (Al 7XXX). [27] This allows for precise control of material properties, opening up an opportunity to develop new alloys to meet specific requirements. For instance: application of Al 2XXX in aircraft industry due to its excellent strength-to-weight ratio or application of Al 6XXX in electrical industry for high strength-conductivity material.

The significance of aluminum in the electrical industry cannot be underestimated, as it plays a crucial role in various electrical applications and infrastructures. Aluminum alloys are widely used in the production of conductors for power transmission and distribution. Its high electrical conductivity, coupled with a significantly lower density compared to traditional copper, enables efficient and cost-effective transmission of electricity over long distances. Low weight is particularly advantageous in overhead power lines where wire slack must be minimized to maintain the overall integrity of the electric infrastructure. Although alloying by various elements increases the strength of the material, it also decreases its electrical conductivity, since impurity atoms and second-phase precipitates act as scattering sites for conducting electrons. Therefore, there is a need to carefully optimize the properties, finding a balance between achieving the desired mechanical strength and maintaining necessary electrical characteristics. One effective approach to solve this problem is the use of severe plastic deformation (SPD) followed by AA. [28]–[30] This method serves a dual purpose. Deformation introduces a high density of defects. These defects subsequently act as potential nucleation sites for precipitates, which increases the number of particles per unit volume. Both effects lead to an increase in the strength of the material. At the same time, the formation of particles of the second phases simultaneously leads to a decrease in the concentration of impurities in the solid solution, which has a beneficial effect on the conductivity of the alloy.

A literature review on this topic reveals a need for further studies. Most SPD procedures performed to date have been limited to laboratory scale samples. Although these laboratory studies contributed to a fundamental understanding of the processes that occur in a material during SPD, in particular the formation of non-equilibrium structures with a high density of defects, the resulting alloy samples were not applicable at an industrial scale. In addition, the crystal structure of precipitates formed in severely deformed aluminum alloys under highly non-equilibrium conditions of crystalline defects remains poorly studied. Using advanced techniques that allow investigation of structural features with atomic resolution is important for understanding the mechanisms of strengthening. The goal of this thesis is to address these gaps by employing high-pressure torsion extrusion (HPTE) as an SPD method, chosen for its potential scalability in an industrial context, and advanced structural characterization of the produced micro- and nanostructural features.

A set of advanced characterization methods was used for a systematic and comprehensive analysis to understand the processes in the material during SPD and AA. The mechanical properties were studied using tensile tests and microhardness measurements; electrical conductivity was measured using the eddy current method; the structural characteristics were investigated using various analysis techniques, including X-ray diffraction (XRD), scanning electron microscopy (SEM), advanced transmission electron microscopy (TEM), and atom probe tomography (APT).

The background for precipitation hardening and its thermodynamics, as well as the phase composition of the investigated aluminum alloy will be discussed in Chapter 2. Chapter 3 will provide an introduction to methods applied for the material characterization, both its physical properties and structural features. The results of the study will be presented in Chapter 4, 5 and 6 along with a discussion and literature review. Finally, a conclusion and outlook will be presented in Chapter 7.

Chapter 2

2. Aluminum and Aluminum alloys

This chapter provides an introduction to strengthening mechanisms of aluminum alloys. Attention is given to a detailed examination of the Al-Mg-Si alloys, with particular emphasis on the impact of solutes on their mechanical and electrical properties. The final section of this chapter is devoted to severe plastic deformation methods and their application to improve the properties of metallic materials.

2.1. Aluminum story

Aluminum is the third most abundant element on Earth and plays a key role in modern engineering. [31] In its pure state, aluminum possesses a face-centered cubic (FCC) crystal structure, belonging to space group 225 ($Fm\bar{3}m$). The lattice constant of aluminum at room temperature is 4.045 Å. [32] Due to a low density of 2.7 g/cm³ and considerably high electrical and thermal conductivity, aluminum finds extensive application in automotive, aerospace, and electrical engineering. [33][34] As shown in Figure 2.1, aluminum production has exceeded that of copper since 1965, and its initial high price has now become comparable to the price of copper. Thus, aluminum has become an effective and competitive alternative to copper in the electrical industry. Despite its lower electrical conductivity compared to copper (~56%), its low density makes it a cost-effective material choice for overhead power lines. Aluminum exhibits good resistance to atmospheric corrosion, which is attributed to the formation of a durable oxide layer that provides protective shielding from further corrosion.
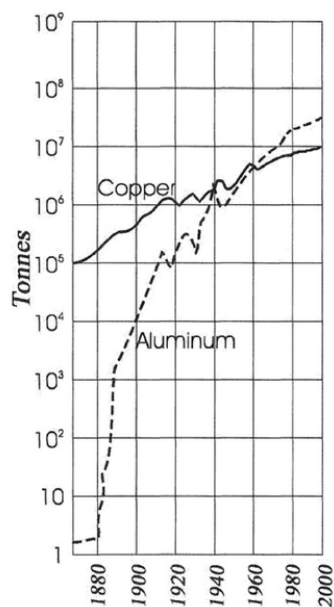
(a)
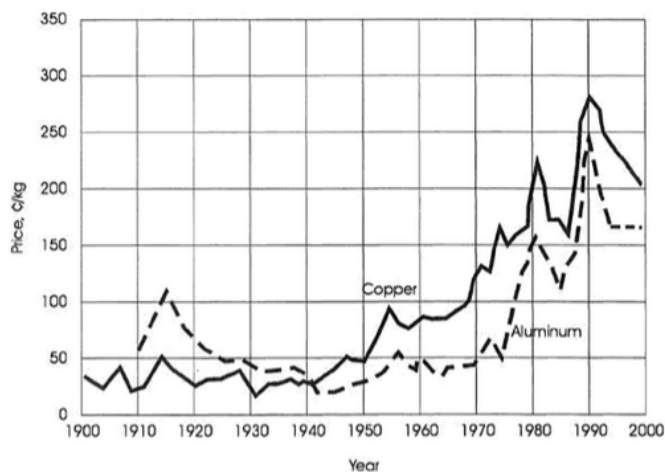
(b)

Figure 2.1. World production and price of Al compared to Cu [31]

Aluminum is not found in its pure form in nature due to its high chemical reactivity. It commonly exists in oxidized states, such as in bauxite, from which aluminum oxide is extracted. This oxide is then subjected to electrolysis to obtain pure metallic aluminum. Pure aluminum, which is soft and silvery-white, has limited applications due to its low tensile strength of around 40 MPa. Therefore, to enhance its strength, aluminum is often alloyed with other elements. The strengthening mechanism is elaborated in next section.

2.2. Strengthening mechanisms in metals and alloys

There are several mechanisms which contribute to strengthening of pure metals and alloys such as solid solution strengthening, strain hardening, grain refinement and precipitation hardening. [35] This section will provide a brief overview of these four key mechanisms.

2.2.1. Solid solution hardening

Atoms of individual elements can form solid solution when the corresponding change in Gibbs free energy (ΔG) is negative, as expressed by the equation $\Delta G = \Delta H - T\Delta S$. [36]

There are two types of solid solutions: 1) interstitial solid solution (Figure 2.2a), in which alloying atoms occupy interstitial sites in the lattice structure. For instance, the FCC and BCC crystal structures can accommodate solute atoms in two different types sites – tetrahedral and octahedral. These sites are smaller than the size of host lattice atoms, so the stable formation of such a solution is only possible for small atoms, such as hydrogen, carbon, nitrogen. 2) substitutional solution (Figure 2.2b) that occurs when a dissolved atom takes the place of a matrix atom in the lattice. Most binary systems form substitutional solid solutions. W. Hume-Rothery formulated a set of rules to predict when significant solubility can be expected: (i) the difference in atomic radii should not exceed 15%, (ii) small difference in electronegativity and (iii) the particular number of valence electrons of the components is required. However, several studies have reported that immiscible components and those with a larger atom size differences can form a meta-stable solid solution, e.g. by mechanical mixing. [37][38]

(a)   (b)
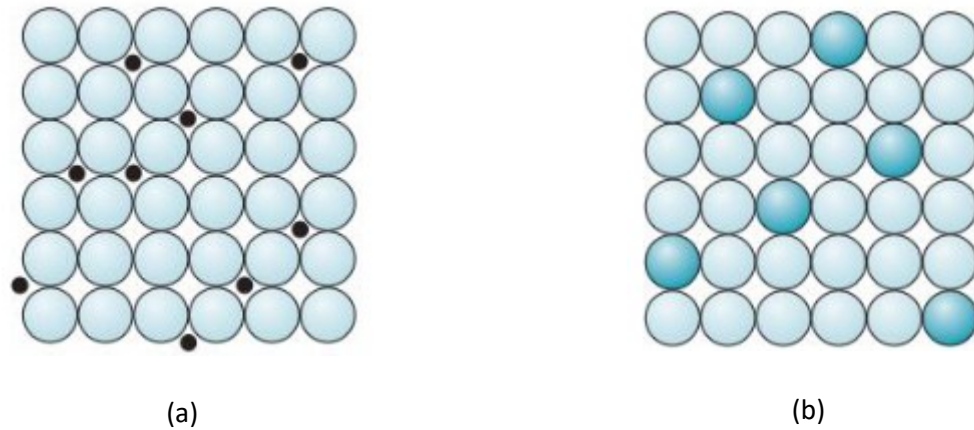
Figure 2.2. Schematic representation of (a) interstitial and (b) substitutional solid solution. Adopted from [39]

The incorporation of solute atoms into the host lattice contributes to its strengthening due to the elastic stress field around the solute atoms. The stress field serves as an obstacle to the movement of dislocations since they require additional external stress to overcome. The contribution to yield strength, σ_{ss}, from elements in solid solution can be expressed as follows: [40]

$$\sigma_{ss} = \sum_j k_j \, c_j^{2/3},$$
         2.1

here, c_j is the concentration of a solute element in solid solution and k_j is its corresponding scaling factor.

Reyen et. al investigated the effect of magnesium and manganese solid solution in aluminum alloy. [35] They found that the both elements show linear concentration dependence of strength at a given

strain. Figure 2.3 (a and b) show the stress at various strain level against the concentration of Mg and Mn (in at. %). The result corresponds to the equation 2.1 when the exponent is close to unity. They also reported that Mn solutes contribute larger in strengthening compared to Al-Mg case.

(a)   (b)
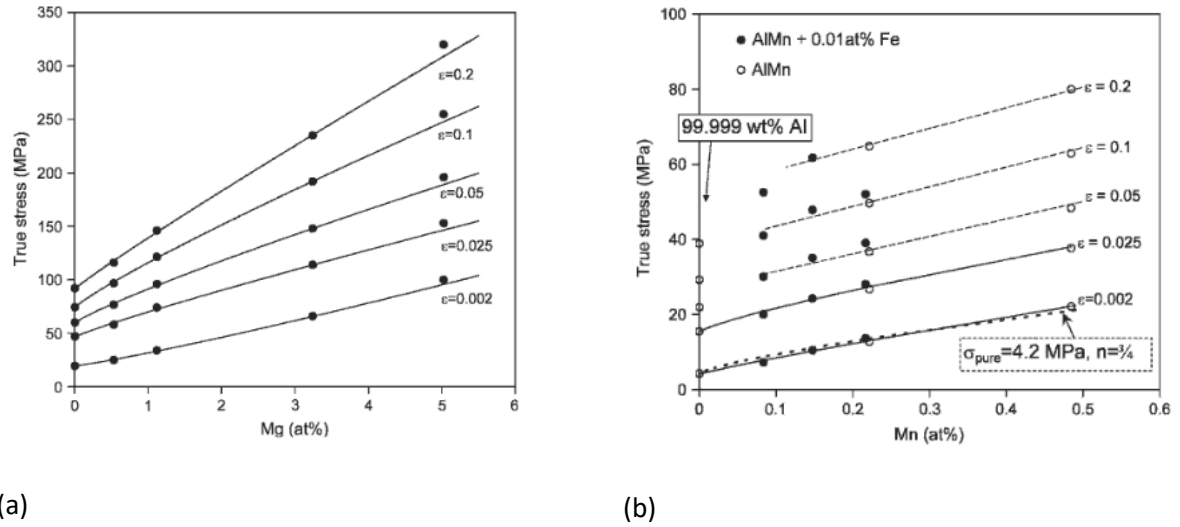
Figure 2.3. Flow stress at various strain levels as a function of (a) Mg and (b) Mn content (at. %) [35]

2.2.2. Dislocations and strain hardening

Plastic deformation is a permanent change in shape where the displacement of interatomic bonds remains even after the applied forces are removed. During plastic deformation of a metal, along with a change in a sample shape, mechanical properties usually also change — in particular, strength increases. This phenomenon is called strain hardening. A large number of dislocations are formed in a deformed material, since dislocation glide is the most important deformation mechanism. Dislocations create long-range stress fields, which act on neighboring dislocations and makes it difficult for them to glide easily, thereby contributing to the strengthening effect. Additionally, some dislocations lie in a plane that is not the gliding plane of the material (sessile dislocations) and also act as an obstacle to the gliding of other dislocations, also contributing to the hardening effect. [41] The degree of strain hardening is influenced by factors like applied strain, temperature, and the initial microstructure of the material. Strain hardening plays an important role in the formation of the mechanical properties during deformation processing, such as rolling, extrusion, forging, *etc*. The contribution from dislocations to the yield stress can be expressed by the Bailey-Hirsch relation:

$$\sigma_d = M\alpha Gb\sqrt{\Lambda}, \qquad\qquad 2.2$$

where M is Taylor factor, α is constant of the order 0.2–0.3, depending on alloy composition, G is shear modulus, b is burgers vector and Λ is dislocation density. M is considered to be 3 for non-textured FCC structure. [42]

Dislocation density can be determined by means of TEM and XRD methods. For example, in order to calculate dislocation density, following equation can be used [43][44]:

$$\Lambda = \frac{2\sqrt{3}\varepsilon}{db}, \qquad\qquad 2.3$$

where d is the mean crystallite size and ε is micro strain in material. Williamson and Smallman proposed another equation for dislocation density as follow [45]:

$$\Lambda = 16.1^{\frac{\varepsilon^2}{b^2}}. \qquad\qquad 2.4$$

Both micro strain and crystallite size can be determined from the analysis of the line broadening of the diffraction peaks. However, the recently developed convolutional multiple whole profile (CMWP) fitting method is more accurate to determine the dislocation density by applying combine Levenberg-Marquart fitting procedure and Monte Carlo statistical method. [46]

Dislocation density also possible to measure by direct methods such as TEM, however, the determination of average dislocation density values in heterogeneous microstructures by TEM is time consuming owing to the demanding sample preparation technique involved. [47] Furthermore, it analyzes dislocations only in a very small volume of the sample, which may not be a representative of the bulk sample and hence may not give correct estimation of dislocation density. Gallet. *et al*. has conducted a quantitative comparison study in dislocation density measurement between different techniques. [48] They reported that for small dislocation density ($< 10^{13}$ m^{-2}) imaging methods are rather performant, whereas XRD measurements suffer from high uncertainty levels. For higher dislocation density levels, imaging methods are no longer relevant because of the increasing uncertainty arising from local contrast variation and overlapping of dislocations.

The dislocation density usually decreases quite quickly during annealing of deformed metals. The rate of this process is determined by the annealing temperature and also by the stacking fault energy (SFE) of the material. Aluminum is a material with high SFE, which enhances the ability of dislocations to cross-slip, and leads to a drain of dislocations at grain boundaries, or to their mutual annihilation during annealing. [49] Gubicza *et al*. investigated the changes in dislocation density by CMWP method with X-

ray diffraction in Al-Zn-Mg-Zr alloy deformed by high pressure torsion (HPT). [50] They found that the HPT-processed alloy has a small grain size of about 200 nm and a high dislocation density of about 8×10^{14} m^{-2}. However, aging at 120 and 170 ˚C resulted in a significant decrease in the dislocation density to ~ 2.6×10^{14} m^{-2} and 0.4×10^{14} m^{-2} respectively due to high driving force of recovery.

2.2.3. Grain refinement

Reduction in grain size of a polycrystalline material also leads to strengthening. Grain boundaries act as barriers to dislocation glide in crystallographic lattice planes, hindering dislocations from propagating through the material, and thereby increasing its strength. [51] The contribution of grain boundaries to the yield stress is expressed by the Hall-Petch equation:

$$\sigma_{GB} = kd^{-1/2}, \qquad\qquad 2.5$$

where d is the average grain diameter and k is a constant, which depend on the material. It is equal to 0.065 MPa·m^{-1} for pure Al. [52]

However, it is important to note that for nanostructured materials with a grain size less than approximately a few tens of nanometers, this law is violated and the so-called inverse Hall–Petch behavior is observed. [53][54] This behavior is a consequence of the transition of the deformation mechanism from the dislocation glide to thermally-activated phenomena. [55][56] These thermally-activated phenomena, including diffusional creep, grain-boundary sliding, or mutual grain rotation, have been experimentally observed at room temperature in certain nanograined materials. [57][58][59]

Various techniques can be used for grain refinement. One common way involves the use of SPD methods, in which the material is subjected to large shear deformation and the grain size can be reduced to sub-micrometer or nanometer levels depending on the experimental conditions. [60] A brief description of the two SPD techniques, i.e., HPT and HPTE is given in section 2.5.

Numerous studies have been conducted on aluminum and its alloys can be cited as an example of the use of SPD for structural refinement. [61]–[63] Pure aluminum has a rather low yield strength, approximately 30MPa [64], and grain refinement is one of the ways to increase its strength characteristics. Lucif *et al*. conducted experiments to study the evolution of the microstructure of a commercial Al-0.6% Mg-0.4% Si alloy and its hardness during HPT processing. [65] HPT was performed at various degree of deformation (number of anvil rotation). The σ *vs.* d$^{-1/2}$ plot is shown in Figure 2.4. It exhibits the usual Hall–Petch relationship at larger grain size, d$^{-1/2}$ less than 1500 m$^{-1/2}$, whereas at smaller

grain size there is a deviation towards the inverse Hall-Petch relationship. Similar deviation has been reported in other studies for different materials. [66][67][68]
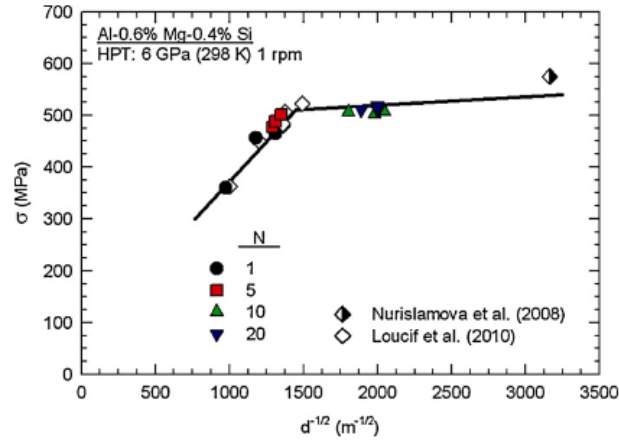
Figure 2.4. The Hall–Petch relationship for samples processed through 1, 5, 10 and 20 turns of anvils during the HPT treatment. [65]

2.2.4. Precipitation hardening

Precipitation hardening, also known as age hardening, is another strengthening method often used in metallurgy. Precipitation hardening is based on the formation of finely dispersed particles within the alloy. Particles formed during the aging process create obstacles to the dislocation glide and therefore increase the strength of the material. These particles or precipitates typically result from the controlled decomposition of a supersaturated solid solution (SSSS) during annealing. The key to successful precipitation hardening is a carefully selected heat treatment process. Aging can be natural or artificial. Natural and artificial aging differ in their mechanisms, driving forces, and dependence on temperature and time. While natural aging occurs spontaneously at ambient temperature and is driven by thermodynamic reasons, artificial aging involves a controlled heat treatment process at higher temperature to accelerate the diffusion of solute atoms. The final product of these processes will be determined by both thermodynamic and kinetic factors.

The first stage of artificial aging is solution heat treatment, in which the alloy is heated to a temperature above the solvus temperature to dissolve all secondary phases and form a homogeneous solid solution. Equally important is the cooling procedure, in which slow cooling can lead to precipitation at triple junctions and grain boundaries, leading to embrittlement and possible fracture at grain boundaries. This undesirable result can be avoided by rapid cooling to form a SSSS. Upon subsequent

heating, the precipitates uniformly nucleate within the grains due to low temperature. Therefore, in the final stage, the SSSS is heated to an elevated temperature to decompose and form finely dispersed precipitates. This process is shown schematically in Figure 2.5.
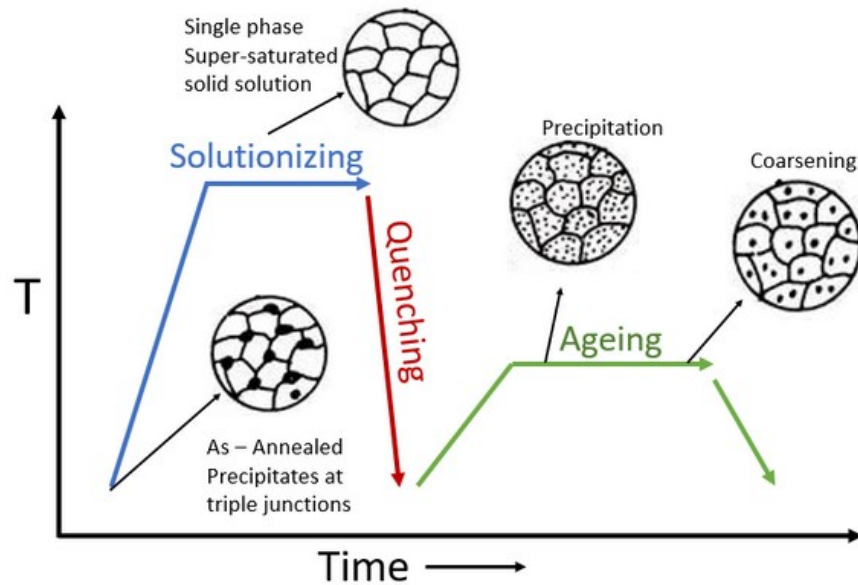
Figure 2.5. Steps of age-hardening treatment. Adopted from [69]

With increasing annealing time at a given temperature, the precipitates grow in size. The driving force behind this process is the thermodynamic potential (ΔG) associated with the formation of stable precipitates from a supersaturated solid solution, and decrease in the particles interfacial energy. This process initially leads to an increase in hardness (Figure 2.6), which at a certain point reaches a maximum associated with a high number density of metastable, semi-coherent precipitates – a condition known as the peak-aged state. With further AA, the hardness decreases due to the transformation into a coarser precipitates structure. This condition is usually referred to as the over-aged state.
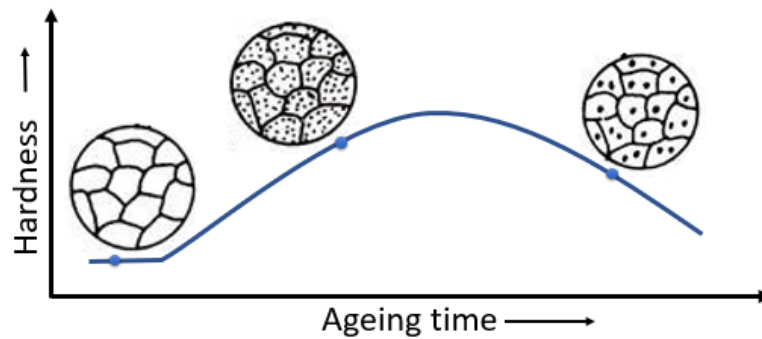
Figure 2.6. Hardness behavior vs. precipitate size. Adopted from [69]

The efficiency of age hardening is determined by several factors, in particular the volume fraction and size of precipitates, as well as the degree of coherence between the lattices of the solid solution and the particles. [70] The latter affects the nature of the interaction between the precipitates and the gliding dislocations. Figure 2.7a illustrates the two possible mechanisms of interaction between dislocations and precipitates. In the case of small precipitates that are coherent or semi-coherent with the solid solution matrix, a typical response is cutting of particles by dislocations during deformation. As a result, a shift of one part of the particle relative to the other part is observed (Figure *2.7* (a)top). Another way to overcome obstacles, known as the Orowan mechanism, occurs if the lattices of the particle and the solid solution are incoherent. In this case, dislocations can overcome precipitates by bending around particles. As a result, a dislocation loop is formed around the precipitate (Figure 2.7a bottom). Figure 2.7b shows the influence of the particle size on the yield strength for the competition between dislocation shearing and Orowan hardening, in which a maximum strength is reached at the critical diameter r_0 for a fixed volume fraction.
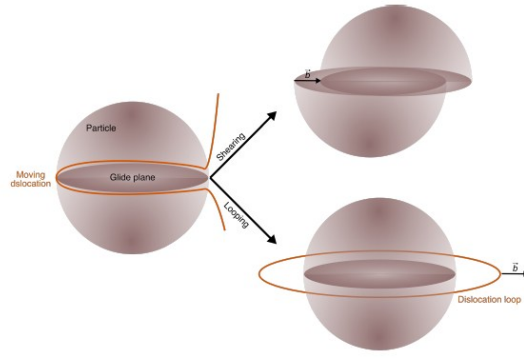
(a)
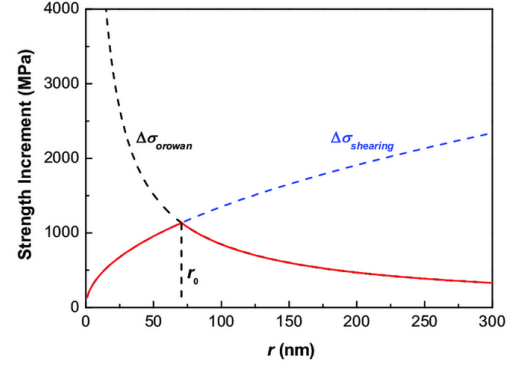
(b)

Figure 2.7 (a) Schematic illustration of a moving dislocation interacting with a spherical precipitate. The precipitate is either sheared or looped by the dislocation and, (b) the variation tendency of yield strength increment with the particle size. The figures in (a) and (b) are adopted by [71] and [72] respectively.

As the dislocation interacts either by looping or shearing mechanism, the contribution of the precipitate hardening to the yield strength can be calculated differently by the following equations:

For shearable particles [73]:

$$\sigma_{prec}^{shear} = \frac{M}{b^2 \sqrt{\beta G}} \sqrt{N \cdot r} \cdot F^{3/2}, \qquad 2.6$$

with G and b being defined as above, β is a constant ($\beta = 0.28$), r is the precipitate radius. N is the number of particles and the obstacle strength for shearable precipitates is determined to be $F = 2\beta G b^2 (r/r_c)$ with r_c being the transition radius between particle shearing and bypassing.

For non-shearable particle:

$$\sigma_{prec}^{Orowan} = \frac{2M\beta G b}{L}, \qquad 2.7$$

where M, β, G and b were defined above. L is inter-particle spacing, which was calculated as $L=N^{-1/3}$. [74] The method to calculate N will be described in details in Chapter 4.

The total yield strength of a material is usually represented as the sum of several different contributions:

$$\sigma_{tot} = \sigma_f + \sigma_{ss} + \sigma_{dis} + \sigma_{GB} + \sigma_p, \qquad 2.8$$

13

here, σ_f is the friction strength of pure Al and σ_{dis}, σ_p, σ_{GB}, σ_{ss} represent dislocation hardening, precipitation hardening, Hall-Petch effect, and solid-solution strengthening.

2.3. Electrical conductivity

The high electrical conductivity of aluminum is attributed to the abundance of free electrons in the lattice. [75] Commercially pure aluminum exhibits higher electrical conductivity compared to aluminum alloys. Despite this advantage, its practical application is limited due low mechanical strength and toughness. [76][77] There is a growing demand for aluminum alloys that possess both high strength and excellent electrical conductivity, especially for applications such as power transmission lines. As discussed above, addition of alloying elements to pure aluminum can significantly enhance its strength. However, this improvement often comes at the cost of reduced electrical conductivity due to the introduction of solute atoms and impurities in the solid solution resulting from the alloying process. Alloys of the Al-Mg-Si system are a widely used as conductors in the electrical industry. Recently, attempts have been made to improve their mechanical characteristics, in particular strength, while maintaining the high formability and electrical conductivity. However, simultaneously achieving this combination of physical properties poses a significant challenge.

In general, all the strengthening mechanisms mentioned in the section above cause distortions in the crystal lattice structure, which can be quantitatively described using well-developed models. [78][79][56][80] The movement of conduction electrons in normal metals is described by the phenomenological Drude´s theory based on Newton's laws of motion and Maxwell-Boltzmann statistics [81], according to which the interaction of electrons with structural defects contributes in the electrical resistance of the material. In particular, distortions of the crystal lattice cause electron scattering and contribute to an increase in electrical resistivity. The electrical resistivity of a metal can be explained based on Matthiessen's rule. It says that the total electrical resistance consists of two components: the temperature-dependent lattice resistivity (ρ_T) and the temperature-independent residual resistivity (ρ_R). The thermal component is due to electron-phonon scattering, and the electrical resistivity of metallic materials tends to increase with increasing temperature. The residual part takes into account the contributions of lattice imperfections and impurities. [82]

The limited applicability of aluminum age-hardening alloys associated with the mutually exclusive behavior of strength and electrical conductivity has generated interest in innovative research. The key strategy for satisfying and harmonizing multidirectional requirements for material properties was the formation of a structure containing finely dispersed precipitates in aluminum matrix. [83] Such a structure

is achieved using special heat treatments, when an SSSS decomposes with the formation of particles of secondary phases and a decrease in the solutes content. With a controlled decomposition process, nano-sized precipitates can be obtained, which effectively strengthen alloy by creating barriers that impede the dislocations mobility. [84] The reduced content of solutes in the matrix increases the mean free path of conducting electrons, which in turn has a positive effect on the electrical conductivity of the alloy. [83][85]

2.4. Al 6XXX alloys and its typical precipitates

As mentioned above, aluminum alloys are known for their versatility and wide application in various industries. This section will review the literature on Al-Mg-Si alloys (series 6XXX), since one of them (grade 6101) is the object of research in this work. Along with the low specific gravity characteristic of aluminum and its alloys, the distinctive features of the Al-Mg-Si system are high strength, good formability, excellent corrosion resistance and considerably high electrical conductivity. Possessing such properties, these alloys have found wide application, including construction engineering, automotive, aerospace, and electrical industries. [86][87][88] The main strengthening method in Al-Mg-Si alloys is recognized as age-hardening, which occurs due to the formation of Mg/Si-based precipitates. [89] Detection of these particles is generally difficult by XRD due to their low volume fraction and small size. Therefore, electron microscopy techniques are commonly used to study these precipitates. Electron microscopy studies of the crystal structure of precipitates in these alloys reveal the presence of several specific compounds, as listed in Table 2.1.

In particular, Lai et al. conducted a study on dislocation-induced precipitates in slightly deformed Al-Mg-Si alloys using high-resolution TEM (HRTEM). [90] Their findings revealed that all precipitates in the AA-treated sample were β''-phase particles (Figure 2.8a). However, after pre-deformation, the precipitate structure in the post-deformation aged sample became significantly more complex. While the majority of matrix precipitates remained as β''-phase, nearly all dislocation-induced precipitates showed varying degrees of disorder, making them difficult to identify (see as Figure 2.8c–f). Under specific imaging conditions, many of these particles displayed locally recognizable periodic features. For example, unit cell dimensions corresponding to β' and U2 phases were identifiable in the precipitates shown in Fig. 3c and d. The precipitate in Fig. 3e exhibited a periodicity of 0.99 nm along <510>Al, characteristic of the β'-phase. Conversely, some precipitates appeared entirely disordered with no recognizable features, as illustrated in Figure 2.8f.
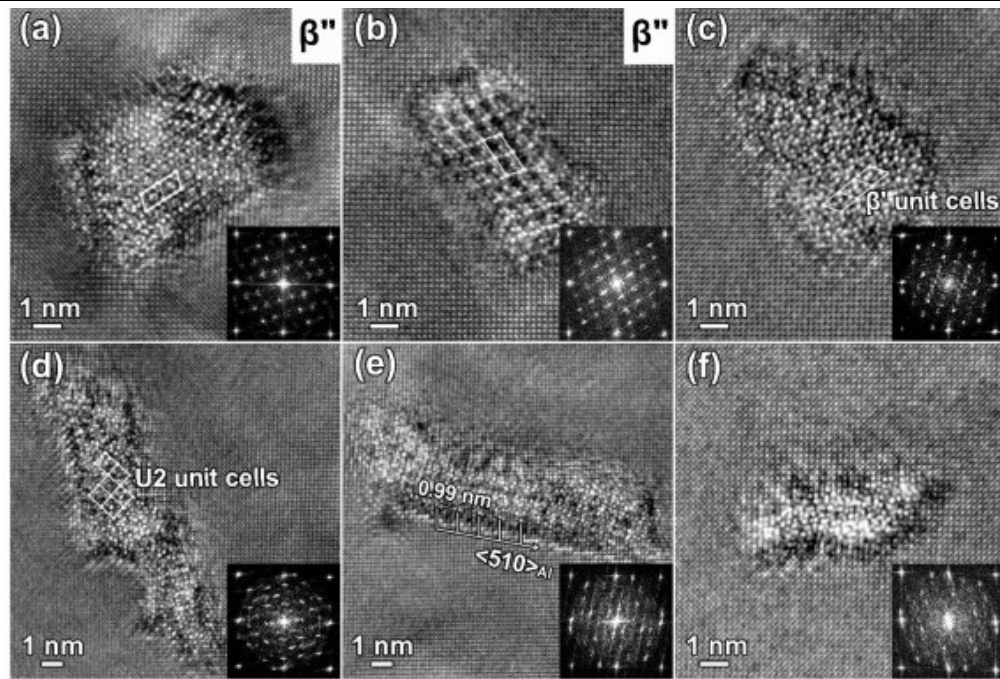
Figure 2.8. HRTEM images showing typical precipitates in (a) AA-treated, and (b–f) the post-deformation aged alloy after peak-aging at 250 °C. The inset in each image is the corresponding FFT pattern. Adopted from [90]

The addition of trace elements to Al-Mg-Si based alloys is another hot topic in research on these materials which can be improved the mechanical properties. [91][92] For instance, addition of traces of Sc results in an improved thermal stability. However, the structural reason for the improvement in properties is not completely clear. Liu *et al*. investigated precipitates formed in an Al-Mg-Si-Sc alloy by means of HR(S)TEM. [93] They demonstrated that this alloy has a distinctly different precipitate microstructures compared to its Sc-free counterpart, in which disordered β" precipitates composed of Sc-free β" sub-units and Sc-containing disordered regions are primarily formed. Upon over-aging, the disordered β" precipitates then evolve into fine composite precipitates containing β" sub-units instead of the coarse β' precipitates.
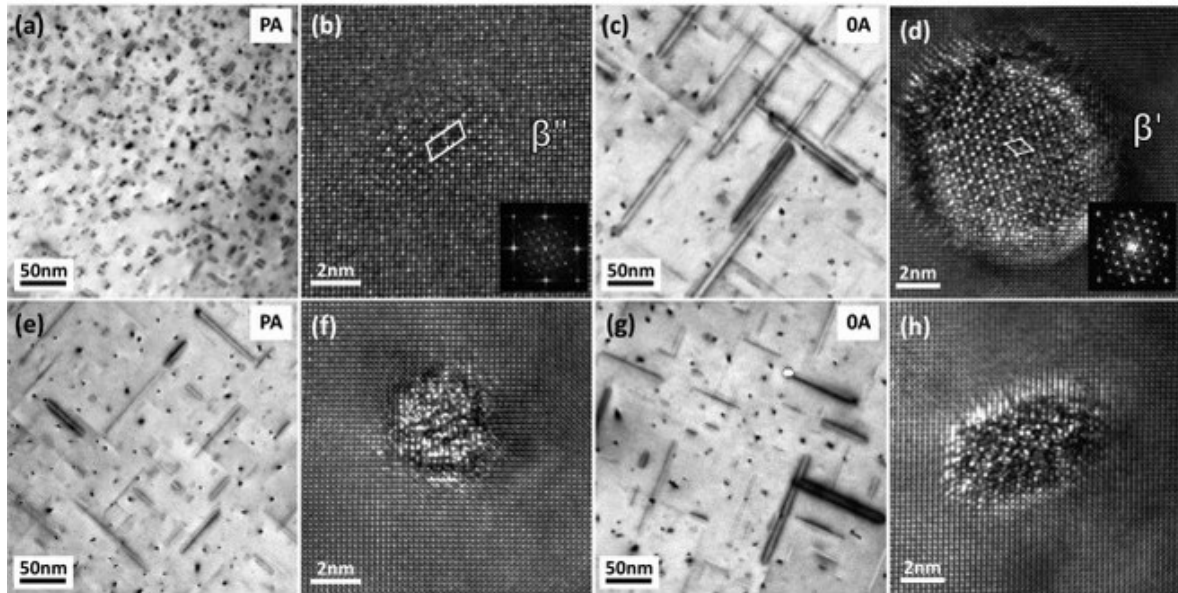
Figure 2.9. TEM bright-field images and the corresponding HRTEM images of the typical precipitates in two alloys aged at 180 °C for different time. (a–d) Sc-free alloy, (e-h) Sc-containing alloy; (a, b, e, and f) 8 h peak-aging, (c, d, g, and h) 100 h over-aging. Adopted from [93]

Low-magnification TEM images and corresponding HRTEM images of the precipitates formed in two alloys under two different aging conditions are presented in Figure 2.8. For Sc-free alloy, the precipitates under both peak-aging and over-aging conditions are uniformly dispersed in the matrix. Their length increased significantly in overaged state compared to the peak aged state. FFT revealed a periodicity corresponding to β" and β' (Figure 2.8 b and d). This indicates that the primary precipitates in peak-aged and over-aged samples are the needle-shaped β" and rod-shaped β' precipitates. In contrast, the Sc-containing alloy exhibits a distinctly different precipitate morphology. In the peak-aging state, both fine needle-like and relatively coarse rod-like precipitates are formed in the matrix. Representative HRTEM images of fine needle-like precipitates dominated in the structure are shown in Figure 2.8e, g and Figure 2.8f, h. It can be seen that these precipitates have no recognizable periodic features and are hard to be identified. As for the rod-like precipitates, their crystal structure revealed by HRTEM is the same as of β'.

The interaction of dislocations with precipitates in these alloys is also a focus of recent research. Christiansen *et al*. [94] investigated the shearing of β" precipitates by dislocations in peak-aged and deformed Al-Mg-Si alloy using HR(S)TEM. They compared the structure of precipitates in undeformed and deformed samples and showed that deformation affects their internal structure (Figure 2.10). In particular, in the undeformed state, precipitates usually produce HRTEM images in which the crystal lattice of the β" precipitate is visible. With a gradual increase in deformation, the images of the precipitates become increasingly unclear. In this case, the observed blur is not uniform, and the

periodicity of the crystal lattice of the β" precipitate along one of <110>$_{Al}$ directions is usually preserved. In addition, high-resolution HAADF STEM images reveal maintaining of the expected β" structure in the precipitate interior (Figure 2.11). That is, the blurring of the HRTEM images cannot be attributed to an overall structural change. It is assumed that when β" precipitates undergo shear, their internal structure experiences local changes. The authors of the study suggest that these local changes are planar defects. The shear parameters are incompatible with the precipitate structure, indicating that the precipitates are sheared by matrix Burgers vectors.
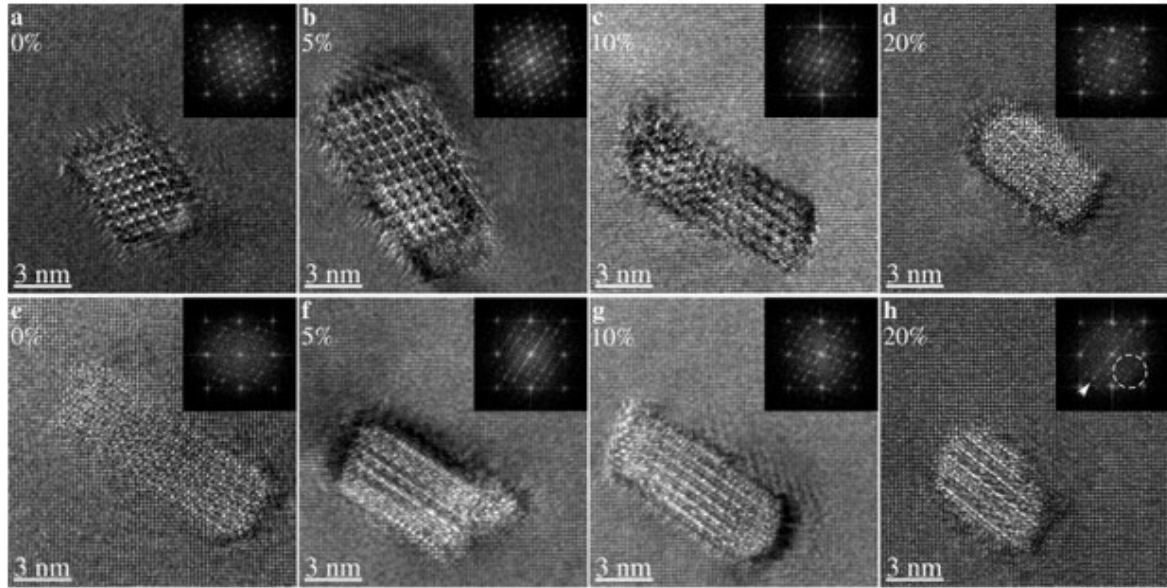
Figure 2.10. Representative [001]$_{Al}$ zone axis HRTEM images of precipitate cross-sections in undeformed condition (a, e), and after 5% (b, f), 10% (c, g), and 20% (d, h) compressive engineering strain. The global compression axis lies in-plane. Power spectra of fast Fourier transforms of each image are inset in top-right corners. The top row (a–d) is representative of precipitates with the sharpest outline and sharpest lattice, while the bottom row (e–h) is representative of precipitates with the most blurred lattices. In (h), the missing precipitate frequencies are marked in the fast Fourier transform spectrum by a dashed circle, and the remaining frequencies are marked by an arrow. Adopted from [94]
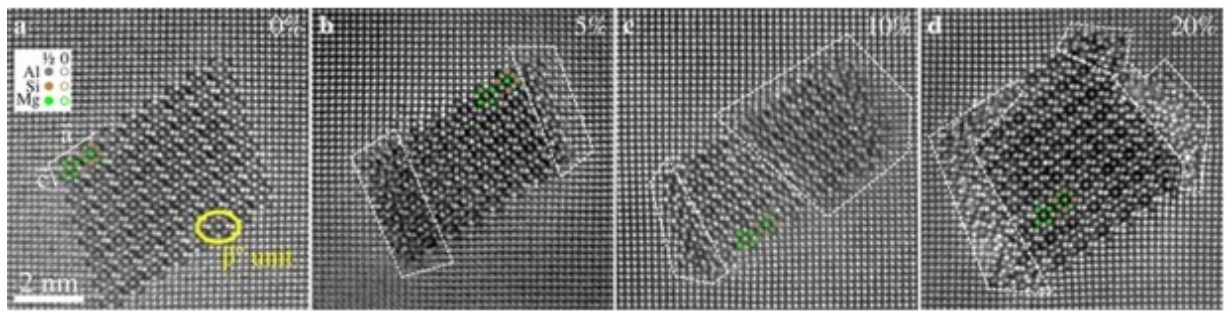
Figure 2.11. Smart-aligned and filtered $[001]_{Al}$ zone axis HAADF STEM images of precipitates in (a) undeformed, and after (b) 5%, (c) 10%, and (d) 20% compressive engineering strain. The relative position of the overlaid atoms in the out-of-plane direction is indicated by full and empty circles, referring to 1/2 $b_{\beta''}$ and 0 $b_{\beta''}$, respectively. A β" unit referred to as a β" "eye" is circled in yellow in (a). Precipitates in deformed specimens typically have regions (dashed) with reduced contrast/resolution along some of the edges. Adopted from [94]

Table 2.1 The list of intermetallic compounds reported for Al-Mg-Si system

Precipitates	Composition	Space group	Lattice parameters (nm)	Ref.
GP zone I	Mg_4AlSi_6	C2/m	$a = 1.48, b = 0.405, c = 0.648, \beta = 105.3°$	[95]
GP zone II	Mg/Si = 1	–	$a = 0.405$	[96]
β''	$Mg_4(Al_xMg_{1-x})Si_4$	C2/m	$a = 1.516, b = 0.405, c = 0.674, \beta = 105.3°$	[97]
U1	$MgAl_2Si_2$	$P\bar{3}m1$	$a = b = 0.405, c = 0.674, \gamma = 120°$	[98]
U2	MgAlSi	Pnma	$a = 0.675, b = 0.405, c = 0.794$	[99][100]
B'	$Mg_9Al_3Si_7$	$P6_3/m$	$a = b = 1.04, c = 0.405, \gamma = 120°$	[101]
β'	$Mg_6Si_{3.3}$	$P6_3/m$	$a = b = 0.715, c = 0.405, \gamma = 120°$	[102]
β'	$Mg_6Si_{3.3}$	$P6_3/m$	$a = b = 0.715, c = 1.215, \gamma = 120°$	[103]
β	Mg_2Si	$Fm\bar{3}m$	$a = 0.635$	[104]

Phase identification is challenging when several phases appear simultaneously. Vogel et.al [105] presented the correlative study of 4D scanning transmission electron microscopy (4DSTEM) and energy-dispersive spectroscopy (EDX) mapping to overcome this limitation. They presented detailed

characterizations of needle-shaped β precipitates, revealing distinct diffraction patterns (DPs) and compositional differences. Figure 2.12 shows the correlated 4D STEM and EDX mapping for peak-aged Al-Mg-Si sample.

Figure 2.12a shows the mean diffraction pattern of the scan, with circular and annular apertures marked, which were used to create the virtual dark-field (DF) images presented in Figure 2.12b and c. The dashed rectangular region in Figure 2.12c indicates the area selected for correlative EDX mapping, displayed in Figure 2.12d. The precipitates (numbered 1–8) are clearly distinguished and divided into two groups: Mg-rich and Si-rich particles, as shown in Figure 2.12e. Referring to this, Figure 2.12g presents the mean diffraction pattern for each precipitate, framed in yellow or blue based on the EDX results. Although the diffraction patterns appear similar at first glance, comparison with literature data and compositional analysis enables their identification as either β'' or β' precipitates.
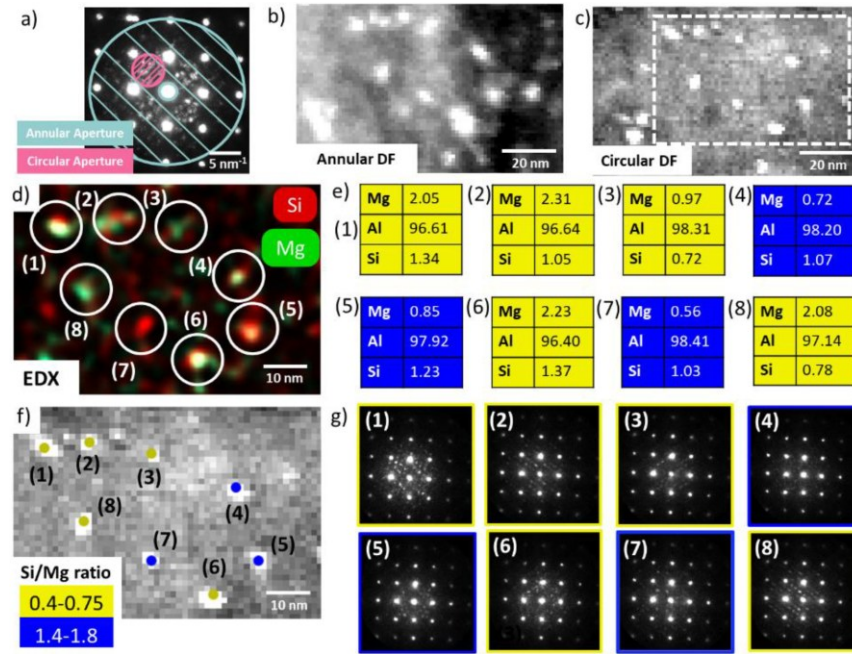
Figure 2.12. (a) Mean diffraction pattern of the 4DSTEM scan (dwell time = 100 ms, step size = 1 nm, probe size = 1.5 nm, convergence angle = 0.8 mrad). The annular and circular apertures are indicated. (b) corresponding virtual annular DF image (collection angle= 12 mrad) and (c) virtual circular DF image (collection angle = 5.5 mrad). The dashed rectangle marks the EDX scan area. (d) EDX mapping (Si, Mg signal). The detected precipitates are circled and numbered consecutively. (e) atomic fraction of Mg, Al, Si of the precipitates. Yellow: Magnesium-rich. Blue: Si-rich. (f) Virtual circular DF image and grouped precipitates according to their Si/Mg ratio. (g) DP of each precipitate obtained from the position indicated in f. [105]

2.5. Severe Plastic Deformation

SPD methods have become popular tools in materials science. They are versatile and can be used to deform various materials, such as polymers [106], ceramics [107], glasses [108], semiconductors [109]. SPD methods lead to various changes in the structure of the material. Their most well-known feature is the ability to reduce the grain size of materials to the submicron and nanometer scale due to the accumulation of high shear strain. In addition, the use of SPD, depending on the experimental conditions and the initial state of the samples, can lead to the several outcomes. These include the decomposition of a supersaturated solid solution, or to mixing, including immiscible components [110]–[112], amorphization of the material or to its nanocrystallization [113][114] ,phase transformations in the material and to the formation of phases, including metastable ones [115]. The strain during SPD can increase continuously, but the relaxation processes occurring in the sample lead to the so-called. a steady-state, when a parameter of the system, for example, grain or particle size [116][117], hardness [118], lattice parameter of the solid solution [119], reaches saturation.

Many SPD methods have been developed for various applications, such as Accumulative Roll Bonding [120], Twist Extrusion [121], Cycling Extrusion and Compression [122]. However, the most well-known are Equal Channel Angular Pressing (ECAP) [43] and High Pressure Torsion (HPT) [123].

2.5.1. High pressure torsion

The initiation of the HPT method is attributed to Prof. Percy W. Bridgman. In 1935, he published a work that became a pioneer in the study of materials under simultaneous action of shear and high pressure. [124] Bridgman's groundbreaking efforts involved applying a unique combination of high torsional stress and elevated hydrostatic pressure to a variety of materials. Bridgman discovered that the application of high strain could initiate phase transitions and lead to mixing of immiscible materials. HPT originated from his innovative approach and stands out as the most efficient tool for SPD. This method is widely used by the researchers to investigate fundamental aspects of materials behavior and microstructural evolution under severe deformation. [123]

The principle of HPT process is illustrated in Figure 2.13. The sample, typically in the form of a disk, is located between two anvils and is subjected to compressive pressure either at room or an elevated/cryogenic temperature. Simultaneously, torsional force is applied through the rotation of the lower anvil. The frictional force between the sample and anvils surfaces leads to the deformation of the disk through by shear strain. [123]
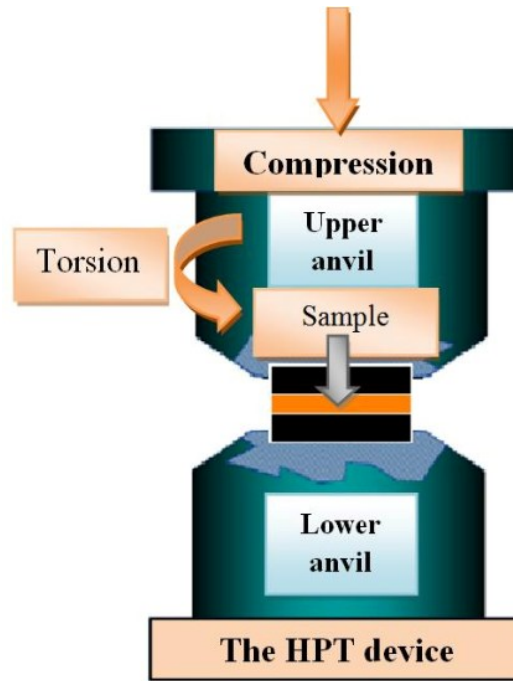
Figure 2.13. Principle of HPT [125]

The shear strain at HPT can be calculated as:

$$\gamma = \frac{2\pi N r}{t},$$
2.9

where N is the number of revolutions, r is the radius from the disk center and t is the thickness of the disk. [123]

The HPT method makes it possible to achieve very high strain levels, leading to significant changes in both structure of the material and its properties. The processing parameters of during HPT (pressure and degree of deformation) can be easily controlled, which provides a tool for influencing the structure and properties of the material. Moreover, the ability to regulate and control the temperature during the HPT process is important since it can affect the grain refinement and material properties.

It should be noted that the combination of SPD with subsequent heat treatment is attractive for age-hardenable alloys, since it allows one to influence the type and characteristics of precipitates. [84] It is known that SPD is accompanied by the formation of a large number of various lattice defects, vacancies, dislocations, and grain boundaries. [126] These defects serve as potential sites for the nucleation of precipitates. Consequently, this helps to increase the precipitates density while simultaneously reducing the solute content in the matrix. Thus, the combination of SPD and AA can be an effective approach to improve both the mechanical and electrical properties of aluminum alloys. [127][128] In particular,

Sauvage *et al*. demonstrated that the formation of ultrafine grains with intragranular nanoscale precipitates is an effective strategy for enhancing the synergy between strength and electrical conductivity in aluminum alloys. [129] In their study, they used HPT to refine the grains of the Al6101 alloy followed by AA at different temperatures. They found that AA at 130˚C for 48 hours revealed optimal conditions for electrical conductivity and mechanical properties, as shown in Figure 2.14.
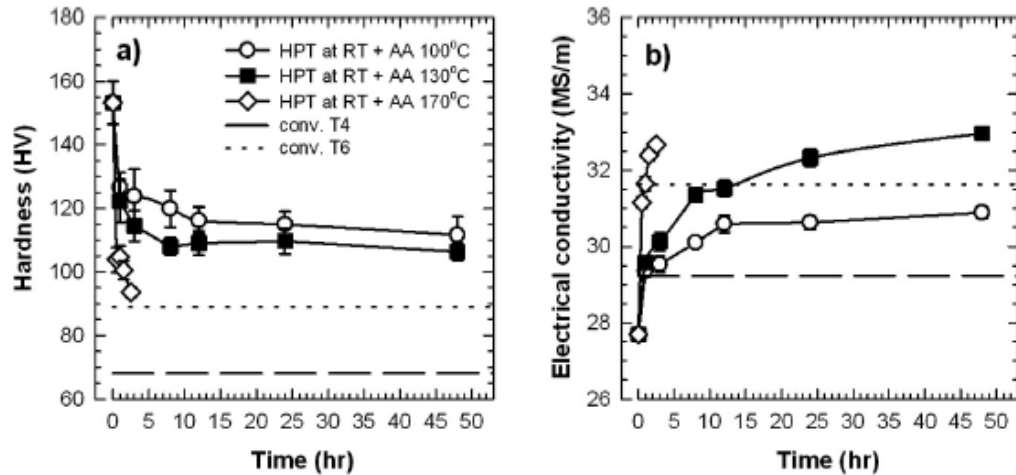
Figure 2.14 (a) evolution of micro hardness and (b) electrical conductivity of Al 6101 alloy processed by 20 turns by HPT as a function of the post-HPT aging time for different temperatures. Horizontal lines are set for comparison with the conventional T4 (natural aging) and T6 (peak hardness) treatments of the same alloy. [129]

They also reported that the large globular shape precipitates have been formed at grain boundaries, while others are mostly needle-shaped with a length of 40 nm and only a few nanometers in diameter (see Figure 2.15). The globular precipitates exhibit a Mg/Si ratio of about 2 (estimated from EDX) and have been identified as β′. The needle shaped precipitates exhibit some typical features of the other metastable phase, β″, in the Al-Mg-Si system; they are aligned along the <001>$_{Al}$ directions and exhibit an average Mg/Si ratio of about one (also estimated from EDX measurements), which is close to the stoichiometry of Mg_5Si_6 (Mg/Si=0.83). However, their study lacked atomic-resolution analysis of the crystal structure of the precipitates to conclusively confirm the presence of β′ and β″ phases.
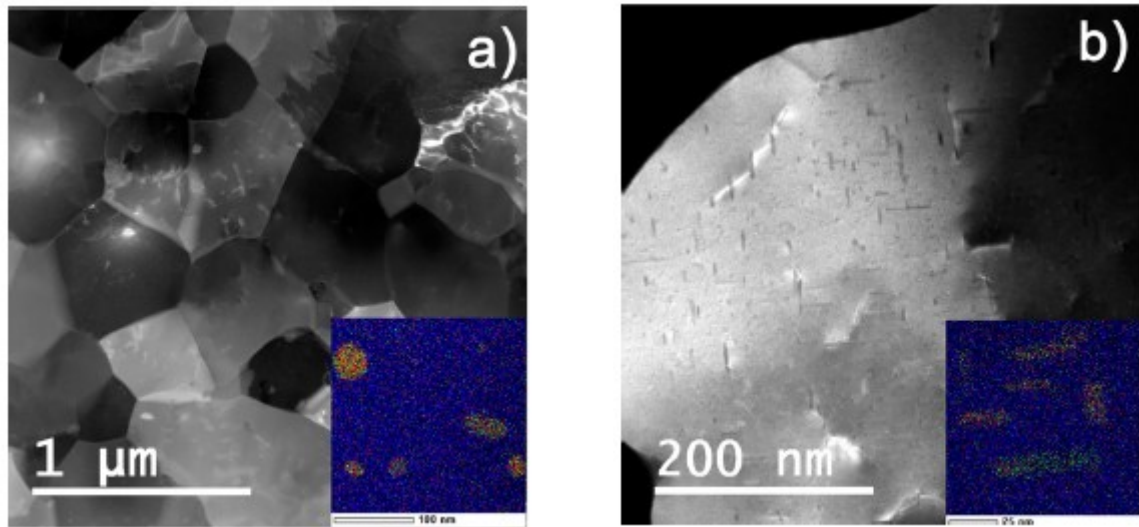
Figure 2.15 Microstructure of the 6101 Al alloy processed up to 20 turns by HPT at RT followed by aging at 130 ˚C during 48 h. (a) STEM-DF image showing the ultrafine grained structure with an EDX map (inset, display: Al-K blue, Mg-K red and Si-K green) showing large and globular shaped Mg and Si rich precipitates located at GBs (measured Mg/Si ratio close to 2); (b) STEM- DF image, showing mainly needle shaped precipitates that have nucleated during the aging treatment inside a grain. The EDX map (inset, display: Al-K blue, Mg-K red and Si-K green) clearly shows that these needle-shaped precipitates do contain a large amount of Mg and Si (measured Mg/Si ratio close to one). [129]

Despite its promising advantages, HPT method is not without its drawbacks. Limited sample size and inhomogeneity of applied strain along the diameter need to be addressed. Future directions in HPT research involve overcoming these challenges, exploring novel materials, and optimizing processing parameters to further enhance its applicability. As a solution to these limitations and to scale up the HPT process, HPTE was introduced by Ivanisenko *et al*. [130] which this method enables simple shear conditions and high hydrostatic pressure to be implemented in a rod-shaped specimen, allowing large strain to be accumulated in a single pass. Further elaboration on this method is provided in the Chapter 3.

2.6. Motivation and outline of present work

A literature review on this topic reveals several areas that require further investigation. First, all SPD procedures performed to date have been limited to laboratory-scale samples. Although these laboratory studies have significantly contributed to the fundamental understanding of processes occurring in materials during SPD—such as the formation of non-equilibrium structures with a high density of defects—the resulting alloy samples have not been applicable on an industrial scale. Additionally, the crystal structure of precipitates formed in severely deformed aluminum alloys under conditions of highly

defective structure remains poorly understood. Advanced techniques capable of investigating structural features with atomic resolution are essential for elucidating the mechanisms of strengthening in these materials.

The goal of this thesis is to address existing gaps by employing HPTE as a method of SPD, chosen for its potential scalability to industrial applications. Furthermore, this study aims to conduct an advanced structural characterization of the produced micro- and nanostructural features. By doing so, this research seeks to bridge the gap between laboratory-scale studies and industrial-scale applicability, providing a deeper understanding of precipitate crystal structures and their role in material strengthening. This approach not only advances fundamental knowledge of SPD-processed aluminum alloys but also develops practical methodologies for producing high-strength, high-conductivity Al-Mg-Si alloys suitable for industrial applications.

Chapter 3 provides a comprehensive overview of the HPTE method and the foundational aspects of material preparation and characterization methods. This chapter includes detailed descriptions of the mechanical and electrical testing devices, as well as the electron microscopy characterization approaches utilized in this study. By thoroughly outlining these methodologies, the chapter aims to equip the reader with a solid understanding of the experimental procedures and techniques employed.

Chapter 4 presents the results of the microstructural investigation of the HPTE-deformed samples. This chapter focuses on the initial microstructural state following deformation, providing critical insights into the baseline characteristics of the material before further treatments. The analysis includes an evaluation of the defect structures and their distributions, which are crucial for understanding subsequent material behavior.

Chapter 5 delves into the effects of AA on the properties of the deformed samples. This chapter discusses the microstructural evolution, particularly in terms of grain size and precipitate formation, and provides a comprehensive analysis of how these changes impact the material properties. Detailed discussions on the kinetics of precipitation and the morphological changes in precipitates during aging are included, supported by relevant data and observations.

Chapter 6 explores the mechanical and electrical properties of the deformed samples, offering a comparative analysis between the as-deformed and aged counterparts. This chapter aims to correlate the microstructural changes observed in previous chapters with the corresponding changes in material properties. The mechanical testing results, such as hardness, tensile strength, and elongation, are analyzed alongside electrical conductivity measurements to provide a general understanding of the

material performance. Additionally, this chapter presents the modeling of strength and conductivity properties based on the obtained microstructural data. By integrating experimental results with theoretical models, it aims to offer a thorough understanding of the relationship between microstructure and material properties, highlighting the interplay between structural characteristics and the resultant mechanical and electrical behaviors.

Finally, Chapter 7 summarizes the primary findings of this thesis, offering a comprehensive conclusion and insights into potential pathways for future research and advancements in the field of Aluminum alloys.

Overall, this thesis systematically examines the HPTE process, its immediate effects on microstructure, and the subsequent modifications induced by aging. By providing a detailed analysis and integrating experimental investigations with modeling efforts, this study offers valuable insights into the behavior and performance of Al-Mg-Si alloys. Ultimately, this work contributes to the advancement of material science and engineering applications by enhancing the understanding and practical implementation of HPTE for high-performance aluminum alloys.

Chapter 3

3. Materials and experiments methods

3.1. HPTE principles

The operational concept of the HPTE technique is as follows [130]: a material is extruded through two containers (see Figure 3.1), one of which remains stationary while the other rotates. In detail, the HPTE process includes the following steps. In the beginning, the channels of all containers have to be filled completely with the material. This can be achieved by either using a specially shaped initial specimen, or by closing the outlet with a plug. Once both channels are filled, the plug is removed. The extruded material then acts as a plug and ensures that the two containers remain fully filled during the process. The reduction of the channel diameter and friction result in forces acting opposite to the extrusion direction and creating hydrostatic pressure in the shear zone. Therefore, a specimen is deformed by the punch (moving with the velocity v) as well as by the containers (one of them rotates with the velocity ω). Once a specimen is extruded for the whole length of the punch, the process is stopped, the punch is raised and the next specimen is loaded into the container; the process then starts over. Consequently, the entire length of a specimen is torsionally deformed, as a specimen gradually passes through the shear zone.

Notably, the channel diameter varies across different sections: D_0 measures 12 mm at the inlet, D_1 expands to 14 mm within the deformation zone, and D_2 contracts to 10.6 mm at the outlet.
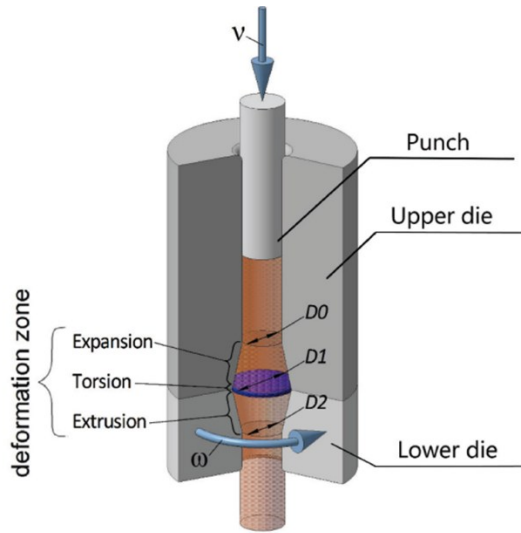
Figure 3.1 Schematic diagram of the HPTE process. [131]

The strain accumulated in a specimen after one pass can be calculated by following equation:

$$\varepsilon = 2\ln\frac{D_1}{D_0} + 2\ln\frac{D_1}{D_2} + \frac{WR}{\sqrt{3}V}\frac{D_1}{D_2}, \qquad 3.1$$

where D_0 and D_2 are the inlet and outlet diameter of the container channels, D_1 is the diameter of extrusion container channel, v is the translational velocity and ω is velocity of rotation. [130] According to this equation, the highest deformation occurs in the region closest to the edge of the specimen, where R reaches its peak value. Elevating the value of W and reducing the value of V leads to a higher total strain value (ε) imposed on the specimen.

3.2. Materials deformation via HPTE processing

In this study, we used extruded 6101 aluminum alloy grade as a starting material. The chemical composition of the alloy was determined by means of inductive coupled plasma optical emission spectroscopy (ICP-OES). It is presented in Table 3.1. The surplus of silicon, exceeding the standard value (less than 1 atomic percent), can be attributed to inclusions that formed during the casting process. Rods of the alloy were machined into a cylindrical shape with a length of 35 mm and a diameter of 11.8 mm to obtain the required sample dimensions for HPTE processing.

Table 3.1 Chemical composition of the studied alloy

Element	Al	Mg	Si
Content, at.%	Balance	0.94	1

HPTE experiments were conducted at 100 °C employing Molybdenum Disulfide (MoS_2) as a lubricant to minimize friction between the die and the specimen. All samples underwent a solid solution treatment in an air furnace at 550 °C for 1 h followed by quenching in water to RT. To find the optimum processing parameters for HPTE, three sets of regimes were chosen as mentioned in Table 3.2. The von Mises equivalent strain at different sample locations during HPTE was calculated using equation 3.1.

Table 3.2 Notation of HPTE regimes and corresponding processing parameters

	V(mm/min)	W (rpm)	Equivalent strain		
			Center	Mid-radius	Edge
V1 W 1	1	1	0.86	2.8	5.2
V 3 W1	3	1	0.86	1.5	2.3
V10 V1	10	1	0.86	1.1	1.3

Subsequently, the samples were subjected to AA at different temperature and duration (Table 3.3) to induce precipitation. After each treatment, microhardness and electrical conductivity (EC) were measured to determine the optimal deformation and aging parameters in terms of improvement in physical properties of the alloy.

Table 3.3 Parameters of the artificial aging applied to the material

AA temperature	Time (h)				
	5	10	15	24	48
130 °C		×			×
160 °C	×	×	×	×	
190 °C		×			

3.3. Alloy characterization

In this work, the determination of mechanical and physical properties was carried out using tensile tests, microhardness and resistivity measurements. An in-depth study of the alloy microstructure, as well as

the crystalline structure, morphology, and elemental composition of the precipitates, was carried out using XRD and APT as well as advanced microscopic techniques including (S)TEM, HR(S)TEM, EBSD.

3.3.1. Microhardness

Microhardness measurement is a fast method for rapid evaluation of materials mechanical properties [132]. The Vickers hardness test consists of two steps: (i) a Vickers indenter (136° diamond pyramid) is brought into contact with the test specimen in a direction normal to the surface, and the test force F is applied. The test force is held for a specified dwell time and then removed. (ii) The lengths of the two diagonals of the resulting imprint are measured and the mean diagonal length is used to calculate Vickers microhardness HV using the following equation:

$$HV \sim \frac{1.891\, F}{h^2},$$ (3.2)

where *F* is the applied force in kgf, *h* is the length of the imprint diagonal left by the indenter in millimeters. Samples were prepared by manual grinding on SiC paper down to a roughness of P4000 grade followed by polishing with diamond and alumina suspensions. Vickers microhardness profiles were then obtained along the sample diameter in a plane perpendicular to the extrusion direction. These measurements were performed using a Buehler hardness tester with a 50 g load applied for a dwell time of 10 seconds. The microhardness value for each point along the measurement line was averaged over at least five measurements.

3.3.2. Nano indentation

Nanoindentation is an advanced testing method used to determine the mechanical properties, such as elastic modulus and hardness, of materials whose properties are initially unknown. This technique involves indenting the material with a known hard material, allowing for precise measurements at the nanoscale. Unlike macroscopic indentation tests such as Brinell or Vickers, which involve pushing one material into another at larger scales, nanoindentation operates at a penetration depth on the order of nanometers.

A key distinguishing feature of nanoindentation is the indirect measurement of the contact area between the indenter and the specimen. Given the extremely small size of the residual indentation impression, typically in the micron range, direct measurement is challenging. Instead, the depth of penetration of the indenter into the material surface is recorded. By combining this depth measurement with the known geometry of the indenter, the contact area can be accurately estimated.

To evaluate the mechanical properties of the indented material, obtaining the graph of applied load versus indenter displacement is crucial. The elastic modulus of the indented sample can be inferred from the initial unloading contact stiffness, $S=dP/dh$, which is the slope of the initial portion of the unloading curve (see Figure 3.2). In Figure 3.2, P_{max} is the maximum load, h_{max} is the depth beneath the specimen surface, h_c is the depth of the contact circle, h_r is the depth of the residual impression, and h_e is the displacement associated with the elastic recovery during unloading.

To understand and explain the relationship between the material response to the indenter tip and its mechanical properties, classical nanoindentation analysis is introduced. [133] The solution for the elastic deformation is obtained by equating the projected area in contact under the indenter to the area of the indent impression, leading to the following equation:
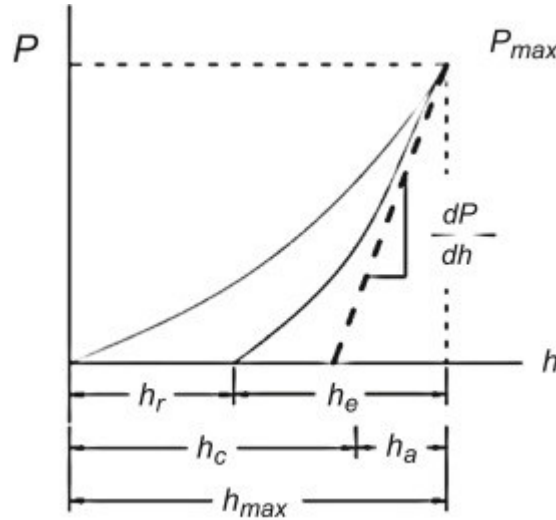
Figure 3.2. Plot of applied indenter load versus indenter displacement. Adopted from [133]

$$\frac{dP}{dh} = 2\sqrt{\frac{A}{\pi}} E_r,$$ (3.3)

where E_r can be calculated as:

$$\frac{1}{E_r} = \frac{1-v^2}{E} + \frac{1-v_0^2}{E_0},$$ (3.4)

with dP/dh for the slope of the unloading curve, A for the projected area, E_r for the indentation modulus, E and v for the Young's Modulus and Poisson's ratio of the sample, and E_0 and v_0 for the same parameters for the indenter. The projected area A, for the commonly used Berkovich indenter, is given by $A = 3\sqrt{3}h_p^2 \tan^2 \theta$. Substituting for the projected area, A, in (3.3), we obtain:

$$\frac{dh}{dP} = \frac{1}{2h_p} \sqrt{\frac{\pi}{24.5}} \left(\frac{1}{E_r}\right), \qquad (3.5)$$

here dh/dP is the reciprocal of the unloading slope known as compliance. From these equations, Young's modulus can be calculated, provided that Poisson's ratio is known.

Hardness has been found to depend on strain rate, especially when the hardness values are calculated from the data along the loading curves. Hardness is the equivalent of the average pressure under the indenter, calculated as the applied load, P, divided by the projected area, A, of contact between the indenter and the sample:

$$H = \frac{P}{A}. \qquad (3.6)$$

3.3.3. Tensile testing

Tensile testing is one of the most important methods of mechanical testing that provides information on the strength (tensile strength, yield strength) and plastic (relative elongation and contraction) characteristics of materials.

During testing, a specimen with an initial cross-section a_0 and gauge length l_0 is fixed in a mechanical testing apparatus, where it undergoes elongation at a constant rate, with both the applied force F and the resultant elongation Δl being recorded. The engineering stress, denoted as σ, is defined as the ratio of the applied force F to the initial cross-sectional area a_0, and the engineering strain, denoted as ε, is determined by normalizing the elongation Δl to the original gauge length l_0. A schematic representation of the engineering stress-strain curve along with the true stress-strain curve is presented in Figure 3.3a. At the initial stages of deformation, the correlation between stress and strain adheres to Hooke's law, corresponding to the elastic segment of the stress-strain curve. Within the region of elastic deformation, the solid body spontaneously reverts to its initial undeformed state after the removal of the applied force. The elastic phase terminates upon reaching the proportionality limit, followed by a plastic deformation stage, where the material deforms plastically and stress increases with increasing strain — a phenomenon known as strain hardening. Eventually, at a certain strain, the stress attains its peak value, known as the ultimate tensile strength (UTS). After reaching the UTS, the deformation loses stability, and any local inhomogeneity of the deformity leads to its localization and the formation of a neck. This occurs when the strain hardening rate $d\sigma/d\epsilon$ ceases to compensate for the increase in stress due to a decrease in the cross-section of the sample, which is described by the criterion introduced by Armand Considère:

$$d\sigma/d\epsilon \geq \sigma. \qquad\qquad 3.7$$

In this way, an ideally plastic material, in which there was no strain hardening, could become unstable in traction and initiate necking as soon as the flow began. [134][36] Some materials have significant ductility and can undergo significant plastic deformation beyond their elastic limit before reaching fracture. In contrast, brittle materials fail without noticeable plastic deformation.

Since engineering stress is calculated for the original – unloaded – area, it does not take into account that the cross-sectional area is changing during plastic deformation of the sample. More accurate stress and strain data during tensile testing are obtained by the true stress (σ_{true}) – true strain (ε_{true}) diagram. [135] It is plotted based on the actual cross-sectional area at any given time, allowing for a conversion from engineering stress-engineering strain data using the equations 3.83.9. As a result, the true stress-strain curve typically exhibits higher stress values and a more pronounced strain hardening effect compared to the engineering stress-strain curve:

$$\sigma_t = \sigma_e \times (1 + \varepsilon_e), \qquad\qquad 3.8$$

$$\varepsilon_t = ln(1 + \varepsilon_e). \qquad\qquad 3.9$$

In this work, tensile tests were carried out on dog-bone shaped specimens machined in the extrusion direction of a rod with 10 mm gauge length (Figure 3.3 b) at a constant strain rate of 10^{-3} s^{-1} on a Zwick Z100 tensile testing machine. Three samples were prepared for each treatment condition in order to demonstrate the reproducibility of the results.
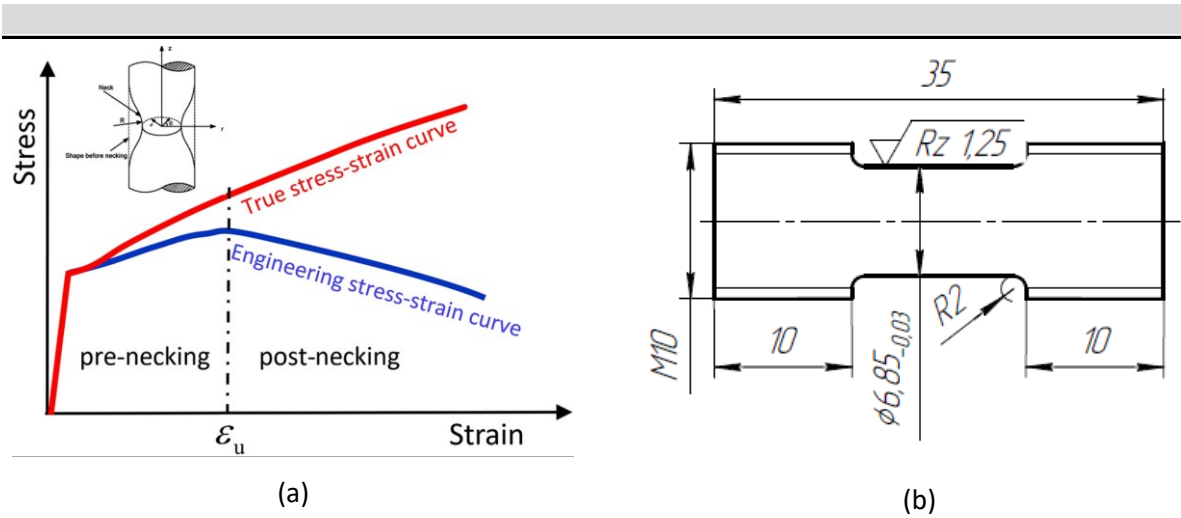
Figure 3.3. Schematic representation of (a) engineering vs. true stress-strain curve and (b) tensile test sample geometry [71][136]

3.3.4. Electrical conductivity measurements

Electrical conductivity was measured on the specimen surface by the eddy current method using a Sigmascope device (Helmut Fischer GmbH) with a frequency of 480 kHz according to DIN EN 2004-1 and ASTM E 1004 (Figure 3.4b). The phase-sensitive eddy current test method according to draft DIN 50994 was invented to measure the electrical conductivity of non-ferrous metals such as copper, aluminum and even stainless steel. As illustrated in Figure 3.4a, the structure of phase-sensitive eddy current probes, which feature a ferrite core encircled by two coils. The exciter coil generates a high-frequency magnetic field (ranging from kHz to MHz), inducing eddy currents within the sample. The second coil, known as the measuring coil, is used to measure the probe's AC resistance (impedance). The eddy currents in the sample alter this probe impedance, causing it to be out of phase (phase angle ф) with the excitation current (when the probe is not in contact with the sample). The phase angle ф is influenced by the thickness of the layer and the material's electrical conductivity.

Each value was determined as the average of four measurements. Calibration of the device was performed before each measurement with appropriate reference samples.

<div align="center">(a)   (b)</div>
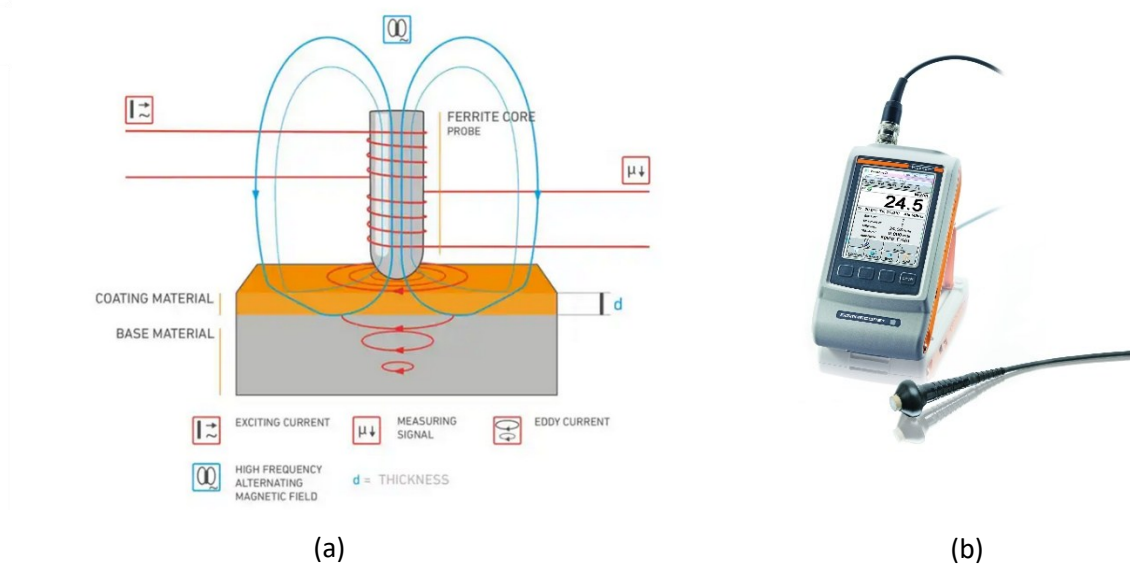
Figure 3.4 (a) schematic of phase-sensitive eddy current method and (b) Sigma scope device for electrical conductivity measurement. Adopted from [137]

3.3.5. X-ray diffraction

In this section, the concept of diffraction will be briefly described. In order to understand how diffraction works, we need to understand the concept of reciprocal lattice. After a brief description of reciprocal lattice, the principle of X-ray diffraction will be presented.

3.3.5.1. Real and reciprocal lattice

The structure of a crystalline substance can be represented by atoms or groups of atoms periodically arranged in space. To describe the structure of the crystal lattice, a coordinate system is used, with three axes pointing in non-coplanar directions (Figure 3.8a). The smallest translation volume that can reproduce the full crystalline structure is called a unit cell, characterized by the length of the unit cell vector in the three non-collinear directions (translation vectors a, b and c), the angles between them α, β and γ and the arrangement of the atoms in the unit cell. In addition, specific directions within the crystal lattice are described using crystallographic direction indices (uvw), which represent vectors in terms of the unit cell axes. These directions are defined as integer multiples of the unit cell vectors (a, b, and c) and written in the form of $R = ua + vb + wc$.

In crystallography, the concept of reciprocal space is widely used. As will be shown below, this approach allows one to greatly simplify explanation of the diffraction geometry. Like the crystal lattice, the reciprocal lattice is built on unit vectors a^*, b^* and c^*, which are mathematically related to real space vectors as:

$$a^* = \frac{b \times c}{a \cdot [b \times c]}; \ b^* = \frac{c \times a}{b \cdot [c \times a]}; \ c^* = \frac{a \times b}{c \cdot [a \times b]}. \qquad\qquad 3.10$$

The reciprocal lattice vector (see Figure 3.5b) is given by:

$$g_{hkl} = ha^* + kb^* + lc^*. \qquad\qquad 3.11$$

It can be shown that any reciprocal lattice corresponds to a crystallographic plane; the vector g_{hkl} is a normal to the plane of the crystal with indices (*hkl*), and its length is the reciprocal of the interplanar distance $|g_{hkl}| = 1/d_{hkl}$. This is a general rule that applies to crystals of any system.

(a)   (b)
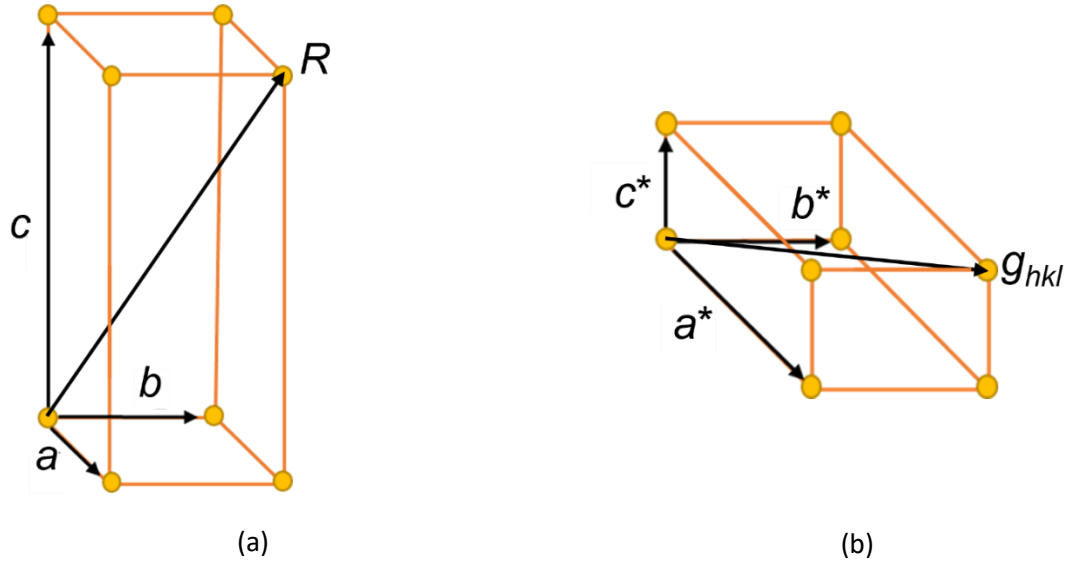
Figure 3.5. (a) Representation of a primitive orthorhombic unit cell ($a{\neq}b{\neq}c$, $\alpha{=}\beta{=}\gamma{=}90$ °) and (b) corresponding reciprocal unit cell.

A crystal can be represented as a set of planes in which atoms or groups of atoms are located. Each plane is described by a triple of numbers (*hkl*), which are called the Miller indices of the crystallographic plane. As shown in Figure 3.6they are defined as the reciprocal of the length of the segments that this plane cuts off on axes parallel to the translation vectors *a*, *b* and *c*.
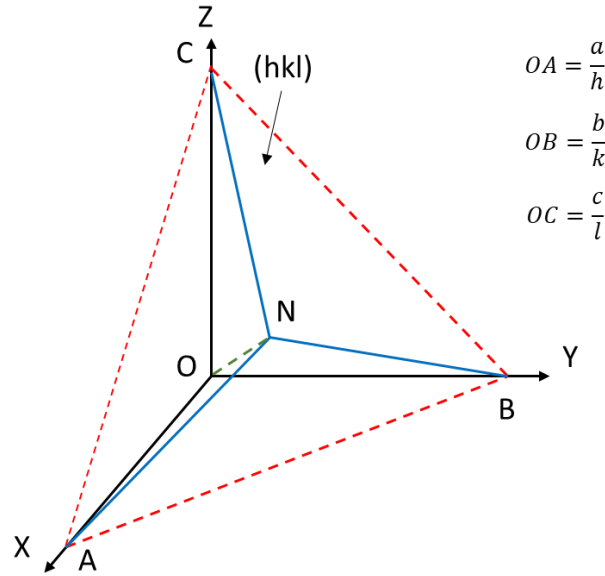
Figure 3.6. The plane ABC has Miller indices (*hkl*). The vectors OA, OB, and OC have lengths *a/h*, *b/k*, and *c/l*

3.3.5.1.1. Reciprocal space for the lattice with a basis

The 3D crystal structure can be classified into seven types of cells: cubic, hexagonal, tetragonal, rhombohedral, orthorhombic, monoclinic, and triclinic. Among these systems, depending on the set of translation vectors inside the cell, fourteen Bravais lattices are distinguished. The diffraction pattern of a crystalline sample arises from the periodic arrangement of atoms within these lattices, and understanding this requires an analysis in reciprocal space. To determine the intensity of reflections in the diffraction pattern from a crystalline sample, the contributions of individual atoms of the crystalline unit cell are summed up, taking into account their atomic scattering amplitude and position in the lattice. From equation3.12, the intensity of the scattered waves from an individual atom can be summed for all atoms in the unit cell and the resulting amplitude, called the structure factor, can be calculated as follows:

$$F_{hkl} = \sum_i f_i e^{-2\pi i (hx_i + ky_i + lz_i)}. \qquad 3.12$$

The structure factor defines certain selection rules that determine the possibility of a particular reflection in the diffraction pattern for a given crystal lattice. This means that a reflection from a certain plane is not observed if the corresponding structure factor is equal to zero. For example, in the FCC lattice (see Figure 3.7 a), the atom coordinates are (x, y, z) = (0, 0, 0), (1/2, 1/2, 0), (1/2, 0, 1/2), (0, 1/2, 1/2). Substituting these values into equation yields:

$$F = f\{1 + e^{\pi i (h+k)} + e^{\pi i (h+l)} + e^{\pi i (k+l)}\}. \qquad 3.13$$

Here h, k and l are all integers. If all three are either even or odd, the exponential terms become $e^{2n\pi i}$, resulting in diffracted wave phases to be a multiple of 2π and thus in phase. However, if one of h, k or l is odd and the others are even (or *vice versa*), then two of the three phase factors become odd multiples of π, leading to two terms of -1 in equation 3.13. Thus, the structure factor is equal to:

$$F = 4f, \text{ if } h, k, l \text{ are all even or all odd,}$$

$$F = 0, \text{ if } h, k, l \text{ are mixed even and odd.}$$

The selection rules above determine the permissible reflections in the diffraction pattern from an FCC structure. Similarly, the allowed reflections for other structures such as bcc, hcp, or others can be ascertained.

(a)   (b)
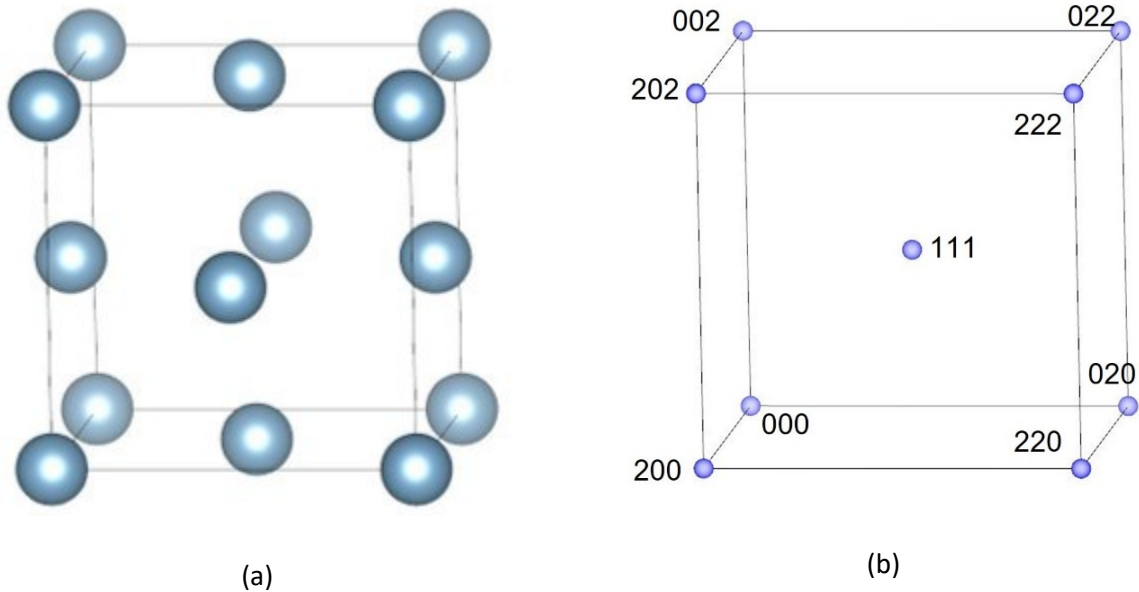
Figure 3.7. (a) Face-centered cubic crystal structure with the atomic positions at (0, 0, 0), (1/2, 1/2, 0), (1/2, 0, 1/2) and (0, 1/2, 1/2); (b). The reciprocal lattice for the FCC crystal structure constructed based on the selection rules; the sites with a systematic extinction are removed, so the actual arrangement of points makes a bcc lattice (and *vice versa*).

3.3.5.2. Principle of XRD

X-ray diffraction analysis is one of the diffraction methods for studying the structure of materials. It is the most common method for determining the crystal structure of a sample due to its simplicity and versatility. This method is based on the phenomenon of X-ray diffraction on a three-dimensional crystal lattice. As the atoms are regularly arranged within a crystal, the interaction of X-rays with the crystal lattice results in a diffraction pattern due to constructive interference, which occurs in certain directions when the path difference between waves scattered from adjacent crystal planes equals an integer multiple of the wavelength. The theoretical justification for the phenomenon was given by, Lawrence Bragg and William Henry Bragg in 1913, who derived an equation relating the diffraction angle θ with the interplanar distance d at a given wavelength λ (Bragg´s equation) [138]:

$$n\lambda = 2d\ sin\theta, \qquad 3.14$$

where n is the diffraction order.

The most widely used X-ray spectrum acquisition scheme for XRD analysis is the Bragg-Brentano geometry. In Bragg–Brentano geometry, the sample is located at the center of the diffractometer circle, which is the center of rotation of both the X-ray source and detector; the angle of incidence is equal to the angle of detection (Figure 3.8). The diffraction pattern is obtained by measuring the intensity of the scattered waves as a function of scattering angle. Strong intensities known as Bragg peaks are produced at angles where the interplanar distance in the sample satisfies the Bragg condition 3.14).

The acquired X-ray diffraction pattern contains a lot of information on the sample; in particular, it is possible to establish its phase composition, determine the lattice parameter of the constituent phases, and their preferred orientation. Based on the angular dependence of the peak broadening, it is possible to figure out the internal stress and crystallite size. To extract information contained in the X-ray spectrum, full-profile analysis methods have been developed, a well-known one is the Rietveld refinement. [139]
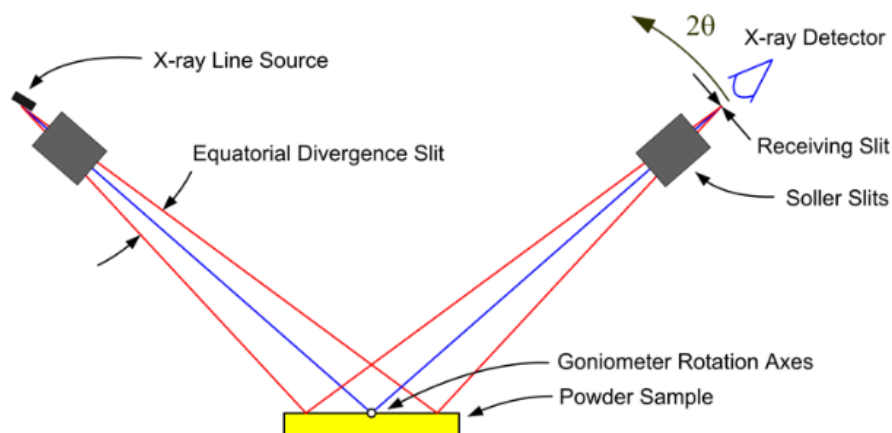
Figure 3.8. A schematic diagram illustrating the operation and optical components of a Bragg-Brentano X-ray powder diffractometer. Adopted from [140]

In this work, samples were examined on an Empyrean series 3 diffractometer (Malvern Panalytical) with a Cu-Kα anode. Samples have been prepared by mechanical polishing, followed by electrolytical polishing using a QATM - QETCH 1000 device; polishing parameters: 10 V, −20 °C in A2 Struers electrolyte. XRD measurements were conducted at the center and mid- radius of the sample with a beam diameter of about 1 mm. The diffraction patterns were evaluated for dislocation densities and crystallite size estimation by means of the Convolutional Multiple Whole Profile (CMWP) procedure. [46] The CMWP method uses well established profiles for the determination of coherently scattering domain size and dislocation density based on the physical properties of lattice defects. The contribution of dislocations to broadening is described using the so-called contrast factor. This factor takes into account the relative orientation of the dislocation line, its Burgers vector, and the diffraction vector. The method is predicated on the following assumptions: (i) lognormal characteristic of grain size distribution, (ii) spherical shape of the grains, and (iii) dislocations as the primary source of internal stress. The calculated physical profiles are convoluted with the instrumental profile and matched with the measured patterns using the combination of the statistical Monte-Carlo method and the analytical Levenberg-Marquardt approach. Uncertainties in the dislocation density were determined by the p% statistical confidence method where p was selected to be p=3%. [46] This number correspond to 2 σ confidence interval. The instrumental effect was determined by measuring a LaB_6 standard specimen under the same diffraction conditions as the investigated samples. Lattice parameters were calculated by using the Fityk software version 1.3.1. [141]

3.3.5.3. Random and systematic error in XRD

The X-ray diffraction method allows one to measure the lattice parameters of crystalline substances, which is important when studying the change in the parameter of a solid solution with a change in the concentration of solutes, or, for example, when measuring the coefficients of thermal expansion. Since, as a rule, variations in the concentration of a dissolved substance or changes in temperature result in only minor alterations to the lattice parameter. Therefore, it is crucial to measure this parameter with high precision. Additionally, identifying and evaluating the sources of both random and systematic errors is essential to understand their impact.

Although the measurement of the lattice parameter is indirect, it can yield highly accurate data. For cubic substances, the lattice parameter a is directly related to the distance d between specific sets of Bragg planes, and it is determined using Bragg's law. The magnitude of the measurement error a can be estimated from differentiation of Bragg's law with respect to θ: [143]

$$d = \frac{\lambda}{2 \sin \theta}, \qquad\qquad (3.15)$$

$$\Delta d = \sqrt{\left(\frac{\Delta \lambda}{2 \sin \theta}\right)^2 + \left(\frac{\lambda}{2 \sin \theta} \cdot \cot \theta \cdot \Delta \theta\right)^2}. \qquad\qquad (3.16)$$

Neglecting $\Delta\lambda$, we obtain: $\frac{\Delta d}{d} = |\cot \theta\, \Delta\theta|$; for cubic materials $\frac{\Delta a}{a} = |\cot \theta\, \Delta\theta|$.

The fractional error in a, caused by the error in determining θ, approaches zero as θ approaches 90° (or 2θ approaches 180°). Therefore, the key to the accuracy of the parameter measurements is to use back-reflected rays having values of 2θ as close to 180° as possible. [143] The error of the angle measurement $\Delta\theta$ can be estimated as 0°.01, which is a common value for modern diffractometers and is related to the accuracy of goniometer positioning using a stepper motor via a worm gear. In particular, when determining the parameter of the Al solid solution, for the reflection with the maximum observed angle 2θ=116°.56, the fractional error is $\sim 4\times10^{-4}$.

Another parameter that affects the accuracy of the lattice parameter determination and that must be taken into account is the accuracy of the experimental profile fitting by the approximating functions. As a figure of merit for the fit quality, the Fityk program uses the R^2 value, which is ideally equal to one.[142] For all performed lattice parameter measurements, the R^2 value exceeds 0.97, indicating a reliable fit of the XRD profile. The error in determining the lattice parameter calculated by the Fityk program is $\sim 1\times10^{-4}$, i.e., lesser than the value calculated using the aforementioned formular, thereby demonstrating the reliability of the obtained results.

The main sources of systematic error in determining the distance *d* include:

1. Instrument Misalignment: The incident beam's center must intersect the diffractometer axis and align with the 0° position of the detector slit. This axis is the rotation axis for the detector, sample, and beam exit slit. Mechanical alignment helps minimize this error.

2. Sample Shape: Using a flat sample instead of one curved to match the focusing condition of the focusing circle can introduce errors. This issue is mitigated by reducing the horizontal divergence of the incident beam with slits, though it results in a loss of intensity.

3. Sample Off-Axis Position: This is often the largest error source. It causes an error in determining d as given by the equation: [143]

$$\frac{\Delta d}{d} = -\frac{D \cos^2 \theta}{R \sin \theta},\qquad\qquad 3.17$$

where *D* represents the displacement of the sample parallel to the normal to the diffraction plane, and *R* is the radius of the diffractometer. In this study, the diffractometer used has *D*=0.01 µm and *R*=10 cm, resulting in a fractional error that is several magnitudes smaller than the previously mentioned value.

4. Vertical Divergence of the Incident Beam: This error is minimized by reducing the vertical aperture of the detector slit, which also leads to a loss of intensity.

5. Sample Absorption: Samples with low absorption should be made as thin as possible to minimize this error.

It is necessary to consider separately the issue of errors characteristic for the CMWP method. These systematic errors are a consequence of the basic assumptions, underlying the method including the log-normal grain size distribution, idealized spherical grain shapes, and dislocations as the primary source of internal stress. Among other possible error sources the following can be mentioned: (i) errors stemming from the peak convolution uncertainties, from the optimization procedures, and simplified elastic constant models; (ii) experimental and data processing errors, originating from incorrect background subtraction, instrumental broadening corrections. [46][144]

The significance of these error sources varies depending on the material system under investigation. For instance, in aluminum and its alloys, peak overlap issues are less critical due to the simple cubic structure of the matrix, though assumptions about microstructural characteristics remain crucial and can lead to significant systematic errors if they deviate from reality.

Overall, to minimize systematic errors, mechanical adjustment of the instrument is necessary, along with the use of a standard sample to control the adjustment performed by diffraction spectra. Minor

corrections of the error associated with the displacement of the sample, its shape and absorption factors are included in the routine of the program used to process the obtained spectra.

3.3.6. Differential scanning calorimetry

Differential scanning calorimetry (DSC) is an analytical technique utilized to measure the heat released or absorbed by a sample during heating or cooling across a range of temperatures. [145] This method is essential for characterizing the thermal properties of materials and determining the specific temperatures at which phase transitions occur, such as glass transition, fusion, and crystallization events. DSC instruments are available commercially in two main types: Heat Flux DSC and Power Compensation DSC. Heat Flux DSC involves varying the temperature of the sample unit, which consists of both the sample and a reference material, according to a specified program. The temperature difference between the sample and the reference material is measured as a function of temperature. In contrast, Power Compensation DSC measures the difference in thermal energy applied to the sample and the reference material per unit time as a function of temperature. [146] This technique aims to equalize their temperatures while varying the temperature of the sample unit, which includes both the sample and the reference material, according to a specified program.
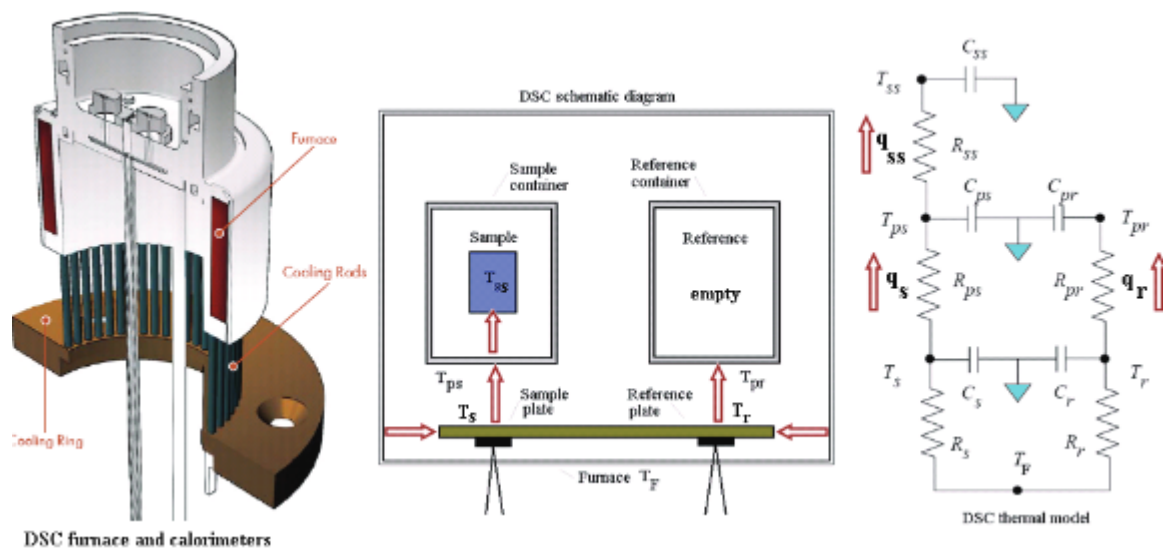
Figure 3.9. A schematic diagram of a heat flux type DSC and the corresponding DSC thermal model [147]

Figure 3.9 illustrates the block diagram of a Heat Flux DSC. The main components include the sample and reference holder, the heat resistor, the heat sink, and the heater. Heat from the heater is supplied

to both the sample and the reference through the heat sink and heat resistor. The heat flow is proportional to the temperature difference between the heat sink and the holders. The heat sink possesses a significantly larger heat capacity compared to the sample.

When the sample undergoes endothermic or exothermic phenomena, such as transitions or reactions, these phenomena are compensated by the heat sink, maintaining a constant temperature difference between the sample and the reference. The amount of heat supplied to the sample and the reference is proportional to the temperature difference between both holders. By calibrating with a standard material, quantitative measurement of an unknown sample becomes achievable.

3.4. Basics of electron microscopy

Electron microscopy proves to be a highly effective technique in examining materials structure with high spatial resolution down to the sub-angstrom level. Spatial resolution in microscopy signifies the smallest discernible separation between two distinct object points. The Rayleigh criterion is a common approach to define the spatial resolution which is expressed as $\delta = \frac{0.61 \lambda}{N \sin \beta}$, where λ represents the wavelength of the radiation used for imaging, N is the refractive index of the medium between the lens and the sample, and β is the semi-collection angle. [148] The resolution depends on the electron wavelength, which is linked to the acceleration voltage of the electron microscope, which is typically in the range of $5 - 300$ kV. The corresponding wavelength of the electrons is between around $10 - 2$ pm, which is shorter than the interatomic distance, theoretically enabling high-resolution imaging. However, because of the imperfections in the optical system and limited electron source coherence, the experimental resolution limits are significantly worse than this value.

Analysis of images obtained in an electron microscope requires an understanding of the mechanisms of incident electron beam interaction with atoms of the material. The negatively charged electrons of the beam experience a strong interaction with matter. When the accelerated electrons encounter atoms in the sample, a variety of response signals is produced as shown in Figure 3.10. Accelerated electrons can either pass through a sample with virtually no interaction, or they can scatter elastically (retaining their initial energy but changing momentum) or inelastically (losing energy). Both elastic and inelastic scattering produces signals that can be used for imaging, as well as for (semi) quantitative information about the elemental composition of a sample through the generation of characteristic X-rays. Elastic scattering occurs as a result of the interaction of the incident beam with the electron shell of the sample atoms. These coherently scattered electrons form an electron diffraction pattern that is used to analyze

the crystal structure of the sample. High-angle scattering occurs predominantly during the interaction of the incident beam with the atomic nucleus, so-called Rutherford scattering. The probability of high-angle scattering is roughly proportional to the square of the atomic number (Z) of the element. In the case when the incident electrons experience a direct collision with the nucleus, the scattering angle can exceed 90 °, resulting in the generation of backscattered electrons (BSE).
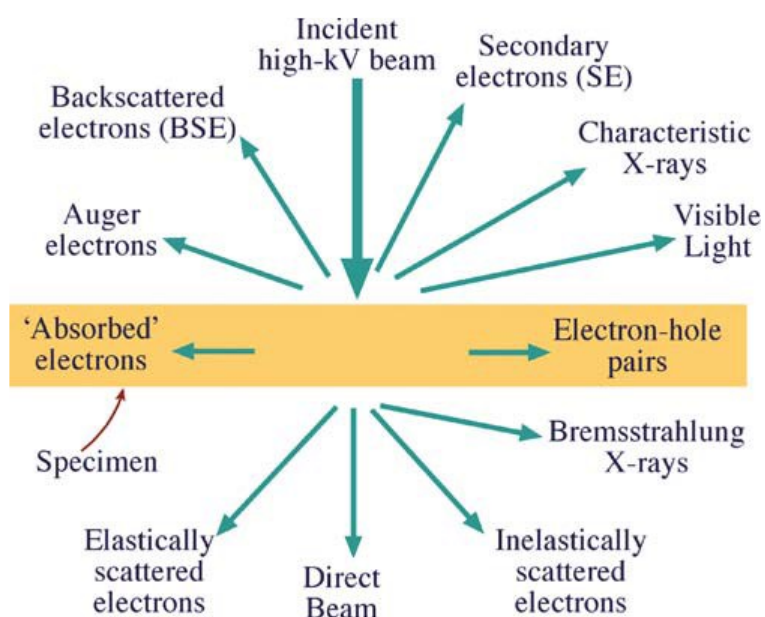
Figure 3.10. Signals generated from the interaction between electrons and a thin specimen; the transmitted signals are used for TEM imaging techniques. Adopted from [148]

3.4.1. Scanning electron microscopy

SEM imaging is one of the most widely used electron microscopy techniques for morphological and topological characterization of a wide class of materials using an electron beam focused on a surface of a bulk sample and subsequent collection of emitted signals. The basic SEM setup is schematically shown in Figure 3.11. An electron beam originates from a source – electron gun. There are different types of electron sources such as thermionic or field emission gun (FEG). The electron beam is initially emitted with a low energy and then accelerated to energy of typically 30 keV, and is precisely focused into a nanometer-sized electron probe using a condenser lens system. An image of the sample surface is formed by scanning the probe across the samples using a set of deflection coils.
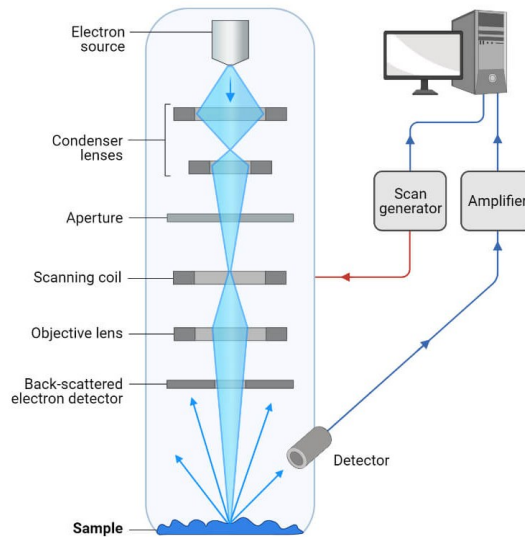
Figure 3.11. SEM schematic layout. Adopted from [149]

Upon interaction with a sample, the primary electron beam initiates a cascade of events within the interaction volume, a pear-shaped region extending from a few hundred nanometer to micrometer depths beneath the surface. The size of this volume depends on factors such as the initial energy of the electron beam, the density and orientation of the sample material, as well as the type of signal generated. The interaction results in backscattered electrons, secondary electrons, as well as electromagnetic radiation in the X-ray wavelength range. A variety of detectors are integrated in modern SEMs to collect the generated signals. Examples include an Everhardt-Thornley detector for collecting secondary electrons sensitive to the topography of the sample surface, and the BSE detector for backscattered electrons providing material contrast. Another, important element of a modern SEM is an energy dispersive X-ray detector for elemental composition (EDX) analysis using the characteristic X-rays.

3.4.1.1. Focused ion beam

Focused ion beam (FIB) is a technique, which enables imaging of the sample surface, like in SEM, but also allows mask-less milling of sample (Figure 3.12). It has the ability to fabricate structures with feature size of a couple of nanometers. Therefore, it can be used for prototyping or manufacturing high precision micro structures in a wide range of materials.

| (a) | (b) | (c) |
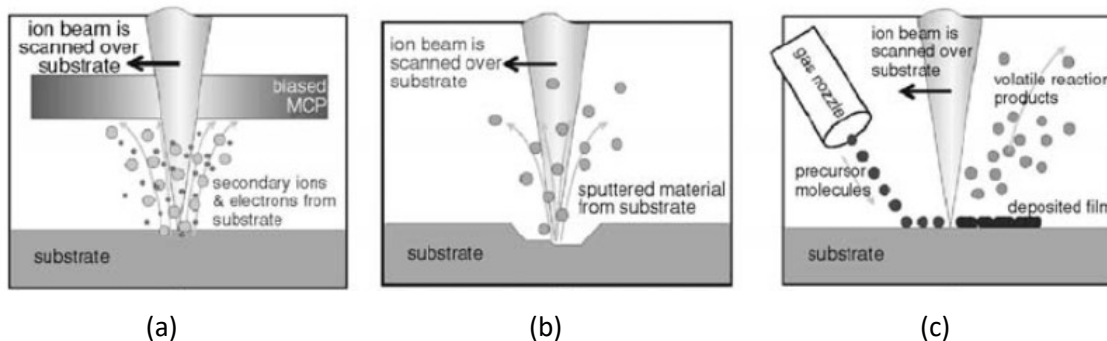
Figure 3.12. Principles of FIB) (a) imaging, (b) milling and (c) deposition. Adopted from [150]

The FIB system operates similarly to a SEM, with the main difference being the use of a gallium ion (Ga+) beam instead of an electron beam. This ion beam is generated from a liquid-metal ion source (LMIS) by applying an electric field. The electric field prompts the emission of positively charged ions from the Taylor cone, formed underneath the apex of the tungsten needle. Most of Ga+ ions that reach the sample surface are implanted and produce local sputter damage. The depth of this implanted region correlates with ion energy and angle of incidence, and also depends on the sample material. [150] Imaging with ion beams is possible through the formation of secondary electrons resulting from the interaction between ions and the sample (Figure 3.12 a). Additionally, due to the greater mass of ions compared to electrons, there is a milling effect on the sample (Figure 3.12 b).

To achieve precise targeted preparation within defined areas of a sample surface without damaging the area of industry, SEM and FIB functionalities have been integrated into a single system, commonly referred to as a dual-beam FIB (as illustrated in Figure 3.13). In this setup, the electron and ion guns are located at a certain angle to each other (52 ° for FEI Strata 400s and 54 ° for Zeiss Auriga system). Continuous electron imaging allows to monitor the milling process while limiting the influence of the ion beam on the sample material. Additionally, a gas injection system (GIS) and micromanipulator are employed for lift-out procedure in preparing samples for TEM. GIS also allow the deposition of a broad range of materials including platinum-rich/tungsten-rich/carbon/insulating solid onto the sample. This is used for nano-fabrication and sample protection purposes as shown in Figure 3.12 c. During deposition, a gaseous precursor is released onto the sample and is then cracked by the ion beam or electron beam. The non-volatile products adsorb on the sample surface. The pumps that maintain the chamber vacuum remove the volatile products.
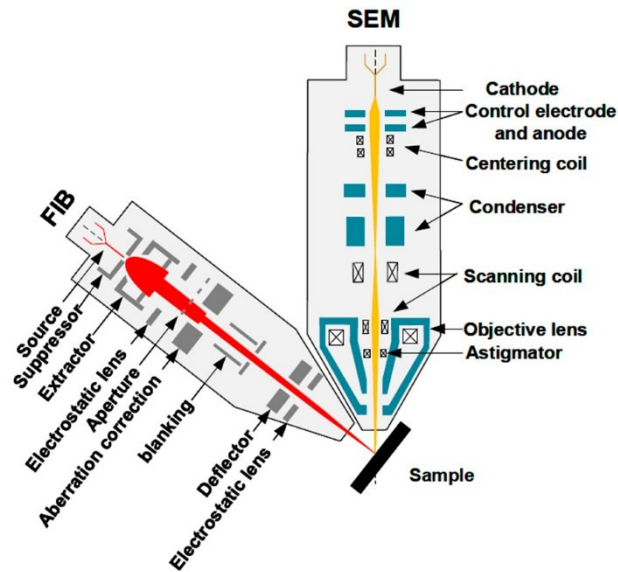
Figure 3.13. Cross-section of a dual-beam FIB instrument. Adopted from [151]

3.4.1.2. Electron back scatter diffraction

Backscattered electrons in SEM can provide insights into the local crystal structure and orientation. Various electron diffraction methods applied to bulk samples are reviewed in Ref. [152]. The EBSD technique involves using an additional CCD camera system to capture Kikuchi bands formed by Bragg diffraction of primary electrons. [153] These diffraction patterns produced in SEM were first reported by Coates. [154]

Backscattered electrons are emitted from the surface in the form of two symmetric Kossel cones, as shown in Figure 3.14 b. These cones intersect with a camera positioned perpendicular to the electron beam. The geometry of the resulting Kikuchi pattern (Figure 3.14 a) is determined by the crystal lattice orientation at the measurement position on the sample surface. Clear diffraction patterns require a sufficiently perfect crystal structure on the sample surface. Therefore, sample preparation for EBSD studies must involve removing layers of material with distorted atomic lattices due to previous mechanical processing. Techniques such as mechanical polishing with silica or alumina suspensions, electrolytic polishing, or polishing with an argon ion beam are used for this purpose.

In EBSD, the sample is tilted at a 70° angle to the primary electron beam using a pre-tilted SEM holder. This tilt enhances the yield ratio of the diffracted electron signal to the background by increasing the excited volume of near-surface material.

(a) (b)
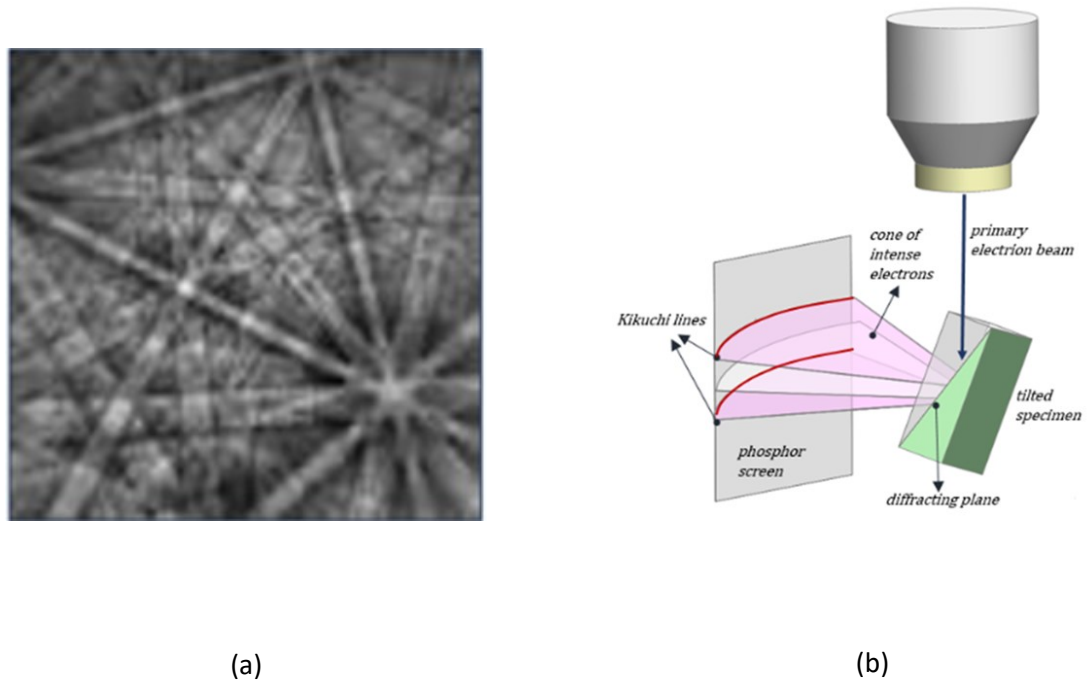
Figure 3.14. Schematic diagram of electron backscatter diffraction patterns: (a) Backscatter Kikuchi pattern and (b) the diffracting cones with respect to the reflecting plane, the specimen, and the phosphor screen. Adopted from [155]

The EBSD scan follows a user-defined raster pattern on the specimen surface. Efficient software for pattern recognition and indexing is crucial for identifying and indexing Kikuchi patterns. Initially, Wright and Adams [156] pioneered automatic Kikuchi patterns recognition using an algorithm proposed by Burns *et al*. [157] based on the bands analysis in diffraction patterns. This algorithm was later replaced by the Hough transform, which is known for its speed and robustness. [158] To improve the identification of patterns, the contrast of Kikuchi bands is enhanced through additional image processing techniques such as background subtraction.

Detecting bands inherently carries a certain level of uncertainty. The confidence index (CI) value is used to express the reliability of determining local orientation. The confidence index is established on a voting scheme and is expressed as $CI = (V1 - V2)/V_{ideal}$, where V1 and V2 represent the number of votes for the first and second solutions, and V_{ideal} is the total potential number of votes from the detected bands. Typically for CI greater than 0.1, ~95% of patterns for an FCC structure are correctly indexed.

In this work, EBSD mapping was performed using an EDAX Digiview camera mounted on a Zeiss Auriga 60 scanning electron microscope operated at 20 kV. The sample was prepared through mechanical

polishing, succeeded by electrolytic polishing utilizing a QATM – QETCH 1000 device. The polishing parameters included a voltage of 10 V and a temperature of -20 °C in A2 Struers electrolyte.

3.4.1.3. Limitation in SEM

Resolution in SEM depends on several factors, including the beam-sample interaction volume and the size of the electron beam. In SEM, the spatial resolution for SE can be as low ~ 1 nm. However, as shown in Figure 3.15 a, a substantial interaction volume reduces the resolution which make challenging to accurately displaying fine features. The size of interaction volume depends on the accelerating voltage and the density of the sample. At higher accelerating voltage, the electron beam penetration is greater and the interaction volume is larger. Therefore, it leads to increased electron scattering and lateral spread of the signal. As a result, the spatial resolution decreases because the emitted electrons or signals come from a broader area of the sample, blurring the image details.

Furthermore, in SE imaging, BSEs can enter the SE detector and degrade resolution because they come from deeper in the sample. Additionally, as shown in Figure 3.15 b, there are three sources for generation of SE: (i) SE1 electrons that are generated at the point where the focused electron beam hits the specimen. (ii) SE2 electrons generated by the BSE when they leave the sample at different angles and from an area around the point of the primary beam incidence, and (iii) SE3 electrons generated by BSE elsewhere on the walls of the microscope chamber or on the lens pole piece. SE1 carry the highest spatial resolution information, since spatial resolution is mainly determined by the size of the electron beam. However, in the ETD the SE2 and SE3 signals cannot be separated from SE1 which would tend to degrade in spatial resolution. However, modern SEMs are equipped with in-lens SE detectors, where the sample is immersed in the magnetic field of the final lens. In-lens SEM detectors mostly collect SE1 secondary electrons, thus capturing the highest spatial resolution information available.
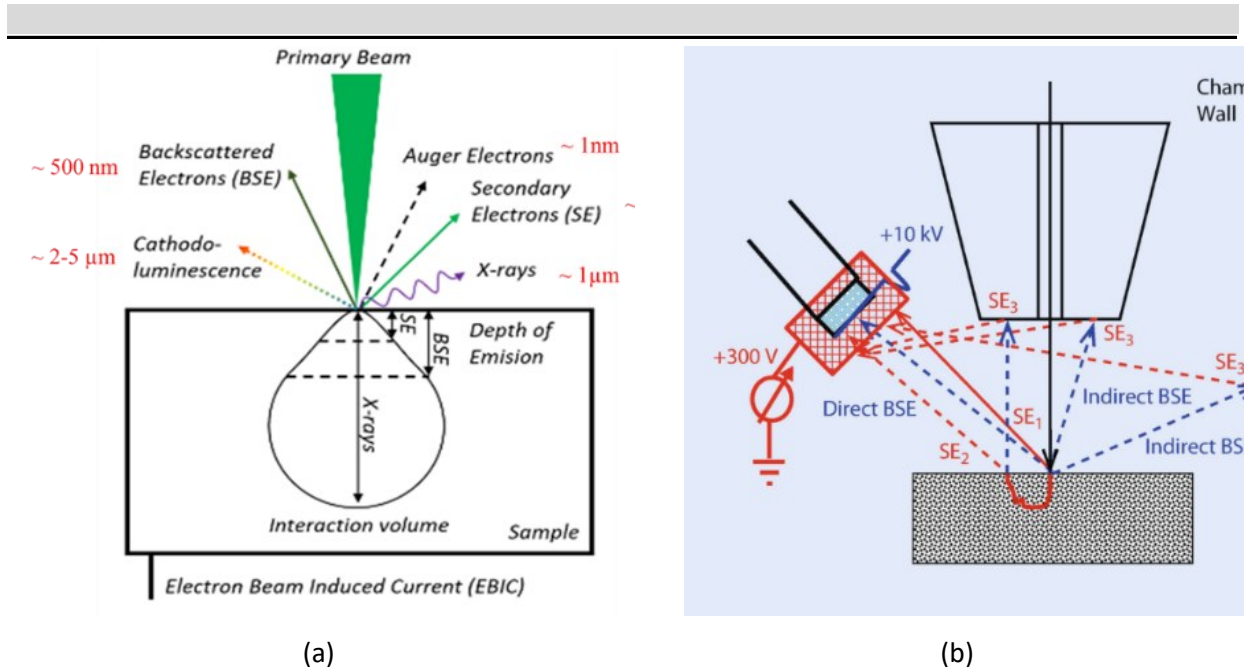
Figure 3.15. (a) Schematic representation of the interaction volume of a focused electron beam with a bulk sample. Different signals are generated which escape from different depths (marked in red) from below the sample surface. [159] (b) three types of secondary electrons collected by the Everhart-Thornley detector. [160]

3.4.2. Transmission electron microscopy

Material characterization is of critical importance for fundamental research in materials science, serving as its cornerstone. Designing materials with new properties involves precise quantification of structural parameters and a comprehensive understanding of material physics and chemistry – all of which requires the use of robust methods capable of studying structure and properties over a wide range of length scales from the macroscopic to the atomic level. TEM is an indispensable characterization tool in materials science, providing information on structure and composition at high spatial resolution down to the atomic level. As industry continually pushes technological boundaries, demanding information about the fine details of materials structure, TEM maintains its key role in shaping the future directions of material development. This section will provide a general overview of TEM, followed by a discussion of TEM components and operation modes, including (S)TEM, diffraction, HR(S)TEM, as well as TEM analytical capabilities.

3.4.2.1. General description of TEM

A Transmission Electron Microscope is a complex instrument to produce magnified images of a sample using an electron beam passing through a specimen. Similar to SEM, the core element in the TEM setup is the electron source, responsible for generating a high-energy electron beam. Electron sources

commonly used include field-emission sources (Schottky/cold FEG) or thermionic filaments (LaB$_6$). In modern instruments, the preferred method has shifted towards Schottky and cold field emission gun, as both provide high brightness and a narrower electron energy spread compared to thermionic emission. In the case of Schottky emitter, a heated tip of oriented tungsten single crystal is used; its surface is covered with ZrO$_2$ from a reservoir to decrease the working function. A cold field-emission gun emitter is normally made of tungsten with the surface of the (310) plane and working at room temperature without heating. In operation, the tip of the source is located in a region of a strong electrostatic field enabling electrons to tunnel into the vacuum. These sources produce a beam of electrons subsequently accelerated by the field, usually within the range of 60 – 300 kV.

Directly below the electron gun is a condenser system consisting of three electromagnetic lenses with apertures that form a beam of electrons used to illuminate the sample, in particular to change its convergence angle and provide either a broad parallel beam for conventional TEM or a convergent beam for STEM. Apertures also cut off electrons at a larger angle to improve coherency. There is a mini condenser lens, which governs the illumination mode onto the sample, either a broad parallel beam for conventional TEM or a convergent beam for STEM. The specimen is located between the upper and lower pole-pieces of the objective lens. It has to be sufficiently electron-transparent, i.e., thin enough to enable electron transmission.

When the electron beam passes through the upper pole piece of the objective lens, it strikes the sample, generating the signals mentioned earlier, which can be used for imaging, diffraction, and spectroscopy. The objective lens is the most important component of the TEM; it forms a diffraction pattern in its back focal plane, and an image of the sample in its image plane, which are then magnified by the projection lenses. Figure 3.16 represents the schematic view of a TEM for the two main operating modes, image and diffraction. Switching between these two modes is performed by changing the strength of the intermediate lens. Further magnification is obtained by the projection system, and the final magnified image can be observed on the viewing screen or using the camera.

Electron lenses are not perfect. They suffer from various kinds of aberrations. The main aberrations are spherical aberration, chromatic aberration and two-fold astigmatism. These aberrations contribute to a degradation in the ultimate resolution of the image. The new generation of transmission electron microscope is capable to correct these lens imperfections using aberration correctors, which opened new possibilities for obtaining images with sub-angstrom resolution. It is worth noting that direct interpretation of the HTREM micrographs especially for complex structure is not possible, so image processing using image simulation with structure models is necessary. [161]

Due to the difference in scattering of electrons by the sample material, areas with different contrasts appear in the TEM image. There are two main types of contrast - amplitude and phase contrast. Amplitude contrast can be created by two mechanisms: mass-thickness and diffraction contrast., Mass-thickness contrast depends on mass and thickness differences of the specimen, with higher Z and thicker regions scattering more electrons, thus reducing the intensity of the direct beam and causing these regions to appear darker in the image. Mass–thickness contrast dominates for non–crystalline materials while for crystalline materials diffraction contrast dominates. In this case, the intensity of the BF image depends on the local orientation of the crystal.
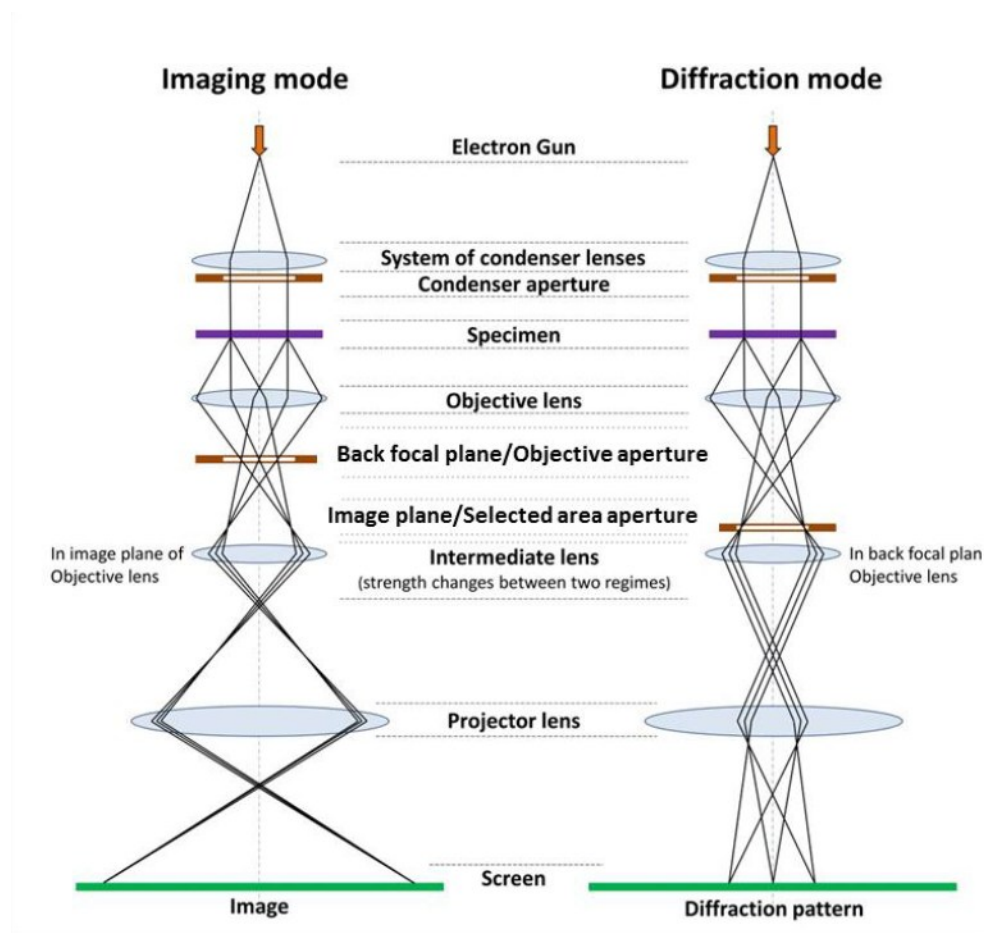
Figure 3.16. TEM ray diagram in (a) image and (b) diffraction modes. Reprinted from Ref [162]

3.4.2.2. Electron diffraction

In this section, the condition of electron diffraction will be briefly described. After a brief description of diffraction condition, the diffraction from a lattice will be presented.

3.4.2.2.1. Condition for diffraction

In general, the condition for diffraction is typically expressed using Bragg's law or in terms of reciprocal lattice geometry, known as the Laue condition. This is illustrated in Figure 3.17 b and states that in terms of reciprocal space for elastic scattering and constructive interference we have:

$$|k_0| = |k|, \Delta k = k - k_0 = g_{hkl}, \qquad 3.18$$

where k_0 and k are the wave vectors in the incident and scattered directions, the magnitudes of both are equal to $1/\lambda$, and the angle between them equals to 2ϑ.

(a)

(b)
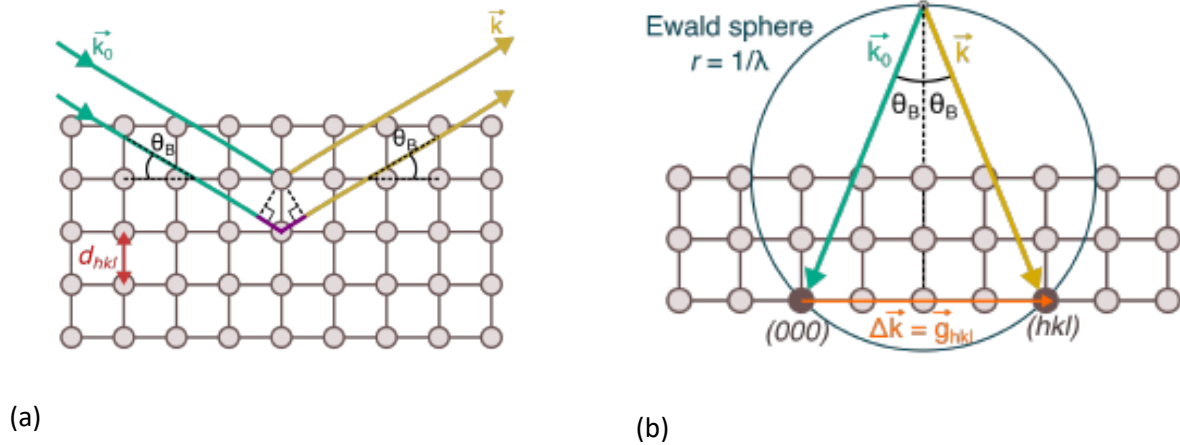
Figure 3.17. (a) Schematics showing Bragg diffraction by a set of lattice plane for an incident plane wave k_0 at the Bragg angle ϑ and (b) schematics of the Laue condition and Ewald sphere construction. [71]

A convenient way to visualize diffraction conditions in reciprocal space is to use the so-called Ewald sphere. It is a sphere of radius $1/\lambda$, passing through the reciprocal lattice origin (000). The incident wave vector k_0 passes through this origin and thus determines the center of the sphere. The scattered wave vectors can be drawn in any direction from this center and will have a magnitude equal to $1/\lambda$. The diffraction condition is satisfied for the reciprocal lattice site (and, accordingly, for the crystal lattice plane) which intersects the Ewald sphere.

Due to the short wavelength of electrons, the radius of the Ewald sphere is much larger than in the case of X-ray diffraction. Therefore, its surface near the zero beam can be approximated by a plane with sufficient accuracy. Additionally, in the case of TEM for a thin sample of thickness t, the lattice sites in the reciprocal space can be considered as rods (relrods) with a length of $2/t$ extending in the sample normal direction. This means that diffraction also occurs at small deviations away from Bragg condition, i.e., equation 3.14 can be rewritten as follows:

$$\Delta k = g_{hkl} + s, \qquad\qquad 3.19$$

where s is the excitation error, which determines the deviation from the Bragg condition. Due to this, a set of reflections appears around the zero site, and electron diffraction patterns can be considered as a two-dimensional projection of the reciprocal lattice plane.

3.4.2.3. High Resolution TEM

HRTEM makes it possible to image the atomic structure of materials and is widely used for advanced characterization of materials, providing information on crystal structure defects, like dislocations, twins, stacking faults, precipitates, grain boundaries. Because HRTEM images are an interference pattern of many electron beams passing through a sample, there is no direct correlation between the contrast in that image and the exact positions of individual atoms in the structure. Thus, the lattice fringes observed in the image are not a direct image of the structure, but they do provide information about the distances and orientation of the lattice.

The formation of HRTEM images can be described using wave optics. In TEM, the incident electron beam is treated as a plane wave, which represents a coherent wave front with uniform amplitude. When the electron beam interacts with the sample, it undergoes a phase shift and possibly changes in amplitude, which reflects the atomic structure and electrostatic potential of the sample. The interaction modifies both the amplitude A and phase ϕ of the incident wave, resulting in the exit plane wave described by:

$$f(\boldsymbol{r}) = A\exp(-i\varphi_t(r)). \qquad\qquad 3.20$$

Here r is a two-dimensional vector in the plane of a sample. Assuming very thin and weakly scattering samples, as well as high electron energies, two simplifications can be made. Firstly, the object (sample) can be seen as a pure phase object; that is, $A = 1$. Secondly, the phase change can be considered to be very small ($\phi^2 \ll 1$), which results in the weak phase-object approximation (WPOA):

$$\psi(\boldsymbol{r}) = 1 - i\sigma V_p(\boldsymbol{r})t, \qquad\qquad 3.21$$

In this approximation, σ is the interaction constant, and $V_p(\boldsymbol{r})t$ is the projected potential of the sample along the z-direction (the direction of electron propagation). The small phase change leads to a linear relationship between the amplitude and the potential, which allows us to represent the wave function $\psi(\boldsymbol{r})$ in this simplified form. To understand how the exit wave is visualized by the microscope, it is necessary to consider the transfer by the optical system. The exit wave experiences phase alterations as it moves through the objective lens and the optical system. The wave transmitted through the optical system can be represented by:

$$\psi_{image}(r) = \psi_{exit}(r) \otimes T(r), \qquad\qquad 3.22$$

where *T(r)* is the transfer function of the general form $e^{-i\chi(r)}$, excluding the aperture and envelope functions. Combining equations 3.21 and 3.22, the wave function in the image plane can be calculated as follows:

$$\psi_{image}(r) = \left[1 - i\sigma V_p(r)t\right] \otimes e^{-i\chi(r)} =$$
$$\left[1 - i\sigma V_p(r)t\right] \otimes \left[\cos\chi - i\sin\chi(r)\right]. \qquad 3.23$$

The image intensity is the wave function multiplied by its complex conjugate and can be expressed as:

$$I(r) = \psi_{image}(r) * \psi_{image}^*(r) =$$
$$= 1 + 2\sigma Vp\,(r)t \otimes \sin\chi(r) + |2\sigma Vp\,(r)t \otimes e^{-i\chi(r)}|^2. \qquad 3.24$$

In the WPOA, $\sigma Vp\,(r)t$ is much smaller than 1, making the squared term in equation 3.24 negligible compared to the linear term. This leads to the linear imaging approximation, where the squared term is omitted.

$$I_{image}(r) = \psi_{image}(r)\psi_{image}^*(r) \approx 1 + 2\sigma V_p(r) \otimes \sin(r). \qquad 3.25$$

This equation describes the contrast in the image resulting from the projection of the sample potential, where the intensity is influenced by both the sample potential distribution and the sinusoidal term arising from interference effects between scattered waves.

Equation 3.25 can be expressed in Fourier space as:

$$I(u) = \delta(u) + 2\sigma Vp\,(u)t * \sin\chi(r), \qquad\qquad 3.26$$

where $Vp\,(u)t$ is Fourier transform of $Vp\,(r)t$, $\chi(u)$ is description of the aberrations in Fourier space.

We introduce a new quantity *T(u)*:

$$T(u) = A(u)E(u)2\sin\chi(u),$$ 3.27

where *A(u)* and *E(u)* are aperture and envelope function respectively, and $\chi(u)$ has been defined above. This quantity is called the intensity transfer function; however, if we are working in WPOA, it is called the phase transfer function (CTF), since there is no amplitude contribution and the output of the transfer system is the observed value (image contrast). The CTF determines the phase shift, expressed as the difference in optical path for different wavelengths, which is affected by aberrations of imaging lenses. For the microscope without the aberration corrector, three terms for the aberration function are usually considered, i.e., spherical aberration, defocus and two-fold astigmatism, Assuming that the astigmatism is corrected, the phase shift is the sum of the two terms. The combined effect of spherical aberration and defocusing of the objective lens causes the point on the specimen to appear as a disk with radius $\delta(\theta) = C_s\theta^3 + \Delta f\theta$, where C_s is the spherical aberration coefficient, and Δf is the defocus of the objective lens. [148] For the full range of available angles, we obtain the radius value as the corresponding integral:

$$D(\theta) = \int_0^\theta \delta(\theta)d\theta = \frac{C_s\theta^4}{4} + \Delta f\frac{\theta^2}{2}.$$ 3.28

Taking into account Bragg's law and the small value of θ, we can assume $2\theta \cong \lambda g$. Thus, we can write an expression for the phase shift:

$$\chi(u) = \frac{2\pi}{\lambda}D(u) = \frac{2\pi}{\lambda}\left(C_s\frac{\lambda^4 u^4}{4} + \Delta f\frac{\lambda^2 u^2}{2}\right) =$$
$$\frac{\pi}{2}C_s\lambda^3 u^4 + \pi\Delta f\lambda u^2.$$ 3.29

This function indicates that the aberration function is the sum of two terms; the first term represents the effect of spherical aberration. Electrons passing through the center of the lens and away from the optical axis are focused differently, so a point on the sample appears in the image as a disk of finite size. Spherical aberration in general is unavoidable for rotationally symmetric electron lenses. This property is known as Scherzer theorem. The imperfections in the objective lens contribute additionally to this term. The second term describes the effect of defocus, which leads to the formation of a disk in the image plane, limiting the ability to magnify details because the feature is degraded in the imaging process. Equation 3.29 holds for paraxial rays only. In a real imaging, paraxial conditions do not apply and the image disk of a sample point broadens to a larger diameter The aberration function χ results in additional phase shifts of the exit wave in back focal plane. In this simple form, the influence of other aberrations is neglected. It can be seen that the phase shift produced by the interaction with the specimen is further modified by the objective system, which leads to the intensity variations in the interference image. This is the phase contrast used in HRTEM imaging.

The CTF represents the phase shift introduced by defocus and spherical aberration as a function of spatial frequency. In TEM, the C_s of the lens is fixed and always positive (unless an aberration corrector is installed in the microscope), but the focus can be changed, affecting the CTF value. CTF is an oscillatory function containing transmittance bands and the area with no transmission (zeros) (see Figure 3.18). CTF can be optimized by balancing the effect of spherical aberration and a definite negative defocus. This defocus value is referred to as Scherzer defocus:

$$\Delta f_{Sch} = - \left(\frac{4}{3} C_s \lambda \right)^{1/2} \qquad\qquad 3.30$$

At the Scherzer focus, the HRTEM image of a weak-phase object represents the projected atomic potential up to the first zero transition of the CTF, which defines the point resolution of the TEM:

$$d_p = 0.66 C_s^{1/4} \lambda^{3/4}. \qquad\qquad 3.31$$

Spherical aberration is a consequence of the rotational symmetrical magnetic field of the objective lens and its value is always positive, since Cs>0. The effect of spherical aberration on CTF can be counterbalanced by some negative defocus value Δf.
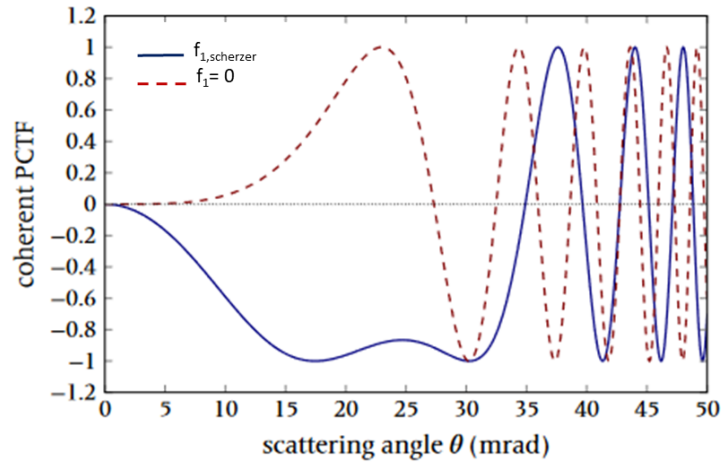
Figure 3.18. Coherent phase contrast transfer function for an aberration corrected 80 kV TEM (C_s = 15 μm) at Scherzer defocus f_1 = −9.14 nm (blue solid line) and for f_1 = 0 (violet dashed line). Adopted from [163]

The TEM is influenced not only by the objective aperture and phase shifts induced by the objective lens post field but also by the coherence of the electron beam illuminating the specimen. In an ideal scenario with a point-like electron source, phase contrast microscopy entails a fully coherent imaging process. However, real electron sources have finite sizes, never being singular points, and produce electrons with slightly varying energies. Consequently, the incident electron beam, k_0, exhibits partial

rather than full coherence. The finite size of the source results in partial spatial coherence, while the beam finite energy spread leads to partial temporal coherence. Thus, phase contrast microscopy is considered a partially coherent imaging technique rather than fully coherent. While the imaging process can be theoretically modeled as fully coherent, the effects of partial coherence are accommodated through damping envelope functions, which effectively diminish and restrict information transfer at high spatial frequencies. [164]

The resolution in HRTEM is ultimately limited by the so-called information limit, where the envelope functions drop below a value of $1/e^2$ (grayed-shaded area). As shown in Figure 3.19, the larger energy width reduces the information limit significantly.
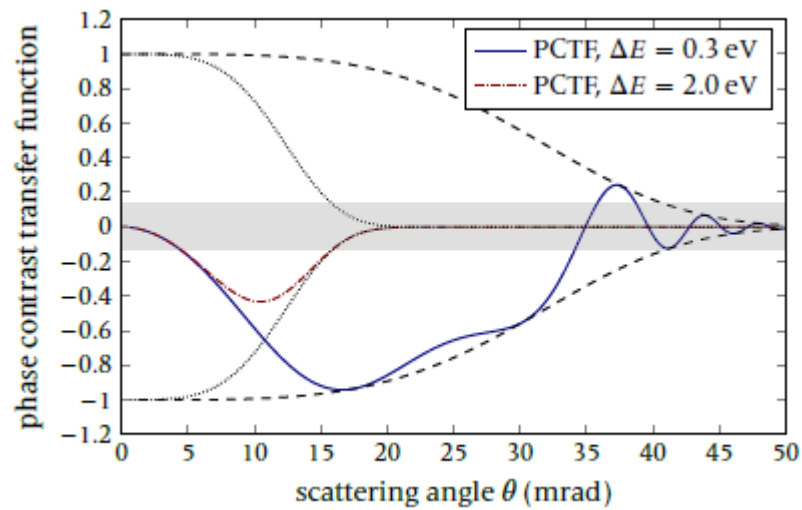
Figure 3.19. Effect of the chromatic aberration on phase-contrast imaging (80 kV, C_s = 15 µm, Scherzer defocus, C_c = 1 mm, θ_s = 0.2 mrad). The blue solid curve exemplifies the full CTF for an energy width of 0.3 eV FWHM (ΔE_{rms} ≈ 0.13 eV), black dashed lines show the combined envelope functions $E_s \cdot E_t$. The red dash-dotted curve shows the CTF for a larger energy width of 2.0 eV FWHM. Adopted from. [163]

In practical HRTEM, point resolution is influenced by objective lens aberrations, which introduce additional phase shifts and affect image quality, particularly in aberration-corrected TEM systems. These aberrations, categorized by their symmetry and order, include third- and fifth-order spherical aberrations, coma, and chromatic aberrations, as outlined in Table *3.4*and corresponding wavefront in Figure *3.20*. Modern correction systems address most third- and fifth-order aberrations, such as spherical, astigmatic, and coma aberrations, as well as certain higher-order chromatic aberrations.

However, dynamic effects, specimen-induced aberrations, and extremely high-order terms remain challenging to correct, even with advancements in hardware, alignment techniques, and software. [165]

Table 3.4. List of axial wave aberrations

Symbol	Name
C_{12}	Twofold astigmatism
C_{10}	Defocus
C_{21}	Axial coma
C_{23}	Threefold astigmatism
C_{34}	Fourfold astigmatism
C_{30}	Third- order spherical aberration
C_{41}	Fourth order coma
C_{45}	Fivefold astigmatism
C_{43}	Fourth order threefold astigmatism
C_{56}	Six-fold astigmatism
C_{50}	Fifth-order spherical aberration
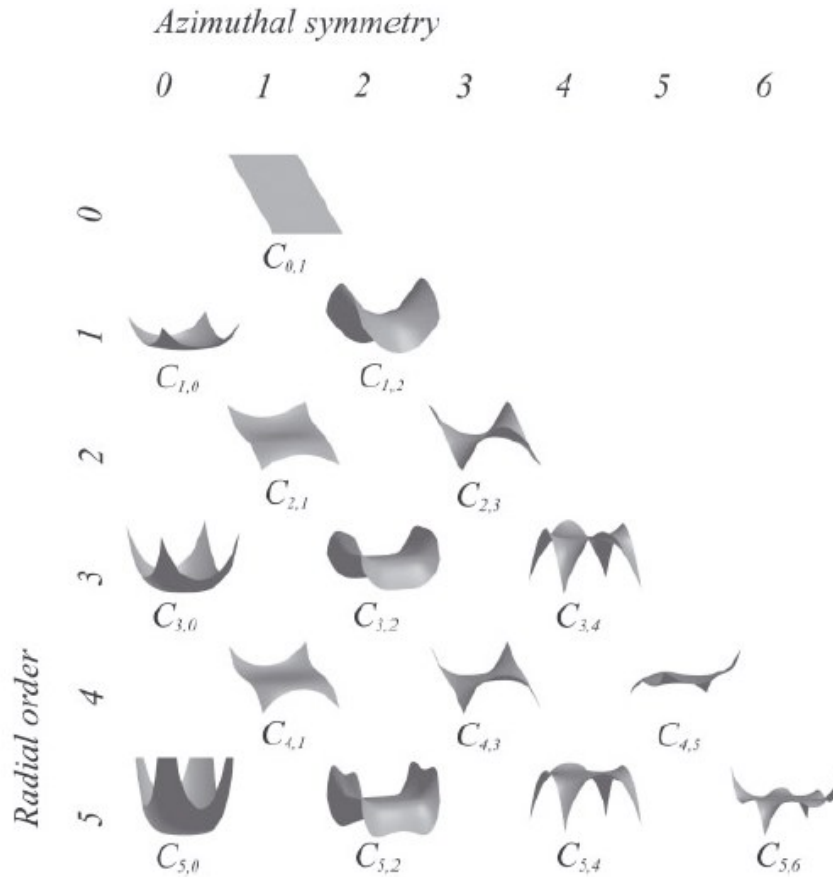
Figure 3.20. Three-dimensional rendering of the distortions introduced in the wavefront by all aberrations up to fifth order. [166]

It is important to note that the image formation process discussed above is based on the WPOA, i.e., implies a thin sample. However, in practice, the sample thickness rarely satisfies this assumption. The propagation of the incident electron wave through the specimen is influenced by the scattering of atoms in the material, where the Coulomb interaction between atoms and incident electrons induces phase shifts in the incident wave. In passing through a real specimen, the phase of the incident wave undergoes large variation due to multiple scattering by specimen atoms. The Bloch wave and the multi-slice methods have been developed to calculate the exit wave function as a result of the dynamic scattering of the incident wave, taking into account the thickness effect on the final contrast (intensity) in the image plane.

This discussion highlights that interpretation of HRTEM images is not always intuitive and requires considering of both the aberrations of the imaging lenses, and the thickness of the sample that introduce phase shifts to the propagating wave. To better interpret the atomic structures seen in HRTEM, image simulations are required to match phase contrast with a real structure model. [167]

3.4.2.4. Scanning transmission electron microscopy (STEM)

STEM is another widely used imaging mode in a modern electron microscope. In contrast to TEM, where the images are formed by a parallel beam, STEM images are generated by rastering a sub-nanometer electron probe across the sample. In this method, a convergent beam moves across the sample and creates transmitted electrons to scatter in various angular ranges. Dedicated annular detectors are used to acquire the scattered electrons and form a STEM image. These detectors are designed to collect electrons scattered over a specific angular range; Figure 3.21 schematically shows their arrangement. A circular bright-field detector collects the central portion of the direct, unscattered beam (up to ~ 10 mrad). These electrons form a BF image. Similar to BF-TEM images, the intensity in BF-STEM is sensitive to mass-thickness and crystal orientation. An annular dark-field (ADF) detector collects the mixture of Bragg diffracted and incoherently scattered electrons in the range $10 - 50$ mrad. The resulting image can be used to visualize strain fields. These strain fields typically emerge around defects such as interfaces, grain boundaries, and dislocations, as a result of the atom displacement. This displacement, in turn, leads to a local bending of the crystal planes and a change in the electrons scattering conditions. Electrons scattered at sufficiently high angles (50 mrad or larger) contain information due to the Rutherford as well as thermal diffuse scattering; they are collected by the high angle annular dark-field (HAADF) detector. The contrast produced by these electrons is mostly sensitive to the atomic number Z of the elements present in the sample. The differential cross section (δ) for Rutherford scattering on the nucleus alone is describe by:

$$\delta = \frac{e^4 Z^2}{16(4\pi\varepsilon_0 E_0)^2} \frac{d\Omega}{\sin^4\frac{\theta}{2}}, \qquad\qquad 3.32$$

where E_0 is the beam energy, ε_0 is the vacuum permittivity, ϑ is the scattering angle, e is the charge of an electron and Ω is the total solid angle of scattering. [168] It shows that the scattering probability at high angels is proportional to Z^2. However, it is important to mention that this formula overlooks the electron screening effect reducing the apparent positive charge of a nucleus for the incident electron. Consequently, the differential cross section is reduced. The screening effect leads to a decrease in the exponent from 2 to approximately $1.6 - 1.8$. [168]
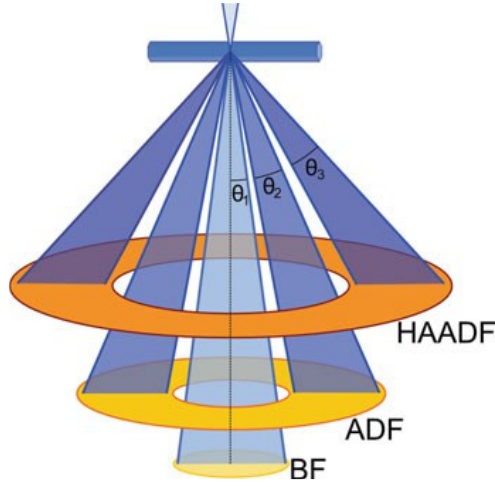
Figure 3.21. Schematics of the scanning probe and the detection system in STEM mode. Adopted from [169]

In STEM, two objects with a distance smaller than the size of the forming probe cannot be resolved. As such, the resolution in STEM imaging is fundamentally limited by the probe size. Therefore, the diffraction-limited resolution of in STEM can be described using the Rayleigh criterion which describe the resolution as a function of wave length and convergence semi-angle ($\delta = \frac{0.61\,\lambda}{N \sin \beta}$).

When electron wavelength is fixed, then the convergence semi angle is critical for resolution. As illustrated in Figure 3.22, there is optimum in convergence semi-angle (α) to reach the minimum size of probe. However, the resolution in STEM is constrained by various other factors such as defocus, aberrations of the probe forming lens and the size of condenser aperture. Equation 3.33 shows the resolution dependency with spherical aberration, spread of electron energy and microscope stability.

$$r(\beta) \propto \left[\left(\frac{\lambda}{\beta} \right)^2 + (C_s \beta^3)^2 + \left(C_c \frac{\Delta E}{E_0} \right)^2 \right]^{1/2}, \qquad 3.33$$

where C_S is the spherical aberration coefficient and C_c is the chromatic aberration coefficient. To achieve higher resolution, one can use higher acceleration voltages. Additionally, an electron beam emitted by FEG has a smaller energy spread compared to tungsten (W) or lanthanum hexaboride (LaB$_6$) electron sources, which also improves resolution.
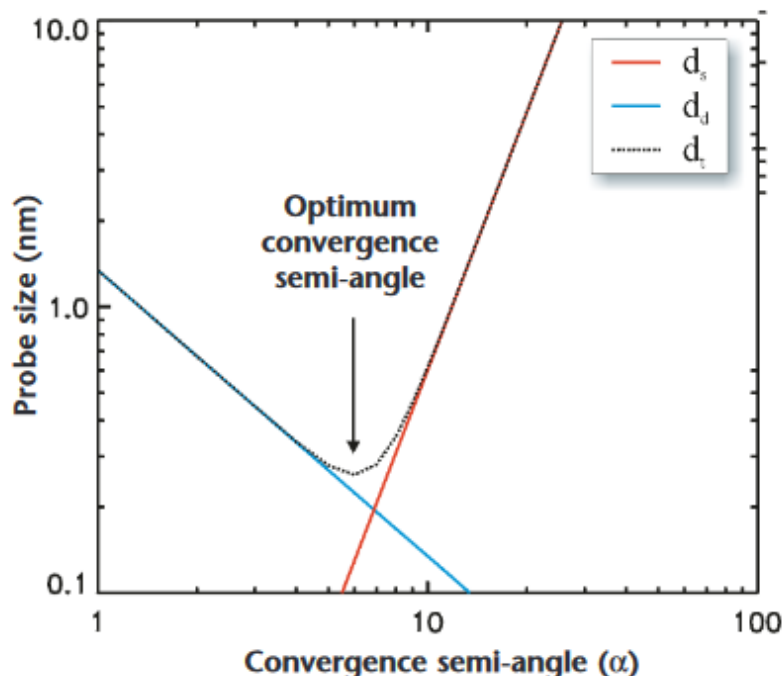
Figure 3.22. Balancing spherical aberration against diffraction. At low convergence semi-angle (α) the diffraction contribution (d_d) term dominates, while at high α the spherical aberration contribution (d_s) is dominant. The terms are calculated by d_d=0.61λ/α and d_s=1/2$C_s\alpha^3$. Terms are added in quadrature to generate the total (d_t). Adopted from [170]

As with HRTEM, the presence of aberrations negatively affects resolution by changing the shape of the probe. With advances in C_s aberration correction technology, modern microscopes are no longer limited to correcting third-order spherical aberration (C_3) and two-fold astigmatism; they are now capable of correcting higher-order aberrations up to the fifth. In cases where some cannot be corrected, methods can be developed to minimize their impact on phase distortions. For example, with a corrector to eliminate C_3, it may be possible to balance the residual C_5 against to C_3 to minimize phase distortion.

Modern microscopes also have low chromatic aberration due to high voltage stability, lens current, and monochromatic electron beam, reducing the electron energy spread from approximately 1 eV to less than 0.1 eV. All this together extends the information limit of the instrument up to sub angstrom.

Further developments are also associated with improving the mechanical stability of the stage; In addition, higher vacuum around the sample area is becoming increasingly important. However, these advances come at a higher cost not only for the instrument itself, but also for ensuring optimal operating conditions, such as minimizing vibrations, stray electromagnetic fields, and air turbulence near the instrument. [165]

3.4.3. Spectroscopy techniques

As noted above, the interaction between primary electrons and the sample generates various signals that can be used for imaging and analysis in TEM. The following section will describe the basics and specific practical aspects of the two main analytical techniques in TEM, namely, energy-dispersive X-ray spectroscopy (EDX) and electron energy loss spectroscopy (EELS).

3.4.3.1. Energy-dispersive X-ray spectroscopy

Characteristic X-rays are produced through a process where electrons are displaced from the inner electron shells of an atom due to the impact of primary electrons. This displacement leads the atom to enter an excited energy state. Consequently, an electron jumping into the vacancy from outer shells fills the vacant electron orbital. The energy released during this process can be emitted as a photon. Since the energy difference is related to the electron configuration of the atom, the resulting characteristic X-ray serves as a distinctive "fingerprint" indicating the atom involved in the interaction. The emitted X-rays are classified by a dedicated notation. K, L or M indicates (Siegbahn notation) that the atom has been ionized by ejecting an electron from the K, L or M shell. The α, β or γ with a number refer to the involved outer shell, from which the inner shell vacancy is refilled. Hence, the characteristic X-rays are labeled as Kα1, Lβ1, *etc*. which stand for different, and element specific X-ray energies. [162] The schematic electronic transition between layers is shown in Figure 3.23a. By collecting characteristic X-ray spectra, the elemental composition of a sample at a point of interest can be analyzed. It is also possible to record an elemental composition map by systematic acquisition of characteristic X-ray spectra using the raster approach.

By measuring the intensity of the corresponding lines in the EDX spectrum, the composition of the sample can be quantified using the Cliff-Lorimer equation: [171]

$$\frac{c_A}{c_B} = k_{AB} \frac{I_A}{I_B},$$
3.34

where $c_{A,B}$ are the weight fraction of elements *A* and *B*, while $I_{A,B}$ denote the peak intensity of the two elements; k_{AB} in the equation is the Cliff-Lorimer (sensitivity) factor. The intensity of characteristic X-rays depends on the sample elemental composition, mass thickness (density and thickness), and detection setup. Key factors include the ionization cross-section, fluorescence yield, and beam current, which influence the generation of X-rays, while the detector geometry and efficiency affect how many X-rays are captured.

The TEMs used in this work were equipped with a Super-X system to record EDX spectra. It consists of four silicon drift detectors (SDD) positioned symmetrically around the optical axis near the sample

65

area, as illustrated in Figure 3.23b. This detector geometry enables a more efficient X-rays collection compared to traditional EDX detector setup. The signals from these four detectors are combined, resulting in reduced overall acquisition time and therefore in enhanced collection efficiency over a wide range of tilt angles. [172][173]

| (a) | (b) |
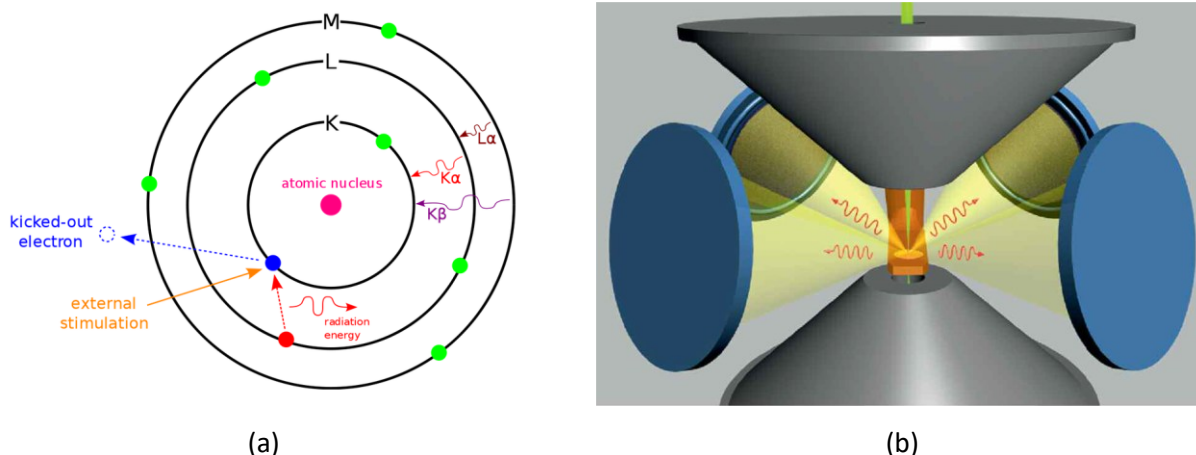
Figure 3.23. (a) Electronic transitions involved in the production of X-rays [174], and (b) Schematic illustration of the Super-X detector geometry including four SDD arranged symmetrically around the sample and the objective lens pole pieces. Adopted from [175]

3.4.3.2. Electron energy-loss spectroscopy

Electron energy-loss spectroscopy provides information on the electronic structure, elemental composition, valence state and bonding of atoms, band gap, and sample thickness. The technique measures the energy lost by high-energy electrons as they pass through a sample, interacting with its atoms. These energy losses arise from several physical processes, including inelastic scattering events where the incident electrons excite atomic electrons to higher energy states or cause collective oscillations of electrons, known as plasmons. To record an EEL spectrum, a spectrometer equipped with a magnetic prism is used. When electrons pass through a magnetic prism, they are deflected by the Lorenz force and split into a spectrum depending on their energy. The resultant energy loss spectrum is recorded by a CCD/CMOS detector located in the energy dispersive plane of the spectrometer.

The EEL spectrum can be divided into three regions: a zero-loss peak, low (up to ~50 eV) and high (above ~50 eV) energy losses. [162] The low-loss region contains information about the weak bound conduction and valence-band electrons. The high-loss region predominantly contains elemental information, bonding coordination numbers and interatomic distances of the elements derived from the more tightly bound core-shell electrons. Figure 3.24 shows a typical spectrum indicating these regions.

An intense peak with zero energy loss is accompanied by a plasmon peak in the energy range 5–30 eV. By measuring the intensity of the plasmon peak, we can estimate the thickness of the sample using the log-ratio method [176]:

$$t = \lambda \ln \left(\frac{I_t}{I_0} \right), \qquad\qquad 3.35$$

where λ is the inelastic mean free path, I_t and I_0 are the total and zero-loss intensity in the spectrum.
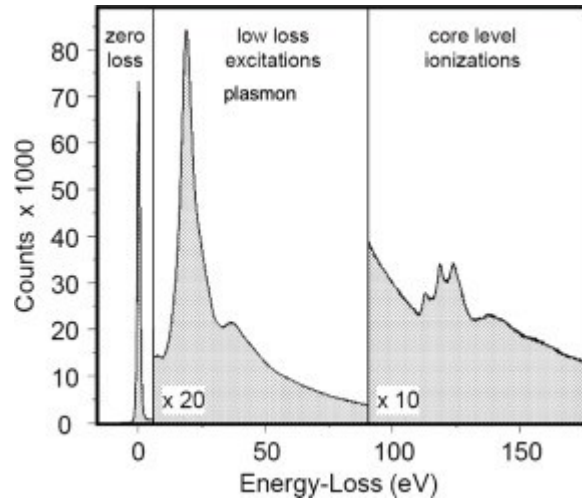
Figure 3.24. An example of EELS spectrum with the three different regions (zero-loss, low-loss, core-loss) labeled. Adopted from [177]

3.4.4. Atom probe tomography

Chemical analysis of nanosize features in STEM-EDX is often difficult because the signal from these features overlaps with each other and with the signal from the matrix. APT shows a very high analytical sensitivity down to ppm range (depending on the element). APT delivers a three-dimensional (3D) image at the atomic scale, where each atom or isotope and its position within the sample volume are precisely defined. This allows one to extract a variety of information about the analyzed material. More information about APT can be found in Ref. [178].

The working principle of the APT is shown in Figure 3.25. The sample for study is prepared in the form of a very sharp tip with a curvature radius of about 50 nm. The sample is in cryogenic conditions (T= 30 K), and a high voltage (5–15 kV) is applied to it. In the most frequently found commercial design, the local electrode atom probe (LEAP), the stage possesses 3D mobility, enabling the alignment of specimens in

front of a microelectrode equipped with an aperture diameter of ~ 40 μm. [179] The very small tip radius and high voltage applied induce a very strong electrostatic field at the tip surface (tens of V/nm). Under the influence of a high-voltage pulse, ions evaporate from the surface of the sample; they are accelerated and projected onto a position-sensitive detector. The detector simultaneously (i) records the position of individual ions and the order of their arrival, which makes it possible to restore the original position of atoms in the sample, and (ii) the time-of-flight (TOF) of the ions to determine the mass/charge ratio. This procedure is repeated, removing sample atom by atom, and a 3D image of the sample can be reconstructed at the atomic scale. [180]. However, in the case of multiphase materials with differing evaporation threshold, the real tip shape changes during the measurement and the projection on a spherical emitter leads to significant distortions in the reconstruction known as local magnification artifacts. [181] Though the composition of features in the APT reconstruction may not be severely affected by local magnifications, the size of embedded nano-precipitates can deviate significantly. [182] To use pulsed evaporation under the influence of an electric field, the sample must be conductive. As an alternative, short laser pulses can be used for non-conducting samples. Vaporization by laser pulses is also used to reduce the risk of destruction of brittle materials. [183]

To analyze spatial correlations of atomic distributions within the reconstructed volume, the Pearson coefficient is often used. The Pearson coefficient quantitatively evaluates the degree of correlation or anti-correlation between different elements. It is defined as the normalized covariance between the local concentrations of two species, accounting for their statistical distributions. A positive Pearson coefficient indicates a tendency for co-clustering (elements are found together), a value of zero indicates random distribution, and a negative value suggests mutual exclusion (segregation). This statistical tool provides critical insights into solute clustering, precipitation, and phase separation at the atomic scale, enabling researchers to better understand nanoscale phenomena within the analyzed material.
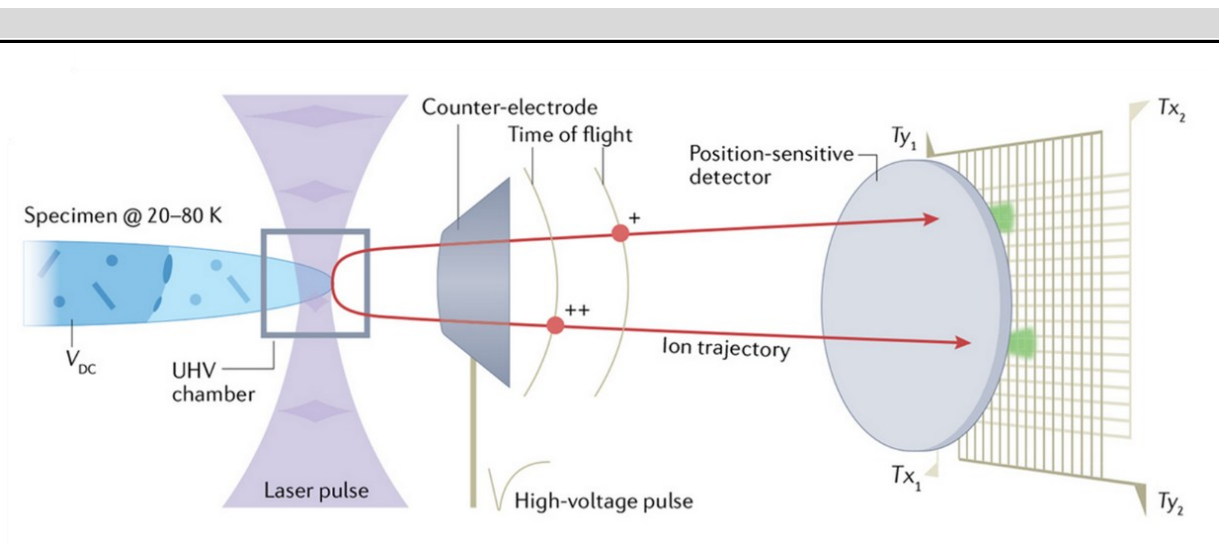
Figure 3.25. Principle of the ATP technique. Atoms at the surface of the specimen are evaporated by field effect and fly towards a detection system. Adopted [184]

3.5. TEM and APT sample preparation and study instrumentation

To study materials by means of TEM it is necessary to prepare ultrathin samples with a thickness around 100 nm or less. The quality of sample preparation is an important part of research, allowing one to obtain reliable results for materials with nanoscale structural features.

Samples of the alloy for TEM studies were prepared by electrolytic polishing. This relatively simple, and fast method for the sample preparation allows one to obtain samples with a large field of view while retaining its original structure. First, the samples are ground and polished mechanically to a thickness of approximate of 150 µm, then disks with diameter of 3 mm are punched out from them. Electrolytic polishing was carried out on a Tenupol-5 device (Struers) using standard A2 Struers electrolyte, 20 V and −20 °C. Polishing automatically stops when a hole appears in the central part of the sample. Before placement in TEM, samples were treated in a Fischione 1020 plasma cleaner in O_2/Ar mixture plasma for 2 minutes to remove carbon-containing organic compounds and prevent carbon contamination during TEM study.

In this work, conventional and high-resolution TEM studies were performed on a double aberration corrected transmission electron microscope Themis Z (Thermofischer Scientific) operated at 300 kV and a probe corrected Themis 300 (ThermoFischer Scientific) operated at 200 kV to reduce knock-on damage. The foil thickness was measured by EELS using a Continuum 963 (Gatan Inc.) spectrometer. Elemental analysis was performed by EDX spectroscopy using a Super-X detector. The experimental data was

evaluated with Digital Micrograph 3, Velox V3.9 and JEMS software. STEM simulation was done using the Prismatic V2 software [185] with the crystal structure modeled in Vesta software [186].

APT tips were prepared by Strata 400S Dual Beam System (FEI). It is equipped with a Schottky field emission gun and a gallium liquid ion metal source. The Gas Injection System (GIS) contains Pt, W and C, which Pt was used in this study. In this work, APT analysis was conducted using a LEAP 4000X HR instrument. In LEAP, a local-electrode geometry [183] allowed to go from a 15 nm field of view to greater than 150 nm. Furthermore, laser pulses have been used to generate pulsed field evaporation meaning that the sample is required for high conductivity. Specific measurement parameters are described in detail in the relevant chapters. The APT reconstruction and data evaluation processes were performed in AP Suite 6 software.

Chapter 4

4. Microstructure and properties of the HPTE-processed alloy

4.1. Introduction

Although aluminum has gained significant attention in recent decades and is widely recognized as a highly demanded engineering material, its relatively low strength remains a critical limitation. This shortcoming presents challenges in applications that require high mechanical performance, often leading to increased service costs and necessitating frequent maintenance or replacement of components. To address these challenges, as discussed in Chapters 1 and 2, recent advancements in materials processing, particularly through SPD techniques, have shown significant promise in enhancing the mechanical performance of aluminum alloys. Techniques such as HPT have been extensively studied for their ability to produce ultrafine-grained (UFG) and nanostructured aluminum alloys, resulting in markedly improved mechanical properties. However, these methods are often constrained by scalability issues, limiting their application to laboratory-scale studies rather than widespread industrial production. To address this limitation, High-Pressure Torsion Extrusion has emerged as a promising alternative. HPTE not only retains the ability to refine microstructures and improve material properties but also offers the potential for scalability, thereby making it a more viable option for industrial applications.

In this chapter, we investigate the structural evolution of an aluminum alloy subjected to HPTE using advanced characterization techniques such as TEM, EBSD, APT, and XRD. Furthermore, we will delve into the reliability and accuracy of the obtained results, discussing both the systematic and statistical errors associated with each characterization method.

4.2. Microhardness and EC

As detailed in Chapter 3, HPTE processing was carried out in three different regimes: V1W1, V3W1, and V10W1. Vickers micro-hardness tests were employed to assess the strength of the samples following each treatment. Figure 4.1a illustrates the microhardness profile across the sample diameter, highlighting a significant increase in hardness at the edges, with lower values at the center. The hardness at the edge is ~ 20% larger compared to that in the center of the sample. This V-shaped hardness profile observed after HPTE is a well-documented phenomenon and can be attributed to the distribution of strain and structural changes induced by the HPTE process, as supported by finite element method (FEM) simulations in Ref. [187]. Similar behavior has been reported for Cu, Ni, and Fe processed via HPT. [188][189]

Analysis of these profiles reveals that the V3W1 regime provides the most favorable results, with higher hardness values along the diameter compared to V10W1 and V1W1. Although V1W1 was expected to exhibit the highest hardness due to the largest strain, it is characterized by numerous cracks, indicating limited plasticity in the Al-Mg-Si alloy under these conditions. The hardness and EC of the V3W1 sample were compared with those of a commercially T81-treated Al alloy, as shown in Figure 4.1b. Although the hardness was improved from 90 to 100 Hv, the EC degraded from 54 to 47 IACS%.

While HPTE processing improved hardness, it also led to a notable reduction in EC, which poses limitations for industrial applications. This change in physical properties, especially the decrease in EC, suggests significant structural alterations in the material. A comprehensive analysis of these structural changes will be presented in the following sections.

(a)

(b)
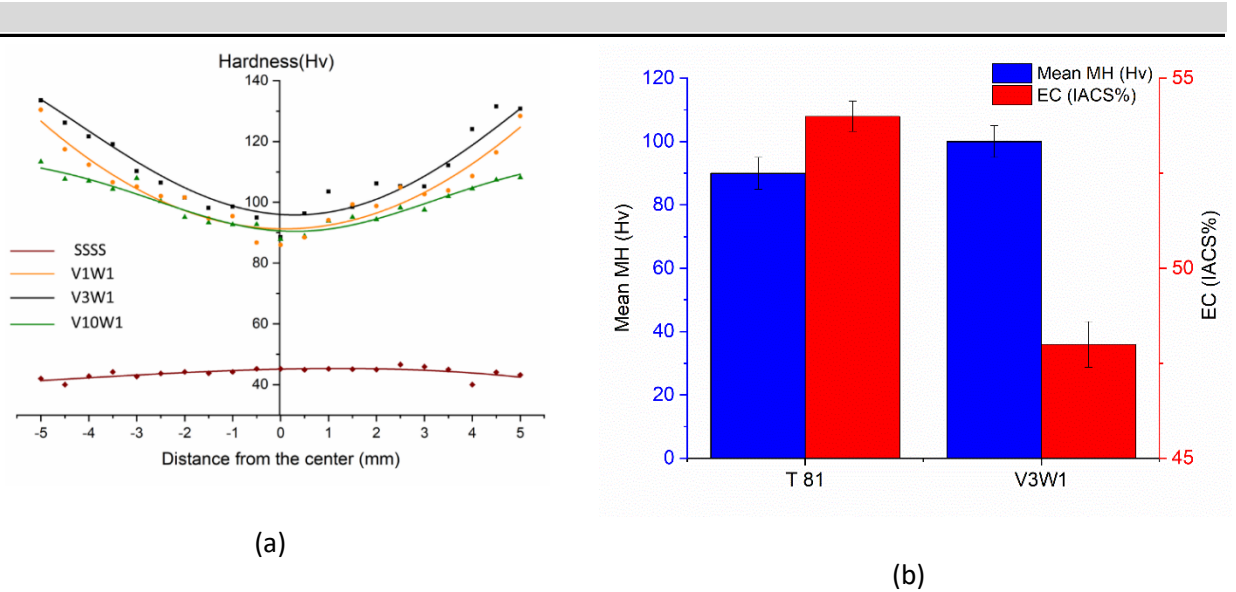
Figure 4.1. (a) Hv hardness profile along the diameter and (b) comparative plot of hardness and EC between the commercially T81-treated alloy and the HPTE-deformed alloy.

4.3. Microstructure characterization

4.3.1. Electron backscatter diffraction

Crystal orientation maps of the alloy in the initial non-deformed state and after the HPTE deformation acquired in the central part of the sample and at the mid- radius are shown in Figure 4.2 and Figure 4.3 along with a schematic representation of the area studied of the processed rod. High angle grain boundaries, HAGBs (≥ 15°) are traced in the maps in black. The microstructure of the alloy in the initial state mainly consists of the large equiaxed grains with an average grain size of ~ 100 µm (Figure 4.2). The deformation did not lead to a significant grain refinement in the central region of the sample. Figure 4.3 shows large grains at the center both in normal and longitudinal direction. It follows from the corresponding misorientation distribution plot, that the microstructure of the sample after HPTE contains a high fraction of LAGBs. In the central part, the fraction of HAGBs is lower in the transverse (0.03) than that in longitudinal section (0.13). The higher amount of HAGBs in the longitudinal section can be attributed to the grain morphology, i.e., the coarse grains, containing numerous LABs, are elongated in the normal direction. The same feature has been reported for HPTE processed copper and for aluminum AA3003 alloys after axisymmetric extrusion. [190][191] More significant grain refinement occurred at the middle of the sample radius, which can be seen in both sections (Figure 4.4 a, b). The mean grain size was reduced down to ~ 2.5 µm in transverse section. The corresponding grain size distribution plot were

provided in appendix in Figure A.1. The grain morphology exhibits a mix of elongated and equiaxed grains in transverse section, a characteristic commonly found in deformed aluminum alloys, and severely elongated grains in the longitudinal view with an aspect ratio of ~ 3. [192] This grain morphology is similar to that reported for ECAP-processed aluminum at 250 ˚C. [193] They suggested that solute atoms can retard grain boundary migration. The fraction of HAGBs increases from the center to the mid-radius, which is consistent with the higher strain during HPTE in this sample area. According to FEM, the accumulated strain in HPTE continuously increases from the center of the billet to its edge. [194] The fraction of HAGBs in both sections is the same ~0.26. This behavior of the HAGB fraction was also reported in a previous study for pure aluminum after HPTE processing. [131] It was reported that for pure aluminum the fraction of HAGBs is ~ 0.55 in the V1W1 regime with an average grain size of 1.2 µm. [131]
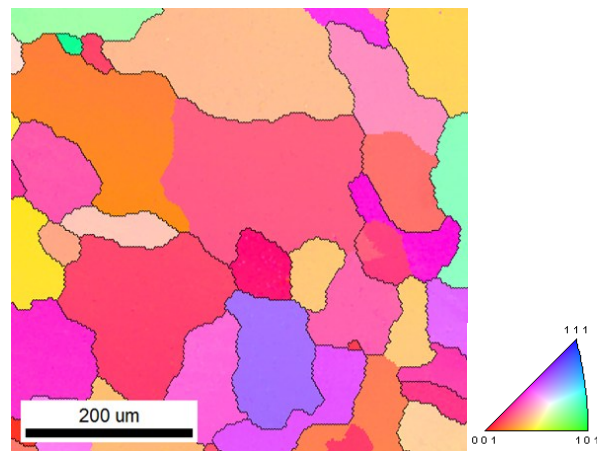
Figure 4.2. Orientation map of the sample after the treatment for solid solution and quenching. The inset shows the color code for the inverse pole figure map.
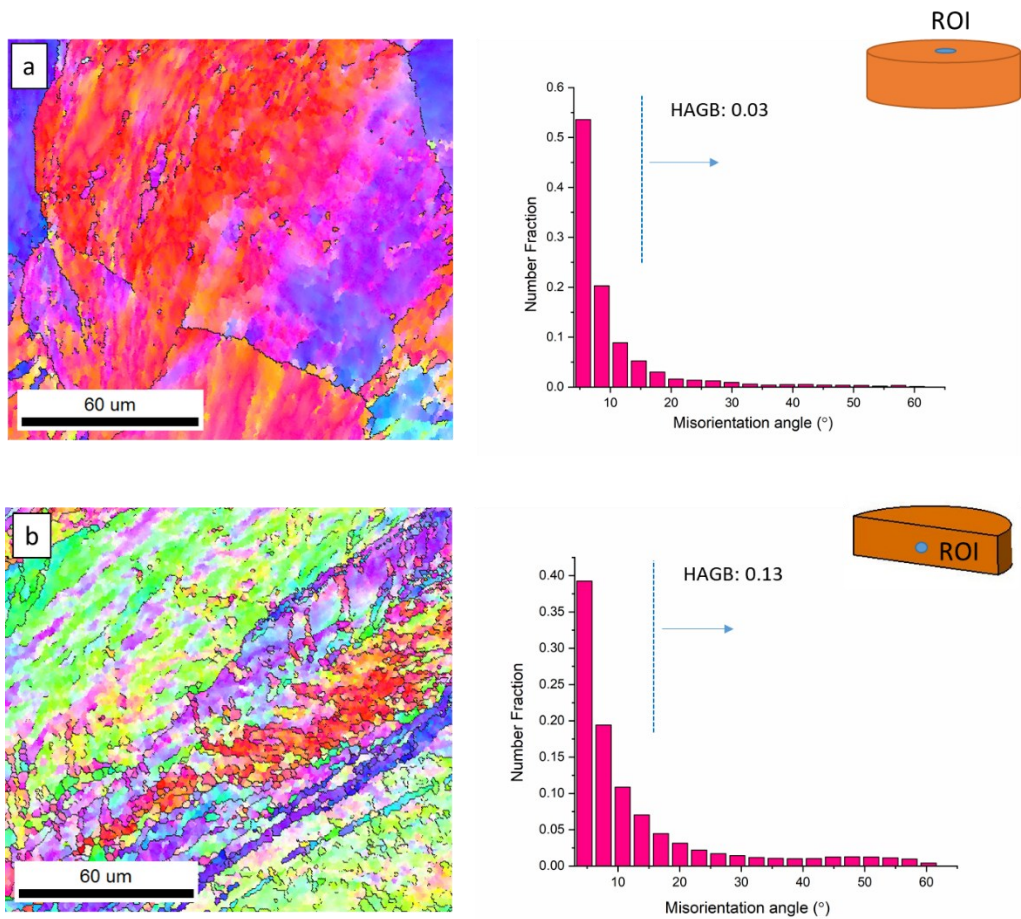
Figure 4.3. (left column) Orientation map for (a) transverse and (b) longitudinal section at the center of the deformed sample. (right column) Corresponding misorientation distribution plot; the number in the plot shows the HAGB fraction. Inset shows the position of the studied sample in relation to the whole rod
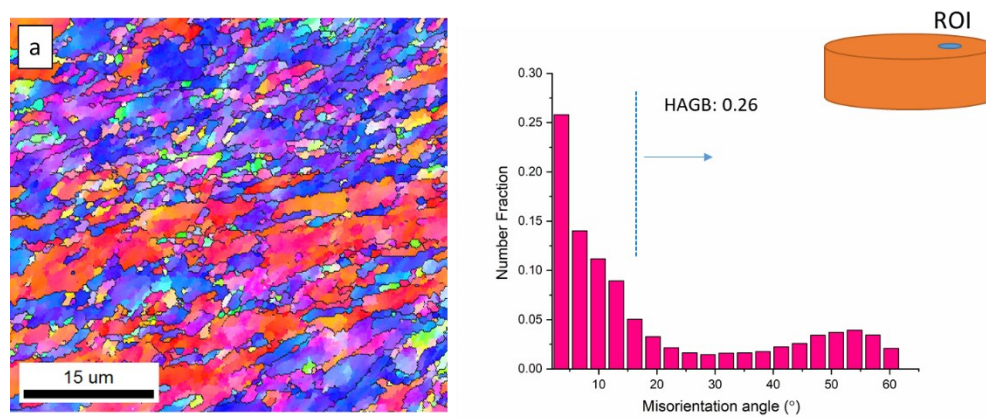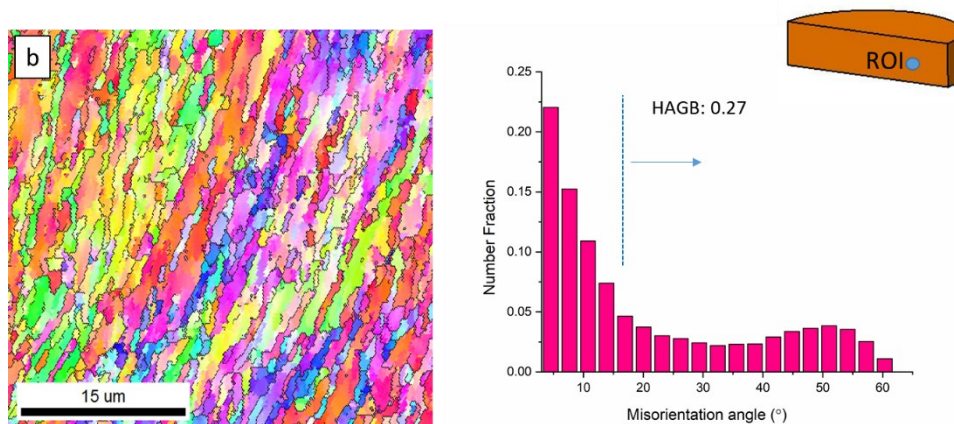
Figure 4.4. (left) Orientation map for (a) transverse and (b) longitudinal section at the mid-radius of the deformed sample. (right column) Corresponding misorientation distribution plot; the number in the plot shows the HAGB fraction. Inset shows the position of the studied sample in relation to the whole rod

4.3.2. TEM and APT

Deformation introduces defects such as grain boundaries, dislocations and excess vacancies can strongly influence diffusion rates in materials. The presence of these defects affects many processes occurring in the deforming material, such as precipitation of hardening phases, which can be accelerated by orders of magnitude due to the introduced defects. [195] Considering that the HPTE process was conducted at an elevated temperature of 100°C, the sample is especially susceptible to cluster formation during deformation. The HPTE process introduces high levels of strain and defects into the material, which serve as nucleation sites for clustering by trapping solute atoms. Furthermore, the elevated temperature enhances the diffusion of solute atoms, and the interaction between this increased atomic mobility and the deformation-induced defects significantly accelerates cluster formation. [196] These early stages of segregation, known as Guinier – Preston (GP) zones, are small-scale (a few nm in size) solute-rich regions of the material. GP zones are completely coherent with the matrix. They create physical obstacles to dislocation motion, which leads to an increase in hardness. However, at the same time, the electrical conductivity of the material decreases due to an increase in lattice distortion and the appearance of scattering points for conducting electrons. [197] In order to study this issue in more details, TEM and APT investigations were performed.

APT was employed to analyze the morphology and composition of the clusters. Figure 4.5 a illustrates the reconstructed volume of the as quenched and HPTE-deformed sample, indicating early-stage of

precipitates formation through iso-composition surfaces of 4.0 at. % Mg and 3.0 at. % Si. In the as-quenched state the cluster concentration detected by APT is low, but they obviously develop during deformation and aging. The emergence of small clusters of Mg and Si during deformation, can be attributed to dynamic aging, as has been reported previously. [198]–[200] In agreement, the fifth nearest neighbor distribution for Mg is shown in Figure 4.6 for the as-quenched and the as-deformed states. After quenching, the average d-pair distance is slightly reduced compared to a fully randomized distribution, indicating a slight tendency of Mg atoms to cluster. In contrast, the pronounced shoulder in the Mg distribution in the as-deformed sample clearly indicates clustering. The corresponding Pearson correlation coefficient increases from 0.18 to 0.30.

These clusters can be assigned to GP zones which are fully coherent with the matrix since the corresponding HRTEM in Figure 4.5 b shows low strain contrast. Elements such as Mg and Si substitute the Al atoms in the crystal lattice to form these clusters, resulting in small strain fields surrounding the clusters. [201] However, no obvious diffraction spots corresponding to these clusters can be seen in the conventional TEM imaging due to the coherency of the clusters. The clusters exhibit a diverse range of compositions, as indicated by the Mg/Si ratio distribution plot, with a slight dominance of Mg-rich clusters. However, some Si-rich clusters are also present. This variable composition of GP zones has also been reported in previous studies. [202] However, Fallah *et al.* claim that regardless of the alloy composition and aging history, the initial precipitates manifest as finely-dispersed Si-rich clusters, which subsequently undergo simultaneous coarsening and Mg-enrichment over time. [203] This study indicates that under highly strained conditions also Mg-rich precipitates form at an early stage of precipitation.

This image was acquired in <001> Al zone axis orientation, which is necessary for HRTEM imaging of typical precipitates in this alloy. [204][205] In this orientation, precipitates can be observed in cross section and perpendicular to their long axis in the images. The precipitates, which lie in the sample plane exhibit a needle-like shape and are visible due to the strain contrast around them. In the present investigation, the as-deformed sample did not reveal any indication for secondary phase particles. Instead, we only noted the presence of GP zones, which are distinctly visible in the image as denoted by red circle; a zoomed view of one GP is shown in the inset. The corresponding FFT does not show any extra reflections due to the coherency of GP zones with the matrix.

(a)

(b)

(c)
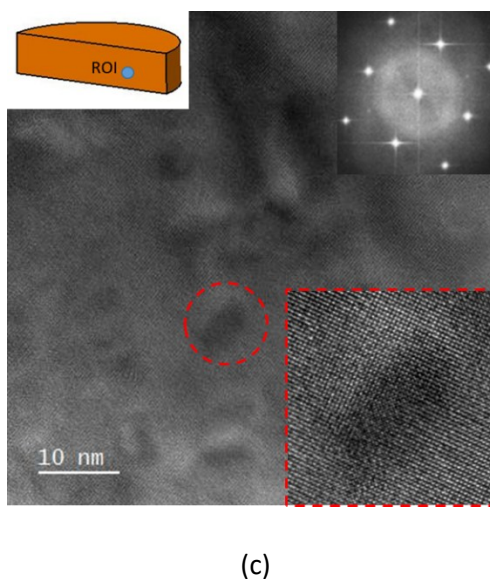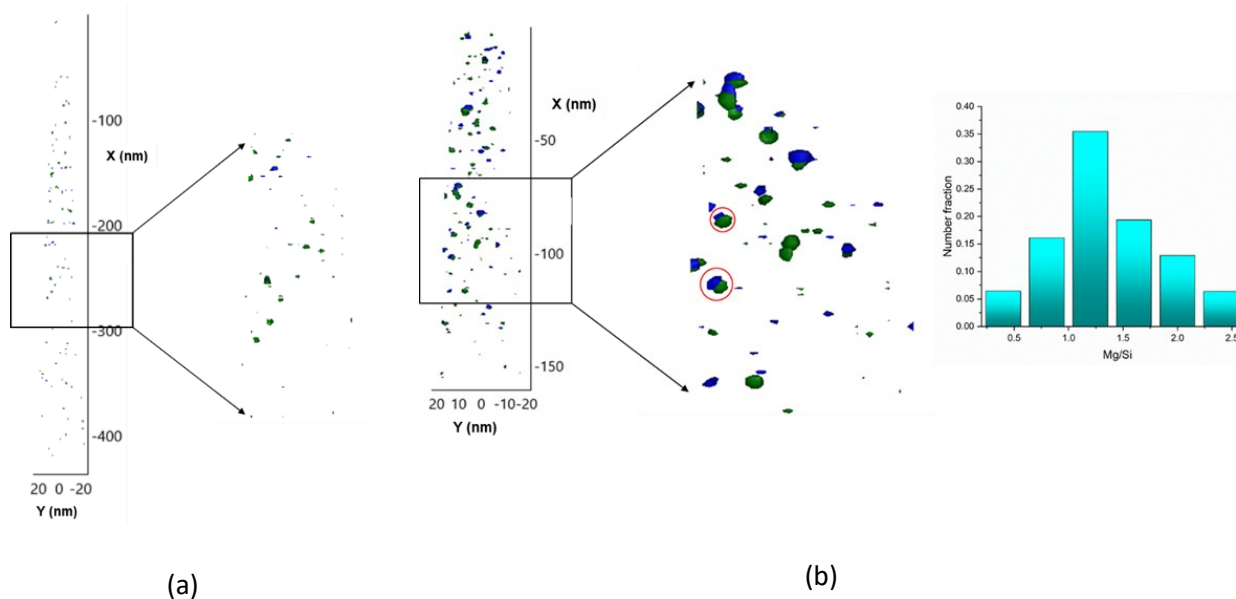
Figure 4.5. APT reconstructed volume of clusters visualized using iso-compositional surfaces of 4.0 at. % Mg (blue) and 3.0 at.% Si (green) indicating precipitates (a) in the as-quenched sample and (b) after HPTE deformation, and (c) the corresponding HRTEM. Low contrast in HRTEM is due to coherency of GP zones with matrix. The location and orientation of the TEM sample in relation to the entire sample rod is depicted schematically as inset.

(a)   (b)
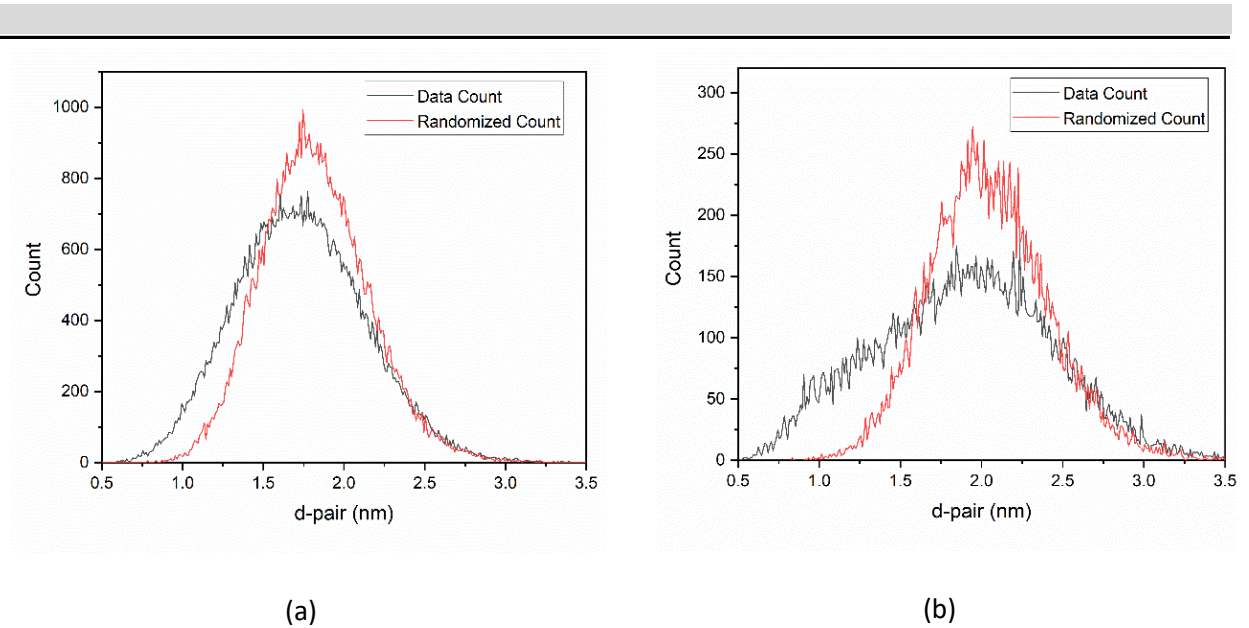
Figure 4.6. Nearest neighbor distribution of Mg for (a) as quenched and (b) as-deformed samples

4.3.3. XRD analysis

As discussed above, the EBSD analysis revealed a gradient in grain size along the sample radius, which can be attributed to the inhomogeneous strain distribution during HPTE. [130] This observation implies that other structural characteristics of the material like texture, dislocation density, lattice parameter also vary for different locations in the sample. XRD analysis was used to analyze the change in dislocation density and lattice parameter of the Al-based solid solution. The study was carried out for the center and mid-radius of the sample.

The acquired XRD spectra are shown in Figure 4.7. As expected, the spectra show only peaks of aluminum. The lattice parameter values are presented in

Table 4.1. It can be observed that the lattice parameter at the center of the sample after HPTE is slightly smaller than that at the mid-radius. Based on the TEM and APT data, such a change in the lattice parameter (

Table 4.1) can be attributed to the partial decomposition of supersaturated solid solution with clusters formation during dynamic ageing. However, the obtained values are still higher than the lattice parameter of pure aluminum (a=4.0494 Å). [206] This variation can be attributed to the incorporation of residual Mg and Si atoms, which modify the lattice parameter because their atomic radii are different from that of aluminum. Specifically, the larger atomic radius of Mg leads to an expansion of the aluminum lattice parameter, whereas the smaller atomic radius of Si results in its contraction. [207]

The observed peak broadening in the XRD patterns is associated with two structural parameters: first, the size of the coherently scattering domains, and second, the dislocations present in the structure of the material, which create long-range stress fields. The full-profile analysis developed by Ungar *et al*. attempt to separate these two contributions in a numerical estimate of the corresponding structural parameters. [46], [208]

The line profile analysis of the diffraction patterns was performed using the CMWP method [46], and the results are summarized in

Table 4.1. These results show that the calculated dislocation density in the central and mid-radius regions has a similar value. This result is somewhat unexpected. Usually, a higher dislocation density is expected in the mid-radius region due to the higher applied strain. This observation may be attributed to systematic errors in the CMWP method. As discussed in Chapter 3, the method assumes a log-normal grain size distribution, idealized spherical grain shapes, and dislocations as the primary source of internal stress. In this study, the shape and size distribution of coherent scattering domains could not be determined independently, and the strain introduced by precipitates may also contribute to the peak broadening along with dislocations. Additionally, as reported by Gubicza *et al.*, that the presence of obstacles to dislocation motion (in their case, Mg atoms) can strongly affect the dislocation density, since the limited mobility of dislocations in the Al matrix can prevent their annihilation during deformation. [209] Therefore, it can be assumed that inhomogeneous distribution of solid solutions (Mg and Si) can influence the dislocation density.
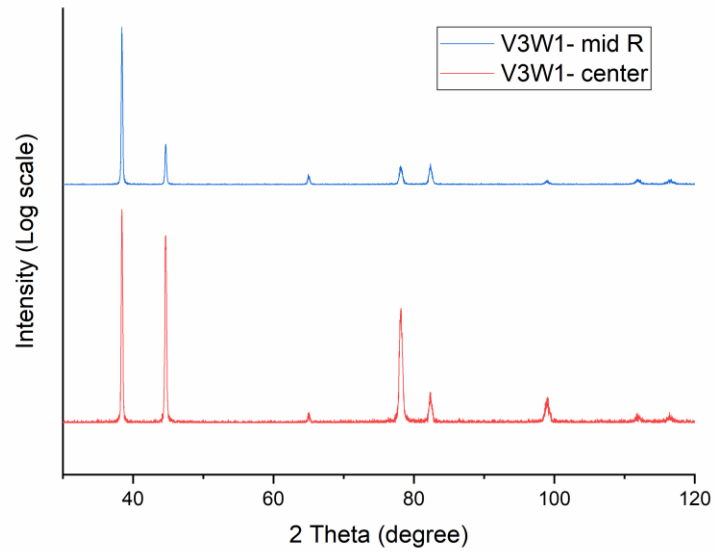
Figure 4.7. XRD diffraction patterns of the HPTE-processed sample collected at center and mid radius part

Table 4.1. Dislocation density and lattice parameters evaluated from the XRD profiles using the CMWP method.

Sample	Dislocation density (m^{-2})		Lattice parameter (Å)	
	Center	Mid-radius	Center	Mid-radius
Quenched	$\sim 10^{10} - 10^{11}$ [73]		4.0574	
V3W1	8×10^{14}	6×10^{14}	4.0571	4.0569
	Accuracy: ± 30%		Accuracy: ± 0.0001 Å	

4.4. Summary

This chapter has illustrated that the HPTE process is effective in producing highly defective-UFG microstructures in an aluminum alloy, significantly enhancing its hardness. Three HPTE regimes V1W1, V3W1 and V10W1 have been tested initially and the hardness was analyzed. Among these, the V3W1 samples exhibited the highest hardness profile, therefore the microstructure of these samples was comprehensively analyzed. The remarkable improvement in hardness highlights the potential of HPTE as

a robust method for material strengthening. However, it was also observed that this process leads to a considerable reduction in EC, which presents a challenge for industrial applications where both high strength and high EC are required. EBSD results indicate significant grain refinement at the mid-radius, where grain size is reduced from an initial ~100 μm to approximately 4 μm in the normal view. The HAGB fraction also increases from the center to the mid-radius, likely due to higher applied strain in this region. In the longitudinal section, the grain morphology looks different, displaying larger, elongated grains. Deformation processing has notably increased dislocation density, while the lattice parameter remains nearly constant. However, there is a slight decrease in lattice parameter from the center to the mid-radius, attributed to partial decomposition of the supersaturated solid solution and cluster formation during dynamic aging.

Chapter 5

5. Structural evolution during artificial aging

5.1. Introduction

The previous section highlighted the potential of HPTE as an advanced processing method for enhancing the mechanical performance of materials. Despite these improvements, a trade-off arises with a reduction in electrical conductivity, which complicates its applicability in electrical contexts. To mitigate this limitation and balance mechanical and electrical properties, an additional processing step, artificial aging, has been introduced. [210]–[212]

AA serves a dual purpose: it can further strengthen the material by promoting the formation of nano-scale precipitates and help to improve the reduced EC caused by the HPTE process by purifying the matrix from solute atoms. Numerous defects introduced during HPTE may alter the microstructural evolution during aging and influence the composition and crystal structure of the precipitates. Studying the structural evolution of a material during aging is necessary to understand the factors that influence the resulting material properties and find optimal treatment conditions.

The deformed samples were subjected to AA at two distinct temperature regimes: 130°C for 48 hours and 160°C for 10 hours. The structural evolution during the aging process was examined by means of advanced characterization techniques, including EBSD for grain structure analysis, HR(S)TEM for detailed imaging of precipitates with consequent analysis of their crystal structure, APT for compositional analysis and 3D reconstructions of the nano-scale precipitates, XRD for the measurements of the lattice

parameter of the Al-based solid solution and dislocation density. Additionally, the effect of the HPTE process on the thermal behavior of the alloy was studied using DSC.

5.2. Optimizing temperature and duration of post deformation annealing

The impact of aging duration and temperature on the microhardness and EC of HPTE processed samples (V3W1) is depicted in Figure 5.1. The reported hardness and EC values represent averages measured across the sample from center to edge. Following HPTE deformation and subsequent AA at 130 °C (Figure 5.1a), a marginal enhancement in both hardness and EC is observed after 48 hours compared to 10 hours of aging. For AA at 160 °C the maximum hardness is achieved after 10 hours (Figure 5.1b) with a peak value of approximately 120 HV and EC around 52.4 ± 1.27 IACS%. At higher aging temperature (190 °C), the hardness is decreasing significantly. Thus, peak hardness is reached by aging at 160 °C, while EC only gradually improves with higher aging temperature The sample aged at 130 °C for 48 hours was also chosen for comparison with the study conducted using HPT with an alloy of the same composition (see Ref. [129]).
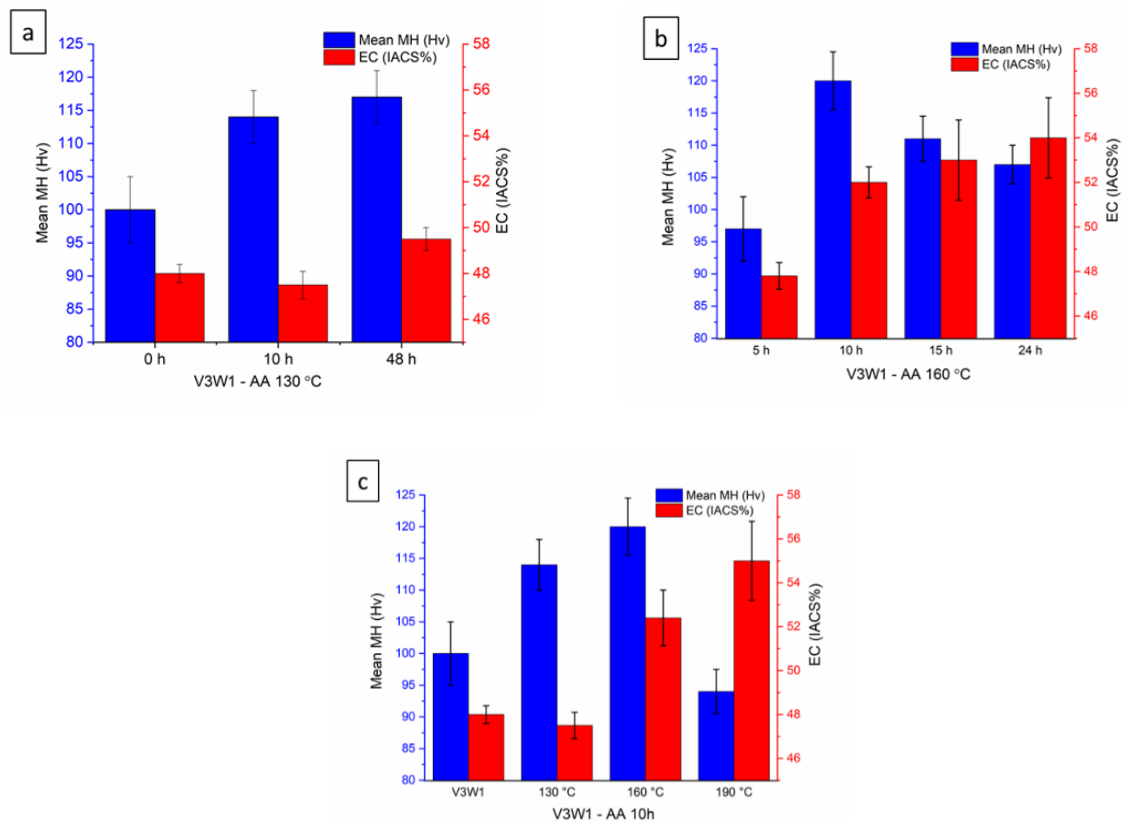
Figure 5.1. Averaged HV hardness and EC depending on aging time at (a) 130 °C and (b) 160 °C and depending on (c) aging temperature with 10 h holding time

5.3. HPTE-processed + AA at 130 °C for 48 h

5.3.1. Grain structure

The EBSD orientation map illustrating the microstructure of the deformed alloy after AA at 130 °C for 48 hours is presented in Figure 5.2. The microstructure exhibits a mix of elongated and equiaxed grains with well-developed subgrain boundaries (LAGBs) with an average size of ~ 2.5 µm which is similar to the deformed state. Horita *et al.* [213] investigated the grain refinement process by ECAP of commercial aluminum alloys at room temperature and subsequently evaluated the thermal stability. Their findings indicated that static annealing led to grain growth at temperatures above ~ 200 °C in the 6061 alloys. These results are in good agreement with the findings of this investigation.
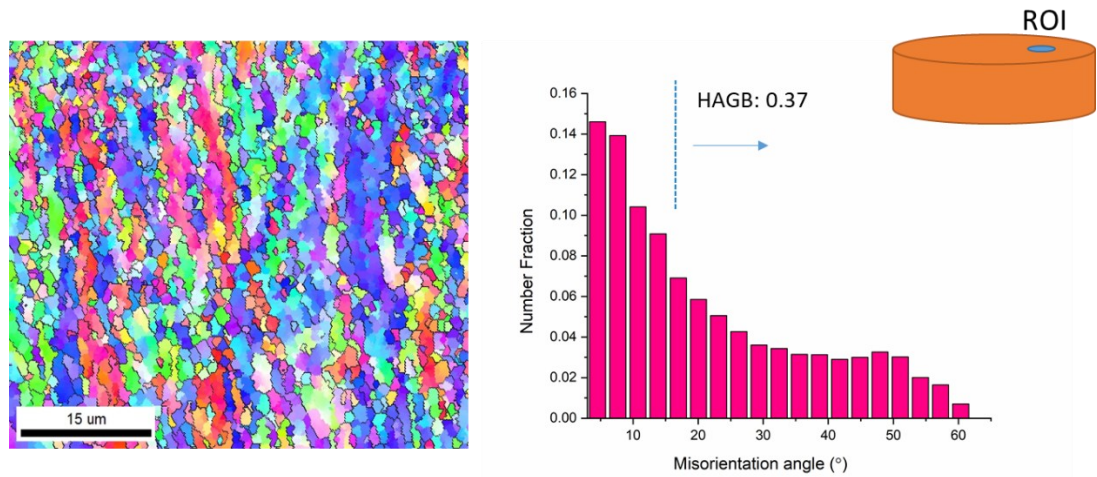
Figure 5.2. IPF map of deformed sample + AA 130 °C, and corresponding misorientation distribution plot. Inset shows the schematic illustration of the sample location

5.3.2. Precipitates spatial distribution

Conventional TEM techniques (BF and DF imaging) and STEM-EDX elemental mapping were employed on <001> oriented Al grains to analyze the composition, size, shape, and spatial distribution of the precipitates. The corresponding TEM images in Figure 5.3 reveal the presence of two dominant types of precipitates – rod and irregular shaped – distributed uniformly throughout the aluminum grain. Additionally, strain contrast is observed in Figure 5.3a, which suggests the presence of GP zones. In the elemental map (Figure 5.4), numerous nano-scale precipitates within the aluminum matrix are evident, observable from both side-on and edge-on projection. However, identifying the crystalline phases based

on measured composition and corresponding Mg/Si ratio is challenging. Since most of the precipitates are very small, this can lead to a large error in the compositional determination.

Similar study was carried out by Sauvage *et al.* [129] for the alloy with the same composition processed by HPT for 20 anvils turns followed by AA at 130°C for 48 hours. They reported an average precipitate size of approximately 40 nm, with a mixture of β″ and β′ phases. Additionally, they observed the formation of 5 nm β″ precipitates after HPT, which may be the reason for the larger precipitate sizes after AA observed in their study compared to those in this research.
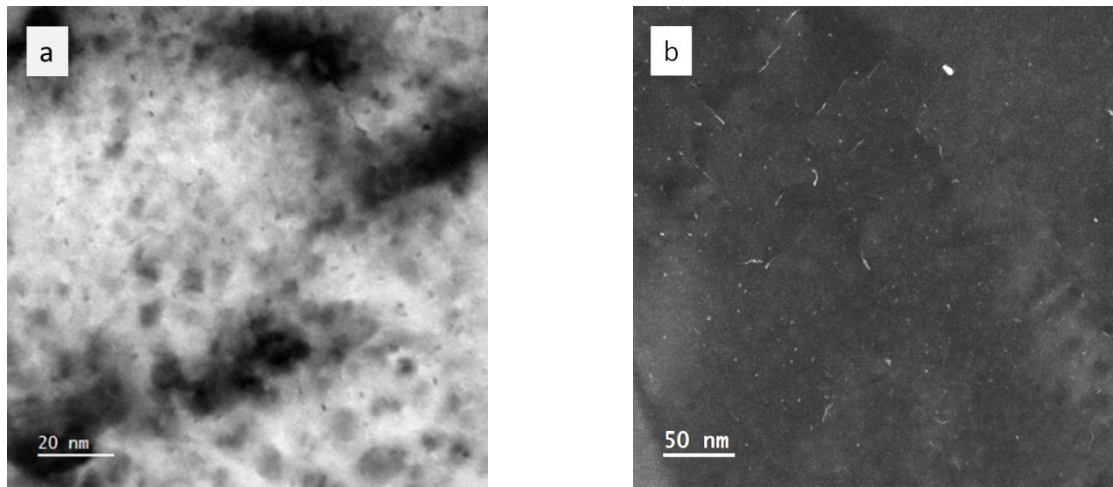
Figure 5.3. (a) BF and (b) DF-TEM images of precipitates in the deformed sample after aging at 130 °C
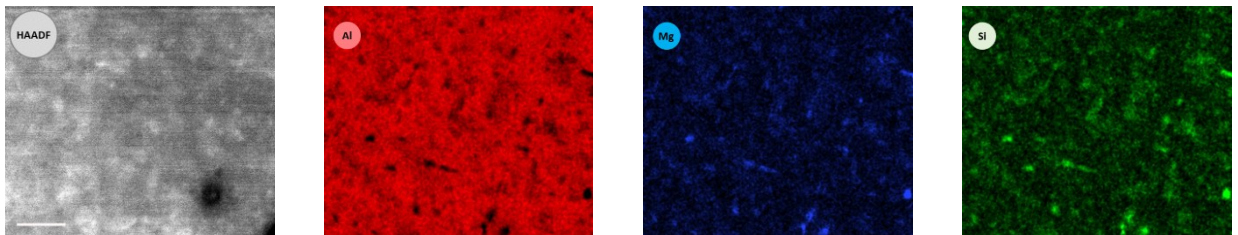
Figure 5.4. HAADF-STEM image and EDX elemental maps of Al, Mg, and Si in the deformed sample after aging at 130 °C. The maps were collected for an Al grain in [001] zone axis. The scale bar is 20 nm

5.3.3. HR(S)TEM study of precipitates after HPTE process followed by aging at 130 ˚C

Figure 5.5 shows high-resolution micrograph of various kinds of precipitates formed in the deformed sample followed by AA 130 ˚C. The majority of the precipitates are arbitrarily oriented in the matrix and their structure cannot be resolved in HRTEM. However, a few of the precipitates reveal several additional reflections in the FFT apart from those of the Al matrix. One of the examples is shown in Figure 5.5a. However, the corresponding interplanar distances (d-values) do not allow for a unique assignment to one of the phases known for this alloy, like β´´, β´, U1, U2 or β. Moreover, the FFT in Figure 5.5a contains multiple sets of reflections, which shows that the particle consists of more than one grain/phase with different orientations. No coherency between precipitates and Al matrix is noticeable in the FFT.

Nonetheless, another type of well-defined precipitate is also observed (see Figure 5.5b). These are fully coherent rod-shaped precipitates oriented parallel to the <100> crystallographic directions of the Al matrix.

Dislocation-induced precipitates are another type of particles, which are commonly found in deformed sample after ageing. [214][90] The dislocations present in the structure provide energetically favorable sites for the nucleation and growth of the precipitates. [215] Figure 5.5c shows two sets of dislocations oriented along two directions in the Al, [110] and [010], which serve as sites for precipitation of secondary phase particles. This type of precipitates has also been reported previously. [216]
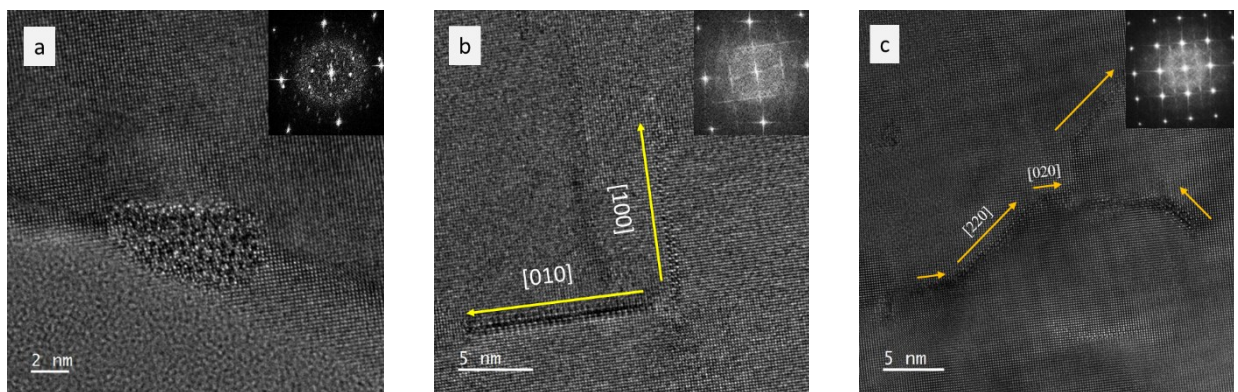
Figure 5.5. HRTEM micrograph of (a) partial disordered, (b) needle-shaped and (c) dislocation-induced precipitates. The inset is the corresponding FFT

A HRSTEM image of the U2 phase in [010] orientation is shown in Figure 5.6a; Figure 5.6b, c are enlarged views of the white dashed area and the corresponding simulated HAADF-STEM image. It can be seen from the image that the precipitate contains several unit cells fitting well to the U2 structure, but exhibits disorder at the bottom interface with the Al matrix. The particle reveals a semi-coherent interface with the Al matrix with the $(30\overline{1})_{U2}$ reflection almost coinciding with $(200)_{Al}$. This phase exhibits a $[001]_{Al} \| [010]_{U2}$ and $[1\overline{3}0]_{Al} \| [001]_{U2}$ OR, which has been reported previously. [99] It should be also mentioned that the reflections in the FFT are slightly shifted from their ideal positions (Figure 5.5e), which can presumably be attributed to the internal stress retained in the particle. The EDX spectrum collected for the precipitate (Figure 5.5d) shows Mg/Si ~ 1 in agreement with the proposed composition of the U2 phase. [99]
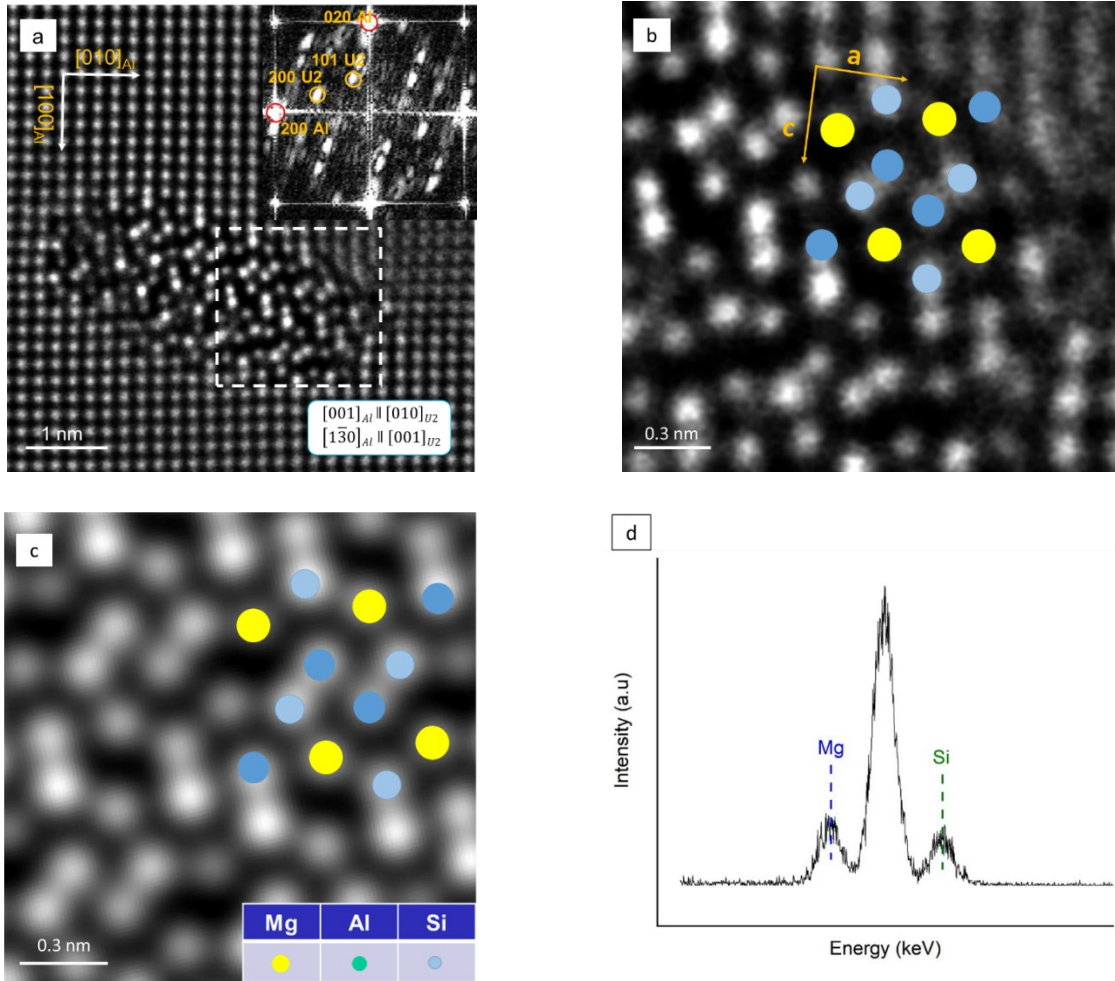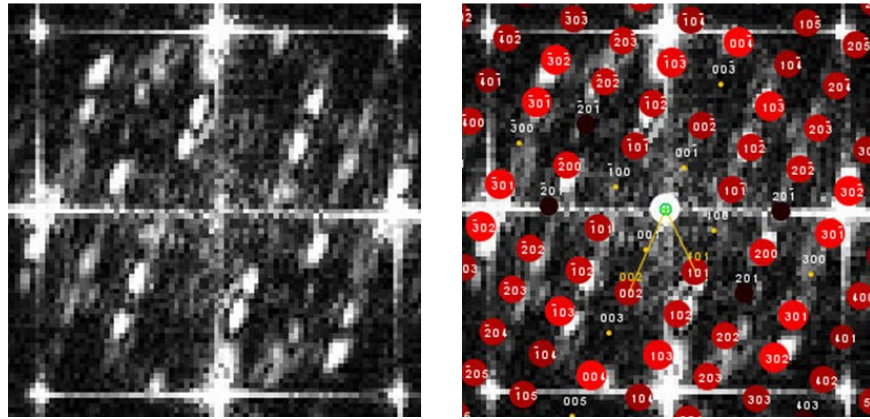
Figure 5.6. (a) HR-STEM image of a U2 phase precipitated with the corresponding FFT (inset); (b) enlarged view of the white dashed square area in (a); (c) HAADF-STEM image simulation of the U2 phase. Legend for the atomic positions of Al, Si and Mg is shown as inset in (c). (d) Corresponding integrated EDX spectrum. (e) Enlarged FFT with the overlay of $[010]_{U2}$ simulated diffraction pattern

5.4. HPTE deformed + AA at 160 °C

5.4.1. Grain structure

An IPF orientation map is presented in Figure 5.7 to show the structural changes that occurred during the aging at 160 °C. As mentioned above, the basic microstructure of the alloy remains stable up to 200 °C [213], therefore no notable alterations in grain size and shape have been observed for this sample and the shape and morphology looks similar to the deformed sample aged at 130 °C.
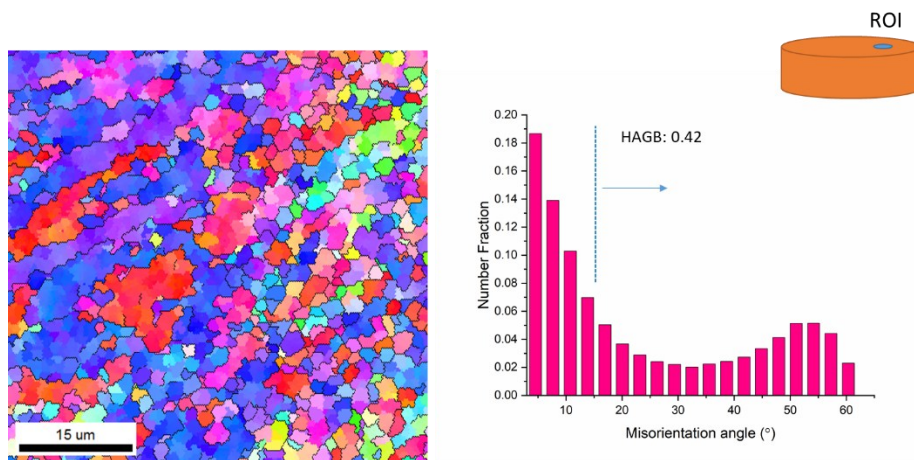
Figure 5.7. IPF map of the deformed sample + AA 160 °C, and corresponding grain boundaries misorientation distribution plot

5.4.2. Precipitates distribution

Figure 5.8 shows DF and BF images of the precipitates distribution, size and shape in this state. One can see clearly the precipitates become larger after aging at 160 ˚C. An EDX elemental map of precipitates inside the [001] Al grain is presented in Figure 5.9. For the phase composition of the alloy, the Mg/Si atomic ratio, was determined for comparison with known phases in the Al-Mg-Si system. Although several intermetallic compounds containing Al exist in this system, Al was not accounted for in the analysis as the particle size is much smaller than the TEM sample thickness and therefore, the Al matrix signal cannot be separated during analysis. In order to draw statistically valid conclusions about the composition of the particles, a histogram of the Mg/Si ratio was plotted for about 60 particles in our statistics. The result is shown in Figure 5.9. The graph shows a distribution with a significant width, which suggests the coexistence of particles with a Mg/Si ratio of ~ 1.2 at its maximum, along with particles demonstrating considerable deviations from this value.
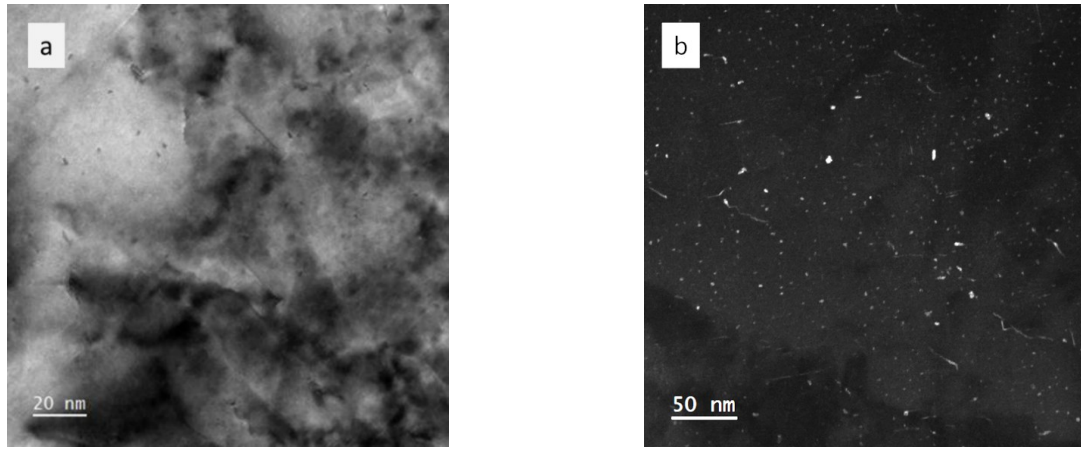
Figure 5.8. (a) BF and (b) DF-TEM images of precipitates in the deformed sample after aging at 160 °C
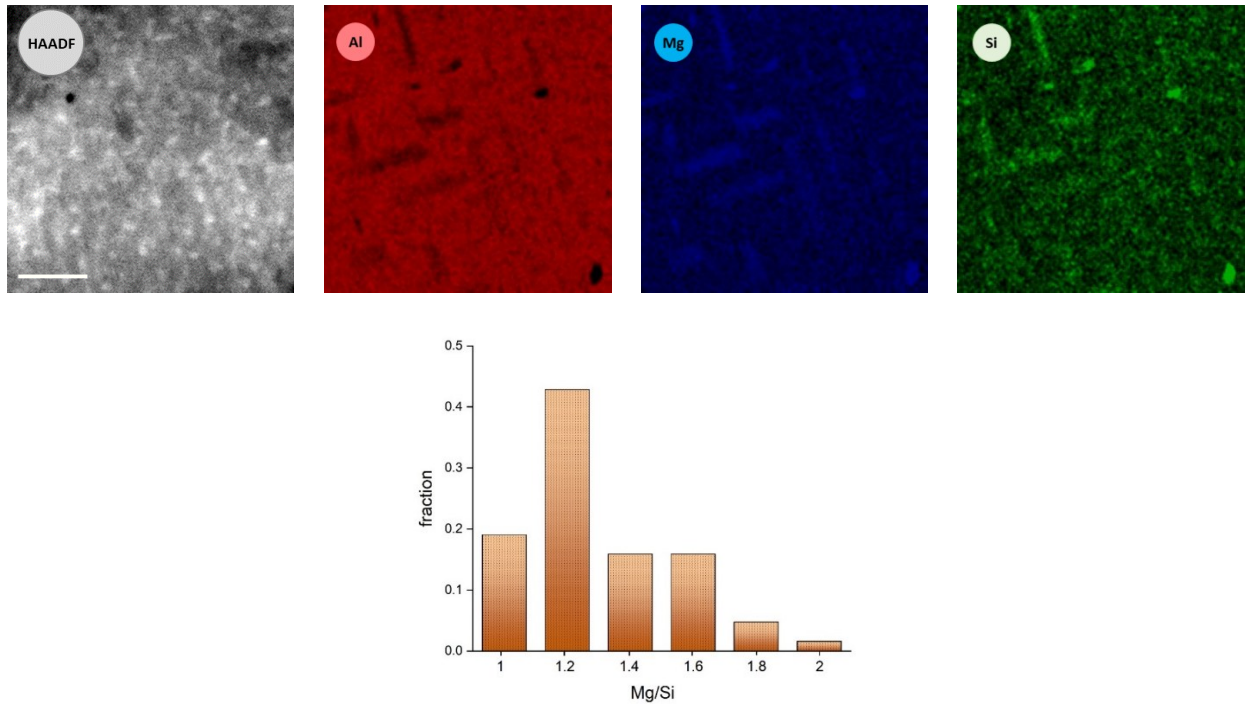
Figure 5.9. HAADF-STEM image and EDX elemental maps for Al, Mg, and Si of the deformed sample after aging at 160 °C. The maps were collected for Al grains in [001] zone axis orientation. The scale bar is 50 nm. Distribution of the Mg/Si ratio of the intra-granular precipitates.

To further characterize the evolution of precipitates, an APT reconstruction of the aged sample was performed and is presented in Figure 5.10. The reconstructed volume reveals two distinct types of precipitates. The first type is rod-shaped, with average length of ~15.2 ± 1 nm and diameter of ~3.1 ± 0.3 nm grown in <001>$_{Al}$ directions in agreement with reference [217], while the other type exhibits an irregular shape. These findings are consistent with the DF images depicted in Figure 5.8b.

The Mg/Si composition distribution plot displays a broad peak, indicating the presence of various phases in agreement with the EDX results shown in Figure 5.9. Compared to the deformed sample, the Mg/Si composition range is narrower, suggesting a reduced variety of compositions. Zandbergen *et al.* also reported that a wide range of particle sizes and compositions was typically present after a given AA. They mentioned that changes in particle sizes and compositions were found to be continuous, without abrupt changes of chemistry or morphology during the evolution of the initial clusters into GP zones and fine-scale precipitates. [218] The magnified views reveal co-segregation and co-precipitation in two adjacent particles (highlighted with a red circle), indicating their nucleation in close proximity and subsequent growth until mutual contact.

It is noteworthy that in both states, Mg and Si clusters are present, although their volume fraction is small. The presence of Mg clusters was previously suggested by Murayama *et al.* [219], and the formation of Si clusters during quenching was proposed for the Al-Si system by Edwards *et al.* [24].
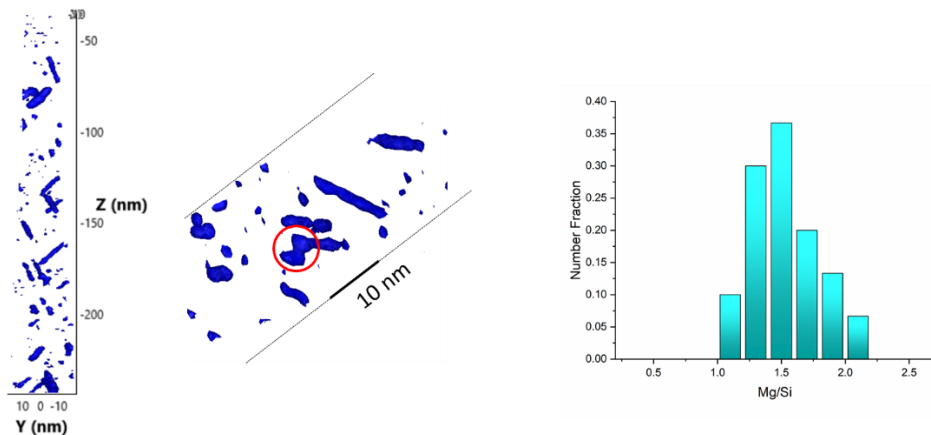
Figure 5.10. 3D reconstructed volume of precipitates visualized using iso-compositional surfaces of 4.0 at.% Mg in deformed + AA 160 °C with magnified view of coprecipitation of two neighboring precipitates marked by red circle. Corresponding histograms show the distribution of the Mg/Si ratio of the precipitates

5.4.3. Electron diffraction analysis

SAED is the most conventional method for phase identification. Figure 5.11b shows the DP corresponding to DF image in Figure 5.11a. In addition to intense Al reflections of the [001] zone, reflections associated

with the secondary phases are observed. Table 5.1 summarizes the interplanar distances measured in the DP to identify the phases present in a sample. For comparison, the d-values of the expected phases are given. It can be seen that for each d-value there is more than one candidate phase matching, which makes it impossible to reliably determine the phase composition of the sample. Therefore, HR(S)TEM imaging was used to identify the structure of the individual precipitates. A detailed analysis of several precipitates will be discussed in next section.
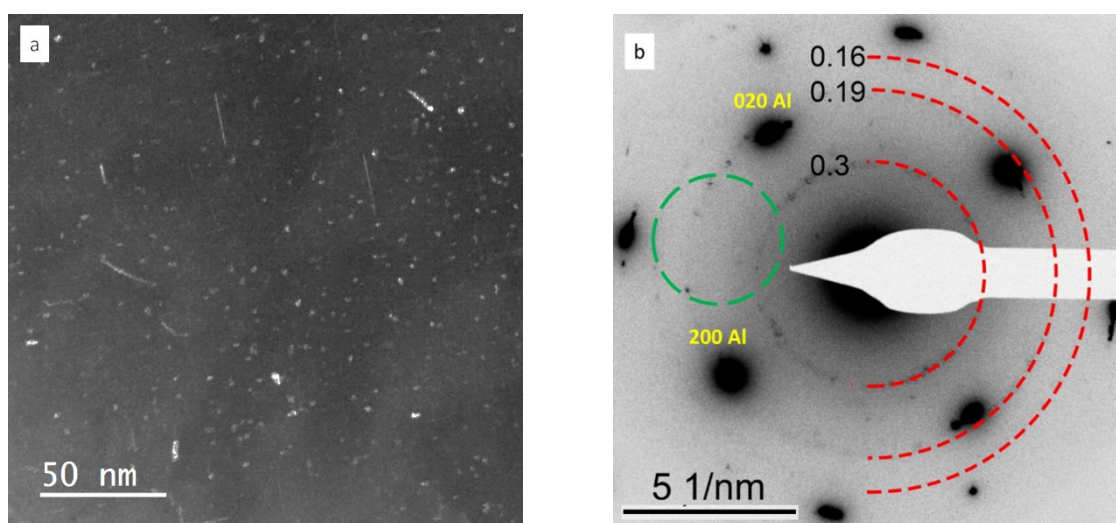
Figure 5.11. (a) DF image of the deformed sample after AA at 160 ˚C; (b) DP with the overlaid semi-circles with the measured d-values for the secondary phases. Objective aperture location for the acquisition of a DF image is indicated by the dashed green circle

Table 5.1. d-values (in nanometers) measured from the DP compared with possible candidate phases

$d_{measured}$	β″ [220]		β′[102]		U1[221]		U2[99]	
	hkl	d	hkl	d	hkl	d	hkl	d
0.30	$31\bar{1}$	0.30	201	0.30	011	0.31	201	0.31
0.19	$22\bar{1}$	0.19	201	0.19	103	0.19	311	0.19
0.16	$71\bar{3}$	0.16	223	0.16			222	0.16

5.4.4. HR(S)TEM investigation of precipitates after HPTE deformation followed by ageing at 160 ˚C

Figure 5.12 shows several HRTEM images of precipitates. It was found that most of the precipitates (~ 90% of them) have a defective, polycrystalline structure, such as the particle in Figure 5.12a, due to stored strain induced by heavy deformation. The corresponding FFT contains many reflections due to various structural motifs and defects present in a single precipitate particle. Therefore, efforts have been focused on identifying the crystallography of individual particles with more clearly identifiable structures. [94] The precipitate in Figure 5.12b shows long-range order in the HRTEM image. Analysis of the FFT suggests a structure closely related to the β′, which crystallizes in space group P6$_3$/m, a = 0.715, c = 0.405 nm, with a small deviation in lattice parameter. [103] This particle demonstrates a $[001]_{Al} \parallel [001]_{\beta'}$ and $[210]_{Al} \parallel [1\overline{1}0]_{\beta'}$ OR. In addition, a number of reflections that do not belong to the Al or β′ phase are also observed in the FFT in Figure 5.12b indicating that the precipitate is no single-crystalline. A HRTEM image of a precipitate containing two grains with different structures is shown in Figure 5.12c. The FFT of the upper region of the precipitate aligns with the U1 phase, while multiple phases or orientations are observed in the lower region of the precipitate. Coherent rod-shaped precipitates oriented along the <001> Al directions are also evident in this state, as shown in Figure 5.12d. This particle can be identified as β′, which is fully coherent with the Al matrix along the c-axis. [222], [223]
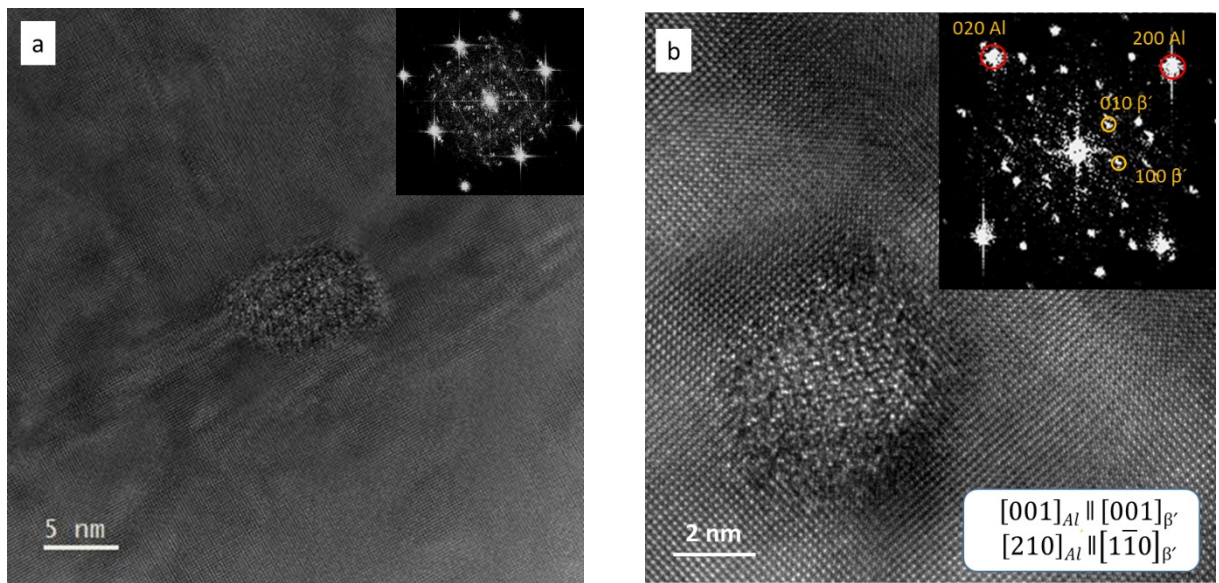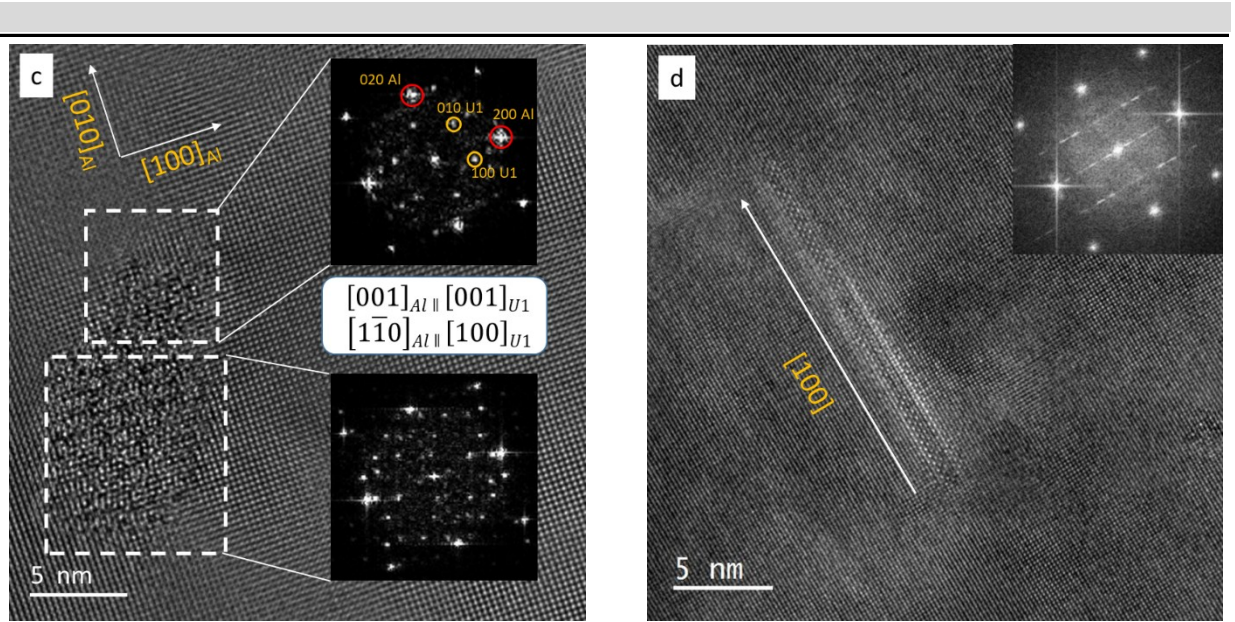
Figure 5.12. HRTEM micrograph and corresponding FFT of (a) defective/highly polycrystalline phase. (b) β´phase particles, (c) a precipitate of partially U1 and of non-indexed structure and (d) coherent rod-shaped particle. The insets show the ORs between particle and matrix

Figure 5.13 shows a HRSTEM image of a β´ precipitates fitting the structure in Ref. [102]. Figure 5.13a shows a six-fold symmetry of the atomic arrangement of Si in both of the two sub-lattice sites as shown in the magnified view in Figure 5.13b. In this variant of the β´ phase [102], there are two Si positions. The projected atomic structure is in agreement with the higher intensity for the Si atoms in the 4e Wyckoff position compared to the Si in the 2d Wyckoff position. The position of the Mg atomic columns is almost invisible in the HAADF-STEM image in agreement with the image simulation (Figure 5.13c).

Another HRSTEM image of a β´ particle acquired by STEM-iDPC is shown in Figure 5.14 with the Al lattice superimposed on the precipitate structure. To separate the matrix and the particle, Fourier filtering using the reflections from Al (Figure 5.15a) and from the β´phase (Figure 5.15b) was performed. The combination of these two filtered images is shown in Figure 5.14c, where columns of Si atoms in two different positions in the β´ lattice are clearly visible. The integrated EDX spectrum of this phase shows a Mg/Si ratio of 1.8, which is characteristic for the β´ phase (Figure 5.14d).

The precipitate in Figure 5.13a shows a $[001]_{Al}\|[001]_{\beta'}$ and $[3\bar{4}0]_{Al}\| [100]_{\beta'}$ OR, whereas the precipitate in Figure 5.14a reveals a $[001]_{Al}\|[001]_{\beta'}$ and $[100]_{Al}\| [100]_{\beta'}$ OR with a semi-coherent phase boundary with the matrix with the $(003)_{\beta'}$ reflection coinciding with the $(200)_{Al}$ reflection (see inset in Figure 5.14a).
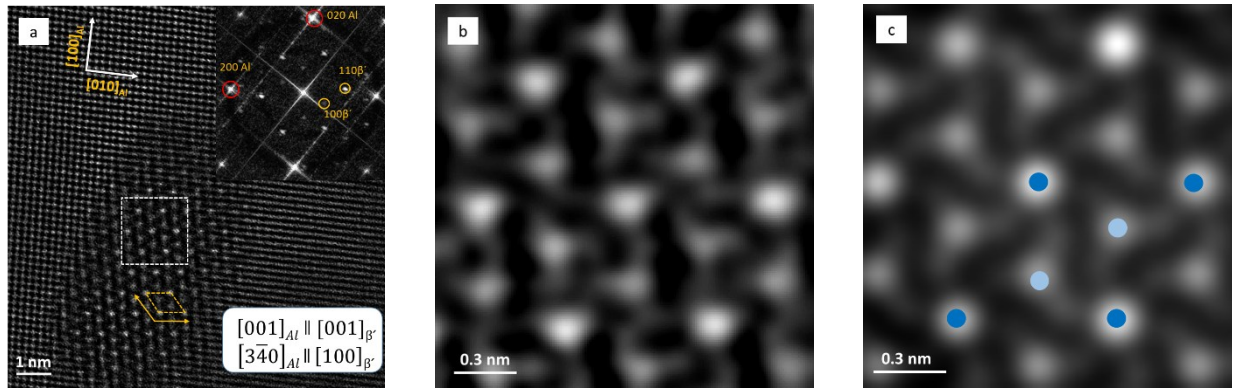
Figure 5.13. (a) HRSTEM images of β´ phase with corresponding FFT (inset); yellow diamond shape in (a) shows the β´ unit cell along the *c*-axis. (b) zoomed view of white dashed square area in (a). (c) Simulated HAAFD-STEM image of β´ phase. Dark and light blue circles show the position of Si1 and Si2
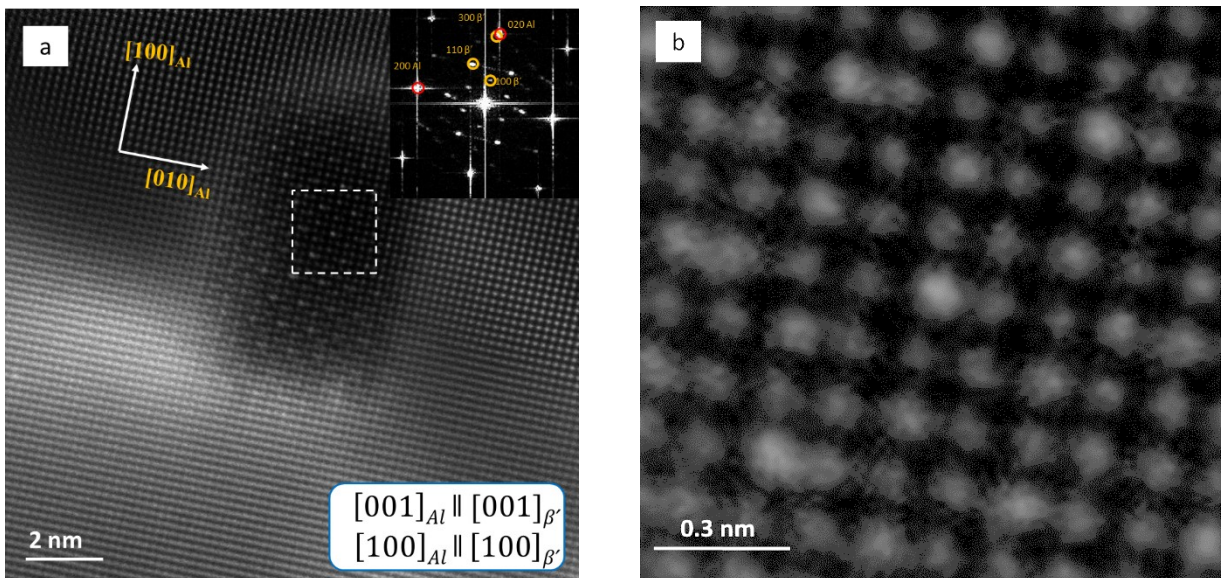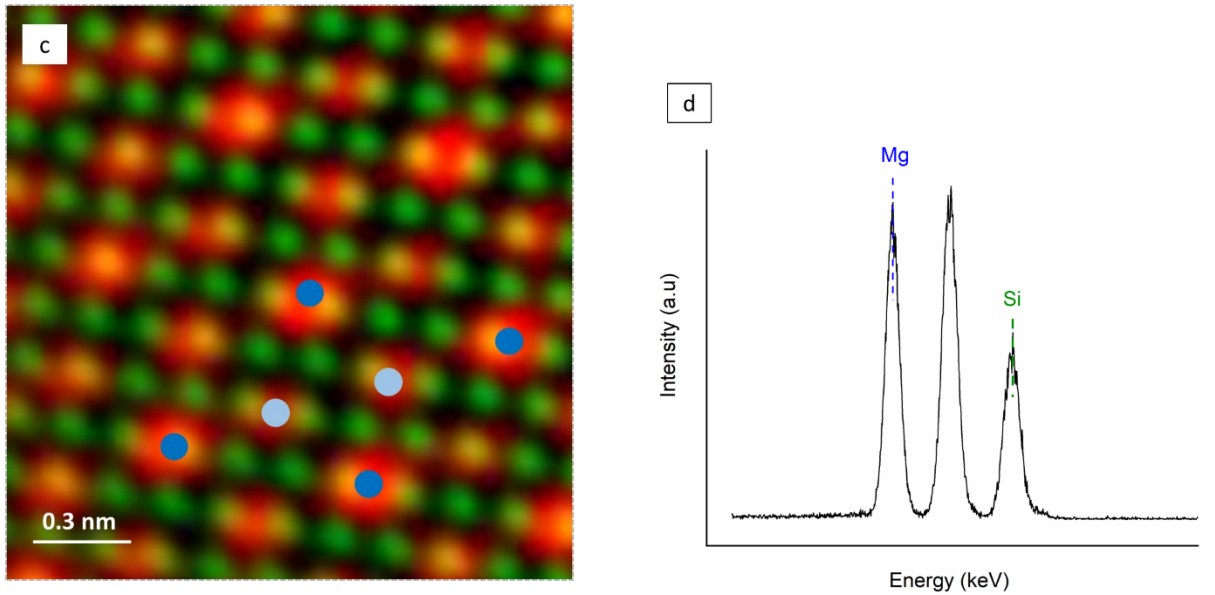
Figure 5.14. (a) HRSTEM images of β´ phase with corresponding FFT (inset), (b) zoomed view of white dashed square area in (a). (c) inversed FFT image of β´ phase in (b). (d) integrated EDX spectrum of precipitate. Dark and light blue circles show the position of Si1 and Si2
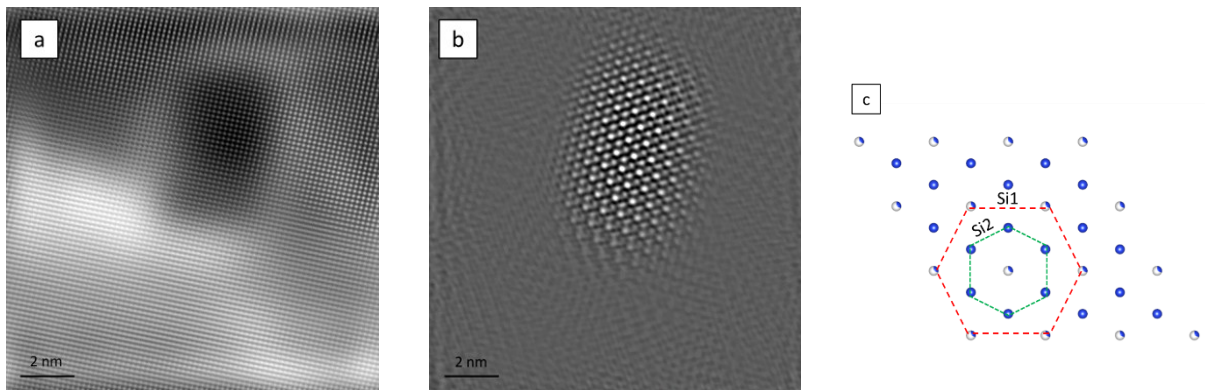
Figure 5.15. IFFT of the (a) Al matrix and (b) the embedded β´ phase. The projected crystal structure in (c) is indicating the Si1 and the Si2 position; the Mg atoms were removed in (c) for better visualization

5.4.5. Core-shell structure

Figure 5.16 (a and c) show a HRTEM micrographs of a particles with a core-shell structure. The core often serves as the main site for precipitate formation and growth, while the shell can influence the particle interaction with the surrounding matrix, thus effecting mechanical strength and resistance to deformation. The FFTs in both images exhibit a spot pattern with six-fold symmetry and *d*-values of

~ 0.61 nm, which can be indexed as β´ phase with OR pointed out in the inset. Figure 5.16 b and d present the IFFTs of the precipitates, which consist of a main phase (core) and an additional shell at the interface between the Al matrix and the precipitates. The IFFT was performed by removing all reflections corresponding to the Al matrix and to the core of the particle, keeping only the additional reflections to confirm the presence of the shell phase and visualize its location. The results indicate that the additional reflection is associated with the shell region of the particle with thickness of ~1nm.

This feature has been reported before and suggested that an intermediate layer reduces the misfit strain between the β' phase and the Al matrix. Furthermore, it has been proposed that this layer may facilitate coarsening, which would influence the mechanical properties with further aging. [224]–[226] Unlike in the bulk β' structure, local compositional variations may be expected in the intermediate layer to optimize the local misfit. [225] However, this goes beyond the structural and composition analysis performed here.
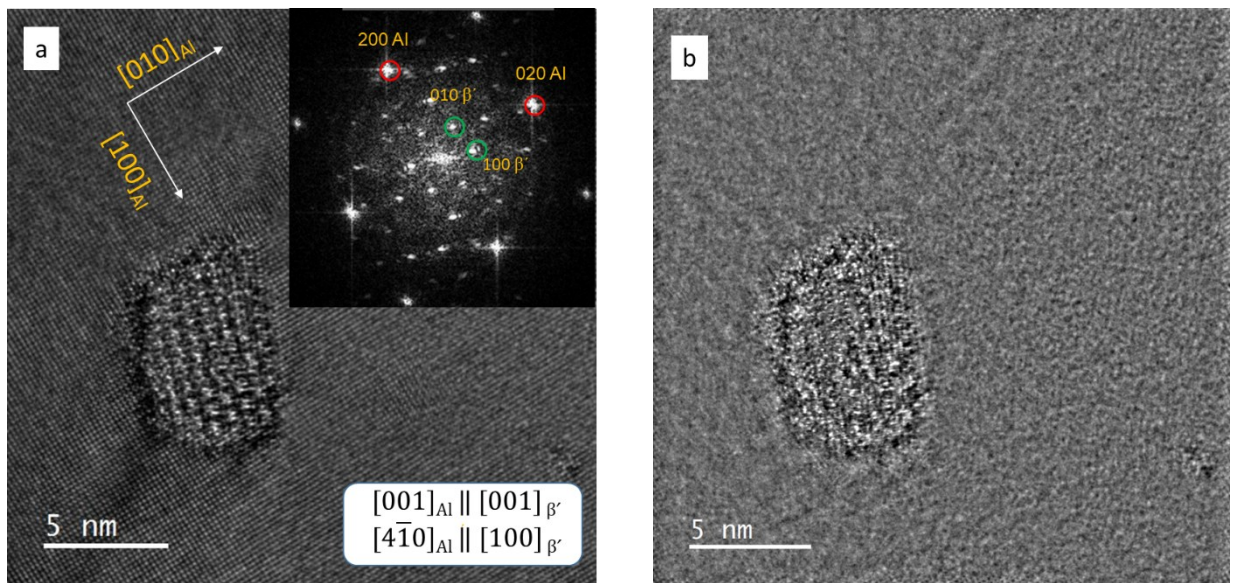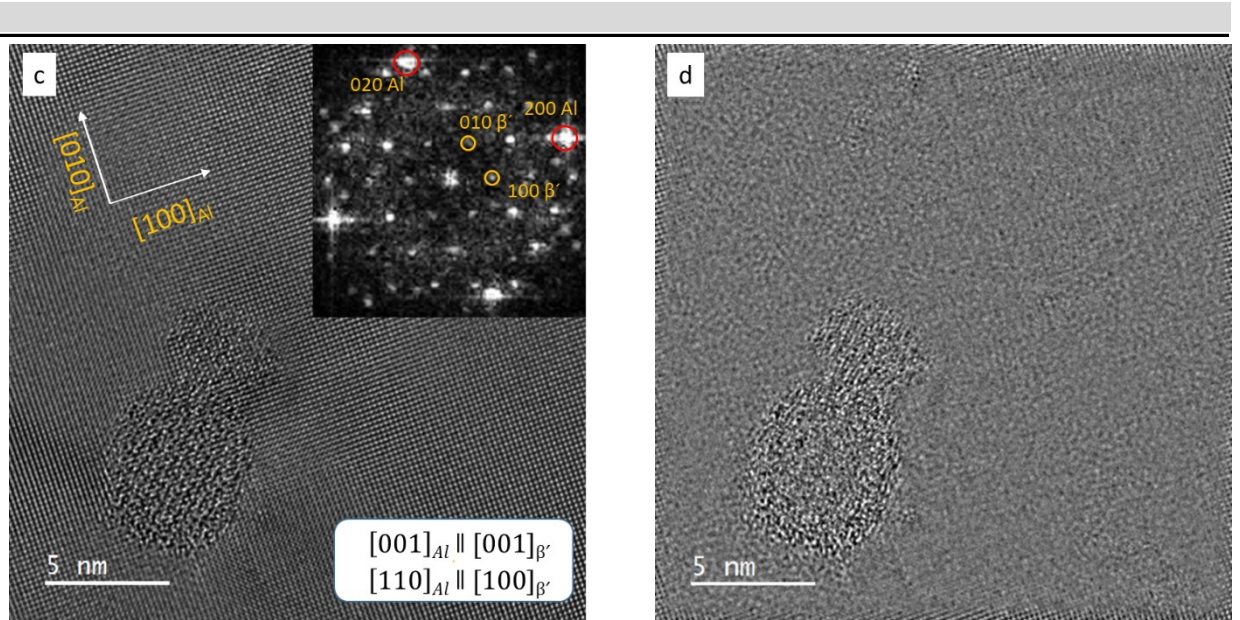
Figure 5.16. (a) and (c) HRTEM micrographs of precipitates with corresponding FFT. (c) and (d) IFFT of reflections excluding of Al and precipitate reflection to reveal the shell structure.

5.4.6. Precipitate free zone and grain boundary precipitates

Grain boundaries and dislocation lines are known to attract solutes from the supersaturated solid solution, leading to short-range diffusion. [227] This process depletes Mg and Si from the aluminum matrix in the vicinity. Dislocations within subgrains are particularly effective in this regard. This phenomenon facilitates the nucleation and growth of rod-shaped precipitates on boundaries or along dislocations by drawing solutes from adjacent regions. Consequently, this creates a region devoid of precipitates, known as a precipitate-free zone (PFZ). PFZs are a typical phenomenon in the precipitation hardening process during AA. [228]–[231]

The width of this zone depends on the activation energy for diffusion and the nature of GBs as was studied in details in Ref. [232]. Figure 5.17. shows PFZ in both deformed samples followed by AA 130 and 160 ˚C. It shows the formation of particles at the GBs with a size of ~ 20 nm and a PFZ with a width of ~ 30 nm after aging at 130 °C. Aging at a higher temperature (160 °C) leads to an increased size of the GB precipitates up to 50 nm and a corresponding PFZ width of about 80 nm. The Mg/Si distribution for the particles that precipitate along the grain boundaries is plotted in Figure 5.17b. The composition maximum is at a higher value of Mg/Si ~ 1.6 compared to the intra-granular precipitates. Thus, it can be assumed that the precipitate phase observed at the grain boundaries after AA at 160 °C differs from the phase inside the grains.
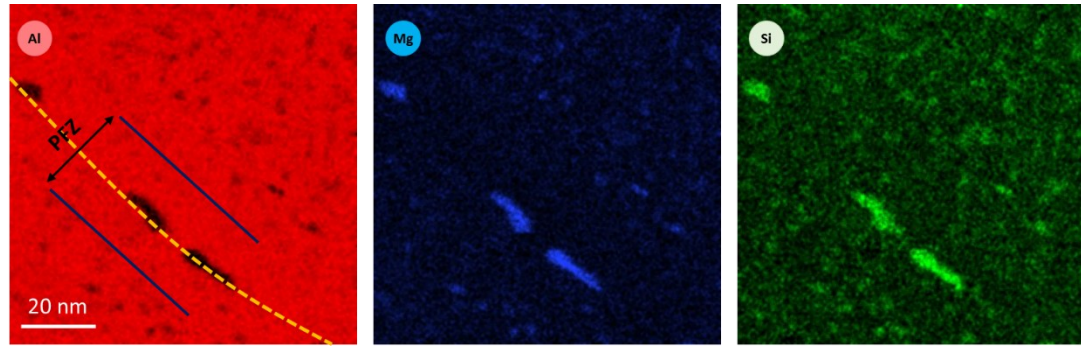
(a)
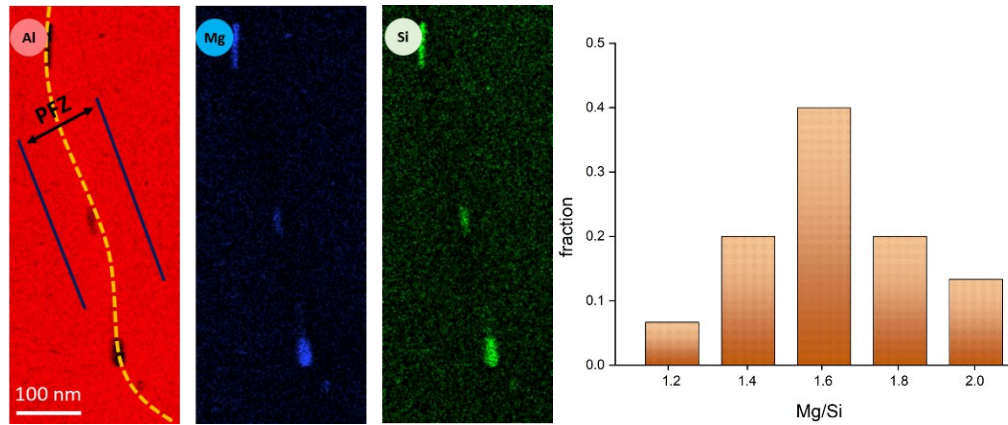
(b)

Figure 5.17. EDX elemental maps for Al, Mg, and Si of deformed sample after AA at (a) 130 °C and (b) 160 °C demonstrating the formation of PFZ and Mg/Si distribution plot for the particles precipitated at grain boundaries

5.4.7. Size and number density of hardening particles

The results presented above indicate the formation of precipitates as a result of aging treatments at 130 and 160 °C. These nanosized precipitates are the main contributors to the age-hardening effect. A visual comparison of the two AA states shows that the size of the precipitates and the average inter-particle distances are different. To assess quantitative characteristics of the alloy after AA at these two different temperatures, statistics were collected on the size of the precipitates, and their number per unit volume was calculated. In this section, the number of particles per unit volume of material N will be quantified according to the formula in Ref. [73]:

$$N = 3n/A(t + l), \qquad\qquad 5.1$$

where *n* stands for the number of precipitates in the field of view, *A* for the area of the field of view, *t* is the TEM sample thickness measured by EELS, and the *l* is corrected average precipitate length. The factor 3 is due to counting only along one of the three <001> Al directions.

n was obtained by counting the precipitates in virtual dark field images from a 4D STEM dataset (see Figure 5.18) for the deformed sample followed by aging at 160 °C. Band pass filtering was used to create a virtual aperture as shown in Figure 5.18b. This allowed to collect the signal for most of the particles present in the field of view. n for the sample aged at 130 °C, was calculated based on DF-TEM images (Figure 5.8)

| (a) | (b) |
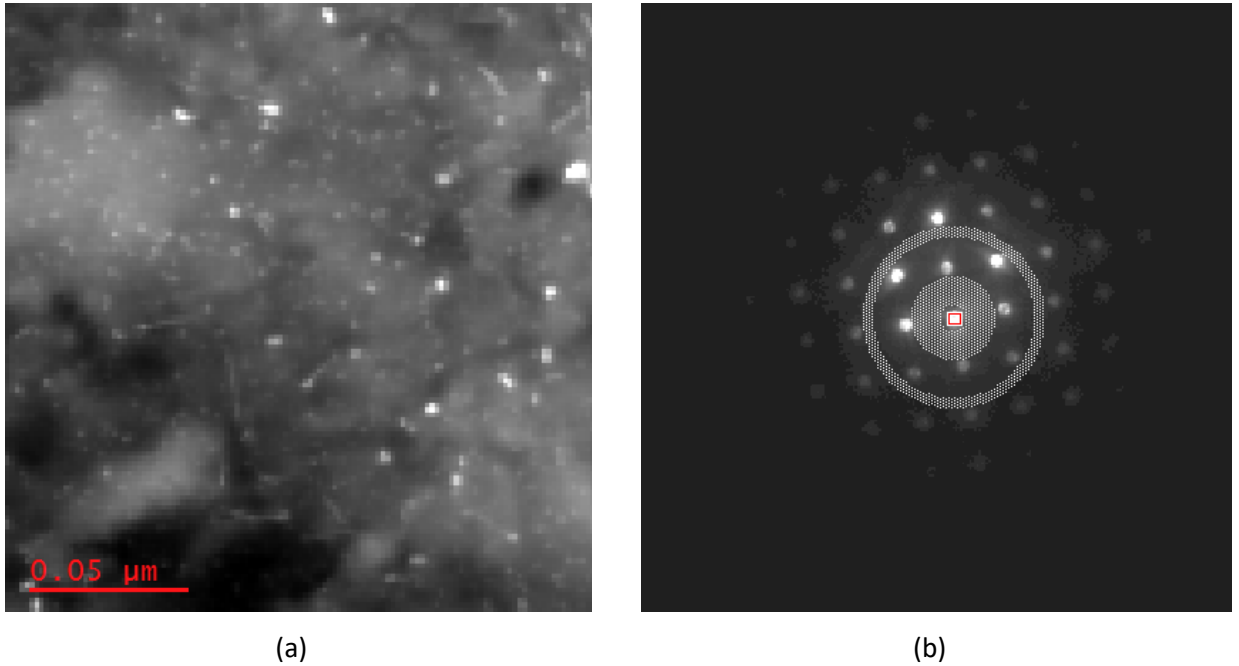
Figure 5.18 (a) Virtual dark field and (b) integrated diffraction pattern with the mask area for creating virtual dark field image for deformed sample + AA 160 °C

The relative thicknesses of the area were determined by EELS measurements. The regions chosen for statistical analysis were carefully selected, avoiding proximity to grain boundaries, large particles, or other features that could introduce irregularities in the precipitate distribution. Figure 5.19 displays the thickness map acquired via EELS, indicating a thickness of 30 nm. Given that all TEM samples were prepared using the same method, a sample thickness estimate of 30 nm was used in all particles density quantification analyses.
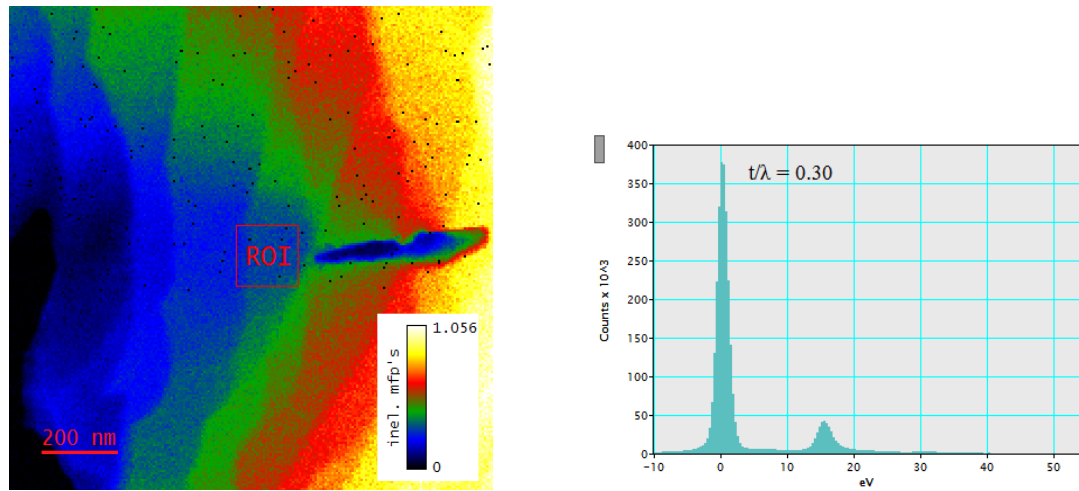
Figure 5.19. Relative thickness map with the corresponding low loss spectra for the deformed sample + AA at 160 °C

The precipitate diameter distributions were plotted for approximately 200 particles based on several dark-field TEM images. The plot for the sample after AA at 130 °C (Figure 5.20a) shows a particle size distribution with an average diameter of ~ 1.4 nm, whereas the sample aged at 160 °C exhibits a bimodal distribution (Figure 5.20b) with maxima at ~ 2.2 nm and ~ 5 nm. Thus, the increase in annealing temperature leads to a growth of the precipitates. However, the number fraction of the bigger particles is small (~7%). Accordingly, The precipitate number density was obtained and increased from $(1.5\pm0.3)\times10^{23}$ m^{-3} at 130 °C to $(2.2\pm0.5)\times10^{23}$ m^{-3} at 160 °C.

Table 5.2. Parameters of the alloy structure based on TEM-DF and 4D-STEM measurements

Processing conditions	Averaged particle diameter (nm)	Precipitate number density (m^{-3})
V3W1 + AA 130 °C 48h	1.4	$(1.5\pm0.3)\times10^{23}$
V3W1 + AA 160 °C 10h	2.2 for small particles 5 for big particles	$(2.2\pm0.5)\times10^{23}$
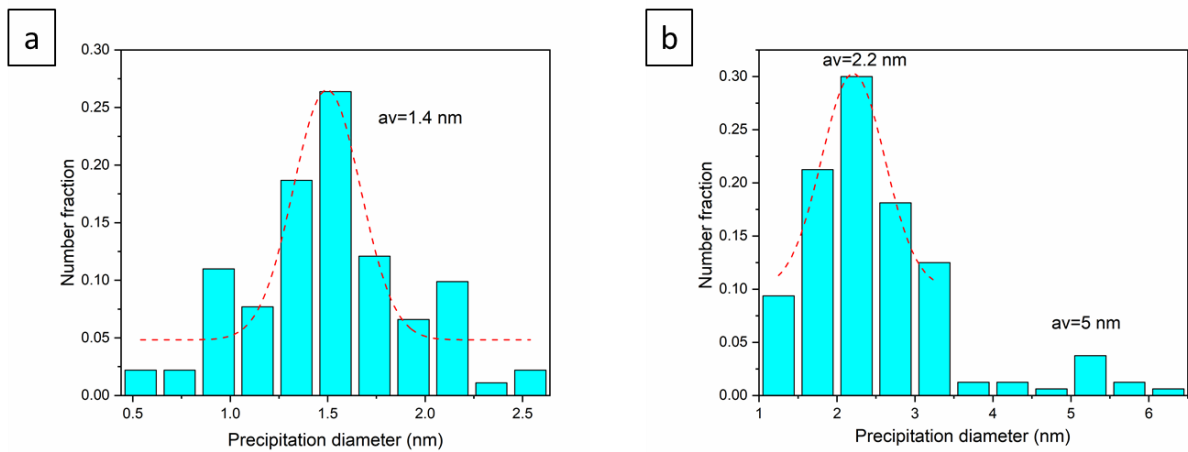
Figure 5.20. Precipitates diameter distribution for the samples after AA at (a) 130 °C and (b) 160 °C

5.5. X- ray diffraction analysis

Analysis of the XRD profiles has been used to determine the lattice parameter of the Al-based solid solution (a) and to estimate the dislocation density (Λ) in the center and at mid-radius of the samples. Figure 5.22 presents the XRD patterns of the deformed and aged samples. Note that only Al reflections are present and no peaks due to precipitates can be detected due to their low volume fraction and small size. The results of the XRD profiles analysis are summarized in Table 5.3. Taking into account the step size, pattern range and the signal to-noise-ratio, the relative measurement uncertainty of the lattice parameter is estimated to be $\sim 4 \times 10^{-4}$. [233] The details of error estimation can be found in appendix.

The measured lattice parameter of the quenched sample is $\sim$ 4.0574 Å. The value after HPTE deformation is marginally decreased (see Table 5.3). A significant decrease in the Al lattice parameter was found for the samples after AA. The lattice parameter after deformation in the center of the sample is $\sim$ 4.0571 Å and after aging at 130 and 160 °C, it decreases to $\sim$ 4.0561 Å and 4.0541 Å. The decrease in the lattice parameter is linked to the decomposition of the solid solution, where solute atoms, Mg and Si, precipitate during aging. Since Si atoms are smaller than Al, their substitution causes lattice contraction, while larger Mg atoms induce lattice expansion. The net effect on the lattice parameter depends on the relative concentrations of Si and Mg, as well as the number of precipitation, which determines how much solute remains dissolved in the matrix. [234][235] Therefore, the observed decrease in lattice parameter suggests that more Mg atoms are consumed during precipitation, reducing their concentration in the matrix and contributing to lattice contraction. The extent of lattice parameter reduction can indicate the degree of aging and effectiveness of heat treatment, correlating with increased hardness.

The dislocation density was assessed using the CMWP method, as illustrated in Figure 5.21. It was anticipated that the dislocation density would be higher at the mid-radius due to the increased accumulated strain in this region. However, the results reveal no significant variation in dislocation density with respect to the distance from the center of the sample. These values might be affected by substantial statistical and systematic errors inherent in the measurement process which is discussed in chapter 3.

In addition, at high temperatures, aluminum experiences thermal recovery processes, which can lead to a reduction in dislocation density. This is because the thermal energy allows dislocations to climb, interact, and annihilate, reducing the overall dislocation density in the material. However, the dislocation density decreased slightly to $(3–5)×10^{14}$ m^{-2} after AA due to thermal recovery, but its magnitude remains at a rather high level. This phenomenon has been previously documented in the literature [236] was interpreted that the precipitates formed during AA effectively impede dislocation movement and hinder their complete annihilation. The presence of these precipitates contributes to a high dislocation density by blocking dislocations from moving freely and thereby contributing to the material strengthening mechanisms.
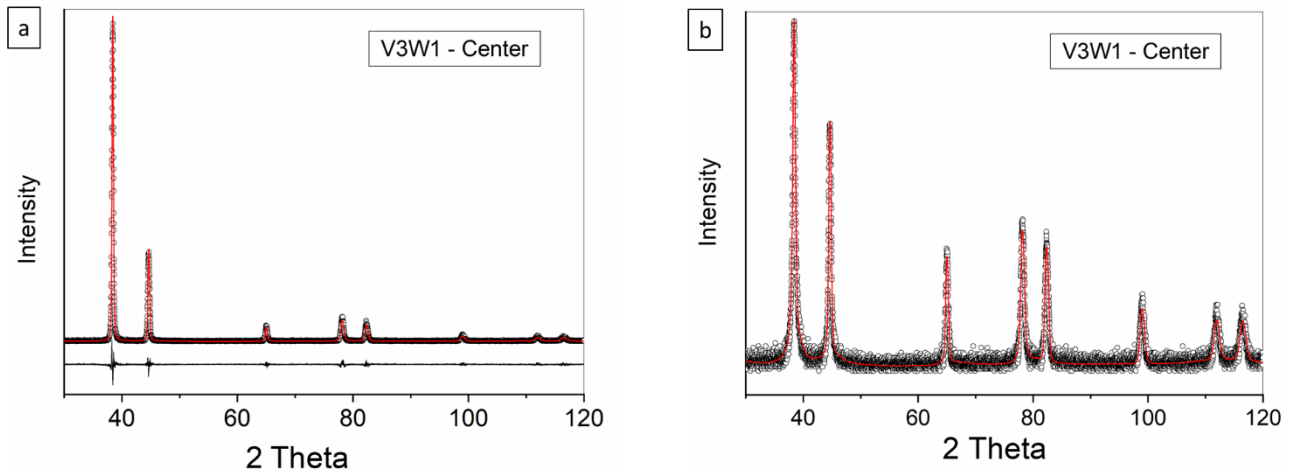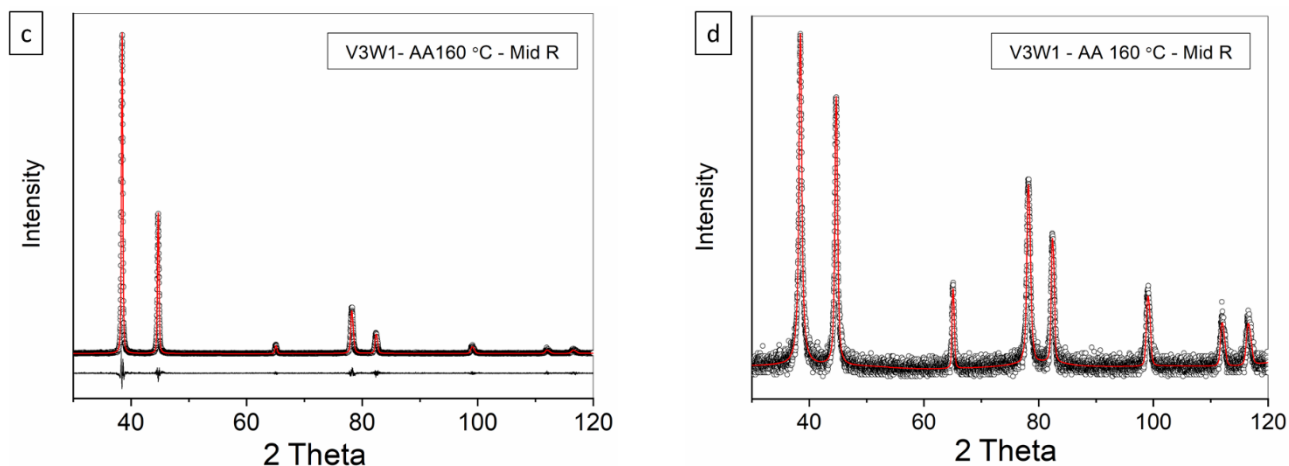
Figure 5.21. Two typical measured (open circles) and CMWP calculated (red lines) diffraction patterns for V3W1-Center (a, b) and V3W1-AA160 °C-Mid-Radius (c, d) samples with linear (a, c) and logarithmic (b, d) intensity scale. The black lines at the bottom of (a) and (c) are the difference plots between the measured and CMWP calculated patterns. In (b) and (c) it can be seen that the peaks related to the V3W1 - Center sample are broader than those related to the V3W1- AA 160 °C - Mid-Radius sample, which is in a good correlation with the dislocation density values listed in Table 5.3
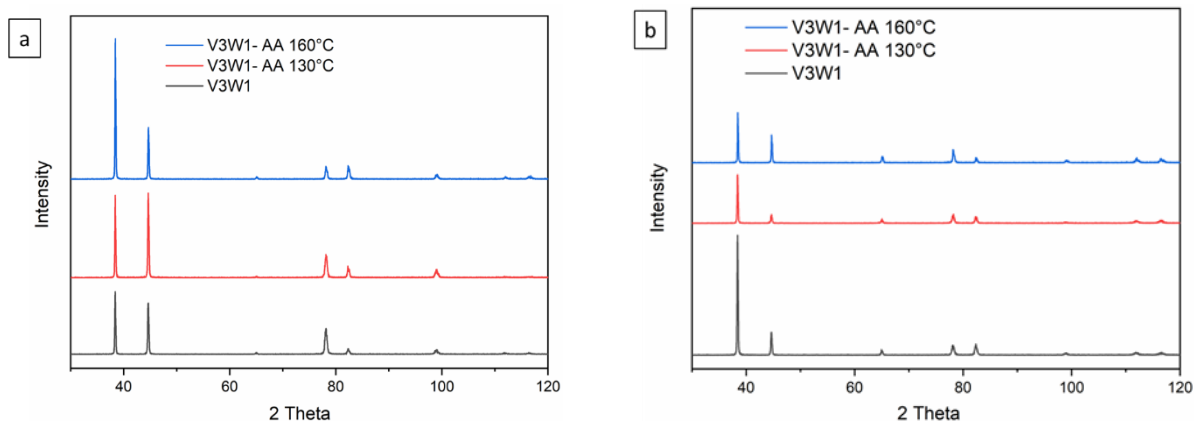
Figure 5.22. XRD diffraction patterns of the HPTE-processed sample followed by AA collected at its (a) central and (b) mid radius part

Table 5.3. Dislocation density and lattice parameters evaluated from the XRD profiles using the CMWP method

Sample	Dislocation density (m^{-2})		Lattice parameter (Å)	
	Center	Mid-radius	Center	Mid-radius
Quenched	$\sim 10^{10} - 10^{11}$ [30]		4.0574	
V3W1	8×10^{14}	6×10^{14}	4.0571	4.0569
V3W1- AA 130 °C	4×10^{14}	3×10^{14}	4.0561	4.0561
V3W1- AA 160 °C	5×10^{14}	4×10^{14}	4.0541	4.0518
Accuracy: ± 30%			Accuracy: ± 0.0001 Å	

Given the high error estimation, it is essential to validate the obtained results using additional methods. To address this, the dislocation density was also measured using the interception method on a STEM HAADF image, as depicted in Figure 5.23. A 15 × 15 grid was superimposed on the image using the grid creator script in Digital Micrograph (Gatan). The number of intersections between the grid lines and dislocations was counted, and the dislocation density was calculated using the formula provided below:

$$\Lambda = 2K/xt, \qquad\qquad 5.2$$

where K is number of intercepts, x is the length of the grid lines, and t is the thickness of the sample. It gives us:

$\Lambda = 2 * 250/(30 * 838\ nm) * 30\ nm \approx 6.6 \times 10^{14}$ m^{-2}
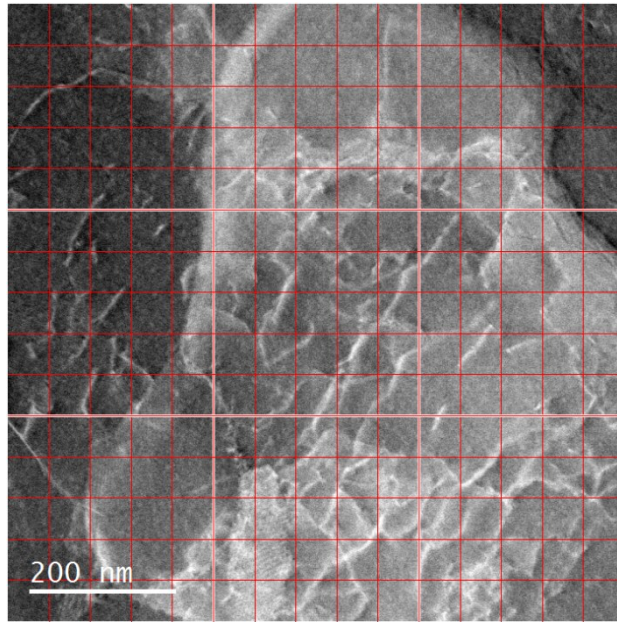
Figure 5.23. HAADF STEM image of the deformed sample followed AA 130 °C acquired at the camera length 91 mm

The results obtained from this method are consistent with those measured by XRD. However, it is important to note that this method also has limitations. Factors such as sample thickness and the limited field of view can affect the accuracy and introduce potential errors in the measurement.

5.6. DSC measurements

Figure 5.24 shows DSC curves of the as-quenched and deformed samples. The endothermic and exothermic peaks on the DSC curve represent the evolution of the microstructure during the heat treatment. Therefore, differences in the curves indicate differences in their thermal and microstructural behavior. For the quenched sample, the presence of several peaks is visible, which corresponds to the known sequence of phase formation in this alloy. [237][238] The peak at low temperature (~180 °C) is characteristic for Mg-Si clusters and GP zone formation, and the other peaks at higher temperature correspond to a precipitation of secondary phases as indicated. For the deformed sample, only one main peak is observed, and the corresponding heat transfer is noticeably smaller compared to the quenched counterpart. Such a modification of DSC curves was also reported after ECAP in previous study, which reported a GP zone peak at approximately 240 °C, followed by a broad peak at 375 °C representing an overlap of β″ and β′ phase formation. [238] They conducted ECAP at room temperature, and probably no clusters formed during deformation. The absence of a peak for the GP zone formation in this study

can be explained by the fact that they had already formed during HPTE deformation (see APT and HRTEM results in pervious chapter Figure 4.5)
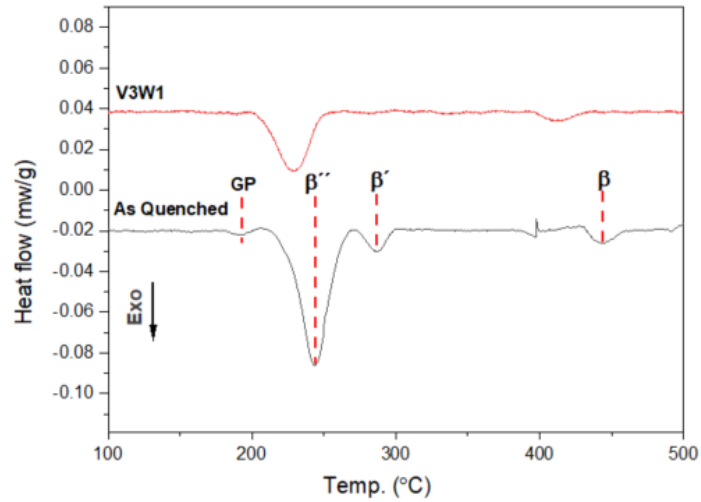
Figure 5.24. DSC curves of as quenched and deformed samples

5.7. Discussion

5.7.1. Microstructure and precipitate evolution

Based on the TEM and EBSD, the microstructural evolution of A6101 Al at mid-radius during the HPTE deformation followed by AA at different temperatures can be described schematically as it is shown in Figure 5.25.
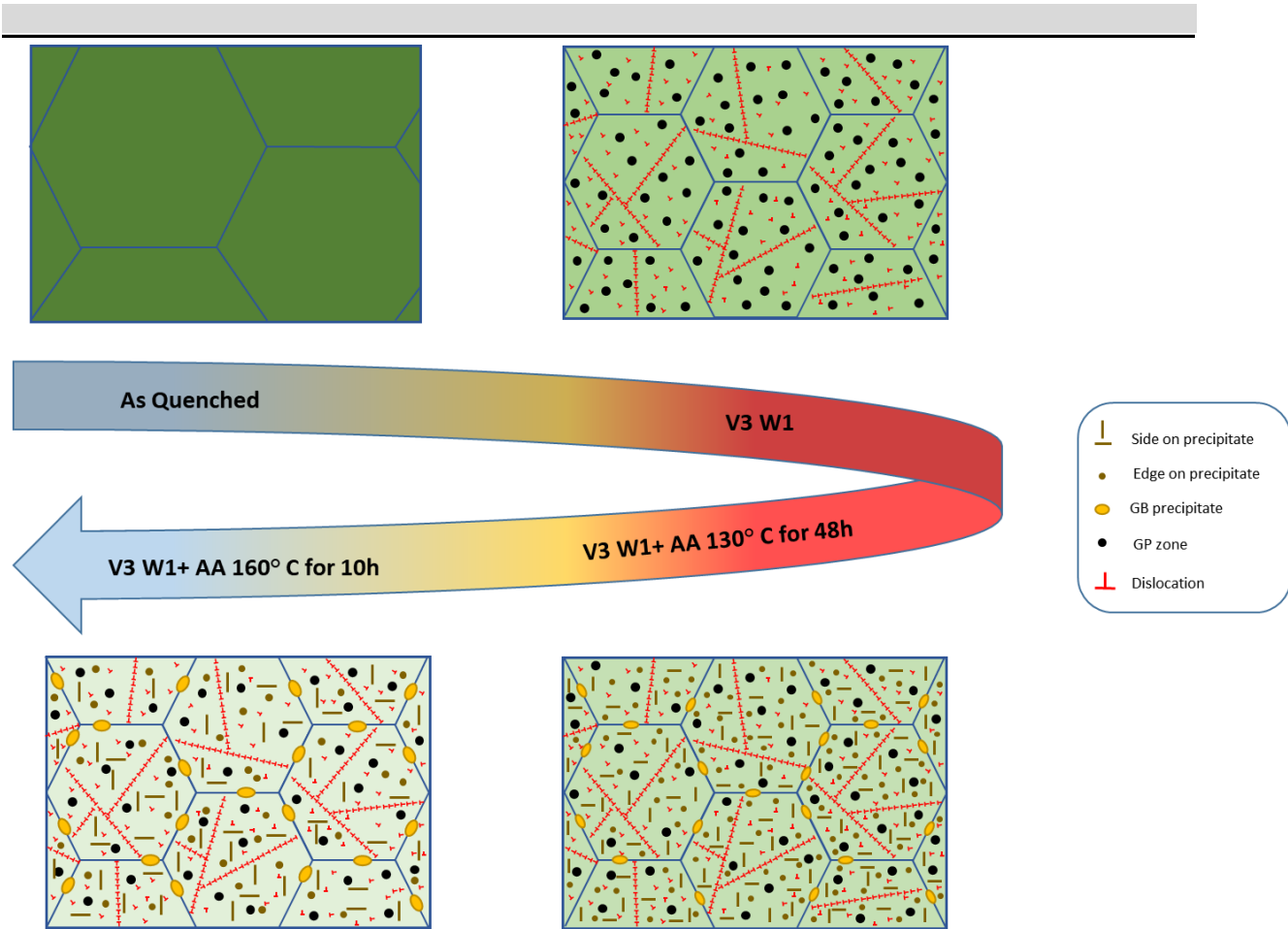
Figure 5.25. Schematic illustration of microstructure evolution of 6101 Al grade after quenching and during the HPTE followed by AA in mid-radius region. HPTE induces a high dislocation density resulting in the formation of dislocation walls; GP zones are observed in Al grains. Annealing at 130 °C leads to the precipitation of particles and development of PFZs. Raising the annealing temperature to 160 °C causes an increase in size of both the precipitates and the PFZs. The background color indicates the concentration of solutes inside the matrix

Severe plastic deformation of the aluminum alloy results in a substantial increase in dislocation density as shown in Table 5.3. The dislocations multiply and interact, leading to the formation of dislocation pile-ups, tangles and subgrain boundaries (dislocation walls, LAGBs). [239] LAGBs make up to approximately 75-90% of grain boundaries, depending on the sample location. In the deformed state, secondary phase particles were not detected, but GP zone formation was observed (refer to Figure 4.5).

Quantifying the volume fraction of GP zones from TEM images is nearly impossible due to their small size and coherence with the matrix.

The aging process leads to a transformation of GP zones into secondary phase particles. During aging at 130 °C, intra-granular precipitates with an average diameter of ~ 1.4 nm are formed. Subsequent aging at a higher temperature (160 °C) led to an increased size of intra-granular precipitates with a distribution of the Mg/Si ratio implying the presence of one main phase and other phases of different composition coexisting (Figure 5.9b).

In general, for Al-Mg-Si alloys after solid solution treatment, the sequence of phase formation with increasing temperature and aging time has been established. First, the solute atoms cluster together, which leads to the formation of GP zones. Then a metastable β″-phase is formed. It is followed by the formation of β′, U1, U2 and β phases. The β″-phase is reported to be the most important hardening phase in the Al-Mg-Si system, but its formation can be suppressed by accumulated strain. [240][241] In this case, β′ dominates dispersion strengthening. The β-phase, as the last one in this series, is not coherent with the Al matrix and its contribution to the strengthening of the material is not significant. [202], [242], [243]

5.7.2. Nucleation and growth of particles

In undeformed materials, precipitates form uniformly during AA, with particles of β″ phase being the main contributors to hardening. Their effectiveness in enhancing mechanical properties is due to their small size and homogenous distribution. [244]–[246] However, in deformed materials, precipitates, predominantly of the post-β″ type, form heterogeneously, often clustering around dislocations. The density of dislocations influences the distribution. As the dislocation density increases, it provides more nucleation sites for precipitates and accelerates the diffusion process by almost three orders of magnitude. [195] In this scenario, dislocation-assisted diffusion becomes more prominent compared to the slower bulk diffusion, leading to a more heterogeneous distribution of precipitates. [244]–[246] However, the drawback of pre-deformation can be seen in faster coarsening of the precipitating phases, reducing their effectiveness in blocking dislocation motion over time due to increasing the interparticle distance. This phenomenon results in a decrease in the material hardness and strength during prolonged aging, limiting the long-term mechanical performance. Therefore, the balance between the deformation-induced increase in nucleation sites and the accelerated coarsening of precipitates is a critical factor in optimizing the mechanical properties of age-hardenable alloys.

During aging of the deformed alloy, there is no sequential process for precipitation of hardening phases, but they coexist at the heat treatment conditions. The highly defective structure of the formed precipitates is apparently due to the deformation applied during HPTE [240] and results in the accelerated growth of the formed particles due to enhanced diffusivity of the solutes.

The precipitation of the secondary phase particles is associated with the decomposition of the supersaturated Al-based solid solution. This process can be monitored by changes of the lattice parameter. In the deformed sample, as well as in the sample after subsequent AA, the lattice parameter is smaller in the mid-radius region compared to the center. As the AA temperature increases, the lattice parameter continues to decrease. Thus, based on the XRD analysis, it can be concluded that the content of solute atoms in the solid solution decreases and this effect is more pronounced at the mid-radius compared to the center of the sample. This is explained by the higher applied strain, and, consequently, an increased concentration of defects, mostly – grain boundaries, which contribute to an increase in the diffusion mobility of solutes.

Accelerated grain boundary diffusion gives rise to the formation of phases with a higher Mg/Si ratio and PFZs along the grain boundaries (see Figure 5.17). The width of PFZs increases with increasing aging temperature. A comprehensive investigation of the PFZs was not the aim of the present study, but PFZs were found for both states of the alloy after AA.

5.7.3. Coherence and orientation relationships of precipitates

The precipitates examined by HR(S)TEM exhibit a (semi)coherent structure. Their ORs often differ from those reported for the alloy in literature. It should be noted that detailed HR(S)TEM analysis was carried out only for particles with well resolvable crystal structure; for many precipitates this was not possible. This is due to the fact that most of precipitates exhibit a high defect density, consist of more than one grain, or their orientation does not allow obtaining images with atomic resolution. Recently, several studies have been published establishing the ORs and their role in determining precipitate morphology for various precipitates in Al-Mg-Si alloys. [226], [247], [248] These studies report that the morphology of precipitates in the equilibrium state is determined by anisotropic misfit strain, which depends on the mutual orientation of the phase and matrix lattices. Furthermore, OR effects mechanical properties by determining the shape and aspect ratio of precipitates. For example, elongated precipitates intersect more slip planes, increasing the contact area with dislocation, thereby enhancing material strength. In this study, several ORs were discovered that have not been previously reported, whose presence seems

to be associated with the growth of precipitates in a defective structure. The primary driving force for phase transformation is the energy accumulated during deformation. Thermal activation of the phase formation process during AA was low, which is related to the high defect density. High solute diffusivity in a defective structure can lead to fast atomic transport to form a precipitate with growth directions determined by the local diffusion flux conditions. Another feature observed in the alloy after AA, which is also related to the high defect density, is the co-precipitation of particles (see Figure 5.10), when dislocations and grain boundaries provide many nucleation sites in close proximity.

5.7.4. DSC measurements and heat transfer

Understanding the structural features of the HPTE-deformed sample provides insights into the DSC measurements (Figure 5.24). The DSC curve displays only one broad exothermic peak at a temperature slightly below the typical β″ transformation temperature, which exhibits a significantly reduced heat transfer compared to the as-quenched reference.

A substantial number of GP zones formed during HPTE, indicating that no significant additional GP zone formation occurs during subsequent heating. The HR(S)TEM studies suggest that the observed β″ peak should be interpreted as a convolution of heat releases from multiple phases that precipitate simultaneously within this temperature range. This behavior is likely due to the high solute mobility induced by the high defect density. The reduced heat transfer in the deformed state can be attributed to a lower volume fraction of particles precipitating as clusters already formed during HPTE and the high defect density within these particles reducing the energy release. Additionally, the unusual and presumably less energetically favorable ORs of the particles contribute to a smaller amount of energy being released during precipitation. Finally, we can hypothesize that controlling OR and particle morphology through adjustments in material processing parameters may enable the targeted design and management of material microstructure, thereby optimizing the properties of Al alloys for specific applications.

5.8. Summary

This chapter has demonstrated that AA can enhance both the hardness and electrical properties of severely deformed aluminum alloys. EBSD analysis confirms that the grain size remains stable at the applied aging temperature; therefore, the observed enhancement is mainly attributed to the formation

of nano-scale precipitates within the matrix. The precipitate diameter distribution and number density were calculated, showing a Gaussian distribution with a number density of $(1.5\pm0.3) \times 10^{23}$ m^{-3} at 130 °C. At 160 °C, however, the number density increases to $(2.2\pm0.5) \times 10^{23}$ m^{-3} with a bimodal diameter distribution. These precipitates contribute to strength by effectively impeding dislocation motion.

XRD results show that the dislocation density remains largely unchanged after AA, suggesting that the precipitates effectively impede dislocation movement and therefore retard recovery. Additionally, the observed decrease in lattice parameter following AA indicates a reduction in solute concentration within the matrix, which likely contributes to the improved EC.

The morphology of the precipitates has been investigated by APT and rod-shaped and irregular shaped precipitates were observed. The Mg/Si distribution plot obtained by EDX elemental mapping and APT reveals the presence of variety of phases formed simultaneously. By HR imaging of individual precipitates, it can be concluded that most of the precipitates (more than 90%) contain of defective/poly crystalline structure. Moreover, new ORs have been identified, which may be related to the stored strain affecting the preferential growth of particles.

Furthermore, DSC curves of samples after HPTE show obvious difference compared to as-quenched counterpart with a single broad peak, reflecting a convolution of the heat released from all kinds of precipitates.

Chapter 6

6. Mechanical and electrical properties

6.1. Introduction

In the previous two chapters, the capability of HPTE to produce UFG aluminum structures as rod-shaped samples was demonstrated, highlighting its potential for industrial applications. However, a notable drawback of the severely deformed sample was observed in the deterioration of EC, which poses a limitation for its broader application in the electrical industry where both high strength and high conductivity are required. AA has been applied to restore the EC of materials through the controlled formation of nanoscale precipitates and cleaning the matrix from solute atoms. [212][249] The previous chapters provided a detailed analysis of the precipitate statistics, crystal structures, and their evolution during the AA process. While these discussions laid a strong foundation for understanding the microstructural changes induced by HPTE and subsequent aging, they did not fully address the implications of these changes for the material functional properties, specifically the interplay between precipitates, mechanical strength, and EC.

In this chapter, the focus is on an in-depth examination of how the mechanical properties and electrical conductivity of HPTE-deformed samples can be tailored and optimized through AA. This involves not only a continued exploration of the microstructural characteristics but also a comprehensive modeling effort to correlate these structural features with the observed mechanical and electrical

behavior. The chapter aims to elucidate the mechanisms which contribute to the strengthening of the material while simultaneously mitigating the adverse effects of SPD on EC.

6.2. Results

Figure 6.1a shows the Vickers hardness profiles along the sample diameter after different aging times. The hardness after HPTE deformation is not uniform across the sample, displaying a value of approximately 90 HV in the center, which increases to around 125 HV at the edge. However, for the sample aged at 160 °C for 10 hours, the hardness in the center increased remarkably, exhibiting a behavior distinct from the other samples. This anomaly is likely due to differences in phase transformations occurring during aging, as all other processing parameters remained constant.

   Figure 6.1b depicts the dependence of EC on the processing parameters. It is evident that electrical conductivity is highly sensitive to the aging temperature, increasing steadily with longer aging times and higher temperatures, reaching 52.4 ± 1.27 IACS % after aging at 160 °C for 10 hours. Error bars indicate measurement accuracy within 1σ. In Figure 6.1 d, the measured data are compared to the values from the EN 50183 Standard for overhead conductor lines [250] and data from Ref [74]. An important conclusion from this data is that both electrical conductivity and mechanical properties were improved for V3W1 – AA160 C- 10h sample, which is on the trade—off line obtained by literature. Zheng *et al.* investigated the influence of aging time on the hardness and EC of an undeformed Al-Mg-Si alloy. Their study reported that after aging at 170 °C for 6 hours, the sample exhibited the optimal combination of hardness and EC, with the hardness reaching 127 HV and the electrical conductivity ∼ 44% IACS. [251]
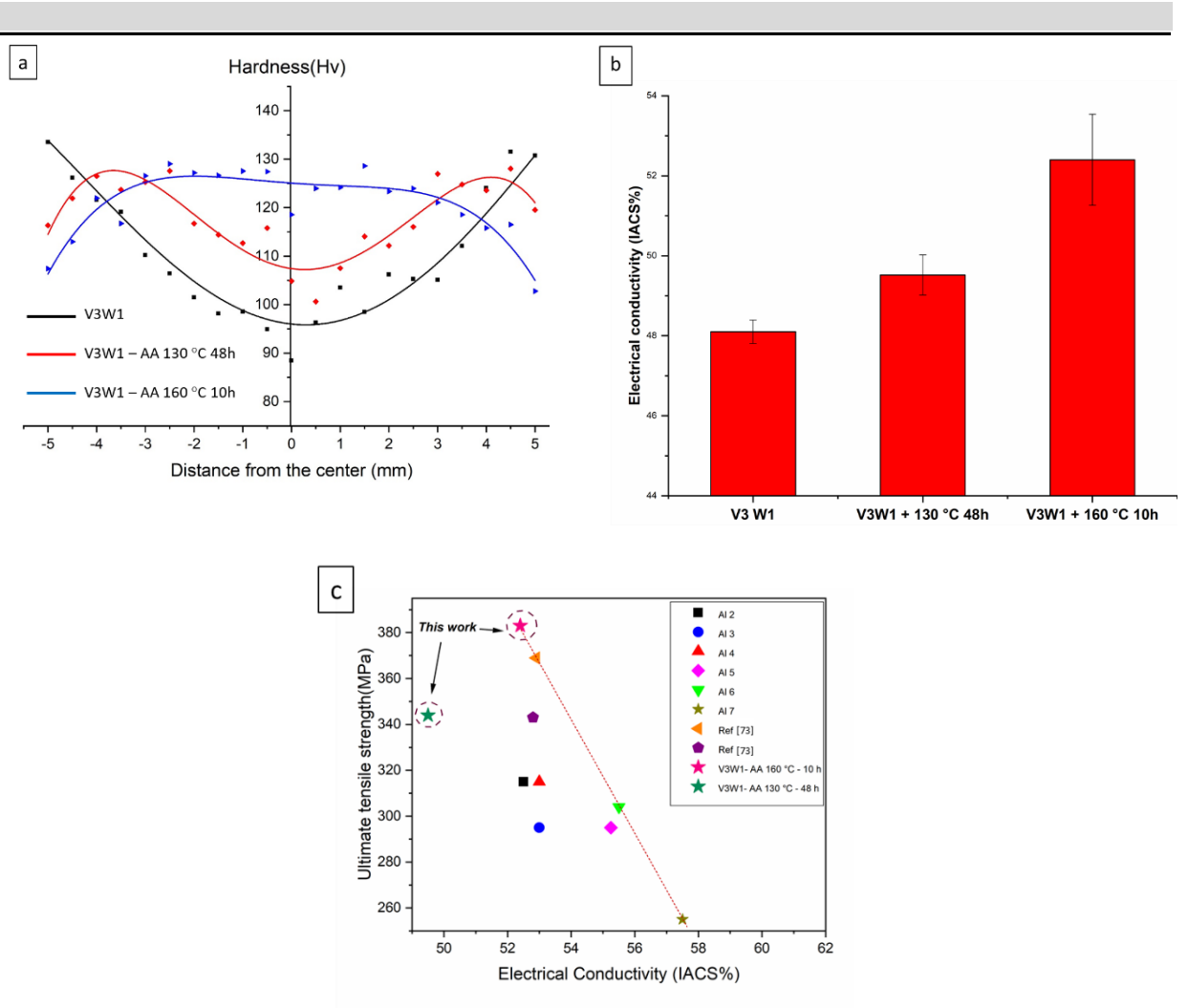
Figure 6.1. (a) HV hardness profile along the sample diameter, and (b) EC values for different processing parameters. (c) Comparison of the measured UTS and EC for the alloy studied to the values reported in EN 50183 standard (Al2–Al7) [250] and in Ref [74]

In addition to the measured HV profiles for the deformed sample followed by aging at 160°C, which exhibits an optimal combination of mechanical and electrical properties, a nanohardness map was created at the mid-radius of this sample. For comparison, a map was also generated for the specimen after deformation and subsequent AA at 160 ˚C. The results are demonstrated in Figure 6.2. An increase in hardness is evident after aging, with the average hardness of the sample after aging being 1.33 ± 0.07 GPa, compared to the as-deformed sample average hardness of 1.14 ± 0.06 GPa (Figure 6.2c). This improvement is attributed to the formation of intermetallic phases, as explained in further chapter.
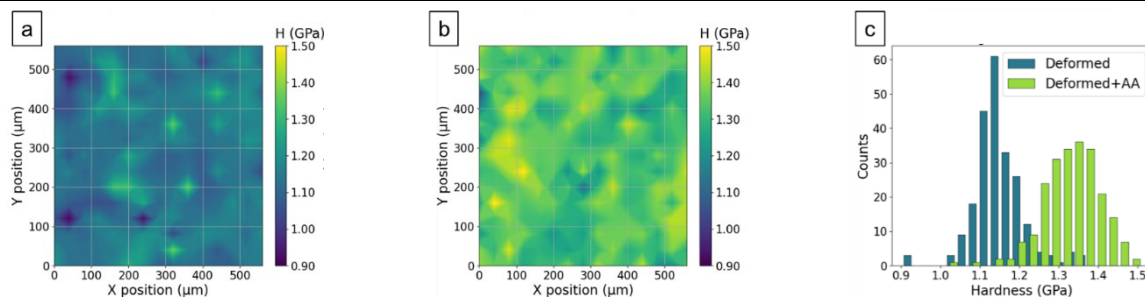
Figure 6.2. Nanoindentation maps of deformed (a) and deformed + AA (b) samples. (c) Histograms of hardness for deformed and deformed + AA samples

The true stress-strain curves for the HPTE-deformed samples and those subjected to AA are presented in Figure 6.3. Notably, the sample deformed by HPTE and subsequently aged at 160°C exhibits a significant increase in strength, with the yield strength rising from 260 MPa to 375 MPa. Additionally, elongation at failure improves after aging at 160°C compared to aging at 130°C. Specifically, the elongation to failure decreases from 13.2% in the as-HPTE state to 3.3% after aging at 130°C but increases to 5.2% following aging at 160°C.

This behavior can be attributed to the effective pinning of dislocations by precipitates, which enhances the strain hardening capacity. Detailed discussions on this phenomenon are provided in Section 6.5.1. A summary of the tensile test results is available in Table 6.1. Furthermore, mechanical properties are compared with a commercial counterpart (tempered T81) in Table 6.2. The observed substantial improvement in mechanical properties, while maintaining unchanged electrical conductivity, addresses the challenge of balancing high mechanical strength with good electrical performance. This suggests a potential for manufacturing advanced conductors suitable for overhead power lines.
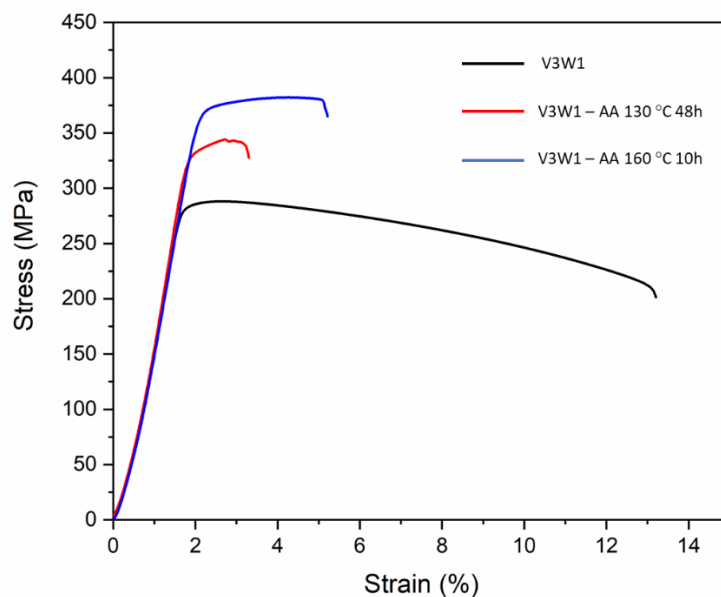
Figure 6.3. True stress-strain curve of the samples in the as-deformed state and after AA at 130 and 160 °C

Table 6.1. Mechanical properties measured for 6101 aluminum grade

Processing conditions	Yield Stress (MPa)	UTS (MPa)	Uniform Strain (%)	Elongation to failure (%)
V3W1	280	283	2	13.2
V3W1 + AA 130 °C 48h	336±2	345.5±1.5	2.7±0.1	3.6±0.2
V3W1 + AA 160 °C 10h	375±2	383 ± 3	4.94±0.2	5.1± 0.1

Table 6.2. Comparison of properties for the 6101 grade (HPTE + AA 160 °C) and for T 81 commercial alloy

Sample	HV	UTS (MPa)	EC (IACS %)
HPTE + AA 160 °C	125	383	~ 52.4
T 81 [252]	90	300	~ 54

6.3. Strength modeling based on microstructural parameters

Strength and EC can be modeled based on microstructural features. The model for the deformed sample aged at 160 °C is presented here as it shows the best tradeoff relationship between strength and EC. The modeling parameters for other states can be found in Table 6.3 and the modeling results are shown in Figure 6.4. In addition, the details of the error estimation can be found in the appendix section.

Several strengthening mechanisms are known for the metallic materials. These are precipitate or age hardening, solid-solution strengthening, dislocation or work hardening, and grain-boundary (Hall-Patch) hardening. By modeling the mechanical strength based on the contribution of the different hardening mechanisms, it is possible to calculate the yield strength of an alloy in a given state, assuming that the contribution of each mechanism is additive:

$$\sigma_{total} = \sigma_{f\,Al} + \sigma_{dis} + \sigma_{prec} + \sigma_{GB} + \sum \sigma_i^{SS}. \qquad 6.1$$

Here, $\sigma_{f\,Al}$ is the friction strength of pure Al and σ_{dis}, σ_{prec}, σ_{GB}, σ_i^{SS} represent dislocation hardening, precipitation hardening, Hall-Petch effect, and solid-solution strengthening. The yield stress of the aluminum matrix is around 35 MPa according to the data for annealed pure 1100-O aluminum. [253]

The Bailey-Hirsch relationship can be applied to estimate the contribution of dislocations to the strength [79]:

$$\sigma_{dis} = \alpha M G b \Lambda^{1/2}, \qquad 6.2$$

where $\alpha = 0.3$ is a dimensionless constant for Al, M is the Taylor factor which was determined from EBSD dataset and shown in Table 6.3, $G = 26.9$ GPa is the Al shear modulus, and $b = 0.29$ nm is the Burgers vector of ½<110> full dislocations in the Al lattice. [254] The dislocation density Λ for the deformed sample after AA at 160 °C was estimated to be ~ 4×10^{14} m^{-2} based on the X-ray line profile analysis (see Table 4.3) with an accuracy ~ 30%. [46] Therefore, the contribution of dislocations to the yield strength is *ca*. 120 ± 20 MPa.

The well-known Hall–Petch equation can be used to estimate contribution of grain boundaries to the strength [255]:

$$\sigma_{GB} = k_{HP} d^{-1/2}, \qquad 6.3$$

where k_{HP} is a Hall-Petch constant taken as 0.06 MPa·m$^{1/2}$ for Al [256] and d is the average grain size. The grain size at mid-radius differs in normal and longitudinal section of the sample. However, average value of 2.6 μm was considered, which led to $\Delta\sigma_{GB}$ = 37 ± 13 MPa.

The strength contribution of secondary phase precipitates σ_{prec} is caused by either shearing or bypassing of the particles by dislocations, depending on their size. According to Refs. [73][74][252], the increase in yield strength is related to the average strength of an obstacle F. They considered all precipitates to be non-shearable, however there was not enough justification given for this.

In this study, the particle size distribution exhibits a bimodal character (Figure 5.20b). First, we considered the part with a smaller size as shearable, and that with a larger size as non-shearable. To calculate their contributions to the strength the corresponding formulas were used:

For shearable particles: [73]

$$\sigma_{prec}^{shear} = \frac{M}{b^2\sqrt{\beta G}}\sqrt{N \cdot r} \cdot F^{3/2}, \qquad 6.4$$

with G and b being defined as above, β is a constant (β = 0.28), r is the precipitate radius. N is the number density of particles, and the obstacle strength for shearable precipitates is determined to be $F = 2\beta Gb^2(r/r_c)$ with r_c being the transition radius between particle shearing and bypassing. This term is usually mentioned to be 2.5 nm. [73]

For non-shearable particles the Orowan mechanism is active and the corresponding strength can be calculated as:

$$\sigma_{prec}^{Orowan} = \frac{2M\beta Gb}{L}, \qquad 6.5$$

where M, β, G and b were defined above. The L is inter-particle spacing which was calculated as $L=N^{-1/3}$. [74]

It is important to mention that the contribution of the precipitate hardening to the yield stress is dominant. It directly depends on the particle number density; therefore, counting accuracy is critical. Accurate determination of the particle density is challenging due to factors like sample thickness variation, non-uniform distribution, and low precipitate image contrast, leading to notable counting errors. Moreover, only a minor part of the precipitates is visible in dark-field images, *viz.* those whose diffraction beams pass through the objective aperture. In contrast, the particle density calculated based on the 4D-STEM dataset (Figure 5.18) with a virtual aperture and taking into account the signal from all particles in the field of view, allows for a more accurate analysis.

Shearable particles make up $\sim$ 93% of N and give $\sim$ 81 ± 53 MPa gain in strength; the remaining 7% are considered as non-shearable, providing a contribution of ~ 318 ± 36MPa to the yield strength. It is evident that the total contribution is considerably overestimated. One plausible explanation for the overestimation lies in the uncertain nature of particles in the deformed state. Observations indicate that the majority of precipitates, approximately 90%, exhibit a defective/polycrystalline structure. This structural characteristic may allow dislocations to cut through the particles, even when their size exceeds the critical threshold. On the other hand, the threshold value of particle size for their transition from shearable to non- shearable was made for a very specific alloy, and for the material studied in this work it may be different. Therefore, it is assumed this part also as shearable, which gives ~112 ± 45 MPa. In total, it yields 193 ± 70 MPa contribution to strength.

Solid solution strengthening arises from variations in atom sizes between the main alloy element and solutes. This variation results in the creation of a long-range stress field that influences dislocation glide. The contribution from solid solution strengthening to the yield stress can be written according to Myhr *et al.* as [252]:

$$\sigma_i = k_i C_i^{2/3},$$

6.6

here σ_i is the strengthening contribution of solute i, k_i is a scaling factor for solute i ($k_{Mg} \approx$ 29 and $k_{Si} \approx$ 66.3 MPa (wt. %)$^{-2/3}$), and C_i is the concentration of solute i in wt. %. The EDX analysis may not be a reliable method to determine the remaining amount of Mg and Si in the Al-based solid solution; due to their low concentration this method leads to a high measurements inaccuracy. The most reliable approach instead would be to use Vegard's law. However, the available data for ternary alloys only provide lattice parameter *vs.* solute concentration relations for some specific Mg/Si ratios in Al-Mg-Si alloys. Furthermore, based on the data available the mutual influence of Si and Mg content is not a linear function of their total amount. [257] In addition, APT measurements indicate $\sim$ 0.35 at.% Si and ~ 0.4 at.% Mg in the matrix, but this concentration value is limited by Si diffusion during APT measurements. Therefore, the residual concentration of solutes is estimated based on the volume fraction of secondary phase particles, and on the amount of substance needed for their formation. This procedure is described in more detail in Appendix and yields a residual concentration of 0.73 ± 0.05 and 0.2 ± 0.05 wt% for Si and Mg respectively. Based on calculated value, the contribution of the solid solution to the total strength of the alloy is 63 ± 30 MPa.

The calculated yield strength of the deformed 6101 Al alloy after AA at 160 °C according to Eq. (1) is 448 ± 79 MPa. The predicted value of σ_{total} turned out to be overestimated compared to the measured

value (375 MPa), but fully within the 1σ confidence interval. Several factors contribute to the discrepancy between the calculated and experimental values of the yield strength. Firstly, an inaccurate estimate of the contribution from solid solution strengthening is notable. This inaccuracy is linked to errors in determining the residual concentration of solutes, which does not take into account the precipitates at grain boundaries. Additionally, another source of error here relates to the estimation of average particle composition performed using APT. Significant local magnification artifacts in the APT measurements lead to inaccurate determination of aluminum content in nano-size precipitates, and ultimately to quite high error in determination of solutes concentration. Secondly, it should be noted that the contribution to yield strength from precipitation hardening is directly proportional to the square of the particle size. As demonstrated, the secondary phase particles in the alloy exhibit a core-shell structure (Figure 5.16). In this context, the shell can be considered a transitional layer between the central part of the particle and the Al-based solid solution, possessing properties distinct from the core concerning resistance to dislocation glide. Consequently, including the particle shell in the calculation of dispersion strengthening can lead to a significant overestimation of the contribution of this mechanism. Thirdly, the modeling was conducted using microstructure data obtained at the middle of radius of the sample. However, the central part of the sample also influences the overall tensile strength. Therefore, the microstructure gradient across the sample from the center to the mid radius, introduces some inaccuracy in the strength modeling.

The summary of the contribution of microstructural features to strengthening in this model is presented in Figure 6.4 for all three states.

Table 6.3. Parameters for modeling of deformed sample and deformed sample + AA 130 °C

	V3W1	V3W1 – AA 130 °C	V3W1 – AA 160 °C
Dislocation density Λ (m^{-2})	$(6\pm1.8)\times10^{14}$	$(3\pm0.9)\times10^{14}$	$(4\pm1.2)\times10^{14}$
Average grain size d_{15} (µm)	3.8 ±2.2	4.3±2.7	4.8±2.6
Precipitate number density, N (m^{-3})	–	$(1.5\pm0.3) \times 10^{23}$	$(2.2\pm0.5) \times 10^{23}$
Average precipitate radius, r (nm)	–	0.7±0.2	1.1±0.3
Residual Mg content (wt.%)	0.84	0.7	0.2
Residual Si content (wt.%)	1	0.98	0.73
Taylor Factor (M)	3.2 ±0.1	3.1±0.1	3.1±0.1
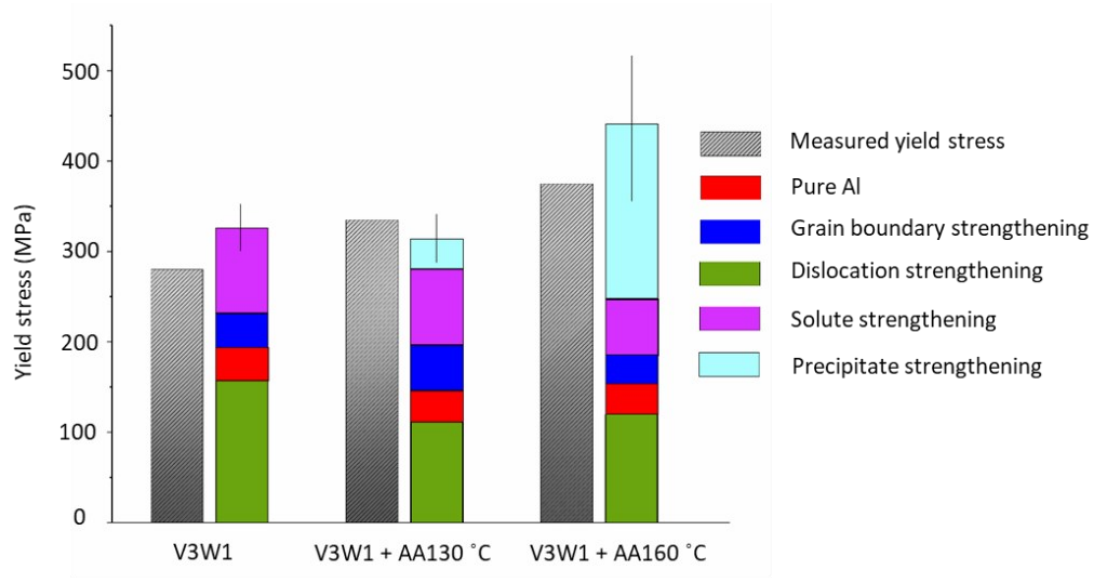
Figure 6.4. Comparison of the measured strength and the modeled values for the as-deformed sample and after AA at 130 and 160 °C based on the measured structural characteristics. Different colors show the contributions from different mechanisms

6.4. EC modeling based on microstructural parameters

All strengthening mechanisms discussed above cause lattice distortions that affect the electrical resistivity of metals and alloys. Matthiessen's rule [258] is used to take into account the influence of the microstructural characteristics on the electrical resistivity. The total electrical resistivity ρ_{total} can be described as a sum of the contributions of each individual mechanism:

$$\rho_{total} = \rho_{Al} + \Lambda\rho_{dis} + S_{GB}\rho_{GB} + \frac{\rho_{prec}}{\sqrt{(L)}} + \sum C_i^{sol}\ \rho_i^{sol}, \qquad 6.7$$

where ρ_{Al} is the resistivity of the ideal Al lattice; ρ_{Al} was assumed to be 2.79×10^{-6} Ω·cm, measured for AA1350–O at room temperature (equivalent to 61.8 %IACS) [74]. The other terms in Eq. (2) stand for the contribution from dislocations, grain boundaries, solute atoms and precipitates. ρ_{dis} and ρ_{GB} were defined to be 2.7×10^{-25} Ω·m^3 and 2.6×10^{-16} Ω·m^2 in [259]; Λ is the dislocation density, which was obtained by X-ray diffraction data (Table. 4.3), and S_{GB} is the fraction of the grain boundary area. In this study, a Kelvin tetrakaidecahedron model has been used to fill the space with full density. [260] Based on this model, for

a material with an average grain size d, S_{GB} can be calculated as $3.3/d$. With this, the contribution of dislocations and grain boundaries to the electrical resistivity are estimated to be 9×10^{-9} and 2×10^{-8} $\Omega\cdot$cm. These values are several orders of magnitude lower than the resistivity of the aluminum matrix. Therefore, the contribution of these two mechanisms can be ignored.

The contribution of the precipitates ($\frac{\rho_{prec}}{\sqrt{(L)}}$) is calculated based on the method described in Ref. [259]. In this approach, ρ_{prec} was determined to be 12 $\Omega\cdot$nm$^{3/2}$ with L representing the inter-particle spacing in nanometers. The average particle distance is calculated using $L = N^{-1/3}$ as described in the above section, which yields values of 17 nm for small precipitates and 41 nm for larger precipitates, in a good agreement with (HR)TEM micrographs. With this, the precipitate contribution to the resistivity is calculated to be $0.47\times10^{-6} \pm 1.1\times10^{-9}$ $\Omega\cdot$cm.

The corresponding factors in the Eq. (2) for the Mg and Si solutes were taken from the Ref. [252]: ρ_{sol}^{Mg} = 0.445×10^{-6}, and ρ_{sol}^{Si} = 0.496×10^{-6} $\Omega\cdot$cm/at. %. The addition to the total resistivity from the solute atoms was estimated around $0.45\times10^{-6} \pm 0.3\times10^{-6}$ $\Omega\cdot$cm.

The total electrical resistivity calculate for the sample is 3.71 $\mu\Omega\cdot$cm, which corresponds to EC value of $EC\ (\%IACS) = 172.4/\rho_{total}(\mu\Omega cm) = 46 \pm 3.7\ \%\ IACS$. [261]

The source of the discrepancy between measured and modelled values mentioned in strength modeling also affects resistivity modeling. Furthermore, for modeling the resistivity, the values measured at the mid-radius of the sample were used, whereas the experimental resistivity represents the average value for the entire sample.

The comparison of the measured and calculated values of resistivity in three structural states is plotted in Figure 6.5. The presence of impurities in the solid solution has the greatest influence on the resistivity compared to the influence of precipitates.
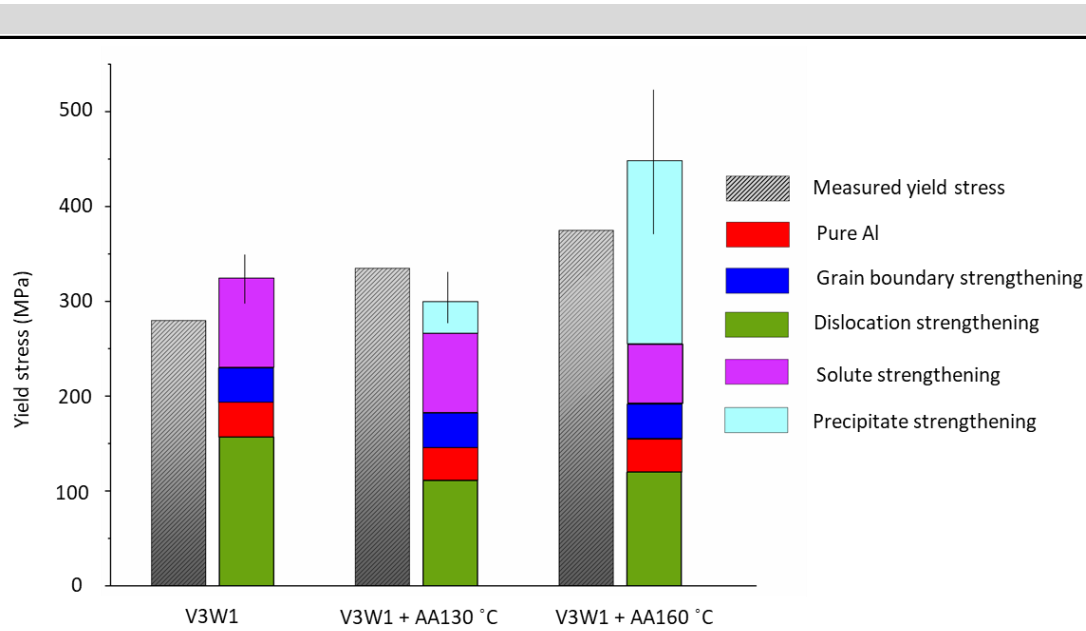
Figure 6.5. Comparison of the measured and the modeled resistivity values based on the structural characteristics for the samples in as-deformed state and after AA at 130 and 160 °C. Different colors show the contributions from different mechanisms

6.5. Discussion

6.5.1. Mechanical properties

As can be seen from measurements presented in Figure 6.1, the hardness profile along the diameter for samples in the as-deformed state and after AA at 130 ° shows a V-shape, typical for materials after treatment by HPT. [262] In contrast, the hardness behavior of the AA160-10h sample is quite unusual: the sample demonstrates an almost constant hardness along the radius from the center to mid-radius, which is reduced at the edges. In general, hardness is predominantly influenced by two key parameters: 1) the density of defects, such as grain boundaries and dislocations, generated during deformation, and 2) the size and volume fraction of precipitates formed during AA. Since the grain size (see EBSD maps in Figure 4.3 and Figure 4.4) and dislocation density (see Table 5.3) for the samples in as-deformed state and in the state after AA at 160 °C are close, precipitates play the main role for the hardness behavior.

Additionally, the formation of precipitates at grain boundaries can influence the overall hardness of the sample. Typically, grain boundary precipitates have no significant effect on the hardening behavior. With larger grain size in the sample center, a larger fraction of precipitates forms inside the grains, thereby contributing more significantly to hardening. The influence of these precipitates can be seen also

in tensile test. From the data in Table 6.1, it is clear that the samples after AA demonstrate higher strength characteristics and lower uniform elongation compared to the as-deformed sample. The presence of intermetallic particles in the structure leads to an increase in the strength of the material while simultaneously reducing ductility. [263] The effect of precipitates on plasticity may depend on a number of factors, such as their size, lattice alignment to the matrix material, the number density of these precipitates, and the uniformity of their distribution in the volume of the sample. At a fixed volume fraction, with precipitates of similar types and morphology, a denser distribution of smaller precipitates is generally stronger than a sparse distribution of coarse precipitates, due to the statistically increased number of dislocations pinning points in each slip plane. Moreover, the crystal structure of the precipitates and their interface with the matrix play a critical role in determining the final mechanical properties of a material. As mentioned earlier, the enhancement of mechanical properties is mainly driven by the interaction between dislocations and precipitates. This interaction is influenced by several factors: (1) the shear modulus difference between the matrix and precipitates, (2) misfit strains induced by thermal effects, (3) the presence of misfit dislocations at the precipitate boundaries due to differences in crystalline structures between the matrix and precipitates, and (4) the alteration of dislocation core energy as dislocations traverse through precipitates. [264]

This study shows that most of the precipitates exhibit a highly defective and/or polycrystalline structure (Fig. 4a), suggesting that they are likely not coherent with the Al matrix. Semi-coherent or incoherent precipitates create strong obstacles to dislocations, as their lattice mismatch generates significant strain or dislocations at the interface. However, the number density of precipitates is extremely high, which is apparently due to the increased number of nucleation sites created during SPD, which determines the enhanced strain hardening capacity and ductile behavior of the material and its high mechanical characteristics.

Thus, it can be assumed that the presence of particles of various phases, most of which are either incoherent or semi-coherent, in combination with the high density of precipitates plays a key role in the formation of mechanical properties of the studied alloy

This study confirmed the strengthening effect of the secondary phase formed after AA. As shown in Table 6.1 , the strength of the V3W1-AA130 °C 48h sample is lower than that of V3W1-AA160 °C 10h due to the lower precipitates density and their smaller size. An additional decrease in ductility in aged samples is also associated with the formation of a PFZ along the grain boundaries. Previous studies have shown that PFZs are softer close to grain boundaries and upon deformation tend to localize stress and cause

premature failure. This also leads to the appearance of structural inhomogeneity and contributes to premature fracture. [265]

A potential explanation for the increased ductility observed in the V3W1-AA160 °C 10h sample compared to V3W1-AA130 °C 48h may be related to the volume fraction and size of the precipitates, their coherence with the aluminum lattice since other structural features of samples are similar such as grain size and dislocation density. The precipitates volume fraction in the V3W1-AA130 °C 48h state is ~ 0.25 %, which increases to ~ 1.5% for V3W1-AA160 °C 10h sample. Previous research also indicates that the ductility of materials is significantly influenced by the size and distribution of precipitates. [266], [267] As the distribution of precipitates changes, the hindrance effect on dislocation movement changes, affecting the strain hardening rate of alloys. [266] The increased number density of precipitates in the V3W1-AA160 °C 10h sample enhances dislocation pinning, leading to improved strain hardening and greater strain capacity.

Peng *et al.* have demonstrated through large-scale molecular dynamics simulations that densely dispersed nano precipitates can function both as dislocation sources and obstacles. This dual role helps to balance deformability with local hardenability, thereby enhancing ductility. [268] In addition, Hamano have shown that the coexistence of coherent and incoherent precipitates increases homogeneous deformation, thus preventing local strain concentration and early cleavage cracking. Accordingly, the actions of coherent precipitates in strengthening the matrix and of incoherent precipitates in promoting homogeneous deformation can be expected to increase both the strength and toughness of the material. [269] Therefore, it is plausible that in the V3W1-AA160°C10h sample, the size, spacing and coherency of precipitates accompanied with PFZ width create a more favorable interaction, achieving an optimal balance between strength and ductility.

6.5.2. Mechanism behind enhanced mechanical and electrical properties in HPTE deformed alloy after AA

Grain boundaries and dislocations can strengthen the material but impair electrical conductivity, posing a trade-off between mechanical strength and EC. In this study, it was discovered that both characteristics can be increased simultaneously within a certain range of AA temperatures The hardness profile and electrical properties after HPTE deformation and subsequent aging at 130°C and 160°C revealed enhanced mechanical and electrical properties in both cases (Figure 6.1). The best results were obtained for the deformed sample after AA at 160 °C, which exhibited a noticeable increase in EC while maintaining a high level of microhardness. This behavior has been linked to the formation of secondary phase particles

inside the Al matrix, as illustrated by the TEM images in the previous chapter. The precipitates are larger and more densely spaced after AA at 160 °C compared to AA at 130 °C (Figure 4.17).

The mechanism of enhanced mechanical properties is already discussed above. However, regarding EC, it is well known that it is directly proportional to the mean free path of conducting electrons. Factors disturbing the free electron path increase resistivity, mainly through scattering by thermal lattice vibrations and lattice defects such as grain boundaries, dislocations, and solute atoms. Formation of GP zones in the deformed samples reduces EC due to strong electron scattering from lattice distortions. The enhanced EC after AA results from matrix purification from dissolved atoms and removal of coherent clusters (GP zones) through transformation into semi- or incoherent particles. TEM results indicate that the increase in conductivity correlates with the precipitation of hardening phases. [270] The increased aging temperature leads to phase growth by consuming dissolved atoms from the matrix, which is enhanced by the dislocation density from the HPTE deformation. The decrease in solute concentration leads to a decreased lattice parameter, confirmed by XRD measurements. This results in an overall increased EC, [271] although precipitates hinder conducting electrons and degrade EC, their impact is lower compared to solutes. A similar correlation between lattice parameter change and EC magnitude has been reported in previous studies. [272][273]

Despite the presence of PFZs, the samples exhibit a high level of plasticity. After AA at 160 °C, the material demonstrates the highest EC along with reasonable ductility. This result is due to the formation of intra-granular precipitates and the effect of solid solution purification. The HPTE process ability to subject specimens to different strain levels enables tailoring defect densities, offering a promising route for tuning mechanical strength and EC. Future work could focus on optimizing the interplay between defect density and aging conditions to maximize precipitate number density and achieve precise control of precipitate distribution. Additionally, exploring alternative aging temperatures and times could further enhance precipitate formation while minimizing the development of PFZs. These adjustments could improve the mechanical performance by extending the balance between strength and ductility while maintaining EC stability.

6.5.3. Summary

In this chapter, the influence of AA on the mechanical properties of aluminum alloys was systematically investigated through microhardness and tensile testing. Significant enhancement in both mechanical strength and electrical conductivity was observed following HPTE deformation and subsequent AA at

160 °C. These improvements are attributed to the formation of dense nano-scale precipitates within the alloy matrix.

Modeling of the yield strength and electrical resistivity, based on the structural data obtained, demonstrates a reasonable correlation with experimental values, despite the inherent statistical and systematic errors. The sources contributing to the error have been addressed. The observed increase in strength is mainly due to the pinning effect of the precipitates, which effectively impede dislocation movement, while the enhancement in electrical conductivity results from the reduction in solid solution concentration due to the incorporation of solutes into the precipitates.

The comparison between modeled and experimental values, as depicted in Figure 6.4, highlights the critical role of precipitate formation in enhancing mechanical strength, while its effect on conductivity is relatively minor. This underscores the significant contribution of precipitates to strength improvement, with minimal impact on conductivity.

The HPTE process, with its ability to fine-tune processing parameters, facilitates the introduction of defects at various levels, which promotes an increased number density of precipitates. This capability emphasizes the potential of intelligent nanostructural design in Al-Mg-Si alloys via the HPTE method. Such design is pivotal for achieving an optimal combination of high strength and high electrical conductivity, a balance that is challenging to attain with conventional thermo-mechanical processing method.

Chapter 7

7. Conclusion and outlook

This chapter presents a summary of the most significant findings and achievements of this research along with directions for potential future studies.

7.1. Conclusion

The motivation for this thesis was to address two problems: (i) developing the high strength – high conductivity Al alloy from an industrial perspective, and (ii) understanding the influence of deformation-induced lattice defects and structural characteristics of precipitates on the physical properties of age-hardenable Al alloy. To answer these questions, a combination of High Pressure Torsion Extrusion processing and artificial aging was employed, providing a promising approach to overcome the inherent trade-off between strength and electrical conductivity, particularly relevant to application in the conductor industry. The mechanical properties were examined through micro- and nano-hardness tests and tensile testing, complemented by an extensive exploration of the microstructure of the material using techniques such as XRD, APT, EBSD and advanced electron microscopy methods, including high-resolution (S)TEM imaging, STEM-EDX and STEM simulation. This combination of characterization methods provides a detailed understanding of the precipitates structure, composition, distribution and the material properties.

   Chapter 4 explores the microstructural evolution following HPTE deformation. Results revealed the formation of graded microstructure with significant grain refinement around mid-radius and larger grains

in the central region of the HTPE rods. APT identified a notable presence of Mg- and Si-rich clusters, suggesting the formation of GP zones due to dynamic aging during deformation. This grain refinement, coupled with cluster formation, is a main factor contributing to the observed increase in hardness of the material. The precipitation of clusters was accompanied by a slight reduction in the lattice parameter.

Chapter 5 examines the changes in the microstructure following AA at 130 °C and 160 °C. The Al matrix grain size remained stable, with no significant grain growth observed after aging, suggesting that the aging conditions did not promote significant recrystallization. The morphology of precipitates was categorized into two types: (i) rod-shaped and (ii) irregularly shaped precipitates, characteristic for both aging temperature states, as evidenced by APT and TEM analyses. However, the size and number of precipitates differed substantially between the two temperature regimes, with increased size and density observed after AA at 160 °C. The observed changes indicate that more efficient hardening behavior occurred after aging at 160 °C, which is likely due to enhanced precipitate growth and their denser distribution at the higher temperature. The Mg/Si ratio obtained from APT and STEM-EDX analysis confirmed that the main phase coexisted with other potential phases in this system, including β´, U1 and U2. High-resolution TEM imaging demonstrated that most precipitates exhibit defective or polycrystalline structures with a variety of ORs between the precipitates and the matrix, which is uncommon for this alloy. These characteristics indicate that the precipitates formation in the presence of structural defects exhibits distinctive behavior compared to the undeformed state. This presumably can be attributed to the influence of stored strain on the process of nucleation, growth, and the development of complex interfaces. Analysis of the DSC data shows a single broad exothermic peak. This is a distinct behavior when compared to the as-quenched state. This phenomenon may be attributed to the simultaneous precipitation of multiple phases, indicating that the aging process at these temperatures favors the nucleation of multiple phases with different thermal behaviors, thereby further complicating the precipitation hardening process.

Chapter 6 investigates the effects of HPTE followed by AA on mechanical strength and electrical conductivity. Tensile testing revealed that the yield strength reached 280 MPa after HPTE, with further improvement following AA at 130°C and 160°C. Additionally, ductility increased more significantly after AA at 160°C compared to AA at 130°C. This suggests that the size, spacing, and coherency of precipitates formed during aging at 160°C create a more favorable interaction, achieving an optimal balance between strength and ductility in the deformed sample. Concurrently, the electrical conductivity recovered to 52.4% IACS, which was the result of the reduction in the concentration of solute atoms. Additionally, XRD demonstrated a decrease of the lattice parameter, indicative the removal of solute atoms from the

matrix. Modeling of mechanical and electrical properties yielded results that were in close alignment with the experimental data, taking into account potential sources of error.

7.2. Outlook

While this research has demonstrated the potential of HPTE processing for producing materials with enhanced strength and electrical conductivity, and provided an in-depth analysis of precipitate crystal structure, further investigation is required in certain areas. These include:

1. Optimization of HPTE Parameters: The objective of study was to optimize HPTE parameters, with a particular focus on a specific HPTE regime (V3W1). Exploring alternative processing parameters, particularly in combination with varying aging temperatures, may provide deeper insights into the effect of strain on mechanical and electrical properties, thereby facilitating performance optimization.

2. Dislocation-Precipitate Interaction: The interaction between dislocations and precipitates remains insufficiently understood. TEM analysis of tensile-tested samples could provide valuable insights into this interaction, shedding light on the microstructural dynamics during plastic deformation.

3. In-situ TEM Study: The real-time observation of precipitate nucleation and growth using a heating holder with aberration-corrected TEM could provide a deeper understanding of the processes, capturing the successive stages of aging and providing a more comprehensive representation of precipitate evolution.

4. Influence of alloy composition: Investigating the effect of alloying elements on precipitate formation, morphology, and distribution could help tailor the mechanical and electrical properties of the material. This could involve systematic alloy composition adjustments and corresponding mechanical and microstructural characterizations.

5. Long-term aging and thermal stability studies: The developed material has potential applications in electrical engineering and is intended to be used for quite a long time. Therefore, future research could focus on the thermal stability of the structure formed during HPTE and aging. This could include investigating how longer (natural) aging affects the precipitate morphology and phase composition of the alloy, potentially leading to a degrade of mechanical and electrical properties over time.

6. Simulation of precipitate growth and coarsening: Numerical simulation of precipitate growth, coarsening, and phase transformations under different processing conditions could complement experimental findings. Modeling the effect of precipitation hardening on the stress-strain behavior of HPTE-treated alloys would provide a predictive framework for tuning alloy compositions and processing parameters for specific mechanical and electrical performance requirements.

References

[1] S. Li *et al.*, "Development and applications of aluminum alloys for aerospace industry," *J. Mater. Res. Technol.*, vol. 27, pp. 944–983, 2023, doi: https://doi.org/10.1016/j.jmrt.2023.09.274.

[2] J. Tan and S. Ramakrishna, "Applications of magnesium and its alloys: A review," *Appl. Sci.*, vol. 11, no. 15, p. 6861, 2021.

[3] S. Kores, S. Strmšek, M. Vončina, and J. Medved, "Innovative Approaches in Development of Aluminium Alloys for Packaging Industry," in *TMS Annual Meeting & Exhibition*, 2023, pp. 535–541.

[4] J. T. Staley and D. J. Lege, "Advances in aluminium alloy products for structural applications in transportation," *Le J. Phys. IV*, vol. 3, no. C7, pp. C7-179, 1993.

[5] B. Stojanovic, M. Bukvic, and I. Epler, "Application of aluminum and aluminum alloys in engineering," *Appl. Eng. Lett. J. Eng. Appl. Sci.*, 2018.

[6] C. Kammer, "Aluminum and aluminum alloys," *Springer Handb. Mater. Data*, pp. 161–197, 2018.

[7] G. Walker, *Solid-state hydrogen storage: materials and chemistry*. Elsevier, 2008.

[8] E. A. Starke Jr and J. T. Staley, "Application of modern aluminum alloys to aircraft," *Prog. Aerosp. Sci.*, vol. 32, no. 2–3, pp. 131–172, 1996.

[9] M. H. Farshidi, M. Kazeminezhad, and H. Miyamoto, "On the natural aging behavior of Aluminum 6061 alloy after severe plastic deformation," *Mater. Sci. Eng. A*, vol. 580, pp. 202–208, 2013.

[10] I. Volokitina, A. Bychkov, A. Volokitin, and A. Kolesnikov, "Natural aging of aluminum alloy 2024 after severe plastic deformation," *Metallogr. Microstruct. Anal.*, vol. 12, no. 3, pp. 564–566, 2023.

[11] S. Liu, C. Li, S. Han, Y. Deng, and X. Zhang, "Effect of natural aging on quench-induced inhomogeneity of microstructure and hardness in high strength 7055 aluminum alloy," *J. Alloys Compd.*, vol. 625, pp. 34–43, 2015.

[12] M. McLean, "Encyclopedia of materials science and technology." Taylor & Francis, 1986.

[13] A. P. Mouritz, *Introduction to aerospace materials*. Elsevier, 2012.

[14] S. Pogatscher, H. Antrekowitsch, H. Leitner, T. Ebner, and P. J. Uggowitzer, "Mechanisms controlling the artificial aging of Al–Mg–Si Alloys," *Acta Mater.*, vol. 59, no. 9, pp. 3352–3363, 2011.

[15] Y. F. Y. Fan, "Precipitation Strengthening of Aluminum by Precipitation Strengthening of Aluminum by Transition Metal Alumin Transition Metal Aluminides," *Mater. Sci. Eng.*, 2012.

[16] M. E. Fine, "Precipitation hardening of aluminum alloys," *Metall. Trans. A*, vol. 6, pp. 625–630, 1975.

[17] Q. Li and F. E. Wawner, "Characterization of a cubic phase in an Al-Cu-Mg-Ag alloy," *J. Mater. Sci.*, vol. 32, pp. 5363–5370, 1997.

[18] S. K. Eswara Moorthy and J. M. Howe, "Kinetic analyses of the growth and dissolution phenomena of primary Si and α-Al in partially molten Al-Si (-Cu-Mg) alloy particles using in situ transmission electron microscopy," *Metall. Mater. Trans. A*, vol. 42, pp. 1667–1674, 2011.

[19] C. Sigli, F. De Geuser, A. Deschamps, J. Lépinoux, and M. Perez, "Recent advances in the metallurgy of aluminum alloys. Part II: Age hardening," *Comptes Rendus. Phys.*, vol. 19, no. 8, pp. 688–709, 2018.

[20] A. Deschamps, F. De Geuser, C. R. Hutchinson, S. W. Lee, and Z. J. Horita, "Dynamic interactions between precipitation and plastic deformation in aluminium alloys," in *Materials Science Forum*, 2014, vol. 794, pp. 1133–1140.

[21] D. Hull and D. J. Bacon, *Introduction to dislocations*. Butterworth-Heinemann, 2001.

[22] S. J. Andersen, C. D. Marioara, J. Friis, S. Wenner, and R. Holmestad, "Precipitates in aluminium alloys," *Adv. Phys. X*, vol. 3, no. 1, p. 1479984, Jan. 2018, doi: 10.1080/23746149.2018.1479984.

[23] A. Perovic, D. D. Perovic, G. C. Weatherly, and D. J. Lloyd, "Precipitation in aluminum alloys AA6111 and AA6016," *Scr. Mater.*, vol. 41, no. 7, pp. 703–708, 1999.

[24] G. A. Edwards, K. Stiller, G. L. Dunlop, and M. J. Couper, "THE PRECIPITATION SEQUENCE IN Al ± Mg ± Si ALLOYS," vol. 46, no. 11, pp. 3893–3904, 1998.

[25] X. Wang, S. Esmaeili, and D. J. Lloyd, "The sequence of precipitation in the Al-Mg-Si-Cu alloy AA6111," *Metall. Mater. Trans. A*, vol. 37, pp. 2691–2699, 2006.

[26] J. Banhart, "Age hardening of aluminum alloys," 2016.

[27] V. M. A. Alza, "A Critical Review of Age Treatment Hardening Mechanisms in Aluminum Alloys."

[28] R. Z. Valiev, M. Y. Murashkin, E. V Bobruk, and G. I. Raab, "Grain refinement and mechanical behavior of the Al alloy, subjected to the new SPD technique," *Mater. Trans.*, vol. 50, no. 1, pp. 87–91, 2009.

[29] L.-M. Rymer, L. Winter, K. Hockauf, and T. Lampke, "Artificial aging time influencing the crack propagation behavior of the aluminum alloy 6060 processed by equal channel angular pressing," *Mater. Sci. Eng. A*, vol. 811, p. 141039, 2021.

[30] Y. Qi, A. Kosinova, E. Lakin, V. V Popov Jr, E. Rabkin, and R. Lapovok, "Effect of SPD Processing on the Strength and Conductivity of AA6061 Alloy," *Adv. Eng. Mater.*, vol. 21, no. 8, p. 1801370, 2019.

[31] G. E. Totten and D. S. MacKenzie, *Handbook of Aluminum: Volume 2: Alloy production and materials manufacturing*. CRC press, 2003.

[32] J. R. Davis, *Aluminum and aluminum alloys*. ASM international, 1993.

[33] H. Jin, "The Solid Solution and Grain Boundary Hardening due to Mg in an Aluminum Alloy System at Room and Elevated Temperatures," *Metall. Mater. Trans. A*, vol. 49, no. 12, pp. 6122–6133, 2018, doi: 10.1007/s11661-018-4949-9.

[34] E. Cervantes, M. Guerrero, J. A. Ramos, and S. A. Montes, "Influence of natural aging and cold deformation on the mechanical and electrical properties of 6201-T81 aluminum alloy wires," *MRS Online Proc. Libr.*, vol. 1275, 2010.

[35] Ø. Ryen, B. Holmedal, O. Nijs, E. Nes, E. Sjölander, and H.-E. Ekström, "Strengthening mechanisms in solid solution aluminum alloys," *Metall. Mater. Trans. A*, vol. 37, pp. 1999–2006, 2006.

[36] G. Gottstein, *Physical foundations of materials science*, vol. 3. Springer, 2004.

[37] S. Xi, K. Zuo, X. Li, G. Ran, and J. Zhou, "Study on the solid solubility extension of Mo in Cu by mechanical alloying Cu with amorphous Cr (Mo)," *Acta Mater.*, vol. 56, no. 20, pp. 6050–6060, 2008.

[38] C. Aguilar *et al.*, "Structural study of nanocrystalline solid solution of Cu–Mo obtained by mechanical alloying," *Mater. Sci. Eng. A*, vol. 548, pp. 189–194, 2012.

[39] R. S. Molla, "A study on Manufacturing of Deformed Bar (G 60-400W) at Elite Iron and Steel Industries," *no. May*, p. 123, 2018.

[40] O. R. Myhr, Ø. Grong, and S. J. Andersen, "Modelling of the age hardening behaviour of Al–Mg–Si

alloys," *Acta Mater.*, vol. 49, no. 1, pp. 65–75, 2001.

[41] M. J. Buehler, A. Hartmaier, H. Gao, M. A. Duchaineau, and F. F. Abraham, "The dynamical complexity of work-hardening: A large-scale molecular dynamics simulation," *Acta Mech. Sin.*, vol. 21, pp. 103–111, 2005.

[42] J. K. Sunde, C. D. Marioara, A. T. J. van Helvoort, and R. Holmestad, "The evolution of precipitate crystal structures in an Al-Mg-Si (-Cu) alloy studied by a combined HAADF-STEM and SPED approach," *Mater. Charact.*, vol. 142, pp. 458–469, 2018.

[43] Y. H. Zhao, X. Z. Liao, Z. Jin, R. Z. Valiev, and Y. T. Zhu, "Microstructures and mechanical properties of ultrafine grained 7075 Al alloy processed by ECAP and their evolutions during annealing," *Acta Mater.*, vol. 52, no. 15, pp. 4589–4599, 2004.

[44] R. S. Ganji, P. S. Karthik, K. B. S. Rao, and K. V Rajulapati, "Strengthening mechanisms in equiatomic ultrafine grained AlCoCrCuFeNi high-entropy alloy studied by micro-and nanoindentation methods," *Acta Mater.*, vol. 125, pp. 58–68, 2017.

[45] G. K. t Williamson and R. E. Smallman, "The use of Fourier analysis in the interpretation of X-ray line broadening from cold-worked iron and molybdenum," *Acta Crystallogr.*, vol. 7, no. 8–9, pp. 574–581, 1954.

[46] G. Ribárik, B. Jóni, and T. Ungár, "The Convolutional Multiple Whole Profile (CMWP) Fitting Method, a Global Optimization Procedure for Microstructure Determination," *Crystals*, vol. 10, no. 7. 2020, doi: 10.3390/cryst10070623.

[47] G. Thomas and M. J. Goringe, "Transmission electron microscopy of materials," *(No Title)*, 1979.

[48] J. Gallet *et al.*, "Experimental measurement of dislocation density in metallic materials: A quantitative comparison between measurements techniques (XRD, R-ECCI, HR-EBSD, TEM)," *Mater. Charact.*, vol. 199, p. 112842, 2023, doi: https://doi.org/10.1016/j.matchar.2023.112842.

[49] P. Snopiński, M. Kotoul, J. Petruška, S. Rusz, K. Żaba, and O. Hilšer, "Revealing the strengthening contribution of stacking faults, dislocations and grain boundaries in severely deformed LPBF AlSi10Mg alloy," *Sci. Rep.*, vol. 13, no. 1, p. 16166, 2023.

[50] J. Gubicza *et al.*, "Evolution of microstructure and hardness during artificial aging of an ultrafine-grained Al-Zn-Mg-Zr alloy processed by high pressure torsion," *J. Mater. Sci.*, vol. 55, pp. 16791–16805, 2020.

[51] V. Samaee *et al.*, "Dislocation structures and the role of grain boundaries in cyclically deformed Ni micropillars," *Mater. Sci. Eng. A*, vol. 769, p. 138295, 2020, doi: https://doi.org/10.1016/j.msea.2019.138295.

[52] J. K. Sunde, C. D. Marioara, and R. Holmestad, "The effect of low Cu additions on precipitate crystal structures in overaged Al-Mg-Si (-Cu) alloys," *Mater. Charact.*, vol. 160, p. 110087, 2020.

[53] C. S. Pande and K. P. Cooper, "Nanomechanics of Hall–Petch relationship in nanocrystalline materials," *Prog. Mater. Sci.*, vol. 54, no. 6, pp. 689–706, 2009, doi: https://doi.org/10.1016/j.pmatsci.2009.03.008.

[54] A. H. Chokshi, A. Rosen, J. Karch, and H. Gleiter, "On the validity of the Hall-Petch relationship in nanocrystalline materials," *Scr. Metall.*, vol. 23, no. 10, pp. 1679–1683, 1989.

[55] K. A. Padmanabhan, G. P. Dinda, H. Hahn, and H. Gleiter, "Inverse Hall–Petch effect and grain boundary sliding controlled flow in nanocrystalline materials," *Mater. Sci. Eng. A*, vol. 452, pp. 462–468, 2007.

[56] C. E. Carlton and P. J. Ferreira, "What is behind the inverse Hall–Petch effect in nanocrystalline materials?," *Acta Mater.*, vol. 55, no. 11, pp. 3749–3756, 2007.

[57] Y. B. Wang, B. Q. Li, M. L. Sui, and S. X. Mao, "Deformation-induced grain rotation and growth in nanocrystalline Ni," *Appl. Phys. Lett.*, vol. 92, no. 1, 2008.

[58] N. Q. Chinh, P. Szommer, Z. Horita, and T. G. Langdon, "Experimental evidence for grain-boundary sliding in ultrafine-grained aluminum processed by severe plastic deformation," *Adv. Mater.*, vol. 18, no. 1, pp. 34–39, 2006.

[59] A. Kobler, A. Kashiwar, H. Hahn, and C. Kübel, "Combination of in situ straining and ACOM TEM: A novel method for analysis of plastic deformation of nanocrystalline metals," *Ultramicroscopy*, vol. 128, pp. 68–81, 2013.

[60] R. Z. Valiev and R. K. Islamgaliev, "andI. V. Alexandrov," *Prog. Mater. Sci*, vol. 45, p. 103, 2000.

[61] R. Lapovok, L. S. Toth, M. Winkler, and S. L. Semiatin, "A comparison of continuous SPD processes for improving the mechanical properties of aluminum alloy 6111," *J. Mater. Res.*, vol. 24, no. 2, pp. 459–469, 2009.

[62] C. Illgen, B. Bohne, M. F.-X. Wagner, and P. Frint, "Thermal stability of SPD-processed aluminum alloys-Internal friction as an indication for recovery, recrystallization and abnormal grain growth," *J.*

Mater. Res. Technol., vol. 17, pp. 1752–1759, 2022.

[63] H. Lanjewar, L. A. I. Kestens, and P. Verleysen, "Damage and strengthening mechanisms in severely deformed commercially pure aluminum: Experiments and modeling," *Mater. Sci. Eng. A*, vol. 800, p. 140224, 2021.

[64] I. Polmear, *Light alloys: from traditional alloys to nanocrystals*. Elsevier, 2005.

[65] A. Loucif, R. B. Figueiredo, T. Baudin, F. Brisset, R. Chemam, and T. G. Langdon, "Ultrafine grains and the Hall–Petch relationship in an Al–Mg–Si alloy processed by high-pressure torsion," *Mater. Sci. Eng. A*, vol. 532, pp. 139–145, 2012.

[66] R. Z. Valiev, F. Chmelik, F. Bordeaux, G. Kapelski, and B. Baudelet, "The Hall-Petch relation in submicro-grained Al-1.5% Mg alloy," *Scr. Metall. Mater.*, vol. 27, no. 7, pp. 855–860, 1992.

[67] M. Furukawa, Z. Horita, M. Nemoto, R. Z. Valiev, and T. G. Langdon, "Microhardness measurements and the Hall-Petch relationship in an Al Mg alloy with submicrometer grain size," *Acta Mater.*, vol. 44, no. 11, pp. 4619–4629, 1996.

[68] M. Furukawa *et al.*, "Structural evolution and the Hall-Petch relationship in an Al Mg Li Zr alloy with ultra-fine grain size," *Acta Mater.*, vol. 45, no. 11, pp. 4751–4757, 1997.

[69] "Precipitation Strengthening," [Online]. Available: https://learnmetallurgy.com/study/mechanical/topic/precipitation-strengthening.php.

[70] G. B. H. M. S. Office, *Age-hardening of Aluminium Alloys*. H.M. Stationery Office, 1931.

[71] E. Thronsen, "The effect of natural ageing on clustering and precipitation in heat-treatable aluminium alloys," 2022.

[72] Q. Wang, Z. Li, S. Pang, X. Li, C. Dong, and P. K. Liaw, "Coherent Precipitation and Strengthening in Compositionally Complex Alloys: A Review," *Entropy*, vol. 20, no. 11. 2018, doi: 10.3390/e20110878.

[73] O. Engler, C. D. Marioara, Y. Aruga, M. Kozuka, and O. R. Myhr, "Effect of natural ageing or pre-ageing on the evolution of precipitate structure and strength during age hardening of Al–Mg–Si alloy AA 6016," *Mater. Sci. Eng. A*, vol. 759, pp. 520–529, 2019, doi: https://doi.org/10.1016/j.msea.2019.05.073.

[74] S. N. Khangholi, M. Javidani, A. Maltais, and X.-G. Chen, "Effects of natural aging and pre-aging on

the strength and electrical conductivity in Al-Mg-Si AA6201 conductor alloys," *Mater. Sci. Eng. A*, vol. 820, p. 141538, 2021, doi: https://doi.org/10.1016/j.msea.2021.141538.

[75] J. P. Holman, "Heat transfer." McGraw Hill Higher Education, 2010.

[76] L. A. Vorontsova, "Alyuminii i alyuminievye splavy v elektrotekhnicheskikh izdeliyakh [Aluminium and aluminum alloys in electrical products]," *Moscow: Energiya*, 1971.

[77] G. I. Meshchanov and I. B. Peshkov, "Innovative approaches in domestic cable engineering," *Russ. Electr. Eng.*, vol. 81, no. 1, pp. 1–8, 2010.

[78] A. Simar, Y. Bréchet, B. De Meester, A. Denquin, and T. Pardoen, "Sequential modeling of local precipitation, strength and strain hardening in friction stir welds of an aluminum alloy 6005A-T6," *Acta Mater.*, vol. 55, no. 18, pp. 6133–6143, 2007.

[79] K. Ma *et al.*, "Mechanical behavior and strengthening mechanisms in ultrafine grain precipitation-strengthened aluminum alloy," *Acta Mater.*, vol. 62, pp. 141–155, 2014, doi: https://doi.org/10.1016/j.actamat.2013.09.042.

[80] A. K. Gupta, D. J. Lloyd, and S. A. Court, "Precipitation hardening processes in an Al–0.4% Mg–1.3% Si–0.25% Fe aluminum alloy," *Mater. Sci. Eng. A*, vol. 301, no. 2, pp. 140–146, 2001.

[81] W. Gao and N. M. Sammes, *An introduction to electronic and ionic materials*. World Scientific, 1999.

[82] Z. S. Basinski, J. S. Dugdale, and A. Howie, "The electrical resistivity of dislocations," *Philos. Mag.*, vol. 8, no. 96, pp. 1989–1997, 1963.

[83] J. P. Hou *et al.*, "Nano-scale precipitates: The key to high strength and high conductivity in Al alloy wire," *Mater. Des.*, vol. 132, pp. 148–157, 2017, doi: https://doi.org/10.1016/j.matdes.2017.06.062.

[84] M. Vaseghi and H. S. Kim, "A combination of severe plastic deformation and ageing phenomena in Al–Mg–Si Alloys," *Mater. Des.*, vol. 36, pp. 735–740, 2012.

[85] S. Cheng, Y. H. Zhao, Y. T. Zhu, and E. Ma, "Optimizing the strength and ductility of fine structured 2024 Al alloy by nano-precipitation," *Acta Mater.*, vol. 55, no. 17, pp. 5822–5832, 2007.

[86] E. F. A. Zeid, "Mechanical and electrochemical characteristics of solutionized AA 6061, AA6013 and AA 5086 aluminum alloys," *J. Mater. Res. Technol.*, vol. 8, no. 2, pp. 1870–1877, 2019.

[87] S. Karabay, "Influence of AlB2 compound on elimination of incoherent precipitation in artificial aging of wires drawn from redraw rod extruded from billets cast of alloy AA-6101 by vertical direct

chill casting," *Mater. Des.*, vol. 29, no. 7, pp. 1364–1375, 2008, doi:
https://doi.org/10.1016/j.matdes.2007.06.004.

[88] Y.-L. Chang, F.-Y. Hung, and T.-S. Lui, "Study of microstructure and tensile properties of infrared-heat-treated cast-forged 6082 aluminum alloy," *J. Mater. Res. Technol.*, vol. 8, no. 1, pp. 173–179, 2019.

[89] B. WANG *et al.*, "Strengthening effects of microstructure evolution during early ageing process in Al-Mg-Si alloy," *Acta Met. Sin*, vol. 50, no. 6, pp. 685–690, 2014.

[90] Y. X. Lai, W. Fan, M. J. Yin, C. L. Wu, and J. H. Chen, "Structures and formation mechanisms of dislocation-induced precipitates in relation to the age-hardening responses of Al-Mg-Si alloys," *J. Mater. Sci. Technol.*, vol. 41, pp. 127–138, 2020, doi: https://doi.org/10.1016/j.jmst.2019.11.001.

[91] F. Qian *et al.*, "Enhanced nucleation and precipitation hardening in Al–Mg–Si(–Cu) alloys with minor Cd additions," *Mater. Sci. Eng. A*, vol. 792, p. 139698, 2020, doi:
https://doi.org/10.1016/j.msea.2020.139698.

[92] E. A. Mørtsell, S. J. Andersen, J. Friis, C. D. Marioara, and R. Holmestad, "Atomistic details of precipitates in lean Al–Mg–Si alloys with trace additions of Ag and Ge studied by HAADF-STEM and DFT," *Philos. Mag.*, vol. 97, no. 11, pp. 851–866, 2017.

[93] Y. Liu, Y. X. Lai, Z. Q. Chen, S. L. Chen, P. Gao, and J. H. Chen, "Formation of β''-related composite precipitates in relation to enhanced thermal stability of Sc-alloyed Al-Mg-Si alloys," *J. Alloys Compd.*, vol. 885, p. 160942, 2021, doi: https://doi.org/10.1016/j.jallcom.2021.160942.

[94] E. Christiansen, C. D. Marioara, B. Holmedal, O. S. Hopperstad, and R. Holmestad, "Nano-scale characterisation of sheared β'' precipitates in a deformed Al-Mg-Si alloy," *Sci. Rep.*, vol. 9, no. 1, p. 17446, 2019, doi: 10.1038/s41598-019-53772-4.

[95] C. D. Marioara, S. J. Andersen, J. Jansen, and H. W. Zandbergen, "Atomic model for GP-zones in a 6082 Al-Mg-Si system," *Acta Mater.*, vol. 49, no. 2, pp. 321–328, 2001, doi: 10.1016/S1359-6454(00)00302-5.

[96] K. Matsuda *et al.*, "High-resolution electron microscopy on the structure of Guinier-Preston zones in an Al-1.6 mass Pct Mg2Si alloy," *Metall. Mater. Trans. A*, vol. 29, no. 4, pp. 1161–1167, 1998, doi: 10.1007/s11661-998-0242-7.

[97] S. J. Andersen *et al.*, "Directionality and column arrangement principles of precipitates in Al-Mg-Si-

(Cu) and Al-Mg-Cu linked to line defect in Al," in *Materials Science Forum*, 2017, vol. 877, pp. 461–470.

[98] S. J. Andersen, C. D. Marioara, R. Vissers, A. Frøseth, and H. W. Zandbergen, "The structural relation between precipitates in Al–Mg–Si alloys, the Al-matrix and diamond silicon, with emphasis on the trigonal phase U1-MgAl2Si2," *Mater. Sci. Eng. A*, vol. 444, no. 1–2, pp. 157–169, 2007.

[99] S. J. Andersen, C. D. Marioara, A. Frøseth, R. Vissers, and H. W. Zandbergen, "Crystal structure of the orthorhombic U2-Al4Mg4Si4 precipitate in the Al–Mg–Si alloy system and its relation to the β' and β" phases," *Mater. Sci. Eng. A*, vol. 390, no. 1, pp. 127–138, 2005, doi: https://doi.org/10.1016/j.msea.2004.09.019.

[100] K. Matsuda *et al.*, "Precipitation sequence of various kinds of metastable phases in Al-1.0mass% Mg2Si-0.4mass% Si alloy," *J. Mater. Sci.*, vol. 35, no. 1, pp. 179–189, 2000, doi: 10.1023/A:1004769305736.

[101] S. D. Dumolt, D. E. Laughlin, and J. C. Williams, "Formation of a modified β' phase in aluminum alloy 6061," *Scr. Metall.*, vol. 18, no. 12, pp. 1347–1350, 1984, doi: https://doi.org/10.1016/0036-9748(84)90362-4.

[102] R. Vissers, M. A. van Huis, J. Jansen, H. W. Zandbergen, C. D. Marioara, and S. J. Andersen, "The crystal structure of the β' phase in Al-Mg-Si alloys," *Acta Mater.*, vol. 55, no. 11, pp. 3815–3823, 2007, doi: 10.1016/j.actamat.2007.02.032.

[103] R. Vissers, M. A. v van Huis, J. Jansen, H. W. Zandbergen, C. D. Marioara, and S. J. Andersen, "The crystal structure of the β' phase in Al–Mg–Si alloys," *Acta Mater.*, vol. 55, no. 11, pp. 3815–3823, 2007.

[104] N. A. Bul'enkov, A. G. Yakovenko, and O. M. Ul'yanikhina, "X-ray diffraction study of the Mg2Si-Mg2Ge system," *J. Struct. Chem.*, vol. 11, no. 6, pp. 1059–1061, 1971.

[105] L. Vogl, P. Schweizer, J. Donohue, and A. M. Minor, "Correlated 4D-STEM and EDS for the Classification of Fine Beta-Precipitates in Aluminum Alloy AA 6063-T6," *Available SSRN 4804289*.

[106] V. Beloshenko, I. Vozniak, Y. Beygelzimer, Y. Estrin, and R. Kulagin, "Severe plastic deformation of polymers," *Mater. Trans.*, vol. 60, no. 7, pp. 1192–1202, 2019.

[107] M. Naseri, A. Hassani, and M. Tajally, "Fabrication and characterization of hybrid composite strips with homogeneously dispersed ceramic particles by severe plastic deformation," *Ceram. Int.*,

vol. 41, no. 3, pp. 3952–3960, 2015.

[108]   L. Krämer, K. S. Kormout, D. Setman, Y. Champion, and R. Pippan, "Production of bulk metallic glasses by severe plastic deformation," *Metals (Basel).*, vol. 5, no. 2, pp. 720–729, 2015.

[109]   Y. Ikoma, "Severe plastic deformation of semiconductor materials using high-pressure torsion," *Mater. Trans.*, vol. 60, no. 7, pp. 1168–1176, 2019.

[110]   A. Mazilkin *et al.*, "Mechanisms of structural evolution of laminates with immiscible components under high-pressure torsion," *Acta Mater.*, vol. 269, p. 119804, 2024, doi: https://doi.org/10.1016/j.actamat.2024.119804.

[111]   I. Sabirov and R. Pippan, "Characterization of tungsten fragmentation in a W–25% Cu composite after high-pressure torsion," *Mater. Charact.*, vol. 58, no. 10, pp. 848–853, 2007.

[112]   I. Sabirov and R. Pippan, "Formation of a W–25% Cu nanocomposite during high pressure torsion," *Scr. Mater.*, vol. 52, no. 12, pp. 1293–1298, 2005.

[113]   S. K. Mohapatra, V. Ranjan, and S. Tripathy, "Study of severe plastic deformations of metallic materials:- A move towards Amorphization," *Mater. Today Proc.*, vol. 56, pp. 735–741, 2022, doi: https://doi.org/10.1016/j.matpr.2022.02.244.

[114]   R. Valiev, D. Gunderov, A. P. Zhilyaev, A. G. Popov, and V. G. Pushin, "Nanocrystallization induced by severe plastic deformation of amorphous alloys," *J. Metastable Nanocrystalline Mater.*, vol. 22, pp. 21–26, 2004.

[115]   A. Mazilkin, B. Straumal, A. Kilmametov, P. Straumal, and B. Baretzky, "Phase Transformations Induced by Severe Plastic Deformation," *Mater. Trans.*, vol. 60, no. 8, pp. 1489–1499, 2019, doi: 10.2320/matertrans.MF201938.

[116]   B. B. Straumal *et al.*, "Structure refinement and fragmentation of precipitates under severe plastic deformation: A review," *Materials (Basel).*, vol. 15, no. 2, p. 601, 2022.

[117]   J. M. Rosalie, P. Ghosh, J. Guo, O. Renk, and Z. Zhang, "Microstructural and texture evolution of copper-(chromium, molybdenum, tungsten) composites deformed by high-pressure-torsion," *Int. J. Refract. Met. Hard Mater.*, vol. 75, pp. 137–146, 2018.

[118]   Y. Ito and Z. Horita, "Microstructural evolution in pure aluminum processed by high-pressure torsion," *Mater. Sci. Eng. A*, vol. 503, no. 1–2, pp. 32–36, 2009.

[119] B. B. Straumal *et al.*, "Structure and properties of nanograined Fe–C alloys after severe plastic deformation," *Adv. Eng. Mater.*, vol. 13, no. 6, pp. 463–469, 2011.

[120] S. M. Ghalehbandi, M. Malaki, and M. Gupta, "Accumulative roll bonding—a review," *Appl. Sci.*, vol. 9, no. 17, p. 3627, 2019.

[121] Y. Beygelzimer, R. Kulagin, Y. Estrin, L. S. Toth, H. S. Kim, and M. I. Latypov, "Twist extrusion as a potent tool for obtaining advanced engineering materials: a review," *Adv. Eng. Mater.*, vol. 19, no. 8, p. 1600873, 2017.

[122] M. Richert, Q. Liu, and N. Hansen, "Microstructural evolution over a large strain range in aluminium deformed by cyclic-extrusion–compression," *Mater. Sci. Eng. A*, vol. 260, no. 1–2, pp. 275–283, 1999.

[123] A. P. Zhilyaev, G. V Nurislamova, B.-K. Kim, M. D. Baró, J. A. Szpunar, and T. G. Langdon, "Experimental parameters influencing grain refinement and microstructural evolution during high-pressure torsion," *Acta Mater.*, vol. 51, no. 3, pp. 753–765, 2003.

[124] P. W. Bridgman, *Studies in large plastic flow and fracture: with special emphasis on the effects of hydrostatic pressure*. Harvard University Press, 1964.

[125] A. Drai and B. Aour, "Analysis of the temperature effect on the plastic strain of polymers during high pressure torsion (HPT) process," *Eurasia Proc. Sci. Technol. Eng. Math.*, no. 1, pp. 41–51, 2017.

[126] R. Z. Valiev, R. K. Islamgaliev, and I. V Alexandrov, "Bulk nanostructured materials from severe plastic deformation," *Prog. Mater. Sci.*, vol. 45, no. 2, pp. 103–189, 2000.

[127] N. Zhao, C. Ban, H. Wang, and J. Cui, "Optimized combination of strength and electrical conductivity of Al-Mg-Si alloy processed by ECAP with two-step temperature," *Materials (Basel).*, vol. 13, no. 7, p. 1511, 2020.

[128] R. Z. Valiev, M. Y. Murashkin, and I. Sabirov, "A nanostructural design to produce high-strength Al alloys with enhanced electrical conductivity," *Scr. Mater.*, vol. 76, pp. 13–16, 2014, doi: https://doi.org/10.1016/j.scriptamat.2013.12.002.

[129] X. Sauvage, E. V Bobruk, M. Y. Murashkin, Y. Nasedkina, N. A. Enikeev, and R. Z. Valiev, "Optimization of electrical conductivity and strength combination by structure design at the nanoscale in Al–Mg–Si alloys," *Acta Mater.*, vol. 98, pp. 355–366, 2015, doi:

https://doi.org/10.1016/j.actamat.2015.07.039.

[130]   Y. Ivanisenko *et al.*, "High Pressure Torsion Extrusion as a new severe plastic deformation process," *Mater. Sci. Eng. A*, vol. 664, pp. 247–256, 2016, doi: https://doi.org/10.1016/j.msea.2016.04.008.

[131]   B. Omranpour *et al.*, "Evolution of microstructure and hardness in aluminum processed by High Pressure Torsion Extrusion," *Mater. Sci. Eng. A*, vol. 762, p. 138074, 2019.

[132]   R. L. Smith and G. E. Sandly, "An Accurate Method of Determining the Hardness of Metals, with Particular Reference to Those of a High Degree of Hardness," *Proc. Inst. Mech. Eng.*, vol. 102, no. 1, pp. 623–641, Jun. 1922, doi: 10.1243/PIME_PROC_1922_102_033_02.

[133]   A. C. Fischer-Cripps and A. C. Fischer-Cripps, "Examples of nanoindentation testing," *Nanoindentation*, pp. 159–173, 2002.

[134]   M. Considère, "Mémoire sur l'emploi du fer et de l'acier dans les constructions," *(No Title)*, 1885.

[135]   W. D. Callister Jr and D. G. Rethwisch, *Callister's materials science and engineering*. John Wiley & Sons, 2020.

[136]   S. Tu, X. Ren, J. He, and Z. Zhang, "Stress–strain curves of metallic materials and post-necking strain hardening characterization: A review," *Fatigue Fract. Eng. Mater. Struct.*, vol. 43, no. 1, pp. 3–19, 2020.

[137]   "https://www.fischerinstrumentation.co.uk/products/material-conductivity-gauges/."

[138]   W. H. Bragg and W. L. Bragg, "The reflection of X-rays by crystals," *Proc. R. Soc. London. Ser. A, Contain. Pap. a Math. Phys. Character*, vol. 88, no. 605, pp. 428–438, 1913.

[139]   H. M. Rietveld, "A profile refinement method for nuclear and magnetic structures," *J. Appl. Crystallogr.*, vol. 2, no. 2, pp. 65–71, 1969.

[140]   J. P. Cline, M. H. Mendenhall, D. Black, D. Windover, and A. Henins, "The optics and alignment of the divergent beam laboratory X-ray powder diffractometer and its calibration using NIST Standard Reference Materials," *J. Res. Natl. Inst. Stand. Technol.*, vol. 120, p. 173, 2015.

[141]   M. Wojdyr, "Fityk: a general-purpose peak fitting program," *J. Appl. Crystallogr.*, vol. 43, no. 5, pp. 1126–1128, Oct. 2010, [Online]. Available: https://doi.org/10.1107/S0021889810030499.

[142]   N. R. Draper, *Applied regression analysis*. McGraw-Hill. Inc, 1998.

[143]   B. D. Cullity and R. Smoluchowski, "Elements of X-ray Diffraction," *Phys. Today*, vol. 10, no. 3, p. 50, 1957.

[144]   G. Ribárik, B. Jóni, and T. Ungár, "Global optimum of microstructure parameters in the CMWP line-profile-analysis method by combining Marquardt-Levenberg and Monte-Carlo procedures," *J. Mater. Sci. Technol.*, vol. 35, no. 7, pp. 1508–1514, 2019.

[145]   P. K. Gallagher and M. E. Brown, "Handbook of thermal analysis and calorimetry," 2003.

[146]   P. Gill, T. T. Moghadam, and B. Ranjbar, "Differential scanning calorimetry techniques: applications in biology and nanoscience," *J. Biomol. Tech. JBT*, vol. 21, no. 4, p. 167, 2010.

[147]   M. Rady and E. Arquis, "A comparative study of phase changing characteristics of granular phase change materials using DSC and T-history methods," *Fluid Dyn. Mater. Process.*, vol. 6, no. 2, pp. 137–152, 2010.

[148]   D. B. Williams, C. B. Carter, D. B. Williams, and C. B. Carter, *The transmission electron microscope*. Springer, 1996.

[149]   "https://microscopewiki.com/scanning-electron-microscope/."

[150]   S. Reyntjens and R. Puers, "A review of focused ion beam applications in microsystem technology," *J. micromechanics microengineering*, vol. 11, no. 4, p. 287, 2001.

[151]   "https://encyclopedia.pub/entry/45846."

[152]   A. J. Wilkinson and P. B. Hirsch, "Electron diffraction based techniques in scanning electron microscopy of bulk materials," *Micron*, vol. 28, no. 4, pp. 279–308, 1997.

[153]   Y. Kainuma, "The theory of Kikuchi patterns," *Acta Crystallogr.*, vol. 8, no. 5, pp. 247–257, 1955.

[154]   D. G. Coates, "Kikuchi-like reflection patterns obtained with the scanning electron microscope," *Philos. Mag. A J. Theor. Exp. Appl. Phys.*, vol. 16, no. 144, pp. 1179–1184, 1967.

[155]   K. Lee, "IMAGE BASED FE-MODELLING OF ELECTRON BACKSCATTER DIFFRACTION FOR ULTRASONIC WAVE PROPAGATION IN DISSIMILAR METAL WELDS."

[156]   B. L. Adams, S. I. Wright, and K. Kunze, "Orientation imaging: the emergence of a new microscopy," *Metall. Trans. A*, vol. 24, pp. 819–831, 1993.

[157]   J. B. Burns, A. R. Hanson, and E. M. Riseman, "Extracting straight lines," *IEEE Trans. Pattern Anal. Mach. Intell.*, no. 4, pp. 425–455, 1986.

[158]   K. Kunze, S. I. Wright, B. L. Adams, and D. J. Dingley, "Advances in automatic EBSP single orientation measurements," *Texture, Stress. Microstruct.*, vol. 20, no. 1–4, pp. 41–54, 1993.

[159]   P. Schweizer, "Gezielte Manipulation einzelner Defekte in Schichtkristallen und 2D-Materialien," 2019.

[160]   J. I. Goldstein, D. E. Newbury, J. R. Michael, N. W. M. Ritchie, J. H. J. Scott, and D. C. Joy, *Scanning electron microscopy and X-ray microanalysis*. springer, 2017.

[161]   D. Timpel, K. Scheerschmidt, and S. Ruvimov, "HREM simulations of particles and interfaces refined by molecular dynamics relaxations," in *European Materials Research Society Symposia Proceedings*, A. BORGHESI, U. M. GÖSELE, J. VANHELLEMONT, M. DJAFARI-ROUHANI, and A. M. B. T.-C. GUÉ H,N and O in Si and Characterization and Simulation of Materials and Processes, Eds. Oxford: Elsevier, 1996, pp. 101–107.

[162]   D. B. Williams and C. B. Carter, *The Transmission Electron Microscope*. Boston, MA: Springer US, 2009.

[163]   M. J. Mohn, "Energy-filtered TEM and low-loss EELS of 2D materials." Universität Ulm, 2020.

[164]   R. Erni, *Aberration-corrected imaging in transmission electron microscopy: An introduction*. World Scientific Publishing Company, 2015.

[165]   B. Fultz and J. M. Howe, *Transmission electron microscopy and diffractometry of materials*. Springer Science & Business Media, 2012.

[166]   R. Brydson, *Aberration-corrected analytical transmission electron microscopy*, vol. 280. Wiley Online Library, 2011.

[167]   C. Kübel and A. Thust, "TrueImage: a software package for focal-series reconstruction in HRTEM," in *Electron crystallography: Novel approaches for structure determination of nanosized materials*, 2006, pp. 373–392.

[168]   S. J. Pennycook and P. D. Nellist, *Scanning transmission electron microscopy: imaging and analysis*. Springer Science & Business Media, 2011.

[169]   J. A. Gott, "Methods BT - Defects in Self-Catalysed III-V Nanowires," J. A. Gott, Ed. Cham:

Springer International Publishing, 2022, pp. 39–60.

[170]   M. Weyland and D. A. Muller, "Tuning the convergence angle for optimum STEM performance," *arXiv Prepr. arXiv2008.12870*, 2020.

[171]   C. B. Carter and D. B. Williams, *Transmission electron microscopy: Diffraction, imaging, and spectrometry*. Springer, 2016.

[172]   P. Schlossmacher, D. O. Klenov, B. Freitag, and H. S. Von Harrach, "Enhanced detection sensitivity with a new windowless XEDS system for AEM based on silicon drift detector technology," *Micros. Today*, vol. 18, no. 4, pp. 14–20, 2010.

[173]   R. D. Deslattes, E. G. Kessler Jr, P. Indelicato, L. De Billy, E. Lindroth, and J. Anton, "X-ray transition energies: new approach to a comprehensive evaluation," *Rev. Mod. Phys.*, vol. 75, no. 1, p. 35, 2003.

[174]   "https://www.analyzetest.com/2021/03/13/a-to-z-of-energy-dispersive-x-ray-spectroscopy-eds/."

[175]   P. Schlossmacher, D. O. Klenov, B. Freitag, S. von Harrach, and A. Steinbach, "Nanoscale chemical compositional analysis with an innovative S/TEM-EDX system," *Microsc. Anal.*, vol. 5, 2010.

[176]   R. . Egerton, *Electron Energy Loss Spectroscopy in the Electron Microscope*. .

[177]   S. Porter and A. K. Datye, "6.10 - Imaging of single atom catalysts," J. Reedijk and K. R. B. T.-C. I. C. I. I. I. (Third E. Poeppelmeier, Eds. Oxford: Elsevier, 2023, pp. 222–243.

[178]   M. K. Miller, *Atom probe tomography: analysis at the atomic level*. Springer Science & Business Media, 2012.

[179]   D. J. Larson, T. J. Prosa, R. M. Ulfig, B. P. Geiser, and T. F. Kelly, "Local electrode atom probe tomography," *New York, US Springer Sci.*, vol. 2, p. 840, 2013.

[180]   G. Da Costa, "Chapter Six - Atom Probe Tomography: Detector Issues and Technology," W. Lefebvre-Ulrikson, F. Vurpillot, and X. B. T.-A. P. T. Sauvage, Eds. Academic Press, 2016, pp. 155–181.

[181]   M. K. Miller and M. G. Hetherington, "Local magnification effects in the atom probe," *Surf. Sci.*, vol. 246, no. 1–3, pp. 442–449, 1991.

[182]   F. Vurpillot, A. Bostel, and D. Blavette, "Trajectory overlaps and local magnification in three-dimensional atom probe," *Appl. Phys. Lett.*, vol. 76, no. 21, pp. 3127–3129, 2000.

[183]   A. Vella and J. Houard, "Chapter Eight - Laser-Assisted Field Evaporation," W. Lefebvre-Ulrikson, F. Vurpillot, and X. B. T.-A. P. T. Sauvage, Eds. Academic Press, 2016, pp. 251–278.

[184]   B. Gault *et al.*, "Atom probe tomography," *Nat. Rev. Methods Prim.*, vol. 1, no. 1, p. 51, 2021, doi: 10.1038/s43586-021-00047-w.

[185]   L. Rangel DaCosta *et al.*, "Prismatic 2.0 – Simulation software for scanning and high resolution transmission electron microscopy (STEM and HRTEM)," *Micron*, vol. 151, p. 103141, 2021, doi: https://doi.org/10.1016/j.micron.2021.103141.

[186]   K. Momma and F. Izumi, "VESTA 3 for three-dimensional visualization of crystal, volumetric and morphology data," *J. Appl. Crystallogr.*, vol. 44, no. 6, pp. 1272–1276, 2011.

[187]   R. Kulagin, Y. Beygelzimer, Y. Estrin, Y. Ivanisenko, B. Baretzky, and H. Hahn, "A Mathematical Model of Deformation under High Pressure Torsion Extrusion," *Metals (Basel).*, vol. 9, no. 3, 2019, doi: 10.3390/met9030306.

[188]   A. I. Almazrouee, K. J. Al-Fadhalah, S. N. Alhajeri, Y. Huang, and T. G. Langdon, "Effect of Long-Term Storage on Microstructure and Microhardness Stability in OFHC Copper Processed by High-Pressure Torsion," *Adv. Eng. Mater.*, vol. 21, no. 5, p. 1801300, 2019.

[189]   O. Renk, A. Hohenwarter, K. Edalati, and M. W. Kapp, "Saturation of grain fragmentation upon severe plastic deformation: Fact or fiction?," *Adv. Eng. Mater.*

[190]   D. Nugmanov, A. Mazilkin, H. Hahn, and Y. Ivanisenko, "Structure and Tensile Strength of Pure Cu after High Pressure Torsion Extrusion," *Metals (Basel).*, vol. 9, no. 10, 2019, doi: 10.3390/met9101081.

[191]   Y. Mahmoodkhani, M. A. Wells, W. J. Poole, L. Grajales, and N. Parson, "The development of grain structure during axisymmetric extrusion of AA3003 aluminum alloys," *Metall. Mater. Trans. A*, vol. 46, pp. 5920–5932, 2015.

[192]   W. Chrominski and M. Lewandowska, "Precipitation strengthening of Al-Mg-Si alloy subjected to multiple accumulative roll bonding combined with a heat treatment," *Mater. Des.*, vol. 219, p. 110813, 2022, doi: https://doi.org/10.1016/j.matdes.2022.110813.

[193]   T. Khelfa, J. A. Muñoz-Bolaños, F. Li, J. M. Cabrera-Marrero, and M. Khitouni, "Microstructure

and mechanical properties of AA6082-T6 by ECAP under warm processing," *Met. Mater. Int.*, vol. 26, pp. 1247–1261, 2020.

[194]   R. Kulagin, Y. Beygelzimer, Y. Estrin, Y. Ivanisenko, B. Baretzky, and H. Hahn, "A mathematical model of deformation under high pressure torsion extrusion," *Metals (Basel).*, vol. 9, no. 3, pp. 1–11, 2019, doi: 10.3390/met9030306.

[195]   J. D. Robson, "Deformation Enhanced Diffusion in Aluminium Alloys," *Metall. Mater. Trans. A*, vol. 51, no. 10, pp. 5401–5413, 2020, doi: 10.1007/s11661-020-05960-5.

[196]   H. J. Roven, M. Liu, and J. C. Werenskiold, "Dynamic precipitation during severe plastic deformation of an Al–Mg–Si aluminium alloy," *Mater. Sci. Eng. A*, vol. 483–484, pp. 54–58, 2008, doi: https://doi.org/10.1016/j.msea.2006.09.142.

[197]   N. Tian *et al.*, "Effect of precipitates on the mechanical performance of 7005 aluminum alloy plates," *Materials (Basel).*, vol. 15, no. 17, p. 5951, 2022.

[198]   H. J. Roven, M. Liu, and J. C. Werenskiold, "Dynamic precipitation during severe plastic deformation of an Al-Mg-Si aluminium alloy," *Mater. Sci. Eng. A*, vol. 483–484, no. 1-2 C, pp. 54–58, 2008, doi: 10.1016/j.msea.2006.09.142.

[199]   M. Liu *et al.*, "DSC analyses of static and dynamic precipitation of an Al–Mg–Si–Cu aluminum alloy," *Prog. Nat. Sci. Mater. Int.*, vol. 88, May 2015, doi: 10.1016/j.pnsc.2015.02.004.

[200]   M. Cai, D. P. Field, and G. W. Lorimer, "A systematic comparison of static and dynamic ageing of two Al–Mg–Si alloys," *Mater. Sci. Eng. A*, vol. 373, no. 1–2, pp. 65–71, 2004.

[201]   Z. Yang *et al.*, "Natural ageing clustering under different quenching conditions in an Al-Mg-Si alloy," *Scr. Mater.*, vol. 190, pp. 179–182, 2021.

[202]   T. Saito *et al.*, "Atomic structures of precipitates in Al–Mg–Si alloys with small additions of other elements," *Adv. Eng. Mater.*, vol. 20, no. 7, p. 1800125, 2018.

[203]   V. Fallah, B. Langelier, N. Ofori-Opoku, B. Raeisinia, N. Provatas, and S. Esmaeili, "Cluster evolution mechanisms during aging in Al–Mg–Si alloys," *Acta Mater.*, vol. 103, pp. 290–300, 2016, doi: https://doi.org/10.1016/j.actamat.2015.09.027.

[204]   W. Yang, M. Wang, R. Zhang, Q. Zhang, and X. Sheng, "The diffraction patterns from β" precipitates in 12 orientations in Al–Mg–Si alloy," *Scr. Mater.*, vol. 62, no. 9, pp. 705–708, 2010, doi: https://doi.org/10.1016/j.scriptamat.2010.01.039.

[205]   C. D. Marioara *et al.*, "HAADF-STEM study of β'-type precipitates in an over-aged Al–Mg–Si–Ag alloy," *Philos. Mag.*, vol. 92, no. 9, pp. 1149–1158, 2012.

[206]   H. E. Swanson, *Standard X-ray diffraction powder patterns*, vol. 25. US Department of Commerce, National Bureau of Standards, 1953.

[207]   P. Villars and L. D. Calvert, "Pearson's handbook of crystallographic data for intermediate phases," *Am. Soc. Met. Cleveland, OH*, 1985.

[208]   J. E. Post and D. L. Bish, "Rietveld refinement of crystal structures using powder X-ray diffraction data," *Mod. powder Diffr.*, vol. 20, pp. 277–308, 1989.

[209]   J. Gubicza, N. Q. Chinh, G. Krállics, I. Schiller, and T. Ungár, "Microstructure of ultrafine-grained fcc metals produced by severe plastic deformation," *Curr. Appl. Phys.*, vol. 6, no. 2, pp. 194–199, 2006, doi: 10.1016/j.cap.2005.07.039.

[210]   S. F. Fang, M. P. Wang, and M. Song, "An approach for the aging process optimization of Al–Zn–Mg–Cu series alloys," *Mater. Des.*, vol. 30, no. 7, pp. 2460–2467, 2009.

[211]   G. Purcek, H. Yanar, M. Demirtas, Y. Alemdag, D. V Shangina, and S. V Dobatkin, "Optimization of strength, ductility and electrical conductivity of Cu–Cr–Zr alloy by combining multi-route ECAP and aging," *Mater. Sci. Eng. A*, vol. 649, pp. 114–122, 2016.

[212]   C. H. Liu, J. Chen, Y. X. Lai, D. H. Zhu, Y. Gu, and J. H. Chen, "Enhancing electrical conductivity and strength in Al alloys by modification of conventional thermo-mechanical process," *Mater. Des.*, vol. 87, pp. 1–5, 2015.

[213]   Z. Horita, T. Fujinami, M. Nemoto, and T. G. Langdon, "Equal-channel angular pressing of commercial aluminum alloys: Grain refinement, thermal stability and tensile properties," *Metall. Mater. Trans. A*, vol. 31, no. 3, pp. 691–701, 2000, doi: 10.1007/s11661-000-0011-8.

[214]   C. You *et al.*, "Dislocations-induced precipitates and their effect on mechanical properties of Mg-Gd-Y-Zr alloy," *J. Magnes. Alloy.*, vol. 7, no. 3, pp. 414–418, 2019, doi: https://doi.org/10.1016/j.jma.2019.05.009.

[215]   A. J. Ardell, "On the coarsening of grain boundary precipitates," *Acta Metall.*, vol. 20, no. 4, pp. 601–609, 1972, doi: https://doi.org/10.1016/0001-6160(72)90015-6.

[216]   C. H. Liu *et al.*, "A tuning nano-precipitation approach for achieving enhanced strength and good ductility in Al alloys," *Mater. Des.*, vol. 54, pp. 144–148, 2014, doi:

https://doi.org/10.1016/j.matdes.2013.08.042.

[217]   V. Tavakkoli *et al.*, "Precipitate-mediated enhancement of mechanical and electrical properties in HPTE-processed Al–Mg–Si alloy," *Mater. Sci. Eng. A*, p. 146556, 2024, doi: https://doi.org/10.1016/j.msea.2024.146556.

[218]   M. W. Zandbergen, Q. Xu, A. Cerezo, and G. D. W. Smith, "Study of precipitation in Al-Mg-Si alloys by Atom Probe Tomography I. Microstructural changes as a function of ageing temperature," *Acta Mater.*, vol. 101, pp. 136–148, 2015, doi: 10.1016/j.actamat.2015.08.017.

[219]   M. Murayama, K. Hono, M. Saga, and M. Kikuchi, "Atom probe studies on the early stages of precipitation in Al–Mg–Si alloys," *Mater. Sci. Eng. A*, vol. 250, no. 1, pp. 127–132, 1998.

[220]   S. J. Andersen, H. W. Zandbergen, J. Jansen, C. TrÆholt, U. Tundal, and O. Reiso, "The crystal structure of the β" phase in Al–Mg–Si alloys," *Acta Mater.*, vol. 46, no. 9, pp. 3283–3298, 1998, doi: https://doi.org/10.1016/S1359-6454(97)00493-X.

[221]   S. J. Andersen, C. D. Marioara, R. Vissers, A. Frøseth, and H. W. Zandbergen, "The structural relation between precipitates in Al-Mg-Si alloys, the Al-matrix and diamond silicon, with emphasis on the trigonal phase U1-MgAl2Si2," *Mater. Sci. Eng. A*, vol. 444, no. 1–2, pp. 157–169, 2007, doi: 10.1016/j.msea.2006.08.084.

[222]   H. W. Zandbergen, S. J. Andersen, and J. Jansen, "Structure determination of Mg5Si6 particles in Al by dynamic electron diffraction studies," *Science (80-.).*, vol. 277, no. 5330, pp. 1221–1225, 1997.

[223]   A. G. Frøseth, R. Høier, P. M. Derlet, S. J. Andersen, and C. D. Marioara, "Bonding in mgsi and Al-Mg-Si compounds relevant to Al-Mg-Si alloys," *Phys. Rev. B*, vol. 67, no. 22, p. 224106, 2003.

[224]   S. Gulbrandsen-Dahl, K. O. Pedersen, C. Marioara, M. Kolar, and K. Marthinsen, "Effect of precipitates/effect of microstructure: mechanical characteristics of post-β" precipitates in Al–Mg–Si alloys," *Proc. 11th Intern. Conf. Alum. Alloy.*, pp. 1634–1640, 2008, [Online]. Available: https://www.scopus.com/inward/record.uri?eid=2-s2.0-84865234103&partnerID=40&md5=3adcf44ec1f3519da9aec75523d61dae.

[225]   K. Teichmann, C. D. Marioara, S. J. Andersen, and K. Marthinsen, "TEM study of β' precipitate interaction mechanisms with dislocations and β' interfaces with the aluminium matrix in Al–Mg–Si alloys," *Mater. Charact.*, vol. 75, pp. 1–7, 2013, doi: https://doi.org/10.1016/j.matchar.2012.10.003.

[226]   Z.-J. Zhao *et al.*, "Orientation relationship prediction and interfacial structure of a nano-scale Si-Mg2Si core–shell precipitate in an aluminum alloy," *Mater. Lett.*, vol. 350, p. 134967, 2023, doi: https://doi.org/10.1016/j.matlet.2023.134967.

[227]   N. L. Peterson, "Grain-boundary diffusion in metals," *Int. Met. Rev.*, vol. 28, no. 1, pp. 65–91, 1983.

[228]   T. Khelfa, M. A. Rekik, M. Khitouni, and J. M. Cabrera-Marrero, "Structure and microstructure evolution of Al–Mg–Si alloy processed by equal-channel angular pressing," *Int. J. Adv. Manuf. Technol.*, vol. 92, pp. 1731–1740, 2017.

[229]   A. P. Sekhar, A. Samaddar, A. B. Mandal, and D. Das, "Influence of Ageing on the Intergranular Corrosion of an Al–Mg–Si Alloy," *Met. Mater. Int.*, vol. 27, no. 12, pp. 5059–5073, 2021, doi: 10.1007/s12540-020-00843-1.

[230]   W. Yang, S. Ji, Z. Li, and M. Wang, "Grain boundary precipitation induced by grain crystallographic misorientations in an extruded Al–Mg–Si–Cu alloy," *J. Alloys Compd.*, vol. 624, pp. 27–30, 2015, doi: https://doi.org/10.1016/j.jallcom.2014.10.206.

[231]   G. Nurislamova, X. Sauvage, M. Murashkin, R. Islamgaliev, and R. Valiev, "Nanostructure and related mechanical properties of an Al–Mg–Si alloy processed by severe plastic deformation," *Philos. Mag. Lett.*, vol. 88, no. 6, pp. 459–466, 2008, doi: 10.1080/09500830802186938.

[232]   E. Christiansen, C. D. Marioara, K. Marthinsen, O. S. Hopperstad, and R. Holmestad, "Lattice rotations in precipitate free zones in an Al-Mg-Si alloy," *Mater. Charact.*, vol. 144, pp. 522–531, 2018, doi: https://doi.org/10.1016/j.matchar.2018.08.002.

[233]   B. D. Cullity, *Elements of X-ray Diffraction*. Addison-Wesley Publishing, 1956.

[234]   J. L. Murray, "The Al– Mg (aluminum– magnesium) system," *J. Phase Equilibria*, vol. 3, no. 1, pp. 60–74, 1982.

[235]   H. J. Axon and W. Hume-Rothery, "The lattice spacings of solid solutions of different elements in aluminium," *Proc. R. Soc. London. Ser. A. Math. Phys. Sci.*, vol. 193, no. 1032, pp. 1–24, 1948.

[236]   G. Lin, Z. Zhang, H. Wang, K. Zhou, and Y. Wei, "Enhanced strength and electrical conductivity of Al–Mg–Si alloy by thermo-mechanical treatment," *Mater. Sci. Eng. A*, vol. 650, pp. 210–217, 2016, doi: https://doi.org/10.1016/j.msea.2015.10.050.

[237]   I. Hamdi, Z. Boumerzoug, and F. Chabane, "Study of precipitation kinetics of an Al-Mg-Si alloy

using differential scanning calorimetry," *Acta Metall. Slovaca*, vol. 23, no. 2, pp. 155–160, 2017.

[238]   Y. Zheng, B. Luo, Z. Bai, and C. He, "Evolution of the Initial Precipitation and Strengthening Mechanism of Al-Mg-Si alloys," *Jom*, vol. 71, no. 12, pp. 4737–4745, 2019.

[239]   J. Zuo, L. Hou, J. Shi, H. Cui, L. Zhuang, and J. Zhang, "The mechanism of grain refinement and plasticity enhancement by an improved thermomechanical treatment of 7055 Al alloy," *Mater. Sci. Eng. A*, vol. 702, pp. 42–52, 2017, doi: https://doi.org/10.1016/j.msea.2017.06.106.

[240]   K. Teichmann *et al.*, "HRTEM study of the effect of deformation on the early precipitation behaviour in an AA6060 Al-Mg-Si alloy," *Philos. Mag.*, vol. 91, no. 28, pp. 3744–3754, 2011, doi: 10.1080/14786435.2011.593577.

[241]   R. S. Yassar, D. P. Field, and H. Weiland, "The effect of predeformation on the β" and β' precipitates and the role of Q' phase in an Al–Mg–Si alloy; AA6022," *Scr. Mater.*, vol. 53, no. 3, pp. 299–303, 2005, doi: https://doi.org/10.1016/j.scriptamat.2005.04.013.

[242]   J. Y. Yao, D. A. Graham, B. Rinderer, and M. J. Couper, "A TEM study of precipitation in Al–Mg–Si alloys," *Micron*, vol. 32, no. 8, pp. 865–870, 2001, doi: https://doi.org/10.1016/S0968-4328(00)00095-0.

[243]   P. H. Ninive *et al.*, "Detailed atomistic insight into the β" phase in Al–Mg–Si alloys," *Acta Mater.*, vol. 69, pp. 126–134, 2014, doi: https://doi.org/10.1016/j.actamat.2014.01.052.

[244]   K. Teichmann *et al.*, "The effect of deformation on the precipitation behaviour of an AlMgSi alloy-A HRTEM study [C]," in *KUMAI S, UMEZAWA O, TAKAYAMA Y, TSUCHIDA T, SATO T. Proceeding of the 12th Intematianal Conference of Aluminium Alloys. Japan Inst of Light Metals*, 2010, pp. 1027–1032.

[245]   S. G. Mazzini and J. C. Caretti, "Effect of deformation at elevated temperature before age-hardening on the mechanical properties of 2024 commercial aluminium alloy," *Scr. Metall. Mater.*, vol. 25, no. 8, pp. 1987–1990, 1991.

[246]   S. G. Mazzini, "Influence of deformation before artificial aging on properties of Al Cu Mg aluminum alloy," *Scr. Metall. Mater.*, vol. 31, no. 9, pp. 1127–1130, 1994.

[247]   Y. Weng, Z. Jia, L. Ding, S. Muraishi, X. Wu, and Q. Liu, "The multiple orientation relationships and morphology of β' phase in Al-Mg-Si-Cu alloy," *J. Alloys Compd.*, vol. 767, pp. 81–89, 2018, doi: https://doi.org/10.1016/j.jallcom.2018.07.077.

[248]   W. Yang, M. Wang, Y. Jia, and R. Zhang, "Studies of Orientations of β" Precipitates in Al-Mg-Si-(Cu) Alloys by Electron Diffraction and Transition Matrix Analysis," *Metall. Mater. Trans. A*, vol. 42, no. 9, pp. 2917–2929, 2011, doi: 10.1007/s11661-011-0680-5.

[249]   D. M. Fellicia, R. Rochiem, M. R. W. Putra, A. D. Utomo, and M. Rosmariana, "The effect of aging on microstructure, mechanical properties, and electrical conductivity of 6061 aluminium alloy for circuit breaker," in *2019 International Conference on Technologies and Policies in Electric Power & Energy*, 2019, pp. 1–5.

[250]   B. S. EN, "50183; Conductors for Overhead Lines-Aluminium-Magnesium-Silicon Alloy Wires," *Br. Stand.*, 2000.

[251]   Y. Zheng, B. Luo, W. Xie, and W. Li, "Microstructure evolution and precipitation behavior of Al-Mg-Si alloy during initial aging," *China Foundry*, vol. 20, no. 1, pp. 57–62, 2023.

[252]   X. Sauvage, E. V. Bobruk, M. Y. Murashkin, Y. Nasedkina, N. A. Enikeev, and R. Z. Valiev, "Optimization of electrical conductivity and strength combination by structure design at the nanoscale in Al-Mg-Si alloys," *Acta Mater.*, vol. 98, pp. 355–366, 2015, doi: 10.1016/j.actamat.2015.07.039.

[253]   J. G. Kaufman, "Understanding the aluminum temper designation system," *Introd. to Alum. Alloy. Tempers*, pp. 39 – 76, 2000, [Online]. Available: https://www.scopus.com/inward/record.uri?eid=2-s2.0-85030103049&partnerID=40&md5=f5ce1590397d78d6cfd9732775d28011.

[254]   J. P. Hou *et al.*, "Origin of abnormal strength-electrical conductivity relation for an Al–Fe alloy wire," *Materialia*, vol. 7, p. 100403, 2019, doi: https://doi.org/10.1016/j.mtla.2019.100403.

[255]   N. Hansen, "Hall–Petch relation and boundary strengthening," *Scr. Mater.*, vol. 51, no. 8, pp. 801–806, 2004, doi: https://doi.org/10.1016/j.scriptamat.2004.06.002.

[256]   S. Thangaraju, M. Heilmaier, B. S. Murty, and S. S. Vadlamani, "On the estimation of true Hall–Petch constants and their role on the superposition law exponent in Al alloys," *Adv. Eng. Mater.*, vol. 14, no. 10, pp. 892–897, 2012.

[257]   W. B. $$QPearso. Pearson William B., "(Pearson, William B.: A handbook of lattice spacings and structures of metals and alloys) : 2." 1967.

[258]   S. Nikzad Khangholi, M. Javidani, A. Maltais, and X.-G. Chen, "Optimization of mechanical

properties and electrical conductivity in Al–Mg–Si 6201 alloys with different Mg/Si ratios," *J. Mater. Res.*, vol. 35, no. 20, pp. 2765–2776, 2020, doi: 10.1557/jmr.2020.249.

[259]   B. Raeisinia, W. J. Poole, and D. J. Lloyd, "Examination of precipitation in the aluminum alloy AA6111 using electrical resistivity measurements," *Mater. Sci. Eng. A*, vol. 420, no. 1, pp. 245–249, 2006, doi: https://doi.org/10.1016/j.msea.2006.01.042.

[260]   W. Thomson, "LXIII. On the division of space with minimum partitional area," *London, Edinburgh, Dublin Philos. Mag. J. Sci.*, vol. 24, no. 151, pp. 503–514, Dec. 1887, doi: 10.1080/14786448708628135.

[261]   W. Wen, Y. Zhao, and J. G. Morris, "The effect of Mg precipitation on the mechanical properties of 5xxx aluminum alloys," *Mater. Sci. Eng. A*, vol. 392, no. 1, pp. 136–144, 2005, doi: https://doi.org/10.1016/j.msea.2004.09.059.

[262]   M. Kawasaki, H.-J. Lee, B. Ahn, A. P. Zhilyaev, and T. G. Langdon, "Evolution of hardness in ultrafine-grained metals processed by high-pressure torsion," *J. Mater. Res. Technol.*, vol. 3, no. 4, pp. 311–318, 2014, doi: https://doi.org/10.1016/j.jmrt.2014.06.002.

[263]   J. Weertman, *Dislocation based fracture mechanics*. World Scientific, 1996.

[264]   A. J. Ardell, "Precipitation hardening," *Metall. Trans. A*, vol. 16, pp. 2131–2165, 1985.

[265]   M. Fourmeau, C. D. Marioara, T. Børvik, A. Benallal, and O. S. Hopperstad, "A study of the influence of precipitate-free zones on the strain localization and failure of the aluminium alloy AA7075-T651," *Philos. Mag.*, vol. 95, no. 28–30, pp. 3278–3304, 2015.

[266]   J. Zhi, M. Guo, W. Meng, W. Zhou, L. Zhuang, and H. Lou, "Precipitation behavior of Al-Zn-Mg-Cu alloys with the coupled soft/hard micro-scale areas and its effect on properties," *Mater. Charact.*, vol. 218, p. 114476, 2024, doi: https://doi.org/10.1016/j.matchar.2024.114476.

[267]   A. K. Vasudévan and R. D. Doherty, "Grain boundary ductile fracture in precipitation hardened aluminum alloys," *Acta Metall.*, vol. 35, no. 6, pp. 1193–1219, 1987, doi: https://doi.org/10.1016/0001-6160(87)90001-0.

[268]   S. Peng, Y. Wei, and H. Gao, "Nanoscale precipitates as sustainable dislocation sources for enhanced ductility and high strength," *Proc. Natl. Acad. Sci.*, vol. 117, no. 10, pp. 5204–5209, 2020.

[269]   R. Hamano, "The effect of the precipitation of coherent and incoherent precipitates on the ductility and toughness of high-strength steel," *Metall. Trans. A*, vol. 24, pp. 127–139, 1993.

[270]   M. H. Mulazimoglu, R. A. L. Drew, and J. E. Gruzelski, "Electrical conductivity of aluminium-rich Al-Si-Mg alloys," *J. Mater. Sci. Lett.*, vol. 8, no. 3, pp. 297–300, 1989, doi: 10.1007/BF00725503.

[271]   C.-S. Tsao, C.-Y. Chen, U.-S. Jeng, and T.-Y. Kuo, "Precipitation kinetics and transformation of metastable phases in Al–Mg–Si alloys," *Acta Mater.*, vol. 54, no. 17, pp. 4621–4631, 2006, doi: https://doi.org/10.1016/j.actamat.2006.06.005.

[272]   M. Y. Murashkin, I. Sabirov, V. U. Kazykhanov, E. V Bobruk, A. A. Dubravina, and R. Z. Valiev, "Enhanced mechanical properties and electrical conductivity in ultrafine-grained Al alloy processed via ECAP-PC," *J. Mater. Sci.*, vol. 48, pp. 4501–4509, 2013.

[273]   M. Murashkin *et al.*, "Enhanced mechanical properties and electrical conductivity in ultrafine-grained Al 6101 alloy processed via ECAP-conform," *Metals (Basel).*, vol. 5, no. 4, pp. 2148–2164, 2015, doi: 10.3390/met5042148.

Appendix

Random error estimation for modeling of strength and electrical conductivity

The yield strength and electrical conductivity in terms of microstructural feature are successfully modeled. The random error for both models is estimated based on following formula:

Random error estimation for strength modeling

Below in the formulas, the bar sign indicates the corresponding average value, Δ designates random error of the corresponding value. The nomenclature of the variables can be found in the main text.

The equation for the strength modeling:

$$\sigma_{total} = \sigma_{Al} + \sigma_{disl} + \sigma_{prec} + \sigma_{GB} + \sum \sigma_i^{SS} \tag{A1}$$

a. contribution from dislocations

$$\overline{\sigma}_{disl} = \alpha M G b \overline{\Lambda}^{-1/2}, \Delta \overline{\sigma}_{disl} = \partial \sigma_{disl}/\partial \Lambda|_{\Lambda=\overline{\Lambda}} = \alpha M G b \Delta \overline{\Lambda}/2\sqrt{\overline{\Lambda}} \tag{A2}$$

b. contribution from grain boundaries

$$\overline{\sigma}_{GB} = k \overline{d}^{-1/2}, \Delta \overline{\sigma}_{GB} = \partial \sigma_{GB}/\partial d|_{d=\overline{d}} = k \Delta \overline{d}/2\overline{d}^{3/2} \tag{A3}$$

c. contribution from precipitates

For Orowan mechanism:

$$\overline{\sigma}_{prec} = 2M\beta Gb/\overline{L} = 2M\beta Gb\overline{N}^{1/3}, \Delta \overline{\sigma}_{prec} = \partial \sigma_{prec}/\partial N|_{N=\overline{N}} = 2M\beta Gb\Delta \overline{N}/3\overline{N}^{2/3} \tag{A4}$$

For shearing mechanism:

$$\overline{\sigma}_{prec}^{shear} = \frac{M}{b^2\sqrt{\beta G}}\sqrt{\overline{N}\cdot\overline{r}} \cdot F^{3/2} = \frac{2^{3/2}Mb\beta G}{r_c^{3/2}}\overline{N}^{1/2}\cdot\overline{r}^2 = A\cdot\overline{N}^{1/2}\cdot\overline{r}^2 \tag{A5}$$

$$\Delta\overline{\sigma}_{prec}^{shear} = A\left(0.5\overline{N}^{-1/2} \cdot \overline{r}^2 \cdot \Delta\overline{N} + 2\overline{N}^{1/2} \cdot \overline{r} \cdot \Delta\overline{\overline{r}}\right) \qquad (A6)$$

d. contribution from solutes

$$\overline{\sigma}_i^{SS} = k_i \overline{C}_i^{2/3}, \Delta\overline{\sigma}_i^{SS} = \partial\sigma_{prec}/\partial C|_{C=\overline{C}} = 2k_i\Delta\overline{C}/3\overline{C}^{1/3} \qquad (A7)$$

Error estimation of solid solution concentration is calculated as follows:

$$\overline{C}_i = \frac{m_{alloy}-m_{paticle}}{m_{alloy}} = 1 - m_p/m_a = 1 - \overline{N}\cdot\overline{V}_p\cdot\rho_p/V_a\cdot\rho_a, \qquad (A8)$$

$$\overline{C}_i = 1 - \overline{N}\cdot\overline{V}_p\cdot\rho_p/V_a\cdot\rho_a = 1 - \frac{\rho_p}{\rho_a}\frac{\pi\cdot\overline{d}^2\cdot\overline{l}\cdot\overline{N}}{4}, V_a = 1 \qquad (A9)$$

In case of indirect measurement, if some quantity $y = f(x_1, x_2, x_3)$, then random error can be calculated as:

$$\Delta y = \sqrt{\left(\frac{\partial f}{\partial x_1}\Delta x_1\right)^2 + \left(\frac{\partial f}{\partial x_2}\Delta x_2\right)^2 + \left(\frac{\partial f}{\partial x_3}\Delta x_3\right)^2}. \qquad (A10)$$

Then $\Delta\overline{C}$ can be found as

$$\Delta\overline{C} = \sqrt{\left(\pi\frac{\rho_p}{\rho_a}\right)^2\left[\left(2\cdot\overline{d}\cdot\overline{l}\cdot\overline{N}\cdot\Delta\overline{d}\right)^2 + \left(\overline{d}^2\cdot\overline{N}\cdot\Delta\overline{l}\right)^2 + \left(\overline{d}^2\cdot\overline{l}\cdot\Delta\overline{N}\right)^2\right]} \qquad (A11)$$

One can use this value to calculate the random error for the solute hardening $\Delta\overline{\sigma}_i^{SS}$.

$$\overline{\sigma}_i^{SS} = k_i\overline{C}_i^{2/3}, \Delta\overline{\sigma}_i^{SS} = \partial\sigma_{prec}/\partial C|_{C=\overline{C}} = 2k_i\Delta\overline{C}/3\overline{C}^{1/3} \qquad (A12)$$

The total error for the strength estimation:

$$\Delta\overline{\sigma}_{total} = \sqrt{\Delta\overline{\sigma}_{disl}^2 + \Delta\overline{\sigma}_{GB}^2 + \Delta\overline{\sigma}_{part}^2 + \Delta\overline{\sigma}_{SS}^2} \qquad (A13)$$

Random error estimation for electrical resistivity modeling:

The equation for the EC modeling:

$$\rho_{total} = \rho_{Al} + \Lambda\rho_{dis} + S_{GB}\rho_{GB} + \frac{\rho_{prec}}{\sqrt{(L)}} + \sum C_i^{sol}\ \rho_i^{sol} \tag{A14}$$

a. We neglected the he values of ρ_{dis} and ρ_{GB} due to their smallness.

b. Error value for the contribution from precipitates:

$$prec = \rho_{prec} \cdot \overline{L}^{-1/2}, \Delta prec = 1/2 \cdot \rho_{prec} \cdot \overline{L}^{-3/2} \cdot \Delta\overline{L}$$

$$\overline{L} = \overline{N}^{-1/3}, \qquad \Delta\overline{L} = 1/3 \cdot \overline{N}^{-4/3} \cdot \Delta\overline{N}$$

c. Error for the contribution from the solid solution:

$$solutes = \overline{C}_i^{sol}\rho_i^{sol}; \Delta solutes = \rho_i^{sol} \cdot \Delta\overline{C}_i^{sol}$$

Grain size distribution:
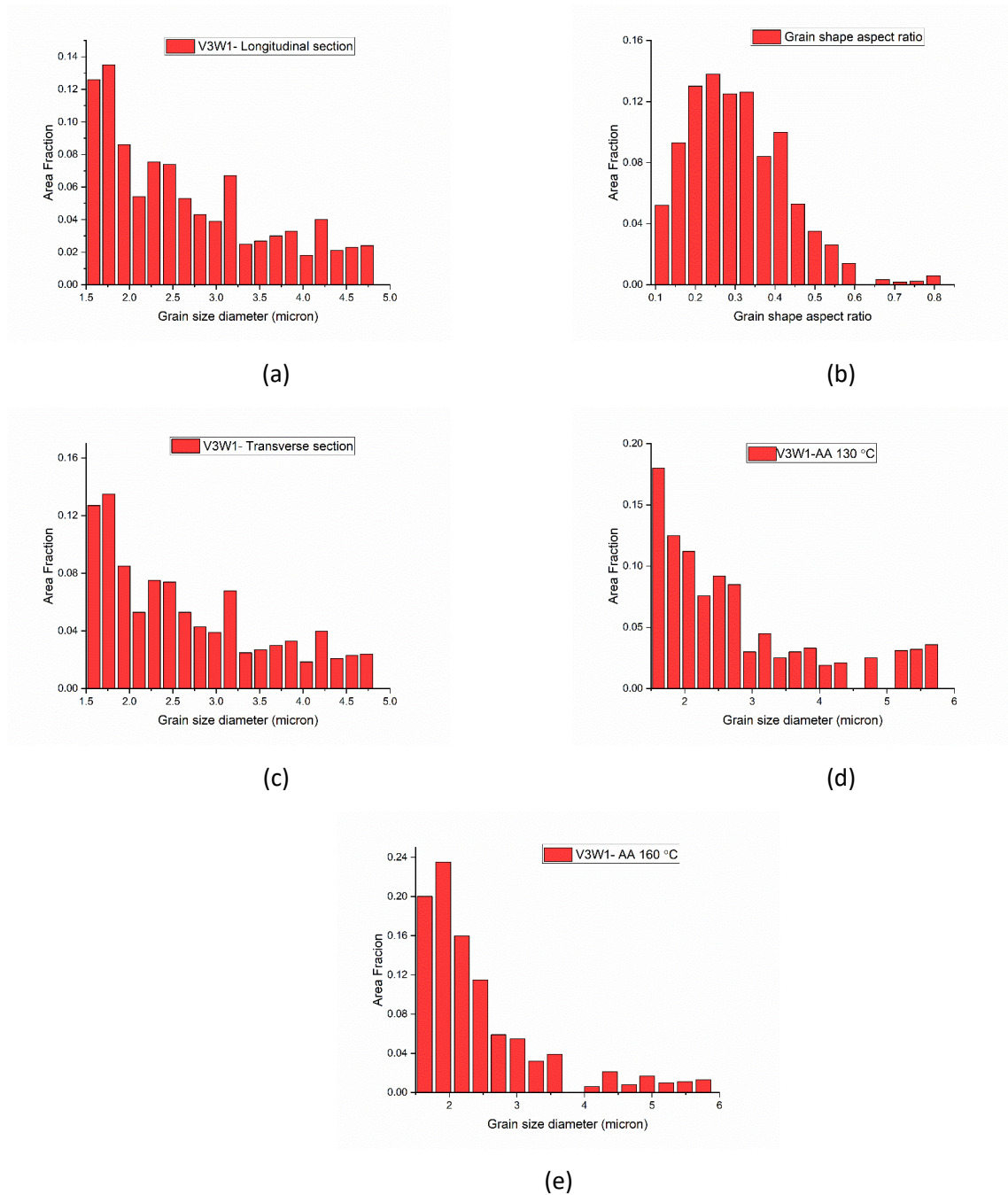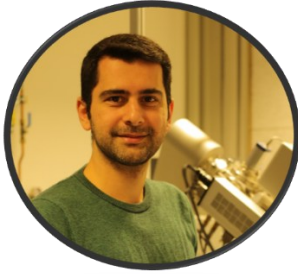

(a)

(b)

(c)

(d)

(e)

Figure A1. Grain size distribution plots for the deformed samples at the sections of (a) longitudinal direction with (b) corresponding aspect ratio, and (c) transverse direction; after AA at (d) 130 and (e) 160 °C at transverse direction.

Curriculum Vitae

Vahid Tavakkolisaiej

🏠 Institute of Nanotechnology (INT), Karlsruhe Institute of Technology (KIT)

✉ Vahid.Tavakkoli@kit.edu

☎ +49 (721) 608-22511, +49 (152) 279 00469

Technical expertise	
02/2020 - now	**Transmission Electron Microscopy (TEM):** FEI Themis Z and FEI Themis 300 • High Resolution TEM (HRTEM) and STEM (HRSTEM) • Electron Energy Loss Spectroscopy (EELS) • Energy Dispersive Spectroscopy (EDX) • 4D STEM
	Scanning Electron Microscopy (SEM): FEI Strata 400S and Zeiss Auriga 60 • Focus Ion Beam (FIB) • Electron Back Scatter Diffraction (EBSD)
	X-ray Diffraction (XRD): Bruker D8 Discover and Malvern Panalytical Empyrean series 3
	Computer skills • **TEM:** Digital Micrograph, TEM Imaging and Analysis (TIA), Velox, Prismatic (STEM simulation), JEMS • **Crystallography:** Vesta • **Others:** Microsoft office, Image J, Origin, and other daily Windows software

Education	
02/2020 – now	Ph.D.: Materials Science – Advanced Electron Microscopy and Spectroscopy
	Technical University of Darmstadt / working at Karlsruhe Institute of Technology
	• High-resolution study of nano-scale intermetallic phases in Al-Mg-Si (Main work)
	• TEM study of twining for tribologically induced stress on the single-crystalline High-Entropy Alloy CoCrFeMnNi (Collaboration)
	• Turbulent mixing of stacked solid-state multilayers by high pressure torsion (Collaboration)
09/2012 – 09/2014	M.S.: Mechanical Engineering – Nanostructured Materials
	University of Tehran – Iran (overall GPA 3.64/4)
	• Anisotropic characterization of highly-deformed Cu-Zn tubes
	• Investigation of energy absorption capacity of nanostructured tubes
09/2008 –09/2012	B.S: Mechanical Engineering – Materials Science
	Babol Noshirvani University of Technology, Babol – Iran (Overall GPA 3.18/4)

Awards
• Awarded DAAD scholarship, 2019
• Granted the "Iranian Nano-technology Initiative" Scholarship, 2015
• Member of Iranian Elite Foundation

Languages

- Persian: Native
- English: Fluent
- German: B1

Publications

- **V. Tavakkoli**, E. Boltynjuk, T. Scherer, A. Mazilkin, Y. Ivanisenko,T. Ungar, C. Kübel. "*Precipitate-mediated enhancement of mechanical and electrical properties in HPTE-processed Al–Mg–Si alloy*", Materials Science and Engineering A, **2024**

- **V. Tavakkoli**, L. Brouch, T. Scherer, A. Mazilkin, Y. Ivanisenko, T. Boll, C. Kübel. "*Atomic resolution analysis of precipitates formed in an HPTE deformed Al-Mg-Si alloy*" – Materials Science and Engineering A, **2024**

- A. Dollmann, J. Rau, C. Kübel, **V.Tavakkolli**, S. Eder, M. Feuerbacher, T. Liening, A.Kauffmann, C. Greiner. "*Probing tribological induced stress stated and distribution with deformation twins*" Communications Materials, **2024**.

- A. Mazilkin, **V. Tavakkoli**, O. Davydenko, Y. Beygelzimer, E. Boltynjuk, B. Straumal, B. Baretzky, Y. Estrin, R. Kulagin. "*Mechanisms of structural evolution of laminates with immiscible components under high-pressure torsion*" Acta Materialia, **2024**.

- **V. Tavakkoli**, A. Mazilkin, T. Scherer, M. Mail, Y. Beygelzimer, B. Baretzky, Y. Estrin, R. Kulagin, "*Instability of a molybdenum layer under deformation of a CuMoCu laminate by high-pressure torsion*" Materials Letters, Volume 302, (**2021**).

- **V. Tavakkoli**, M. Afrasiab, G. Faraji, and M. M. Mashhadi. "*Severe mechanical anisotropy of high-strength ultrafine grained Cu–Zn tubes processed by parallel tubular channel angular pressing (PTCAP)*" Materials Science and Engineering: A 625 (**2015**).